Technische Universität München

Physik Department E20

Molecular Nanoscience and Chemical Physics of Interfaces

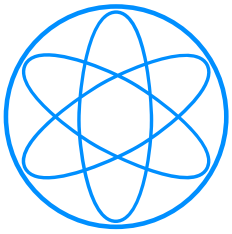

Free-base and metalated porphyrins on metal surfaces - a systematic X-ray spectroscopy and density functional theory investigation

Dissertation

Katharina Diller

TECHNISCHE UNIVERSITÄT MÜNCHEN

Lehrstuhl E20 -
Molekulare Nanowissenschaften & Chemische Physik von Grenzflächen

Free-base and metalated porphyrins on metal surfaces - a systematic X-ray spectroscopy and density functional theory investigation

Katharina Johanna Diller

Vollständiger Abdruck der von der Fakultät für Physik der Technischen Universität München zur Erlangung des akademischen Grades eines Doktors der Naturwissenschaften (Dr. rer. nat.) genehmigten Dissertation.

Vorsitzender:	Univ.-Prof. Dr. Martin Zacharias
Prüfer der Dissertation:	1. Univ.-Prof. Dr. Johannes Barth
	2. Univ.-Prof. Dr. Karsten Reuter

Die Promotion wurde am 10.04.2013 bei der Technischen Universität München eingereicht und durch die Fakultät für Physik am 29.04.2013 angenommen.

Abstract

Tailoring interfacial hybrid systems comprising complex molecules on solid surfaces for possible applications (e.g., solar cells, catalysts, nano-electronics) can be very challenging in view of the multiple factors contributing to the intricate interplay between molecule-molecule and molecule-substrate interactions. The functional species studied in this work, the porphyrins, are a very versatile class of molecules, which exhibit a high degree of flexibility. This thesis addresses how the physicochemical properties, notably the molecular conformation and the electronic structure, of adsorbed porphyrins are influenced by (i) the metalation of the macrocycle, (ii) the substituents, (iii) the nature of the substrate and (iv) the preparation conditions by means of X-ray spectroscopy methods (XPS and NEXAFS). Employing comprehensive density functional theory (DFT) calculations proves to be crucial for a detailed peak assignment of the obtained spectroscopic signatures. A novel metalation technique, the self-metalation, is described and the reaction pathway of metalation using metal-organic chemical vapor deposition is elucidated. In addition, it is shown that the oxidation state of the gold-tetraphenylporphyrin is preserved upon adsorption on a Au(111) surface, which is important for certain types of medical applications. Finally, the templated growth of the macrocyclic prototype free-base porphine is characterized. The orientation of the molecules is found to depend on both the kind of substrate and its temperature during deposition. Molecule-molecule interactions in the multilayer are explicitly taken into account by DFT calculations of stacked porphines, which provide an explanation for the temperature-dependent reorientation of the porphine multilayers.

Kurzzusammenfassung

Hybrid-Systeme aus komplexen Molekülen auf Festkörperoberflächen auf mögliche Anwendungen (z.B. Solarzellen, Katalysatoren, Naonelektronik) zuzuschneiden, stellt in Anbetracht der vielen Faktoren, die zum komplexen Zusammenspiel von Molekül-Molekül- und Molekül-Substrat-Wechselwirkungen beitragen, eine besondere Herausforderung dar. Die in dieser Arbeit untersuchten funktionellen Moleküle, die Porphyrine, sind sehr wandelbar und weisen einen hohen Grad an Flexibilität auf. Die vorliegende Arbeit untersucht mit Röntgenspektroskopiemethoden (XPS und NEXAFS) wie die physikochemischen Eigenschaften, genauer gesagt die Konformation und elektronische Struktur der adsorbierten Porphyrine, beeinflusst werden durch (i) die Metallierung des Makrozyklus, (ii) die Substituenten, (iii) die Art des Substrats und (iv) die Präparationsbedingungen. Die Verwendung von Dichtefunktionaltheorie-Rechnungen erweist sich dabei als grundlegend für das Verständnis der gemessenen spektroskopischen Signaturen. Eine neue Metallierungsmethode, die Selbst-Metallierung, wird genauso beschrieben wie der Reaktionsmechanismus einer Metallierung durch metallorganische chemische Gasphasenabscheidung. Weiterhin wird gezeigt, dass der Oxidationszustand des Gold-Tetraphenylporphyrins bei der Adsorption auf einer Au(111) Oberfläche erhalten bleibt, eine Tatsache, die wichtig für bestimmte medizinische Anwendungen ist. Schließlich wird das templatgestützte Wachstum des allen Porphyrinen zugrunde liegenden Macrozyklus (2H-Porphin) charakterisiert. Dabei wurde festgestellt, dass die Orientierung der Moleküle sowohl von der Art des Substrats wie auch von dessen Temperatur während des Aufdampfens abhängt. Molekül-Molekül-Wechselwirkungen in der Multilage werden bei den DFT-Rechnungen explizit berücksichtigt, welche eine Erklärung für die temperaturabhängige Umorientierung der Porphin-Multilagen liefern.

List of Figures

1.1 Overview Porphyrins 2
1.2 Illustration: Porphyrin on Surface 3
1.3 Overview over the experimental techniques used in this thesis . 4

2.1 (a) Photoelectric effect, (b) Schematics: XPS experiment 8
2.2 (a) Shake-up process, (b) Shake-off process, (c) Auger decay . . 11
2.3 NEXAFS: principle 14
2.4 Angular parameters in NEXAFS 16
2.5 NEXAFS: polarization dependence 17
2.6 Basis sets: STO, GTO, CGTO 25

3.1 UHV end station at the HE-SGM beamline at BESSY II 30
3.2 Molecule evaporators 33
3.3 XPS analysis: (a) Shirley background, (b) linear background . . 38
3.4 NEXAFS analysis 40
3.5 Unit cell for stacking of 2H-P molecules 47

4.1 Structural formulas of 2H-TPP/2H-P and Cu-TPP/Cu-P 50
4.2 Nomenclature of angles for description of adsorption geometries 51
4.3 Self-metalation of 2H-TPP/Cu(111): N1s XP spectra 53
4.4 Angle-dependence of N1s XP spectra 54
4.5 Self-metalation of 2H-TPP/Cu(111): NEXAFS spectra 57
4.6 Calculated 2H-TPP and Cu-TPP NEXAFS spectra 59
4.7 Molecular orbitals of 2H-TPP and Cu-TPP 64
4.8 2H-TPP multilayer: adsorption angles 66
4.9 2H-TPP monolayer: adsorption angles 68
4.10 Adsorption geometries of 2H-TPP and Cu-TPP/Cu(111) 71
4.11 STM images of porphines on Cu(111). 75
4.12 2H-P/Cu(111): Nearest neighbor distributions 76
4.13 N1s XP spectra of 2H-P on Cu(111). 78

4.14 2H-P/Cu(111): XPS N1s data of submonolayer metalation . . . 80
4.15 2H-P/Cu(111): Angle-dependence of XPS N1s data. 82
4.16 Angle-resolved N and C K-edge NEXAFS spectra of 2H-P . . . 84
4.17 Simulated C K-edge NEXAFS spectra of 2H-P and Cu-P 86

5.1 Molecules: 2H-TPP, 2H-TPP^{cd}, $Ru_3(CO)_{12}$ and Ru-TPP^{cd} . . . 94
5.2 C1s and N1s XP spectra of Ru(CO)TPP deposited on Ag(111) . 95
5.3 NEXAFS C K-edge spectra of Ru-TPP/Ag(111). 97
5.4 XPS data of an annealing series of $Ru_3(CO)_{12}$/ Ag(111) 98
5.5 Metalation of 2H-TPP/Ag(111) with $Ru_3(CO)_{12}$ 99
5.6 NEXAFS C K-edge data of partially metalated submonolayers of 2H-TPP and 2H-P 101
5.7 Metalation of 2H-TPP^{cd}/Ag(111) with $Ru_3(CO)_{12}$. 102
5.8 Metalation of 2H-P/Ag(111) with $Ru_3(CO)_{12}$ 104

6.1 C1s and Au4f XPS spectra of $[Au^{III}(TPP)]^+Cl^-$ 108

7.1 Model of 2H-porphine (2H-P) 112
7.2 XPS signatures of 2H-P 114
7.3 Influence of data set choice on XPS signatures 115
7.4 NEXAFS C K-edge signatures of 2H-P 117
7.5 NEXAFS N K-edge signatures of 2H-P 118
7.6 Final state orbitals 120
7.7 Limited growth of 2H-P on Cu(111) at RT 123
7.8 Growth of 2H-P on Cu(111) 125
7.9 Room temperature growth of 2H-P on Ag(111) 127
7.10 Reorientation of 2H-P on Ag(111) and Cu(111) 130
7.11 High resolution carbon NEXAFS and XPS data of a 2H-P multilayer on Ag(111) 131
7.12 Influence of FWHM values on the simulated spectra 133
7.13 Photon energy dependence of XPS C1s spectra 134
7.14 Porphine dimers 136
7.15 XPS calculations for porphine dimers 140
7.16 XPS spectra for different molecule-molecule distances 141
7.17 XPS Cl2p spectra 143
7.18 Self-metalation of differently oriented 2H-P layers. 146
7.19 Summary of the growth and reorientation of 2H-P multilayers . 148

8.1 Summary 151
A.1 Optimized geometry: 2H-TPP 155

A.2 Optimized geometry: Cu-TPP 156
A.3 Optimized geometry: 2H-P 157
A.4 Optimized geometry: Cu-P 158
A.5 NEXAFS background subtraction 159
A.6 2H-P/Ag(111): XPS background subtraction 160

List of Tables

3.1 Evaporation parameters 34
3.2 Parameters for XPS measurements 36
3.3 Basis set overview StoBe 43
3.4 StoBe calculation: correction shifts 45
3.5 Basis set overview FHI-aims 45

4.1 N1s XPS energies for a multilayer 2H-TPP/Cu(111) 55
4.2 2H-TPP N K-edge NEXAFS spectrum: peak assignment 63
4.3 2H-TPP/Cu(111): adsorption angles 70
4.4 Cu-TPP N K-edge NEXAFS spectrum: peak assignment 72

6.1 XPS binding energies of $[Au^{III}(TPP)]^{+}Cl^{-}$ samples 109

7.1 Calculated ionization energies for nitrogen and carbon species in 2H-P 113
7.2 Peak assignment for the 2H-P C K-edge NEXAFS spectrum . . 119
7.3 Peak assignment for the 2H-P N K-edge NEXAFS spectrum . . 121
7.4 Details of the optimized dimer geometries. 137
7.5 Adsorption energies 139
7.6 Adsorption energies and molecule-molecule distances 139
7.7 Binding energies of oxygen and chlorine contaminants. 142
7.8 Quantitative analysis of Cl contaminations. 144

Contents

Abstract i

Kurzzusammenfassung ii

List of Figures iii

List of Tables vi

1 Introduction 1

2 Methods 7

2.1 X-ray Photoelectron Spectroscopy (XPS) 7

2.1.1 Principle 7

2.1.2 Binding energies 9

2.1.3 Intensities 12

2.2 NEXAFS spectroscopy 13

2.2.1 Principle 13

2.2.2 Polarization dependence 15

2.3 Density functional theory (DFT) 18

2.3.1 Kohn-Sham equations 18

2.3.2 Exchange-Correlation Functionals 22

2.3.3 Basis Sets 23

2.3.4 Excited state calculations 26

2.3.5 van-der-Waals corrections 27

3 Experimental and Computational Details 29

3.1 Experimental Details 29

3.1.1 Vacuum systems 29

3.1.2 Sample preparation and measurements 31

3.1.3 Data analysis 38

3.2 Computational Details 42

3.2.1 StoBe . . . 42
3.2.2 FHI-aims . . . 45

4 Self-Metalation 49
4.1 Introduction . . . 49
4.2 2H-TPP on Cu(111) . . . 52
4.2.1 Self-metalation . . . 52
4.2.2 Electronic Properties . . . 61
4.3 2H-P on Cu(111) . . . 74
4.3.1 STM . . . 74
4.3.2 XPS . . . 77
4.3.3 NEXAFS . . . 83
4.4 Conclusions . . . 88

5 Metalation with $Ru_3(CO)_{12}$ 93
5.1 Introduction . . . 93
5.2 Ru(CO)TPP on Ag(111) . . . 94
5.3 $Ru_3(CO)_{12}$ on Ag(111) . . . 97
5.4 2H-TPP and $Ru_3(CO)_{12}$ on Ag(111) . . . 98
5.5 2H-P on Ag(111) . . . 103
5.6 Conclusions . . . 105

6 Adsorption of a gold porphyrin compound on Au(111) 107

7 Growth and reorientation of 2H-P on Ag(111) and Cu(111) 111
7.1 Introduction . . . 111
7.2 Spectroscopic signatures . . . 112
7.3 Growth . . . 122
7.3.1 Growth on Cu(111) . . . 122
7.3.2 Growth on Ag(111) . . . 126
7.3.3 Reorientation . . . 129
7.4 Influence of different parameters on the C1s XP spectra . . . 131
7.4.1 Influence of broadening values . . . 132
7.4.2 Influence of the molecular orientation . . . 132
7.4.3 Influence of the molecular stacking . . . 135
7.5 Role of impurities . . . 142
7.6 Influence of the growth mode on the self-metalation . . . 145
7.7 Summary . . . 146

8 Conclusions and Outlook 149

Appendix **155**
A.1 Optimized molecule geometries 155
A.2 NEXAFS background subtraction 159
A.3 2H-P/Ag(111): background subtraction 160
A.4 Used software 161

List of publications **163**

Bibliography **165**

Acknowledgements **191**

Chapter 1

Introduction

Thinking about surfaces, immediately macroscopic applications like coatings (glasses, textiles, tools) and catalysts or physical effects like friction and surface tension come to mind. Modern surface science[1] as a scientific discipline, however, is directed towards the investigation of atomistic systems: Commonly the topmost layers of clean, well-defined crystals and their interaction with adsorbates are studied.[2] The raise of semiconductor technology in the early days of surface science certainly played a large part in the success of the discipline.[1] The ultimate goal is to understand and control the behavior of surface-adsorbate systems which paves the way to the deliberate construction of applications, e.g., molecular sensors,[3] nanoelectronics,[4] optoelectronics,[5] data storage,[6] organic solar cells[7,8] and heterogeneous catalysis.[9,10]

Over the years, numerous systems comprising molecular layers and architectures at interfaces have been studied with both experimental and theoretical methods. In order to tailor their functionality to specific requirements, it is necessary to use classes of versatile molecules which can be tuned accordingly. A class of molecules which fulfills this prerequisite are porphyrins. Accordingly, they attracted a great deal of attention in recent years as evidenced by an increasingly large number of corresponding publications.

All porphyrins comprise an aromatic tetrapyrrole macrocycle, which consists of four pyrrole rings connected via methine bridges. The prototype unit *free-base porphine (2H-P)* (Fig. 1.1, top) consists only of this macrocycle. All other porphyrins can be constructed by inserting a metal atom in the center (*metalloporphyrin*) and/or attaching additional substituents to the basic macrocycle (Fig. 1.1, bottom). *Free-base porphyrins* are characterized by two pyrrolic (-NH-) and two iminic (=N-) nitrogen atoms. Porphyrins exhibit a high degree of flexibility with both the basic macrocycle and attached substituents showing bending and out of plane rotation in response to different

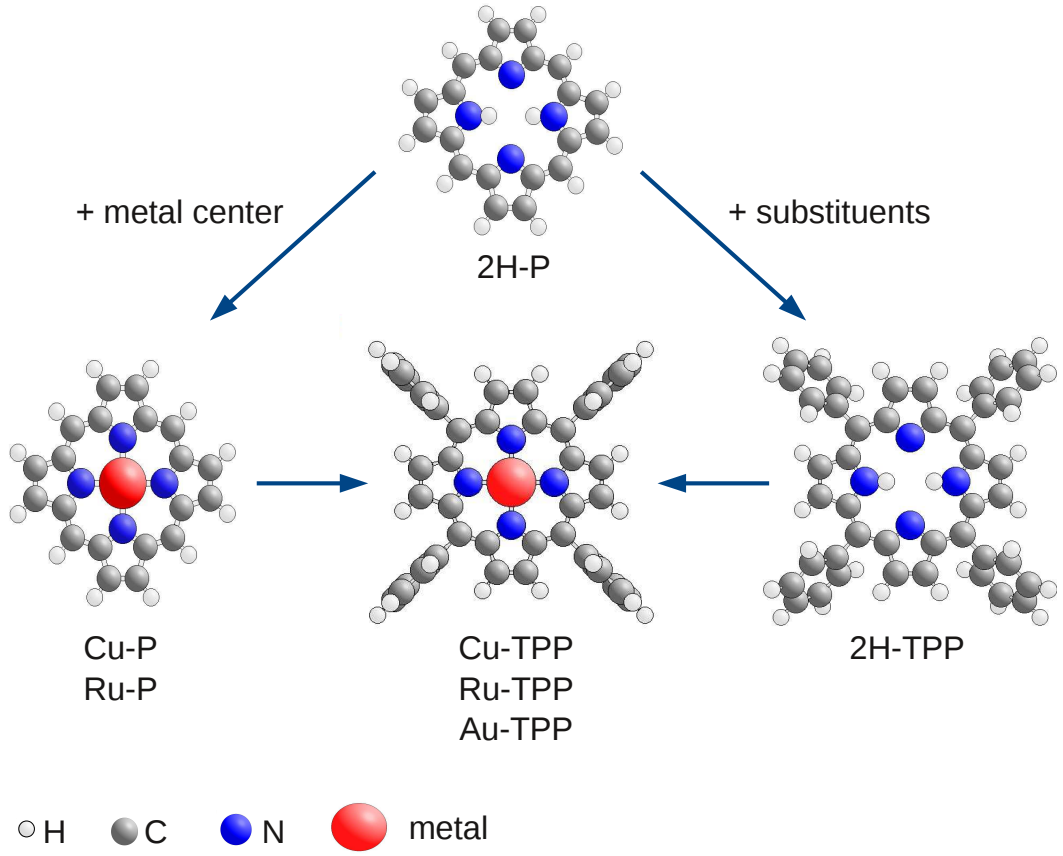

Figure 1.1: Overview over the class of porphyrins. The prototype unit *free-base porphine (2H-P)* is displayed on top. Other porphyrin compounds are formed by inserting a metal ion in the center (left and middle) and/or attaching substituents (right and middle). Under the corresponsing schematics the compounds studied in this work are listed. These range from the free-base porphine and the copper and ruthenium metalated porphines to phenyl meso-substituted free-base and metalated tetraphenylporphyrins.

chemical environments (Fig. 1.2). The conformational flexibility plays an important role in self-assembly[11] and the attachment of ligands.[12,13]

Many porphyrin compounds occur naturally, for example chlorophyll (Mg-center),[14] which is responsible for photosynthesis, or hemeproteins (Fe-center),[15] which for example transport respiratory gases in the blood of mammals. As the functional properties of porphyrins can be tuned by adsorption on (solid) surfaces, porphyrin-metal interfaces are ideal to explore prototype anchored coordination complexes and general aspects of surface-confined coordination chemistry.[16–18] The insight gained by the study of porphyrins on surfaces enables the control of their electronic properties[19,20] and inherent conformational flexibility, which plays an important role for the attachment of ligands[12,13]

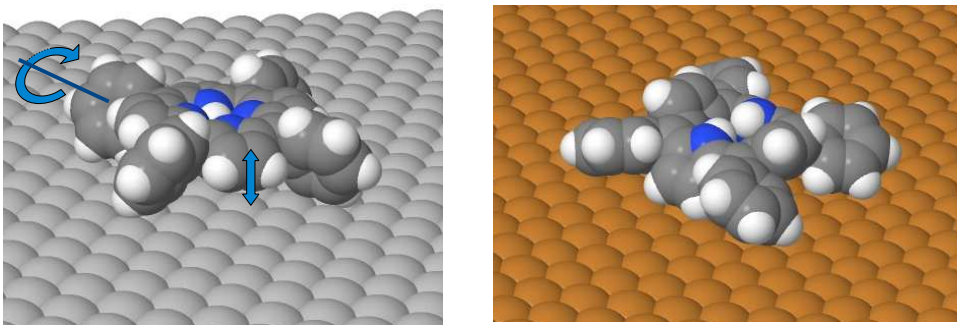

Figure 1.2: Illustration: The chemical environment influences the molecular conformation of surface-anchored porphyrins. A different substrate may induce a different adsorption geometry (right)

and in supramolecular self-assembly.[11,21] Nowadays also a myriad of artificial species is available as building blocks and functional units of applications[22,23] such as chemosensors,[24,25] nano-catalysts,[26–28] but also for medical applications like anti-cancer and anti-HIV drugs.[29,30] Because of their photophysical properties, porphyrins are extensively studied as components in organic light emitting diodes[31] and organic solar cells,[32,33] for example in combination with fullerenes[34] or as sensitizers in dye-sensitized solar cells.[35,36]

The basic properties of the porphyrins, their interaction with the surface and their behavior upon surface treatment (e.g., annealing) are influenced by the choice of the substituents, the central metal atom and -not surprisingly- also depend on the choice of the substrate. This has been demonstrated by numerous studies: Scanning probe methods such as Scanning Tunneling Microscopy (STM) (e.g., refs. 37–45) and Atomic Force Microscopy (AFM) (e.g., refs. 46, 47) provide real-space images of adsorbed molecules on surfaces and are therefore perfectly suited for the investigation of self-assembly properties and molecular arrangements of porphyrins on surfaces. However, many aspects can not be elucidated by scanning probe techniques alone. An example is given in ref. 48 (using data from Chapter 7 of this thesis), where the repulsive interaction between 2H-P molecules on a Ag(111) surface can be evidenced but only tentatively explained based on the STM observations. Here spectroscopy techniques, such as X-ray Photoelectron Spectroscopy (XPS), Ultraviolet Photoelectron Spectroscopy (UPS) or Near-Edge X-ray Absorption Fine-Structure (NEXAFS) spectroscopy provide additional and complementary information, in order to obtain a comprehensive picture of the porphyrin/surface system. In general, X-ray spectroscopy techniques are sensitive to the electronic structure of a sample, which allows to draw quantitative conclusions on how strong the

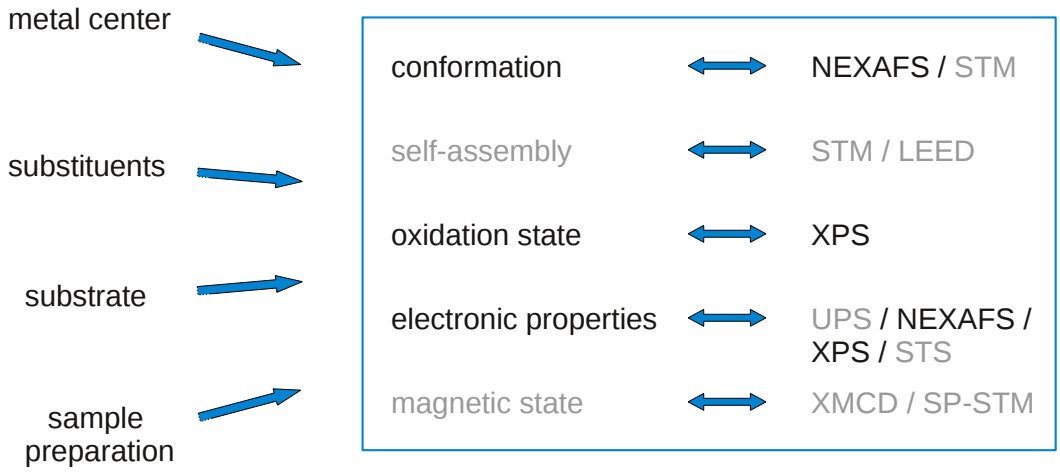

Figure 1.3: Overview over the questions addressed in this thesis and the corresponding experimental techniques (displayed in black). Additional information provided by techniques which were not used as primary source of information in this work are displayed in gray.

porphyrin bonds to the surface[49,50] and on possible charge transfers between the substrate and the molecule.[50] XPS probes the core levels of an atom, which are characteristic of the element and sensitive to its chemical state. Therefore it is an ideal technique to follow the metalation of porphyrins, i.e., the conversion of free-base porphyrins to metalloporphyrins (refs. 38, 51, 52). The dependency of the NEXAFS resonances' intensities as a function of the the angle of photon incidence renders NEXAFS a very valuable tool for the determination of adsorption geometries of porphyrins (refs. 49, 53, 54). However, as it will be shown later in this work, the analysis of the experimental XPS and NEXAFS data can be very challenging or even impossible without additional support by molecular modeling.

Even though porphyrins have been intensively studied, many open questions remain. One difficulty which arises while studying the electronic properties and surface chemistry of adsorbed porphyrins is that these properties are not static and instead they reflect the porphyrin adaptability to its environment. To give an example (which will be addressed in Chapter 4): The metalation of a free-base meso-tetraphenyl-porphyrin (2H-TPP) may lead to changes in both the molecular conformation and the interaction with the surface. But is the modified adsorbate-surface interaction a result of the metalation, i.e, the change in the macrocycle structure or does it originate from the modified adsorption geometry? Hence, the investigation of one single system alone is not sufficient to answer all arising questions, and systematic studies

are crucial for understanding the role of the contributing parameters.

The aim of this work is to compare the behavior of metalated and free-base, as well as substituted and non-substituted porphyrins and study their interaction with different surfaces (see overview in Fig. 1.3), using a combination of XPS and NEXAFS spectroscopy, as well as density functional theory (DFT) calculations. To this end, sample preparation as well as data analysis methods had to be developed and/or refined. As porphyrins are complex species with an astonishing conformational flexibility, the peak assignment (especially of the NEXAFS data) is non-trivial. Therefore a combined experimental and theoretical approach will be employed, which in a first step compares the measured spectra to those simulated by DFT, followed by a detailed peak fitting.

One main point will be the *in vacuo* metalation of the porphyrins. Generally, there are two possibilities to obtain metalloporphyrin layers: Either by depositing already synthesized metalloporphyrins on the substrate or by dosing free-base porphyrins which are metalated *in situ*. The first option has the disadvantage that preparation conditions, e.g., sublimation temperatures, may differ from those of the respective free-base compound which is a source of uncertainty in the interpretation of the data. In contrast, the *in vacuo* metalation allows a direct comparison of metalated and non-metalated species without complications arising from different preparation conditions. The biggest advantage of using *in vacuo* metalation techniques is that the construction of novel nanoarchitectures containing metalated species can even be realized for very complex and/or reactive metalloporphyrins, which can not be sublimed by standard dosing procedures. When starting the work on this thesis, the common way of metalating porphyrins on the surface was the codeposition of molecules and metal atoms on the substrate.[42,44,51,55] This technique, however, has the disadvantage that instrumentation for physical vapor deposition of the desired metal is required and that very high temperatures might be necessary for the sublimation of certain metals. In this work, alternative methods for *in situ* metalation have been explored: Chapter 4 is dedicated to the description of the *self-metalation,* i.e., the metalation of a porphyrin with substrate atoms, of the systems 2H-TPP/Cu(111) and 2H-P/Cu(111). In Chapter 5, another metalation technique, the metalation of 2H-TPP/Ag(111) and 2H-P/Ag(111) with the precursor molecule $Ru_3(CO)_{12}$, will be discussed and compared to data obtained from pre-synthesized Ru-(CO)TPP molecules.

As will be discussed in Chapter 2, NEXAFS spectroscopy is a valuable tool for obtaining information on the electronic structure of molecules in mono- and multilayers and for determining their adsorption geometry on a surface.

A crucial point hereby is the peak assignment in the measured spectra, which, especially for bigger molecules like porphyrins, can be very challenging when relying on information gathered from literature data alone. To improve or even allow the interpretation of the experimental data additional density functional theory (DFT) calculations have been performed in order to simulate both XPS and NEXAFS signatures of the porphyrins used in this work. In Chapters 4 and 5 the spectra of isolated porphyrin molecules are calculated, while for the discussion of 2H-P multilayers in Chapter 7, molecule-molecule interactions are taken into account to study the influence of molecule stacking on the XPS signatures.

The thesis is organized as follows: After presenting the basics of the methods employed in this work (XPS, NEXAFS and DFT) in Chapter 2, the experimental (e.g., sample preparation protocols, data analysis procedures) and computational (e.g., used functionals and basis sets) details are described in Chapter 3. The results of the XPS and NEXAFS measurements and DFT calculations are summarized in Chapters 4-7: Chapter 4 describes the self-metalation of 2H-TPP and 2H-P on a Cu(111) surface. Results for different coverages of metalated and non-metalated species are analyzed with special focus on the adsorption geometry of the porphyrins and the characterization of molecule-surface interactions. The comparison of 2H-TPP and 2H-P allows to study on the influence of the phenyl substituents on the properties of the porphyrin. Chapter 5 is dedicated to the metalation of the two free-base compounds 2H-P and 2H-TPP with $Ru_3(CO)_{12}$ on Ag(111), with special focus to the coverage-dependence of the metalation reaction. The growth of 2H-P on Ag(111) and Cu(111) for different sample temperatures is studied in Chapter 7. The influence of different stacking geometries of the porphines in the multilayer on the XPS signatures is analyzed with DFT. The results are summarized and put in perspective in Chapter 8. Results presented in this thesis have in parts already been published: Chapter 4 in refs. 56 and 57, Chapter 6 in ref. 58 and parts of Chapter 7 in ref. 48.

Chapter 2

Methods

In this chapter the basic concepts of the methods applied in this work are introduced. The experimental part consists of two X-ray spectroscopy techniques: X-ray photoelectron spectroscopy (XPS), which is used to probe the core levels of a sample, is presented in Section 2.1 and near-edge X-ray absorption fine-structure (NEXAFS) spectroscopy, which gives valuable information about the electronic structure of the unoccupied levels and the adsorption geometries of the molecular adsorbates on surfaces, is discussed in Section 2.2. These experimental techniques are complemented by density functional theory (DFT) calculations of electronic properties and simulated XP and NEXAFS spectra, which are crucial for the interpretation of the experimental data (Section 2.3). In this chapter the emphasis lies on the description of the fundamental concepts and theoretical basis of the methods. The measurement procedure and the relevant parameters, the experimental setup and the data analysis procedure as well as the computational details will be described in Chapter 3. For more detailed discussions about the techniques see for example refs. 59 and 60 (XPS), ref. 61 (NEXAFS) or ref. 62 (DFT).

2.1 X-ray Photoelectron Spectroscopy (XPS)

2.1.1 Principle

Photoelectron spectroscopy (PES) is a popular non-destructive surface analysis technique which is used to determine the composition of a sample and the chemical and electronic states of its elements.

PES is based on the photoelectric effect which was discovered by Hertz in 1887[63] and explained by Einstein in 1905.[64] In 1957 the work of Siegbahn and coworkers[65] laid the fundaments for the use of PES as it is known today and

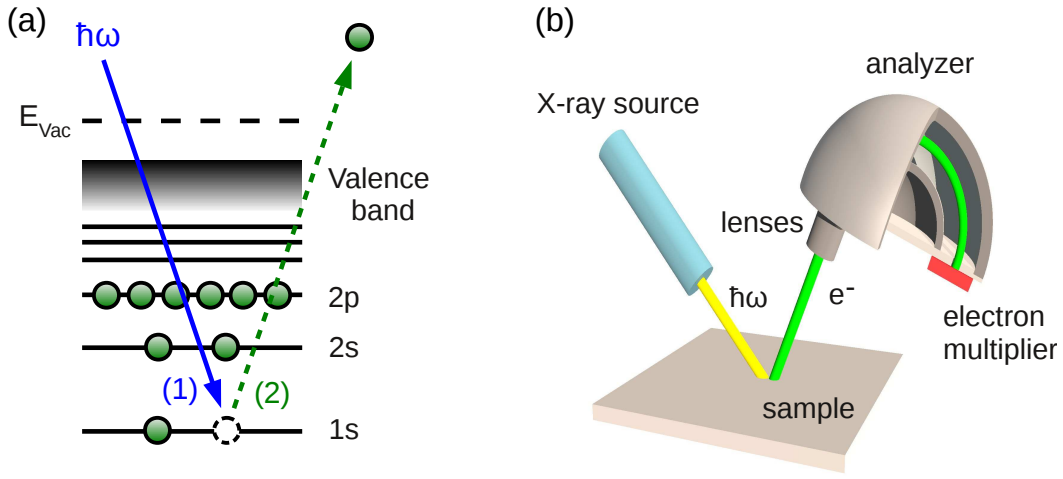

Figure 2.1: (a) Photoelectric effect: Absorption of a photon with energy $\hbar\omega$ (1) leads to the emission of a photoelectron (2), (b) Schematic setup of an XPS experiment: The sample is illuminated by photons (yellow) which are emitted by the X-ray source (blue) and cause the emission of photoelectrons (green). Only photoelectrons of a certain energy can pass an hemispherical analyzer (gray) and are finally detected by an electron multiplier (red).

was later (1981) awarded the Nobel price in physics.[66]

Illuminating a sample with photons of energy $\hbar\omega$ (Fig. 2.1a, (1)) leads with a certain probability (see Section 2.1.3) to the absorption of a photon and to the emission of an electron from the probed material (Fig. 2.1a, (2)). This process is called the photoelectric effect. The emitted photoelectron leaves the sample with the kinetic energy E_{kin}

$$E_{kin} = \hbar\omega - E_b - \phi \tag{2.1}$$

where E_b is the binding energy of the electron in its initial state and where the work function $\phi = E_{vac} - E_F$ of the material is the energy which is needed to excite an electron from the Fermi level E_F to the vacuum level E_{vac}. Thus, by measuring the kinetic energy of the photoelectrons, it is possible to gain information about the binding energy of the electrons in the sample and therefore about the electronic structure of the latter.

The photoionization process in solids can be described by the one-step model, which considers the excitation from the initial state, a Bloch wave, to the final state, a damped wave, that accounts for the short mean free path (cf. Section 2.1.3) of the electrons in the material. A simpler description, the three-step model has proven to be useful[67,68] in treating the photoionization process in an approximate fashion. It separates the whole process into three steps:

First, the photoelectron is excited (1); subsequently it has to move through the solid to the surface (2) and is finally released into vacuum (3) [59, pp. 349-350].

Depending on the photon energy used in the experiment, PES is either referred to as ultraviolet photoelectron spectroscopy (UPS) for photon energies in the range of 10-50 eV or as X-ray photoelectron spectroscopy (XPS) when the photon energies lie in the range of 0.1-10 keV [2, p. 99]. XPS mainly probes core levels, while UPS is used to study the valence energy levels of a material. This work does not include UPS studies, therefore the following discussion will focus solely on XPS.

A typical setup for an XPS experiment (Fig. 2.1b) consists of an X-ray source (blue), which emits photons (yellow) that impinge on the sample and an energy analyzer (gray) coupled to an electron multiplier (red) to detect the photoelectrons (green). X-ray sources can either be laboratory sources, i.e., X-ray tubes with fixed photon energies (typically with Mg $K_{\alpha 1,2}$ or Al $K_{\alpha 1,2}$ radiation) or synchrotrons, which provide light with tunable photon energy and guarantee high intensity and higher energy resolution than the laboratory sources. A very common type of electron analyzer is the hemispherical analyzer (depicted in Fig. 2.1b), which acts as a filter, only letting electrons of a certain energy, the pass energy (PE), reach the exit slits so that they can be counted by the electron detector. Selection of different kinetic energies at fixed pass energy is performed by applying a retarding voltage in the entrance lens section of the analyzer. Due to the strong interaction of electrons with matter, standard XPS experiments are carried out under ultra-high vacuum conditions (cf. Section 3.1.1).

2.1.2 Binding energies

The binding energy E_b of an electron in an atom or molecule is defined as the difference between the total energies of the initial state $|i\rangle$ with N electrons and the final state $|f\rangle$ with N-1 electrons after the emission of a photoelectron [59, p. 72]. Or, put differently, it is the energy that is necessary to excite the electron from the inner shell to the vacuum. Typically, binding energies are given as positive values.

In Eq. 2.1 the level against which E_{kin} and E_b were referenced was not specified. This reference level has to be considered when comparing binding energies. While the kinetic energy is conventionally given with respect to the vacuum level, the binding energies of solids are referenced to the Fermi level, which explains why the work function has to be taken into account in Eq. 2.1.

It follows for the binding energy

$$E_b^F = \hbar\omega - E_{kin}^V - \phi = E_b^V - \phi, \tag{2.2}$$

where the exponents V and F refer to the vacuum and the Fermi level, respectively.

Generally, the binding energy depends on the Coulomb interaction between the electron and the nucleus on the one hand and the screening of this interaction by the other electrons in the atom or molecule on the other hand [2, p. 104]. As a result, the binding energy of a certain core level (e.g., 1s) is characteristic for each chemical element, thus allowing the determination of the chemical composition of a sample. Moreover, as the electrons of a material are involved in the formation of chemical bonds, the binding energy of a given element can vary depending on its chemical environment. The value of this *chemical shift* may amount up to several electron-volts, e.g., for the C1s energies of inequivalent carbon atoms in ethyl trifluoroacetate[69] and is an indicator for the strength of the interaction with the considered atom. The sign of the chemical shift may provide an indication about whether additional charge is transferred to or from the atom [2, p. 104]. Typical examples are oxidized species, e.g., Ti ($E_b(2p_{3/2})$ = 453.9 eV[70]) compared to TiO_2 ($E_b(2p_{3/2})$ = 458.6 eV[71]), protonated species, e.g., the two inequivalent nitrogen atoms (=N- and -NH-) of free base porphyrins (see refs. 51, 72 and Chapters 4 and 5 of this thesis) or the adsorption of adsorbates at surfaces.[73]

For a typical XP spectrum the measured intensities are plotted against the corresponding binding energies. If the initial state is an s-type orbital, one peak for every species is observed, while for p, d and f orbitals typically more than one peak is found. The coupling between unpaired spins and a non-zero orbital angular momentum ($l > 0$) for p, d and f shells leads to two non-degenerate states with total angular momentum $j_+ = l + \frac{1}{2}$ and $j_- = l - \frac{1}{2}$ [74, pp. 219-220] and consequently to a splitting of the peak into a doublet. Nowadays, the energy splitting and the intensity ratio of the single components are known for a given chemical element; this can considerably facilitate the curve fitting of spin-orbit-doublets (see for example Chapter 6).

In addition to the primary photoelectron signals, which typically appear as sharp peaks in the spectrum, a number of other features can be distinguished in a typical XPS spectrum. Energy loss satellites at higher binding energy are present if the primary photoelectron loses part of its kinetic energy in other processes, e.g., for the excitation of plasmons or in *shake-up* or *shake-off* processes. A part of the photon energy can be transferred to another electron in the material which then is either excited to a higher state (shake-up, Fig. 2.2a)

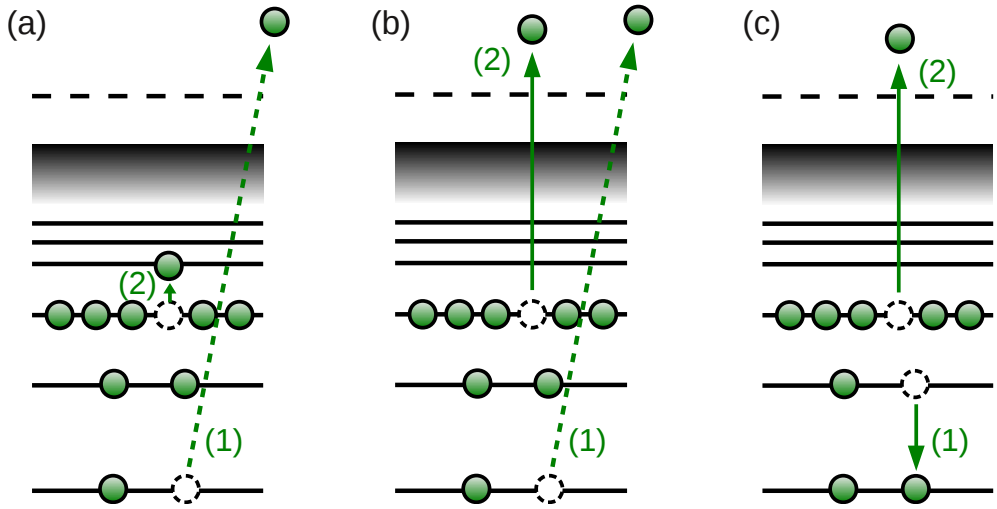

Figure 2.2: (a) Shake-up and (b) shake-off process: The energy of the photoelectron (1) is partly transferred to another electron (2) which is either emitted (shake-off) or excited to a higher state (shake-up), (c) Auger decay of the core hole.

or emitted completely (shake-off, Fig. 2.2b). The reduced kinetic energy of the photoelectron leads, according to Eq. 2.2, to a seemingly higher binding energy in the spectrum. For a quantitative analysis of XPS data (Section 2.1.3) these satellites have to be taken into account. Additional satellites occur for non-monochromatic X-ray radiation, as it is often the case for laboratory photon sources. In addition to the principal $K_{\alpha 1,2}$ radiation, other lines with lower intensity are also produced. For example for an Al source the satellite with the highest intensity (8% of the $K_{\alpha 1,2}$ line) lies 9.6 eV below the binding energy of the main photoelectron peak [60, p. 127].

After the emission of the photoelectron the system is in an excited state which decays by filling the remaining core hole with an an electron from a higher energy level. The hereby gained energy is either released as a photon (radiative core hole decay) or is transferred to another electron, which is emitted from the atom (non-radiative Auger decay, Fig. 2.2c). These *Auger electrons* are also detected and appear as Auger peaks in the XPS spectrum. As their kinetic energy (at variance with that of the photoelectrons) does not depend on the incident photon energy, Auger and photoelectron peaks can easily be distinguished by varying $\hbar\omega$. Auger electrons can also be used for the analysis of a sample, this technique is called Auger electron spectroscopy.

All inelastically scattered and secondary electrons contribute to the general background which increases steplike after each primary photoelectron peak on the high binding energy side. For a quantitative analysis this background has

to be subtracted from the raw data. Different possibilities for background correction will be discussed in Section 3.1.3.

2.1.3 Intensities

XPS is a quantitative method which allows the determination of the stochiometric ratios of the analyzed elements by comparing the respective peak intensities, i.e., the integrated peak areas after background subtraction. Therefore it is possible to investigate the composition of a sample or the molecular coverage on a surface.

The emission of a photoelectron occurs with a certain probability, expressed by the photoionization cross section $\sigma_{ij}(\hbar\omega)$, which depends on the chemical element i, the core level j and the incidence photon energy $\hbar\omega$. In this work the cross section calculations of Yeh and Lindau[75] were used for the analysis of the measured spectra.

Generally, the signal I_{ij} for an element i is given by

$$I_{ij} = J_0 \sigma_{ij}(\hbar\omega) T \int_{\gamma=0}^{\pi} \int_{\varphi=0}^{2\pi} L_{ij}(\gamma) \int_{z=0}^{\infty} n_i(z) \exp\left(\frac{-z}{\lambda_i \cos\theta}\right) \mathrm{d}z \, \mathrm{d}\gamma \, \mathrm{d}\varphi \qquad (2.3)$$

where J_0 is the intensity of the incident X-ray beam, $\sigma_{ij}(\hbar\omega)$ is the photoionization cross-section of level j by photons of energy $\hbar\omega$, T (which is dependent on the kinetic energy) defines the transmission of the analyzer, γ is the angle between the X-ray beam and the direction of the emitted photoelectron, $L_{ij}(\gamma)$ is the angular dependence of the photoemission, $n_i(z)$ is the number of atoms i as a function of depth z. λ_i is the electron attenuation length (see below) and θ is the escape angle of the electron with respect to the surface normal [2, pp. 87 and 102]

The attenuation length λ is the distance after which the intensity of a beam decreases to e^{-1} of its original value because of inelastic interactions with the surrounding matter. The terms attenuation length and inelastic mean free path of electrons (IMFP) are often used synonymously.[i] λ depends on the material and the kinetic energy, e.g., for electrons with kinetic energies of 50-2000 eV λ_i lies in the range of 5-30 Å (cf. universal curve of the mean free path),[77] while the penetration depth of X-rays in matter typically is much larger. The short attenuation length for electrons is the reason why XPS is a surface sensitive technique.

[i] However, measured λ and calculated IMFP in solids are not always identical.[76]

Thus the signal of a substrate which is covered by a layer of molecules is attenuated. The intensity I of the substrate depends exponentially on the thickness t of the overlayer:

$$I = I_0 \cdot \exp\left(\frac{-t}{\lambda \cos\theta}\right) \tag{2.4}$$

where I_0 is the intensity of the substrate without the overlayer and θ is the detection angle [59, pp. 12-13]. Of course, for thick films of molecules the signal of the lower molecular layers is also attenuated. For normal emission the electrons have to travel the shortest way in solid, therefore the contribution from deeper layers is larger than for other detection angles. Hence, by varying θ the surface sensitivity of the method can be tuned.

2.2 Near-edge X-ray absorption fine-structure (NEXAFS) Spectroscopy

2.2.1 Principle

While XPS gives valuable information about the electronic structure of a system, it only probes the occupied (core) levels of a system. Therefore a second X-ray spectroscopy method was used in this work: the near-edge X-ray absorption fine-structure (NEXAFS) spectroscopy, a technique which allows studying unoccupied states. Fig. 2.3 illustrates the basic principle for a diatomic system: Photons of energy $\hbar\omega$ are absorbed, causing the excitation of core electrons[ii] to higher unoccupied states. In contrast to XPS these final states can lie below the vacuum level E_{vac}, i.e., the electron remains in a bound state. As a consequence, it is not possible to measure the absorption in solids directly as the excited electron is not necessarily emitted from the sample. Typically the absorption is monitored by detecting products from secondary processes which follow the excitation of the electron, e.g., fluorescent photons or secondary and Auger electrons. In this work NEXAFS spectra were measured by detecting electrons.

The electric dipole transitions follow strict selection rules, e.g., the angular quantum number of the final state $l_f = l_i \pm 1$ has to differ by 1 from that of the initial state. This implies that, for example, transitions between s-type orbitals are forbidden, while transitions from s- to p-type orbitals are allowed [74, p.

[ii] In this work K-edge spectra are measured, but in general also electrons from higher levels can be excited.

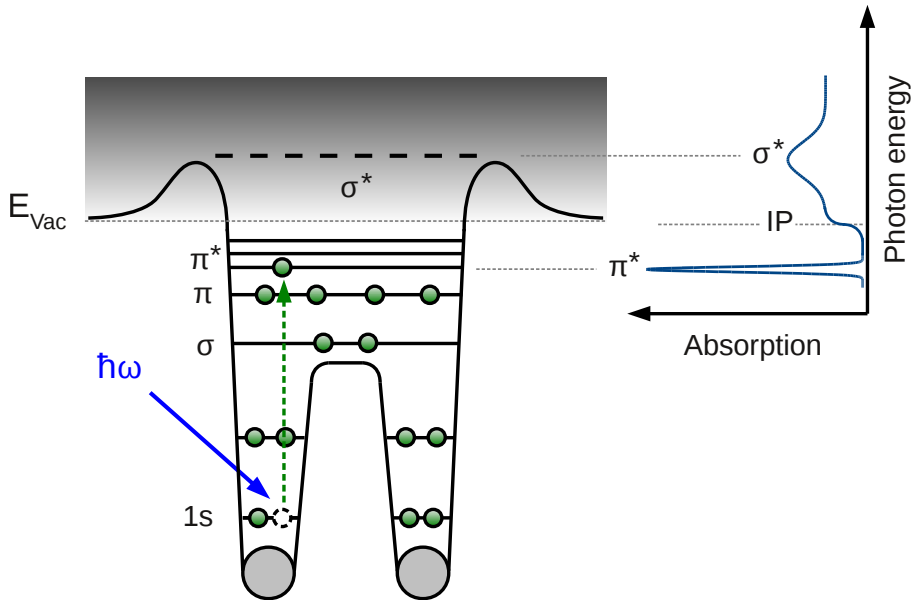

Figure 2.3: Principle of NEXAFS spectroscopy: photons with $\hbar\omega$ are absorbed and core electrons are excited into unoccupied states which may lie below or above the vacuum level. The inset shows a schematic NEXAFS spectrum. Typically π^* resonances at lower energies are sharper than the σ^* signals above the vacuum level, which appears as step in the spectrum.

300]. Additionally, a transition to an unoccupied state is only possible if the photon energy $\hbar\omega$ equals the necessary transition energy $E = E_f - E_i$. Thus, by varying $\hbar\omega$ and measuring the corresponding absorption, it is possible to gain information about the electronic structure of the sample.

Fig. 2.3 illustrates the correlation between energy levels and the characteristic features of a generic NEXAFS spectrum (inset) where the absorption is plotted against the photon energy. Three principal features can be discriminated:

- For $\hbar\omega < E_b$ the core electron is excited to a π^* state which leads to sharp resonances. Typical natural linewidths for carbon and nitrogen K-edge[iii] resonances lie in the range of 0.1 eV [61, p. 14]. Measured spectra are of course additionally broadened by the experimental setup.

- For $\hbar\omega \sim E_b$ a step-like feature, the *continuum step*, appears in the spectrum. It is a result of transitions to states above the vacuum level. The position of the step can not always be determined experimentally as transitions to Rydberg states may already appear as step before the

[iii] By convention orbitals are described in X-ray notation for NEXAFS spectroscopy.

actual ionization potential (IP).

- Superimposed on this background broad σ^* resonances appear typically at higher photon energies. Transitions to σ^* above the vacuum level can be described as a two-step process: In the first step the core electron is excited to a virtual orbital, followed by the emission of a photoelectron in the second step. The lifetime of the excited state is short, thus leading to a broadening of the σ^* signals in the spectrum [61, pp. 93-94].

Of course, depending on the electronic structure of the probed material, "real" spectra may differ considerably from the schematics in Fig. 2.3.

As each distinct species in the sample generates several peaks, NEXAFS spectra are normally more complex than XPS curves, thus complicating the assignment of the peaks to specific excitation centers. For the disentanglement of measured signals the building block principle is often applied. It states that the curve of a complex molecule composed of smaller subgroups can be divided in the signals of the subgroups as long as there is no strong interaction between the corresponding orbitals [61, p. 179] Hence, if the spectral signatures of the subgroups are known, e.g., from literature, it is possible to draw conclusions about the origin of the peaks of the more complex molecule. Of course, this approach is only an approximation, so that it might be necessary to employ additional methods. Another way to conduct the peak assignment of complex molecules is the application of theoretical methods, for example density functional theory (DFT) (see for example refs. 78–82, Chapters 4) to calculate the electronic structure of the molecule and simulate the corresponding X-ray absorption spectra. This topic will be discussed further in Sections 2.3 and 3.2.

2.2.2 Polarization dependence

One strength of NEXAFS spectroscopy is the strong dependence of the intensities on δ, the angle between the direction $\vec{O}$ of the final state orbital and the direction $\vec{E}$ of the electric field (Fig. 2.4a). The intensity I of the signal follows

$$I \propto |\vec{E} \cdot \vec{O}|^2 \propto \cos^2(\delta) \tag{2.5}$$

where δ is the angle between $\vec{O}$ and $\vec{E}$ [61, p. 71].

Fig. 2.5 illustrates the polarization dependence with reference to the case of a planar conjugated system which is adsorbed parallel to the surface. Its p_z orbitals are oriented along $\vec{O}$ which is parallel to the surface normal, while the

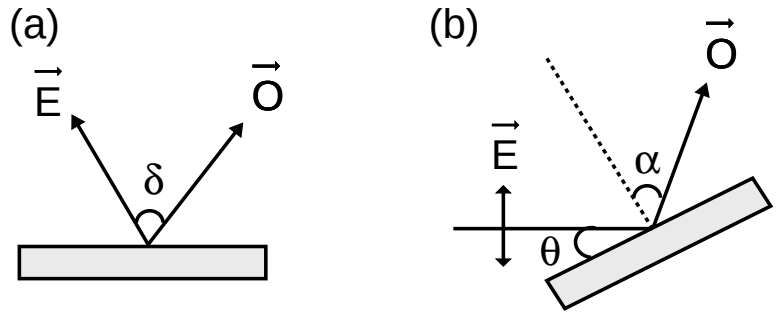

Figure 2.4: Angular parameters in NEXAFS. (a) δ is the angle between the direction of the orbital $\vec{O}$ and the polarization vector $\vec{E}$, (b) α is the angle between $\vec{O}$ and the surface normal, θ is the incidence angle.

σ orbitals lie in the surface plane. In the case of normal incidence (Fig. 2.5a) the linear polarized X-ray beam impinges perpendicular to the surface, i.e., the polarization vector $\vec{E}$ is perpendicular to $\vec{O}$. From Eq. 2.5 it follows that in this case the intensity vanishes for the π^* resonances, while it is maximal for the σ^* resonances. For grazing incidence (Fig. 2.5b) the ratios of π^* and σ^* intensities are inverted: the intensities of the σ^* resonances are minimal and those of the π^* peaks are maximal. In a more general description, $\vec{O}$ is not perpendicular to the substrate, but is oriented with an angle α relative to the surface normal (Fig. 2.4b). Hence it is possible to determine the adsorption geometry of a molecule if the relative intensities of the peaks (dependent on δ) are known. To this end, the sample is rotated with respect to the beam to probe different angles δ and the relative peak intensities with respect to the incidence angle θ (Fig. 2.4b) are evaluated. For a substrate with threefold or higher symmetry (as in the case of Cu(111) and Ag(111) single crystal surfaces), the peak intensities follow

$$\begin{aligned} I &\propto \left\{ P \cdot \left[\cos^2\theta \cos^2\alpha + \frac{1}{2}\sin^2\theta \sin^2\alpha \right] + (1-P)\left[\frac{1}{2}\sin^2\alpha \right] \right\} \\ &\propto \left\{ P \cdot \frac{1}{3}\left[1 + \frac{1}{2}(3\cos^2\theta - 1)(3\cos^2\alpha - 1) \right] + (1-P)\left[\frac{1}{2}\sin^2\alpha \right] \right\} \end{aligned} \tag{2.6}$$

where P is the polarization of the light [61, pp. 282-284]. More details on the general procedure are given in Section 3.1.3. For more complex molecules, the correct interpretation of the NEXAFS curves can be challenging, because different subgroups may be oriented differently with respect to the surface and consequently the corresponding peaks exhibit different angular dependence. In this case a reliable peak assignment is a crucial first step for the determination of the adsorption geometry. Instead of only relying on the building block

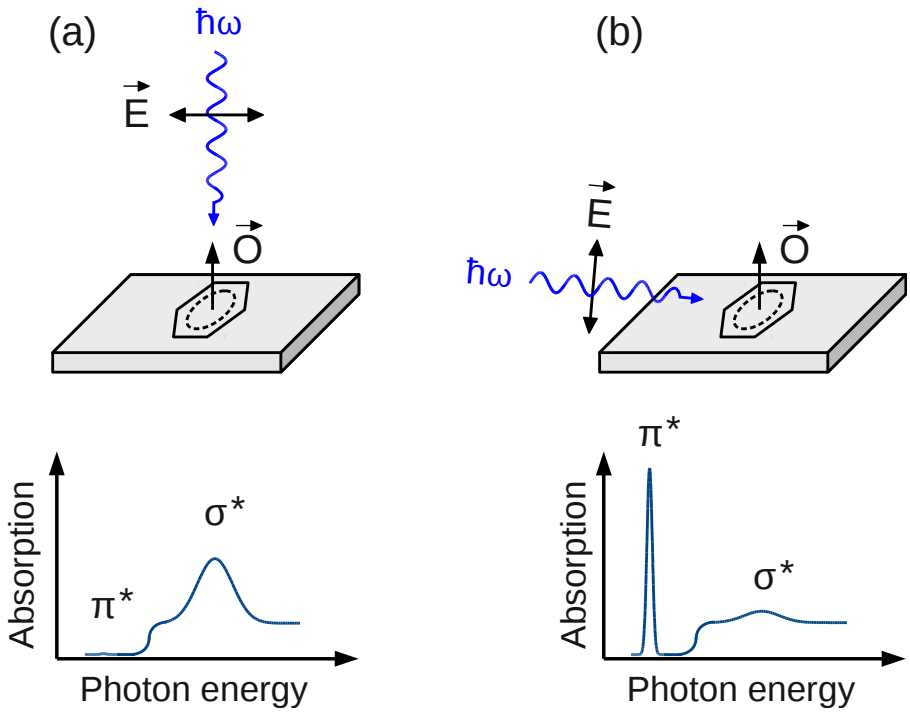

Figure 2.5: Polarization dependence of NEXAFS spectra of a conjugated system. The π^* orbitals are oriented along $\vec{O}$, while the σ^* orbitals lie in the surface plane. (a) normal incidence: $\vec{E} \perp \vec{O} \Rightarrow$ vanishing π^* resonances and maximal intensity of the σ^* resonances, (b) grazing incidence: $\vec{E}$ is nearly parallel to $\vec{O} \Rightarrow \pi^*$ resonances have maximal intensity, σ^* resonances are quenched.

principle, additional DFT simulations were used in this work for a detailed peak assignment (Chapters 4 and 7).

2.3 Density functional theory (DFT)

2.3.1 Kohn-Sham equations

The principal goal of quantum-mechanical electronic structure calculations is to solve the time-independent, non-relativistic[iv] Schrödinger equation

$$\hat{H}\Psi = E\Psi \quad \text{with} \quad \hat{H} = \hat{T}_n + \hat{T}_e + \hat{V}_{ne} + \hat{V}_{ee} + \hat{V}_{nn} \tag{2.7}$$

which means determining the eigenvalue E and the eigenfunction Ψ of the Hamiltonian $\hat{H}$ which includes all kinetic ($\hat{T}$) and potential ($\hat{V}$) energy contributions from nuclei (index n) and electrons (index e). For a system of N electrons and M nuclei (of mass M_A) with coordinates $\mathbf{r}_i$ and $\mathbf{R}_A$ the kinetic contributions have the form

$$\hat{T}_e = -\frac{1}{2}\sum_{i=1}^{N}\nabla_i^2 \tag{2.8a}$$

$$\hat{T}_n = -\frac{1}{2}\sum_{A=1}^{M}\frac{1}{M_A}\nabla_A^2 \tag{2.8b}$$

The potential energy operators are given by

$$\hat{V}_{ee} = -\sum_{i=1}^{N}\sum_{j>i}^{N}\frac{1}{|\mathbf{r}_i - \mathbf{r}_j|} \tag{2.9a}$$

$$\hat{V}_{nn} = \sum_{A=1}^{M}\sum_{B>A}^{M}\frac{Z_A Z_B}{|\mathbf{R}_A - \mathbf{R}_B|} \tag{2.9b}$$

$$\hat{V}_{ne} = -\sum_{i=1}^{N}\sum_{A=1}^{M}\frac{Z_A}{|\mathbf{R}_A - \mathbf{r}_i|} \tag{2.9c}$$

where Z_A is the charge of the nucleus A. All formulas are given in atomic units, i.e., the electron mass m_e, the elementary charge e and the constants $\hbar$ and $1/4\pi\epsilon_0$ are all set to unity. Spin is not explicitly included in the coordinates.

To reduce the complexity of the system ($3N+ 3M$ degrees of freedom) and make the problem manageable approximations are required. Even for the smallest system, the hydrogen atom, the ratio between the mass of the electron and that of the proton is $5{\cdot}10^{-4}$, i.e., the mass of the nuclei is generally much higher than the mass of the electrons. Therefore, according to the *Born-Oppenheimer approximation*, the electronic and nuclear contributions can be

[iv] This is of course only true for the standard DFT method described here, in other approaches time dependence and relativity are taken into account.

separated, i.e., it is assumed that the electrons move in a static field of fixed nuclei.[83] This approach enables to separate the Hamiltonian into an electronic and a (constant) nuclear contribution and reduces the problem to

$$\left[\underbrace{-\frac{1}{2}\sum_{i=1}^{N}\nabla_i^2}_{\hat{T}_e}\underbrace{-\sum_{i=1}^{N}\sum_{A=1}^{M}\frac{Z_A}{|\mathbf{R}_A-\mathbf{r}_i|}}_{\hat{V}_{ne}}\underbrace{+\sum_{i=1}^{N}\sum_{j>1}^{N}\frac{1}{|\mathbf{r}_i-\mathbf{r}_j|}}_{\hat{V}_{ee}}\right]\Psi_{elec}=E_{elec}\Psi_{elec} \quad (2.10)$$

for N electrons in the field of M nuclei. The total energy of the system is then given by $E = E_{elec} + E_{nuc}$, where E_{nuc} is the constant energy contribution of the nuclei [62, p. 5]. In the following the index *elec* is dropped.

The desired electronic ground state $|\Psi_0\rangle$ of the system, i.e., the system with the lowest energy E_0, can be found by applying the *Rayleigh-Ritz variational principle*. For a given trial wave function Ψ_{trial} the energy E_{trial}, i.e, the expectation value of $\hat{H}$, follows

$$E_{trial} = \langle\Psi_{trial}|\,\hat{H}\,|\Psi_{trial}\rangle \geq E_0 = \langle\Psi_0|\,\hat{H}\,|\Psi_0\rangle \quad (2.11)$$

which implies that E_{trial} is an upper limit for E_0 and minimizing $E[\Psi]$[v] leads to the correct ground state energy [62, p. 7].

However, even after the application of the Born-Oppenheimer approximation Eq. 2.10 is still a many-body problem with $3N$ components which are coupled via the electron-electron interaction $\hat{V}_{ee}$. The computational costs therefore increase very fast with the size of the system, which invokes the need for a further simplification of the problem. A very popular method to calculate the properties of big systems is *density functional theory (DFT)*. The basic idea is hereby to reduce the dimensionality of the problem by relying only on the electron density $\rho(\mathbf{r})$, thus reducing the number of variables from $3N$ to three. First attempts by Thomas[84] and Fermi[85,86] in 1927/1928 lead to the *Thomas-Fermi method* which however exhibit several failures, for example it does not predict any stable molecules.[87]

Modern DFT is based on the *Hohenberg-Kohn theorems* which were described by Hohenberg and Kohn in 1964.[88] They proved that for a given system of N interacting electrons there is an unique bijective relationship between the electron density ρ and an external potential V_{ext} (e.g., the potential associated to the nuclei-electron interaction). As the electronic Hamiltonian and all observables depend on V_{ext}, all properties of the system are also determined by ρ. The second theorem states that, according to the variational

[v] Here the standard notation with square brackets is used to denote a functional $F[f(x)]$.

principle, the total energy $E[\rho]$ for a trial density is minimal only for the real ground state density ρ_0. The ground-state energy can be written as

$$E[\rho] = \int V_{ext}(\mathbf{r})\rho(\mathbf{r})\,\mathrm{d}\mathbf{r} + \frac{1}{2}\int\int \frac{\rho(\mathbf{r})\rho(\mathbf{r'})}{|\mathbf{r}-\mathbf{r}'|}\,\mathrm{d}\mathbf{r}\,\mathrm{d}\mathbf{r'} + G[\rho] \tag{2.12}$$

where the second term is the classical Coulomb interaction in a charge distribution and $G[\rho]$ is a universal functional. Kohn and Sham suggested in 1965 to separate $G[\rho]$ in two terms, according to:

$$G[\rho] \equiv T_s[\rho] + E_{xc}[\rho] \tag{2.13}$$

where $T_s[\rho]$ is the kinetic energy of a non-interacting electron system and $E_{xc}[\rho]$ is the exchange-correlation (xc) energy of the interacting system with density $\rho(\mathbf{r})$,[89] incorporating all the complicated many-body effects arising from the quantum-mechanical nature of electrons. Inserting Eq. 2.13 in Eq. 2.12 yields

$$E[\rho] = T_s[\rho] + \int V_{ext}(\mathbf{r})\rho(\mathbf{r})\,\mathrm{d}\mathbf{r} + \frac{1}{2}\int\int \frac{\rho(\mathbf{r})\rho(\mathbf{r'})}{|\mathbf{r}-\mathbf{r}'|}\,\mathrm{d}\mathbf{r}\,\mathrm{d}\mathbf{r'} + E_{xc}[\rho] \tag{2.14}$$

Here, the only unknown quantity for which no explicit form can be given is the exchange-correlation energy for which several approximations have been developed (see Section 2.3.2).

The basic idea for proceeding further is to introduce a reference system built of non-interacting single electron functions $\varphi_i(\mathbf{r})$ (*Kohn-Sham orbitals*) with the same electronic ground state density as the interacting system and an effective local potential $V_{eff}(\mathbf{r})$. The advantage of this approach is that the Schrödinger equation can now be reduced to a system of non-interacting single particle equations for $\varphi_i(\mathbf{r})$:

$$\left[-\frac{1}{2}\nabla^2 + V_{eff}(\mathbf{r})\right]\varphi_i(\mathbf{r}) = \epsilon_i\varphi_i(\mathbf{r}) \tag{2.15}$$

with the ground-state energy

$$E[\rho] = T_s[\rho] + \int V_{eff}(\mathbf{r})\rho(\mathbf{r})\,\mathrm{d}\mathbf{r} \tag{2.16}$$

Now the effective potential V_{eff} has to be determined in a way that the density

$$\rho(\mathbf{r}) = \sum_{i=1}^{N} |\varphi_i(\mathbf{r})|^2 \tag{2.17}$$

equals the ground-state density of the interacting system.

To find the ground state energy, $E[\rho]$ has to be minimized according to the variational principle, subject to the condition that a constant number of electrons N is present, such that:

$$N = \int \rho(\mathbf{r})\,\mathrm{d}\mathbf{r} \tag{2.18}$$

To fulfill this constraint, the Lagrange formalism is used [90, p. 55]:

$$\frac{\delta}{\delta\rho(\mathbf{r})}\left(E[\rho] - \mu\int \rho(\mathbf{r})\,\mathrm{d}\mathbf{r}\right) = 0 \tag{2.19}$$

with the chemical potential μ as Langrange multiplier. From Eq. 2.14 and 2.19 it follows

$$\frac{\delta T_s[\rho]}{\delta\rho(\mathbf{r})} + V_{ext}(\mathbf{r}) + \int \frac{\rho(\mathbf{r'})}{|\mathbf{r}-\mathbf{r}'|}\,\mathrm{d}\mathbf{r'} + \underbrace{\frac{\delta E_{XC}[\rho]}{\delta\rho(\mathbf{r})}}_{\equiv\mu_{xc}[\rho](\mathbf{r})} = \mu \tag{2.20}$$

Minimizing the energy in the same way for the non-interacting system with potential V_{eff} (cf. 2.15) results in

$$\frac{\delta T_s[\rho]}{\delta\rho(\mathbf{r})} + V_{eff}(\mathbf{r}) = \mu_{eff} \tag{2.21}$$

where μ_{eff} is the chemical potential of the non-interacting system [90, p. 63], where μ_{eff} should equal μ. Thus, equating Eqs. 2.20 and 2.21 results in an expression for the effective potential:

$$V_{eff}(\mathbf{r}) = V_{ext}(\mathbf{r}) + \int \frac{\rho(\mathbf{r'})}{|\mathbf{r}-\mathbf{r}'|}\,\mathrm{d}\mathbf{r'} + \mu_{xc}[\rho](\mathbf{r}) \tag{2.22}$$

Now that the expression for V_{eff} is known, Eq. 2.15 and 2.22 can be combined to yield the *Kohn-Sham equations*:

$$\left[-\frac{1}{2}\nabla^2 + V_{ext}(\mathbf{r}) + \int \frac{\rho(\mathbf{r'})}{|\mathbf{r}-\mathbf{r}'|}\,\mathrm{d}\mathbf{r'} + \mu_{xc}[\rho](\mathbf{r})\right]\varphi_i(\mathbf{r}) = \epsilon_i\varphi_i(\mathbf{r}) \tag{2.23}$$

Since V_{eff} depends on the electron density, the Kohn-Sham equations have to be solved self-consistently: In the first step the effective potential is constructed using an initial guess of the electron density. Then the one-electron eigenvalue problem (Eq. 2.23) is solved. The such determined electron density is in turn used to build a new V_{eff}. This cycle is repeated until the difference between the energies or electron densities obtained in two consecutive steps is zero or lies below a predefined threshold.

2.3.2 Exchange-Correlation Functionals

The quality of the determined electron density strongly depends on the quality of the approximation for the exchange-correlation functional E_{xc}.

Local (spin-) density approximation (LDA and LSDA)

The simplest approximation is the *local density approximation (LDA)*, which goes back to the Thomas-Fermi model, was already proposed by Kohn and Sham.[89] $E_{xc}[\rho]$ is approximated by

$$E_{xc}^{LDA}[\rho] = \int \rho(\mathbf{r})\epsilon_{xc}(\rho(\mathbf{r}))\,\mathrm{d}\mathbf{r} \tag{2.24}$$

where $\epsilon_{xc}(\rho(\mathbf{r}))$ is the exchange-correlation energy per electron of a uniform electron gas of density $\rho(\mathbf{r})$.[89] $\epsilon_{xc}(\rho(\mathbf{r}))$ can be further separated into the exchange and the correlation contributions [62, p.71]:

$$\epsilon_{xc}(\rho(\mathbf{r})) = \epsilon_x(\rho(\mathbf{r})) + \epsilon_c(\rho(\mathbf{r})) \tag{2.25}$$

The exchange part ϵ_x can be determined explicitly,[89] while for ϵ_c no such explicit expression is known [62, p.71]. Most of today's LDA functionals use analytical expressions for ϵ_c, based on the work of Ceperly and Alder who performed quantum Monte-Carlo calculations on the homogeneous electron gas.[91] Commonly employed LDA functionals are for example VWN (Vosko, Wilk, Nusair[92]), PZ (Perdew, Zunger[93]) and PW92 (Perdew, Wang[94]).

If the spin is to be considered, the two spin densities $\rho_\alpha(\mathbf{r})$ and $\rho_\beta(\mathbf{r})$ with $\rho_\alpha(\mathbf{r}) + \rho_\beta(\mathbf{r}) = \rho(\mathbf{r})$ are introduced. Equation 2.24 becomes

$$E_{xc}^{LSD}[\rho_\alpha, \rho_\beta] = \int \rho(\mathbf{r})\epsilon_{xc}(\rho_\alpha(\mathbf{r}), \rho_\beta(\mathbf{r}))\,\mathrm{d}\mathbf{r} \tag{2.26}$$

which is called the *local spin-density approximation (LSD)* [62, p. 72].

It can be noted that, as the LDA assumes a uniform electron gas, it generally provides a good description of simple metals, while the description of molecules is less satisfactory due to the large density variations over short distances within the molecules [62, p. 71]. Specifically, LDA tends to overestimate binding energies while consequently underestimating bond lengths. For systems with strong (e.g., covalent, ionic or metallic) bonds, geometric properties are better reproduced than for weakly bound systems. Electron densities close to the core are normally poorly described [90, p. 82].

Generalized gradient approximation (GGA)

Generalized gradient approximation (GGA) functionals follow

$$E_{xc}^{GGA}[\rho_\alpha, \rho_\beta] = \int f(\rho_\alpha(\mathbf{r}), \rho_\beta(\mathbf{r}), \nabla\rho_\alpha, \nabla\rho_\beta)\,\mathrm{d}\mathbf{r} \tag{2.27}$$

where f is a function that depends not only on $\rho_\alpha(\mathbf{r})$ and $\rho_\beta(\mathbf{r})$, but also on the respective gradients $\nabla\rho_\alpha$ and $\nabla\rho_\beta$ to account for the non-homogeneity of the electron density [62, p. 75]. E_{xc}^{GGA} is normally separated in

$$E_{xc}^{GGA} = E_x^{GGA} + E_c^{GGA} \tag{2.28}$$

and both terms are approximated separately.

In comparison to LDAs the GGAs improve the description of binding energies, bond lengths and bond angles. Generally, the description of hydrogen-bonded systems is improved [90, p. 90]. Very commonly used GGA functionals are PBE (Perdew, Burke, Enzerhof[95]) and its derivations, like for example the revised PBE (RPBE)[96] which were also used in this work.

Hybrid functionals

A different class of functionals were suggested by Becke in 1993.[97] As the exact exchange E_x^{exact} is included in the Hartree-Fock formalism, the *hybrid functionals* are designed as a combination of E_x^{exact} with other correlation terms E_c^{KS}. Becke suggested

$$E_{xc}^{hyb} = E_{xc}^{LSDA} + a_0(E_x^{exact} - E_x^{LSDA}) + a_x\Delta E_x^{B88} + a_c\Delta E_c^{PW91} \tag{2.29}$$

where a_0, a_x and a_c are semi-empirical coefficients that can be obtained by fitting experimental data.[98] Hybrid functionals are generally well suited to describe molecular properties[99] and reproduce molecular geometries and binding energies with an accuracy sometimes even comparable to configuration interaction calculations [90, p. 96], but are much more computationally demanding than LDAs or GGAs. In this work B3LYP,[100] which is based on Becke's suggested coefficients but uses a different correlation functional, is tested in Chapter 7.

2.3.3 Basis Sets

The quality and accuracy of a DFT-calculation do not only depend on the choice of the functional, but also on the basis set which is used to describe

the orbitals in Eq. 2.17. In the *linear combination of atomic orbitals (LCAO)* scheme,[101] the orbital φ_i

$$\varphi_i = \sum_{\mu=1}^{L} \mathrm{c}_{\mu i}\eta_\mu \tag{2.30}$$

is described by a linear combination of L atomic orbitals η_μ with corresponding coefficients $\mathrm{c}_{\mu i}$. The advantage of this method is that the non-linear Kohn-Sham equations are transformed into a linear matrix equation which can be solved more easily [62, pp. 94-95].

A very common type of basis functions are Gaussian type orbitals (GTOs). They have the form

$$\eta^{GTO} = N\, x^l y^m z^n \mathrm{e}^{-\alpha r^2} \tag{2.31}$$

where N is a normalization factor, the orbital exponent α determines how compact or diffuse the function is, and the indices l, m, n classify the angular node structure of the GTO. The advantage of using GTOs is that the integration over Gaussian functions can be done in an efficient way. However, the asymptotic behavior for $r \to 0$ and $r \to \infty$ is not correct for GTOs. For these cases Slater type orbitals (STOs) are better suited. They have the form

$$\eta^{STO} = N\, r^{n-1} \mathrm{e}^{-\zeta r} Y_{lm}(\Theta, \phi) \tag{2.32}$$

where ζ is the orbital exponent, n is the principal quantum number and Y_{lm} are the spherical harmonics used to describe the angular part of the function [62, p. 98]. Analytical STOs are used for example in the *Amsterdam Density Functional (ADF)* code.[102]

Since more Gaussian functions are necessary to describe an atom with the same accuracy as with STOs, the use of *contracted Gaussian functions (CGFs* or *CGTOs)* is a good compromise. CGFs are linear combinations of A primitive Gaussians g_a^{GTO} with fixed coefficients d_a

$$\eta^{CGF} = \sum_{a=1}^{A} d_a g_a^{GTO} \tag{2.33}$$

which are used to approximate a single STO function. Fig. 2.6 illustrates the approximation of a simple STO (solid line) by a linear combination of one (STO-1G), two (STO-2G) or three (STO-3G) simple Gaussian type functions. CGFs are for example implemented in the *StoBe* code.[104] The basis sets used in this thesis are listed in Section 3.2.1, with the following notation:

O-ELEMENT (n1s,n2s,...,nKs/n1p,n2p,...,nLp/n1d,n2d,...,nMd)

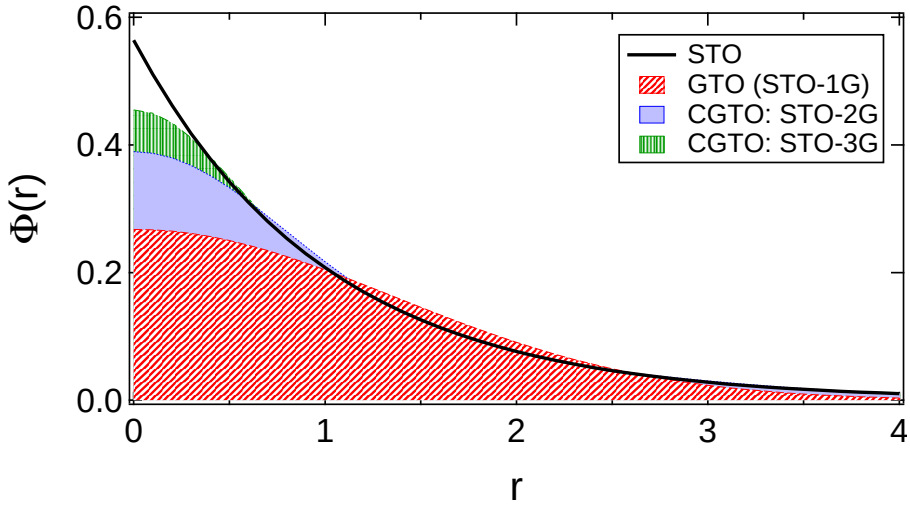

Figure 2.6: Illustration of STO, GTO and CGTO basis sets. The asymptotic behavior for $r \to 0$ and $r \to \infty$ is best for STO basis sets (black solid line), while GTO are easier to integrate. The more Gaussians type functions are combined, the better is the approximation of the STO. STO-1G, STO-2G and STO-3G refers to the simplest linear combination of one, two or three Gaussians. The parameters were chosen to obtain the maximum overlap with the STO.[103]

where K is the number of s-type Gaussians with n1s, ... nKs primitives, L is the number of p-type Gaussians with n1p, ... nLp primitives and M is the number of d-type Gaussians with n1d, ... nMd primitives.[105,106]

A different approach is the use of plane waves as basis functions for DFT calculations which are extended in space. They are conventionally used to describe metal surfaces with periodic boundary conditions. As these functions are not used in this thesis, they will not be discussed further.

Sets with one basis function per atom are called minimal basis sets or single-ζ (SZ) basis sets. Minimal basis sets are not well suited for the calculation of properties of molecular systems, but can be employed for example for a pre-optimization of a geometry. For one or two additional sets per orbital it is called a double-ζ (DZ) or triple-ζ (TZ) basis set [90, p.198].

In order to improve the basis sets, several expansions can be added. *Polarization functions* are functions with higher angular momentum (e.g., for a hydrogen atom additional p-functions) and ensure that the orbitals can distort from their original symmetry if necessary [62, p. 100]. They are denoted for example as TZVP (Triple Zeta Valence Plus Polarization).

Augmented basis sets are large diffuse basis sets which are added to get a better description of states that are not located close to the core, like for

example Rydberg states. In this work, diffuse basis sets were used for the calculation of NEXAFS spectra with StoBe to improve transitions to states lying above or directly below the ionization edge.

The StoBe calculations of electronic properties (for details see Section 3.2.1) are conducted using *effective core potentials (ECPs)* or *pseudopotentials*. The idea behind ECPs is that core electrons (especially for large elements) do not participate in chemical bonding and can therefore be eliminated from explicit consideration. The original charge of the nucleus Z is then replaced by an effective charge $Z_V = Z - Z_{core}$. This reduces the computation time considerably, thanks to the fact that the number of electrons and consequently the size of the basis set are smaller [90, p. 126]. The *FHI-aims* simulations, on the other hand, are conducted using *all-electron* basis sets.

The *FHI-aims* code uses numerical Slater type orbitals, i.e., *NAO (numeric atom-centered orbital)* basis functions of the form.[107]

$$\phi_i(\mathbf{r}) = \frac{u_i(r)}{r} Y_{lm}(\Theta, \phi) \tag{2.34}$$

where $u_i(r)$ is the radial function. Its values are numerically tabulated. This approach has two main advantages: because of the $1/r$ term, the behavior approximates the real potential close to the core better than for example GTOs and each $u_i(r)$ can be strictly localized inside a given sphere so that a large system can be described spatially resolved.[107]

2.3.4 Excited state calculations

In this work DFT is mainly employed to calculate ionization energies for the comparison with the experimental XPS energies and to simulate NEXAFS spectra aiming at a detailed peak assignment of the measured spectra.

The Delta Kohn-Sham (ΔKS) method allows the calculation of excitation energies by subtracting the calculated total energy of the excited state from the total energy of the ground state, i.e., the ionization (XPS) energy E_{ion} for an excitation from the core $1s$ level to the vacuum is determined via

$$E_{ion} = E_{tot}(n_{1s} = 0) - E_{tot}(n_{1s} = 1) \tag{2.35}$$

where n_{1s} is the occupation of the $1s$ level and E_{tot} are the total energies of the ground state ($(n_{1s} = 1)$) and the excited state ($E_{tot}(n_{1s} = 0)$). In the latter, one electron is removed from the 1s core level with a consequent relaxation of the orbitals.[82] Calculations for pyridine show a very good agreement between ΔKS excitation energies and measured gas phase data.[78] Takahashi and Pettersson

studied for 18 molecules how the ionization potential (IP) is influenced by the choice of the functional. They found that, while the absolute values show a large variation, the relative energies between different states hardly vary[108] [109, p. 235].

In the same way it is in principle possible to calculate NEXAFS transition energies, e.g., for the first transition by calculating the total energy of an excited state with $n = 0$ at the core level and $n = 1$ at the LUMO. However, for large molecules this method is not feasible as there are too many transitions to take into account and because of convergence and basis-set limitations [109, p. 236]. In order to calculate the NEXAFS spectra of bigger systems a different method can be used: the transition-potential (TP) approach. It is based on the transition-state method introduced by Slater who showed that the excitation energy can be approximated by exciting half an electron, i.e., the occupation of the core level and the final state orbital are set to $n = 0.5$.[110,111] The TP approach goes one step further and sets only the occupation of the initial state to 0.5, while that of the final state is zero. This has the advantage that only the occupation of the initial state differs from the ground state and therefore only one calculation is necessary to obtain all possible excitation energies for the system.[82]

As DFT is in principle a ground-state theory, the question about the validity of the ΔKS and TP methods arises. Refs. 78, 82, 108, 112, 113 show that both the ΔKS and the transition potential method can successfully be employed for the calculation of ionization and excitation energies, even if the agreement between experiment and TP-DFT is not perfect.

Computational details, including shifts to account for missing relaxation and relativity effects, on the utilization of the TP approach within the program code StoBe employed in this thesis will be given in Section 3.2.1.

2.3.5 van-der-Waals corrections

Generally, semi-local density-functional approximations, such as LDA, GGA, are not well suited to account for the long-range dispersion interaction, the attractive part of the van-der-Waals (vdW) interaction.[114] The performance depends on the investigated system and the used exchange-correlation functional. For a benzene dimer, for example, neither the GGA functional PBE nor the hybrid functional B3LYP yield any binding at all.[115]

One possibility to include vdW interactions is the use of semi-empirical dispersion correction methods that add a R^{-6}-dependent term to the DFT

energy. E_{vdW} is determined by summing over the pairwise interatomic C_6R^{-6} terms:

$$E_{vdW} = -\frac{1}{2}\sum_{A,B} f_{damp}(R_{AB}, R_A^0, R_B^0)\, C_{6AB}\, R_{AB}^{-6} \tag{2.36}$$

where R_{AB} is the distance between atoms A and B, C_{6AB} is the corresponding C_6 coefficient which determines the strength of the interaction, and R_A^0 and R_B^0 are the respective van-der-Waals radii. To eliminate the R_{AB}^{-6} singularity and avoid double counting at small distances, the damping function $f_{damp}(R_{AB}, R_A^0, R_B^0)$ is introduced.[116]

Several different methods have been developed, which differ in the derivation of the C_6 coefficients and damping functions, e.g., Wu-Yang[117] or Grimme.[118] In this work the Tkatchenko-Scheffler method is used, which has the advantage that the relevant parameters do not have to be determined empirically, but are calculated from the ground-state electron density.[116]

Chapter 3

Experimental and Computational Details

In the previous chapter the principal techniques employed in this thesis (XPS, NEXAFS and DFT) and their underlying principles were introduced and described under a general perspective. This chapter, on the other hand, focuses on the experimental and computational details specifically relevant for the work presented in this thesis. In Section 3.1.1 the experimental setups are briefly characterized, followed by detailed descriptions of the procedures for substrate cleaning and molecule deposition, as well as of typical parameters used in the measurements (Section 3.1.2). Appropriate data analysis, e.g., background removal and peak fitting, is crucial for the interpretation of the experimental data: corresponding protocols are therefore discussed in Section 3.1.3. Finally, computational procedures and routines regarding the *StoBe* and *FHI-aims* calculations are presented in Sections 3.2.1 and 3.2.2, respectively.

3.1 Experimental Details

3.1.1 Vacuum systems

The majority of XPS and all of the NEXAFS experiments were performed at the dipole beamline HE-SGM at the synchrotron BESSY II in Berlin. Preparatory experiments, as well as the XPS measurements described in Chapter 6 and displayed in Figs. 7.17 and 7.18 were conducted in our on-campus laboratory in Garching (ESCAlab) using a conventional dual-anode X-ray source. As is typical for X-ray spectroscopy experiments in surface science all measurements were conducted under ultra-high vacuum (UHV) conditions. If the experiments were performed in atmospheric pressure, the photoelectrons would

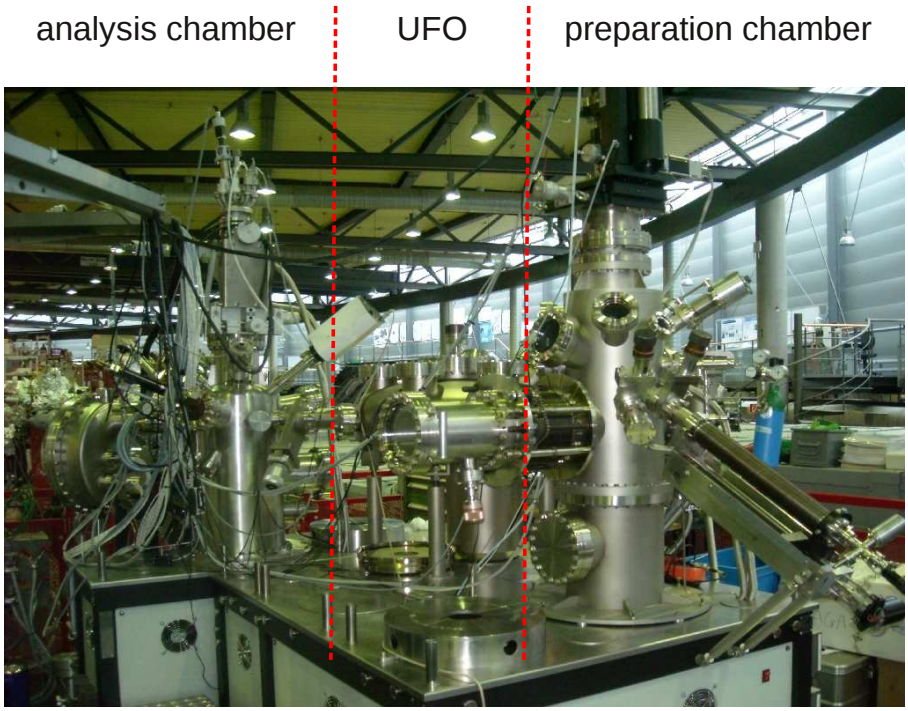

Figure 3.1: The UHV end station at the HE-SGM beamline at BESSY II consists of the preparation chamber where the substrate is cleaned and the molecules are dosed, the distribution chamber (UFO) and the analysis chamber, where the XPS and NEXAFS data are taken.

not be able to reach the analyzer because the mean free path λ of electrons under these conditions is approximately 700 Å. Furthermore, the time τ it takes to cover a clean surface with a monolayer of impurities in ambient conditions lies in the nanosecond range, which clearly prevents clean studies of the interaction between molecules and pristine surfaces. For pressures in the 10^{-9} mbar regime λ increases to 50 km, while τ lies in the hour-range, thus enabling the preparation and analysis of well-defined clean samples [2, p. 20].

Both the commercial *Prevac* setup at BESSY and the home-made (based on ESCAlab-5 of *VG Scientific*) ESCAlab setup follow a similar principle: Sample preparation and measurements are conducted in separated parts of the machine (the preparation and the analysis chamber, respectively) as the sample preparation process normally leads to an increase in pressure and additional contaminants which are undesirable during the data acquisition.

Both preparation chambers are equipped with a sputter gun, one or two molecular evaporators and a LEED optics. At BESSY (Fig. 3.1) the sample is transferred with a transfer arm via a distribution chamber (UFO) to the manipulators of preparation and analysis chamber where it can be fixed and

the transfer arm removed. This allows to close the gate valves between the chambers during data acquisition, so that a second sample can be prepared during the measurement of the first sample. The disadvantage of this setup is that only the manipulators, but not the transfer arm, can be cooled, and therefore the sample temperature may rise during the transfer. The transfer in the ESCAlab chamber is simpler as the sample stays all the time on the transfer arm which guarantees a preservation of temperatures during the transfer. Finally, in the analysis chamber X-ray eletron spectroscopy measurements are performed. For this purpose the ESCAlab is equipped with a non-monochromatized X-ray source with aluminum/magnesium twin anode and a hemispherical electron analyzer (VG Scientific). The BESSY analysis chamber is equipped with a channeltron NEXAFS detector and a Scienta R3000 hemispherical electron analyzer. The beamline is connected via a shutter which is opened only during measurements. Base pressures are in the low 10^{-9} mbar (preparation chamber BESSY) and the low 10^{-10} mbar (ESCAlab and BESSY analysis chamber) regime, respectively.

The manipulators can be cooled with liquid nitrogen (LN_2) which is pumped through capillaries inside the manipulator by connecting them to a dewar of LN_2 on one side and attaching membrane pumps on the other side. At BESSY minimum temperatures of 95 K in the preparation chamber and 120 K in the analysis chamber can be reached in this way, while the transfer arm in the UFO remains at room temperature at all times. ESCAlab sample temperatures reach 88 K minimum.

Sample temperatures are measured with chromel-alumel (type K) thermocouples spot-welded to one of the clamps which fixes the crystal on the sample holder (home-made and Prevac, PTS 1200 EB/C) to ensure that the thermocouple is in direct contact with the sample. The crystal is mounted on top of the sample holder's filament which allows radiative heating of the sample for annealing up to 550 K. If higher temperatures are necessary, e.g., during the cleaning process, it is possible to apply a potential difference between sample and filament in order to use electron beam heating.

3.1.2 Sample preparation and measurements

Substrate

All substrates used in this work (copper, silver, gold) were single crystals with a (111) oriented surface polished to $<0.5°$. They were purchased from *Surface Preparation Laboratory (SPL)* (Ag and Cu) and *MaTecK* (Au).

Prior to the deposition of molecules, the surfaces were cleaned by repeated cycles of sputtering and annealing which is a standard procedure for cleaning surfaces *in vacuo* [2, p. 37]. In a first step the surface was bombarded with Ar^+ ions with an energy of 1 keV, followed by annealing to 720-770 K to smooth the surface which had been degraded by the ion bombardment. The length of the sputtering and annealing steps varied depending on the coverage of molecules and/or contaminations of the sample, but typically the ion bombardment lasted 20 min, the annealing 10 min. Before dosing molecules the surfaces were examined with XPS to make sure that all contaminants were removed and with *low electron energy diffraction (LEED)* to check the order and quality of the (111) surface.

Molecules

The molecules were purchased from *Sigma Aldrich* (2H-TPP and $Ru_3(CO)_{12}$, 99% purity; Ru(CO)TPP, 80% purity) and *LivChem* (2H-P, > 95%). [Au(III)-TPP]$^+$Cl$^-$ was obtained from our collaborators in Linz (Section 6, ref. 58). The molecules were filled in a boron nitride (2H-TPP, Au-TPP) or a quartz (2H-P) crucible for use inside a Knudsen cell. After mounting, the evaporator was baked at 390-420 K for several hours, preferably overnight. Prior to the experiments the molecules were degassed *in vacuo* for several hours, at 520 K (2H-TPP) or 430 K (2H-P), respectively, to remove lighter impurities in the porphyrin powder.

Two different evaporators were used during the work for this thesis. The first was a two-cell evaporator (Fig. 3.2a), where the boron nitride crucible is placed inside a metal pot which is heated by a subjacent tungsten filament. The temperature is measured by a chromel-alumel thermocouple attached to the metal crucible by a washer. During the evaporation process the temperature is set manually by controlling the current through the filament during operation. While the use of this evaporator is simple, its long heating-up times make the experiment time-consuming and may cause alterations of the molecules after several cycles of sublimation.

Therefore a second type of evaporator was developed. The molecules are contained in a quartz crucible which itself is placed inside a boron nitride pot with an exterior thread which contains a platinum wire. The wire is used for heating the crucible and measuring the temperature in alternating intervals. During the measurement interval (1 s) the resistance of the platinum wire is determined by applying a current of 0.1 A and measuring the voltage. The signal is communicated via an analog-digital I/O device (Labjack) to a com-

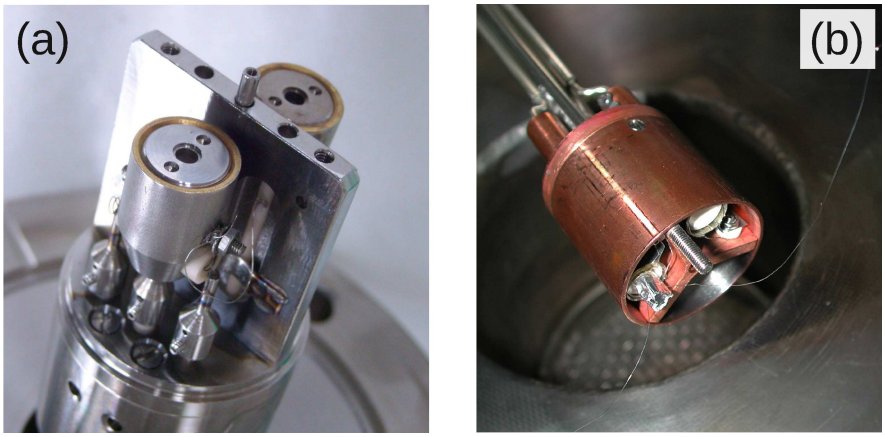

Figure 3.2: (a) Two-cell evaporator: Inside the two metal pots are boron nitrile crucibles which contain the molecules. The temperature is measured with an attached chromel-alumel thermocouple (on the right), the filament is located below the pot inside the ceramics. (b) Calibration of the home-made evaporator inside a vacuum bell: an external thermocouple is placed inside the crucible and fixed with aluminum foil. The temperatures measured in this way lie approximately 5% below the values of the platinum wire.

puter which calculates (based on the Callendar-Van Dusen equation[119]) the temperature for the given resistance with respect to values obtained from reference measurements. Consequently, the control loop determines the necessary heating current for the next heating interval (typically 2 s). If the parameters for the control loop are assigned properly this method has the advantage of exact temperature control and very short heating-up times which allows a well-regulated evaporation of the molecules. Measurements in a vacuum bell jar with a thermocouple inside the crucible (Fig. 3.2b) show that the temperatures inside the quartz crucible lie approximately 5% below the displayed value of the platinum wire.

Dosing temperatures were chosen in a way that enabled sufficient rates while taking into account potential damages to the molecules at exceedingly high temperatures. Table 3.1 lists the evaporation temperatures of the molecules T_{mol}, the corresponding temperatures of the substrate T_{sub} during deposition and the sample temperature during measurements T_{meas} for the different experiments conducted for this thesis.

The ruthenium dodecacarbonyl $Ru_3(CO)_{12}$ is volatile in vacuum, therefore the dosing was carried out by mounting a glass tube containing the compound separated from the chamber by a gate valve and independently pumped, and opening the gate valve for the desired period of time when necessary.

Table 3.1: Parameters for the evaporation of the porphyrins. T_{mol} is the temperature of the crucible, T_{sub} is the temperature of the substrate during deposition and T_{meas} is the sample temperature during measurements.

Section	Preparation	T_{mol}	T_{sub}	T_{meas}
4.2	2H-TPP/Cu(111)	600 K	220 K	200 K
4.3	2H-P/Cu(111)	490 K	300 K	300 K
5.2	Ru(CO)TPP/Ag(111)	563 K	305 K	305 K
5.4	2H-TPP/Ag(111) + $Ru_3(CO)_{12}$	563 K	305 K	305 K
5.5	2H-P/Ag(111) + $Ru_3(CO)_{12}$	483 K	305 K	305 K
7.3 [i]	2H-P/Ag(111) + 2H-P/Cu(111)	490 K	Section 7.3	Section 7.3
6	Au-TPP/Au(111)	743 K[ii]	88 K[iii]	88 K[iii]

[i]For Chapter 7 details are specified further in the corresponding text.
[ii]The value is not very meaningful as these were the first experiments using a new evaporator and the temperature scale calibration is different from that of other experiments.
[iii]For the graphs shown in Chapter 6, but the results are also valid for experiments performed at room temperature (not shown).

The thicknesses of the porphyrin layers were calibrated against the XPS signals of monolayers of 2H-TPP, 2H-P and Au-TPP which were obtained by annealing a multilayer to 550 K and 433 K, respectively. The idea behind this method is based on the assumption that the interaction of the molecules with the substrate is different (in most cases stronger) than the molecule-molecule interaction in higher layers, thus upon stepwise annealing the condensed overlayers are removed and only one monolayer remains. Throughout this work the term monolayer (ML) is used for the maximum coverage of molecules in direct contact with the surface. This method of determining the monolayer is not very precise, for several reasons: One important point is that annealing may result not only in desorption of the overlayers, but also in chemical changes of the molecules (as it will be discussed in the following chapters) and the resulting compound possibly exhibits a different ordering behavior, thus leading to a different molecule density in the monolayer. A second point to keep in mind is the attenuation of the XPS signals due to different ordering in higher layers. The limited mean-free path of the photoelectrons leads to different signals for the same coverage, depending on whether the molecules adsorb flat or per-

pendicular to the surface. Besides, different background subtraction and peak fitting procedures can lead to small quantitative deviations. Therefore, in addition to the stepwise annealing series also successive dosing series are considered when determining the monolayer coverage, e.g., by comparing core level shifts which typically occur between multi- and monolayers. Keeping these points in mind, the preparations in this work are classified as submonolayer, monolayer, bilayer and multilayer without a more detailed quantification.

XPS Measurements

After the deposition of the molecules XPS measurements were carried out to make sure that the sample contained only the expected chemical elements and that the stoichiometric ratios between carbon and nitrogen of the porphyrins were in the expected range. For each preparation XP spectra of the C1s and the N1s region, as well as an overview spectrum were taken. Depending on the investigated problem XPS data of other regions or NEXAFS spectra were recorded as well.

Generally, for higher pass energy (PE) values the energy resolution gets worse and the intensity increases. Therefore for each problem a compromise between the necessary resolution and sufficient counts had to be found. The overview spectra at BESSY were always taken with PE= 100 eV (50 eV at ESCAlab) because it was important to detect all possible elements, while the details of the interesting regions were recorded with higher resolution (mainly 20 eV, 50 eV only in Section 4.2). These parameters are listed in Table 3.2.

The second tunable parameter for synchrotron experiments was the photon energy $\hbar\omega$. By varying $\hbar\omega$ the kinetic energies of the detected electrons change (cf. Eq. 2.1). As the transmission function of the analyzer T is a function of the kinetic energy of the detected photoelectrons, the measured intensity also depends on $\hbar\omega$ (cf. Eq. 2.3). In order to be able to compare the intensities of the N1s and the C1s signal and consequently to calculate the stoichiometric ratios, it is necessary to choose $\hbar\omega$ in a way that the kinetic energies for both regions are the same. A second consequence of varying the kinetic energy of the photoelectrons is the modified surface sensitivity. In this thesis $\hbar\omega$ was chosen so that the kinetic energy of the electrons from carbon or nitrogen atoms was either 100 eV or 150 eV, which corresponds to an electron mean free path of approximately 3-8 Å.[77] This allows to study monolayers and the underlying substrate as well as the top layers of multilayer samples for which it is desirable that no signal from the first layers is detected. Only for the overview spectra a higher photon energy was used to cover all possible regions. The different

Table 3.2: Parameters for XPS measurements of different regions: photon energy $\hbar\omega$ and pass energy PE.

Section	Region	Setup	$\hbar\omega$	Pass energy
all	overview (Ag substrate)	BESSY	770 eV	100 eV
all	overview (Cu substrate)	BESSY	700 eV	100 eV
4.2	C1s	BESSY	435 eV	50 eV
4.2	N1s	BESSY	550 eV	50 eV
4.3, 7.3	C1s	BESSY	385 eV	20 eV
4.3, 7.3	N1s	BESSY	500 eV	20 eV
7.3, 7.3	C1s	BESSY	435 eV	20 eV
7.3, 7.3	N1s	BESSY	550 eV	20 eV
6	overview	ESCAlab	1486.6 eV	50 eV
6	C1s, N1s, Au4f	ESCAlab	1486.6 eV	20 eV

values for experiments on different substrates (see Table 3.2) result from the fact that the variation of $\hbar\omega$ also shifts the position of the Auger peaks from the substrate in the binding energy spectrum. Hence $\hbar\omega$ is selected in a way that the Auger structure does not interfere with the primary photoelectron features.

The variation of the photon energy implies the movement of the monochromator which (at least at the beamline HE-SGM) exhibits a certain hysteresis. Therefore the binding energy scale has to be calibrated. Assuming that the adsorption of the molecules does not change the chemical state of the substrate bulk, for every region a spectrum of characteristic substrate peaks (see Section 3.1.3) was measured.

Unless otherwise stated, the XP spectra et BESSY were taken in normal emission mode, i.e., the aperture of the analyzer was aligned in line with the sample normal. The x- and y-positions with respect to the beam were calibrated at the beginning of each beamtime in a way that the recorded intensity was maximal. During experiments the z-position of the sample was changed from time to time to verify that no radiation damage occurred. ESCAlab measurements were conducted with a fixed angle (nearly normal emission, $\sim 80°$) between sample and analyzer. As the spot of the beam is considerably larger than that at BESSY (approximately 4 cm^2 vs. 1 mm^2) the position has to be

kept fixed to avoid signals from molecules adsorbed on the sample holder.

NEXAFS Measurements

As described in Section 2.2 a direct measurement of the photon energy dependent absorption is not possible for solids. The spectra in this work were taken in the partial electron yield (PEY) mode, where secondary electrons resulting from decay processes following the absorption are detected. Contrary to the total electron yield mode, where all electrons are recorded, the PEY mode uses retarding voltages to prevent slow electrons from reaching the detector. All NEXAFS data in this thesis were recorded with a retarding voltage of -250 V for the N K-edge and -150 V for the C K-edge. Channeltron amplifier voltages were typically kept constant for a series of experiments and were only varied between preparations with considerably varying coverages to obtain the maximum possible intensity before reaching the saturation limit of the detector.

Simultaneously to the PEY spectra the photocurrent signal of a (partly contaminated, see Section 3.1.3) gold grid traversed by the X-ray beam was recorded, which is used for calibrating the photon energy scale (Section 3.1.3). In addition, the comparison of the Au grid curves (Fig. 3.4b) for different preparations allows to identify instabilities of the X-ray beam, which may artifacts in the spectrum.

The incidence angle θ between the surface normal and the electric field ($\vec{E}$-vector) of the linear polarized light was varied by rotating the sample with respect to the incoming beam (see Figs. 2.4b and 3.4d, inset). For the given polarization (90% unless otherwise noted) the magic angle at the measured intensity distribution becomes independent of the molecular orientation amounts to 53°. For each of the three different angles (25°, 53° and 90° if not otherwise noted) several spectra were recorded and averaged. This improves the signal-to-noise ratio and allows to verify that no beam damage occurred. Typically the curves for one angle were not recorded consecutively, but in sets of 25°→ 90° followed by 90°→ 25° to exclude possible hysteresis effects during sample rotation. For all the measurements in this work, no such effects could be found. Normally the rotation of the manipulator in the analysis chamber was not totally symmetric, therefore the determination of the best sample position had to be conducted more accurately than for the XPS measurements. The x- and y-positions were chosen to result in the maximum intensity for all three angles, not only for a single one.

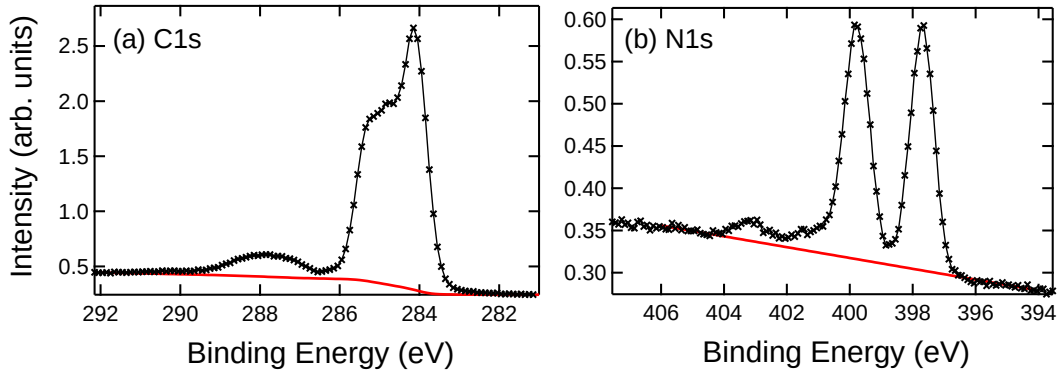

Figure 3.3: XPS raw data (black markers) and different backgrounds (red): The Shirley background (a) accounts for the typical step in XPS intensities before and after the photoelectron peak, the linear background (b) is more straightforward and assumes a constant slope.

3.1.3 Data analysis

The analysis of the XPS and NEXAFS data were performed with the software *Igor Pro*[120] using data processing and fitting routines which were developed in the surface science group E20 (TU München) and further adapted during this work.[121] All graphs in this thesis which show experimental XPS and NEXAFS spectroscopy data were created with Igor Pro.

XPS

As described above, the non-perfect reproducibility of the monochromator position at the nominal photon energy during measurements at BESSY requires a calibration of the binding energy scale. The same routine was applied to data taken at the ESCAlab, even if the energies there are more stable. To this end reference spectra of substrate peaks were recorded for each measurement, using the same set of parameters for both curves. Hence, the first step of the data analysis for each single line consisted in fitting a Gaussian to the Cu3$p_{3/2}$ or the Ag3$d_{5/2}$ peak of the substrate reference. Both the line and the reference spectrum were then shifted by the difference to the reference values for Cu3$p_{3/2}$ (75.1 eV) or Ag3$d_{5/2}$ (368.3 eV).[122] A different approach, namely the measurement of the Fermi-edge, was more problematic: the exact determination of the edge is more difficult than fitting the peaks of the substrate and the counting rates in the Fermi-edge region are typically low.

After the calibration of the energy scale, the raw data was cropped to remove unnecessary parts of the background. To obtain quantitative informa-

tion about the peak intensities, it is necessary to remove the inelastic XPS background before the peak fitting. In this work a linear background was subtracted for the N1s and a Shirley background for the C1s spectra. A linear background, i.e, a straight line between the first and the last points of a spectrum, is used for backgrounds of constant slope (Fig. 3.3b), while the Shirley background accounts for the typical step in intensities before and after the photoelectron peak (Fig. 3.3a). The Shirley background B^{123} has the form

$$B(E) = A \int_{E'>E} |P(E') - P_0| \, \mathrm{d}E' \tag{3.1}$$

where $B(E)$ is the background at energy E, P_0 is the intensity of the background on the low binding energy side of the peak and $P(E')$ the total signal at a given energy E' [2, p. 204]. $B(E)$ is thus proportional to the peak area up to the energy E, i.e., it is assumed that each additional photoelectron gives the same (constant) contribution to the background. For the data analysis in Chapter 5 an empirical polynomial background was subtracted, which is motivated in Appendix A.3.

As the N1s and C1s spectra in this work normally consist of several, sometimes overlapping signals from different species in the molecule, the fitting procedure is crucial for the interpretation of the data. Two main effects contribute to the line shapes of XPS peaks: intrinsic broadening that originates from the photoemission process leads to a Lorentzian lineshape, while additional Gaussian broadening is caused by the finite resolution of the instrumental setup [60, p. 573]. A reasonable choice of fitting functions is therefore given by Voigt curves which convoluting Lorentzian and Gaussian curves. Spectra in this work were fitted with an iterative least-square procedure, where the initial guess for the four Voigt parameters (amplitude, energy, width and shape which determines the ratio of mixing of Gaussians and Lorentzians) is varied within a range of specified constraints in order to obtain the best agreement with the experiment.

Up to October 2012, BESSY II was operating in decay mode, where the beam current was 300 mA directly after the injection of electrons into the storage ring and then it decreased continuously to 180 mA shortly before the next injection. This change in intensity of the X-ray beam was taken into account for quantitative XPS analysis.

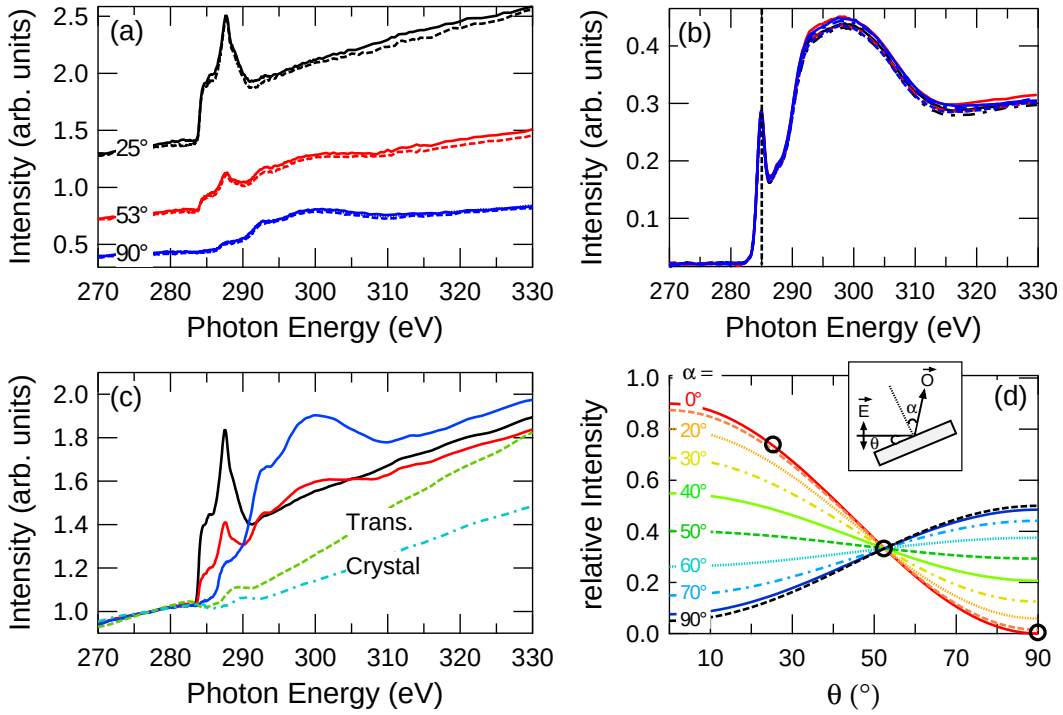

Figure 3.4: Different steps in NEXAFS spectroscopy analysis: (a) Raw data of graph in Fig. 4.16f, taken at three different incidence angles θ, (b) Spectra of contaminated gold grid, which is used for the calibration of the photon energy scale. The reference value (285.0 eV) is indicated by the dotted line, (c) Energy corrected spectra after averaging, smoothing and normalization, the background of the clean crystal ("Crystal") and the transmission function ("Trans.") are displayed, (d) Theoretical curves for different adsorption angles α dependent on the incidence angle θ. Three black circles indicate the relative intensities for a π-system co-planar to the surface.

NEXAFS

The background of NEXAFS curves is more difficult to access than the XPS background. As an example the raw data of Fig. 4.16f are displayed in Fig. 3.4a. Similar to XPS, the first step of the analysis of NEXAFS data is the calibration of the energy scale. The photon energy scales were referenced against characteristic peaks (399.0 eV for nitrogen, 285.0 eV for carbon, Fig. 3.4b) of the Au grid spectra which were recorded simultaneously to the PEY signal (Section 3.1.2).

For XPS the photon energy is kept fixed, thus the intensity of the incident X-ray beam exhibits only minimal variations during one measurement. In contrast, NEXAFS spectroscopy is based on scanning over a photon energy range which can lead to big variations in the intensity of the X-rays impinging the

sample as the transmission of the beam through the (possibly contaminated) beamline introduces an additional energy dependence of the beam intensity. A further effect contributing to the background is given by the energy-dependence of the substrate (bulk) signal. One possibility to account for the transmission dependence is the division by a reference signal recorded simultaneously to the PEY spectrum. However, this method is not well suited for thin layers of adsorbates (as in the case of most preparations in this thesis) as it neglects the contribution of the substrate background [61, p. 157]

Therefore in this work the following procedure was used: After calibrating the photon energy scale, the spectra for each incidence angle θ were averaged, smoothed and normalized to the pre-edge region to account for differences in the ring current (Fig. 3.4c). Afterwards, the signal of the bare crystal (green dashed line in Fig. 3.4c) was subtracted from the sample spectrum, which accounts for the contribution of the substrate to the background [61, p. 161]. The spectra were then divided by the transmission function (cyan dash-dotted line in Fig. 3.4c) of the beamline which was determined once by taking the total energy yield spectrum of a clean gold sample. This procedure was followed by a normalization of the edge jump to one. In some cases the crystal function had to be scaled to account for the damping of the signal due to the adsorption of molecules and/or an additional constant background had to be subtracted from the raw data. Appendix A.2 shows that the deviation of the finally derived adsorption angle for different background subtraction techniques is no more than 5-8°.

After background subtraction the data were fitted to obtain angular dependencies (not shown here). Due to limited photon energy resolution Gaussian functions are well suited for the fit, while Lorentzian curves do not match the shape of experimental resonances [61, p. 214]. The analysis focused on the π^* region as the deconvolution is easier for the sharp π^* resonances than for the broader σ^* structure. To reduce the number of independent parameters the following procedure was applied: The peak assignment (e.g. by using the information from DFT simulations) allowed to deconvolute the spectrum in sets of resonances originating from the same chemical or functional group species. Within each set the intensities of the single peaks had to follow the same angular dependence, while energies and widths were kept at fixed values relative to the first peak. Thus, the fitting procedure had to optimize less independent parameters (compared to an unrestrained fit) for the reproduction of the whole π^* range. The obtained relative intensities were compared to the theoretically expected curves for different adsorption angles α (Fig. 3.4d), thus allowing the

determination of α for the different subgroups of the system. For the definition of the angles see inset of Fig. 3.4d. The relative intensities in the example are indicated by three black circles which shows that the π system adsorbs parallel to the surface ($\alpha = 0$).

The interpretation of monolayer data can be difficult as strong interactions with the substrate can lead to a considerable broadening of the resonances and additional effects like charge transfers can further affect the intensities (cf. Chapter 4). Therefore the interpretation is never conducted for one single preparation, but normally the whole set of experiments has to be taken into account. Typically the peak assignment by comparison to DFT calculations is much easier for multilayer data as the molecule-molecule interaction is less strong than the molecule-substrate interaction. Especially in Chapter 4 these findings are applied to the interpretation of the (sub)monolayer curves to draw conclusions regarding the interaction with the surface.

3.2 Computational Details

3.2.1 StoBe

Geometry optimization and electronic structure calculations in Chapter 4 were performed for isolated molecules (without surface), employing the DFT program package *StoBe (Stockholm-Berlin)*[104] using a RPBE (revised Perdew, Burke, and Ernzerhof,[95,96]) functional. StoBe uses the LCAO approach (cf. Section 2.3.3) to describe the Kohn-Sham orbitals.

In a first step the molecule's geometry was optimized by varying the atomic positions until the forces on the atoms were smaller than 10^{-4} Ha/Bohr. The Hessian matrix was updated between consecutive steps using the Broyden-Fletcher-Goldfarb-Shanno method. For the optimization all-electron triple-zeta plus valence polarization type basis sets were used to describe the nitrogen,[124] carbon[124] and hydrogen[125] atoms in the porphyrins (Table 3.3).

STM measurements show that various porphyrin compounds, e.g., Co-TPP on Ag(111)[54] or TPyP on Cu(111),[44] adsorb in a saddle-shape conformation where the macrocycle is deformed such that two opposite pyrrole rings point upwards and the other two point towards the substrate. Therefore a saddle-shape conformation was used as starting geometry of the optimization. The vibrational analysis of the optimized molecule geometries did not show any negative frequencies which excludes the possibility that the optimization routine merely converged to a saddle point. The optimization lead to a flat conforma-

Table 3.3: StoBe basis sets used for the geometry optimization (GO), the vibrational analysis (Vib) and the electronic structure (ES) calculations for a given excitation center.

Excit. center	Atom	Calculation	Orbital	Auxilary
-	N, C	GO, Vib	(7111/411/1)	(5,2;5,2)
all	H	all	(3111/111)	(3,1;3,1)
all	Cu	all	(63321/531/311)	(5,5;5,5)
N	N (exc.)	ES	III-IGLO	(5,2;5,2)
N	N (rest)	ES	(+5) (321/311/1)	(+5) (4,4;4,4)
N	C	ES	(7111/411/1)	(5,2;5,2)
C	C (exc.)	ES	III-IGLO	(5,3;5,3)
C	C (rest)	ES	(+4) (311/211/1)	(+4) (3,3;3,3)
C	N	ES	(7111/411/1)	(5,2;5,2)

tion of the 2H-P and the Cu-P (cf. Fig. 4.2). The 2H-TPP, however, remained in a saddle-shape geometry with tilted phenyl rings (cf. Fig. 4.2), while the Cu-TPP exhibits a flatter macrocycle with perpendicular phenyl groups (cf. Fig. 4.2). The calculated bond lengths and angles agree well with the solid state structures determined by X-ray diffraction of 2H-TPP and Cu-TPP[126,127] and 2H-P.[128] Details of the optimized geometries and comparison with literature data can be found in Appendix A.1.

The core level energies of the inequivalent nitrogen and carbon atoms, are typically non-degenerate, but can have very similar energies. To ensure the excitation of a specific atom in the molecule, the basis set of this excitation center was of all-electron IGLO-III (individual gauge for localized orbitals[129]) quality for the electronic structure calculations, yielding an improved representation of relaxation effects in the inner atomic shells. ECPs (effective core potentials) for the 1s core and appropriate valence basis sets[130] were used to describe all other atoms of the same element type (Table. 3.3), thus the 1s energy of the excitation center was easily identifiable. This approach has only negligible effects on the calculated excitation spectra[131] which is also confirmed in Section 7 where the XP spectra for 2H-P simulated with this approach are identical to the all-electron calculations with FHI-aims.

Ionization (XPS) energies were determined by calculating the difference between the energies of the ground state and the core-hole state (Eq. 2.35). For

the simulation of NEXAFS spectra the transition potential approach (Section 2.3.4) implemented in StoBe was employed. For the last step of the absorption spectrum calculation the basis set was extended by using additional, large diffuse even-tempered [19s19p19d] basis sets[132] at the excitation center to improve the description of excitations to Rydberg and continuum final states (double basis set technique[132])

To obtain a continuous spectrum for a direct comparison of calculated and measured NEXAFS curves the calculated discrete excitation energies and corresponding dipole transition matrix elements were convoluted with Gaussians. As it had been discussed above, Gaussians are a good approximation to the real lineshapes and, since energy and amplitude are known, a single free parameter (the width) has to be varied for the best agreement between theory and experiment. To account for the reduced lifetime of the σ^* resonances which lead to broader features above the ionization energy E_{ion}, the width of the Gaussians varied according to

$$f(E) = \begin{cases} \mathrm{b}_1, & \text{for } E \leq E_{ion} \\ \mathrm{b}_2, & \text{for } E > E_{ion}+10 \text{ eV} \end{cases} \tag{3.2}$$

with a linear increase from b_1 to b_2 in between. In Section 4.2 the transitions for both C K-edge and N K-edge were broadened with $\mathrm{b}_1 = 0.5$ eV and $\mathrm{b}_2 = 4.5$ eV, while in Sections 4.3 and 7.2 $\mathrm{b}_1 = 0.6$ eV and $\mathrm{b}_2 = 5.5$ eV were used for the C K-edge and $\mathrm{b}_1 = 0.7$ eV and $\mathrm{b}_2 = 5.5$ eV for the N K-edge to reproduce the experimental spectra in the best way.

The missing core hole relaxation of the excited final state due to the transition potential approximation was taken into account by shifting the excitation energy scale by Δ_{ion}

$$\Delta_{ion} = E_{ion}^{TP} - E_{ion}^{\Delta KS} \tag{3.3}$$

where E_{ion}^{TP} is the ionization energy obtained from the transition potential calculation and $E_{ion}^{\Delta KS}$ is determined with Eq. 2.35. For the C K-edge this shift amounted to -1.4 eV, for the N K-edge to -1.6 eV (Table 3.4). An additional global shift Δ_{rel} was introduced to account for relativistic corrections. For carbon $\Delta_{rel} = 0.1$ eV and for nitrogen $\Delta_{rel} = 0.3$ eV.[108] The agreement between the corrected simulated and the measured spectra is high for the N K-edge, for the carbon edge small additional shifts had to be introduced for an optimal agreement between theory and experiment (Table 3.4). They may originate from either numerical basis set and/or experimental calibration effects. For easier comparison these shifts are included in Figs. 4.6 and 4.17.

Table 3.4: Correction shifts of the transition energy scale: Δ_{ion} corrects for the missing core hole relaxation of the TP method, Δ_{rel} is the relativistic shift, Δ_{exp} is the additional shift that is necessary for the best agreement between theory and experiment.

Section	System	Δ_{ion}	Δ_{rel}	Δ_{exp}
4.2	2H-TPP, C K-edge	-1.4 eV	0.1 eV	0.4 eV
4.2	2H-TPP, N K-edge	-1.6 eV	0.3 eV	0
4.3, 7	2H-P, C K-edge	-1.4 eV	0.1 eV	0.1 eV
4.3, 7	2H-P, N K-edge	-1.6 eV	0.3 eV	0.1 eV

Table 3.5: Basis sets used for the geometry optimizations (GO) and calculations of XPS energies with FHI-aims.

Functional	Atom	Calculation	Basis
PBE	N, C	GO	Tier2 Tight
PBE	N, C	XPS	Tier3 Tight
B3LYP	N, C	XPS	Tier2 Light

3.2.2 FHI-aims

Calculations of optimized geometries and XPS energies in Chapter 7 were conducted for isolated molecules and for molecule clusters of varying size using the DFT package *FHI-aims (ab initio molecular simulations)*.[107]

FHI-aims uses all-electron numerical atom-centered orbitals (NAOs), which are grouped in sets of different quality. *Light* basis sets were used for first pre-relaxation steps of geometry optimizations, though (at least for the PBE functional) all relevant electronic structure calculations were performed with *tight* basis sets. The basis sets are further grouped in levels (or *tiers*), where the minimal basis is the lowest one with free-atom-like radial functions. Tier 1-tier 4 employ further sets of radial functions, i.e., the accuracy should increase with increasing tier. Typically the same tier is used for all elements. The basis set level was converged, i.e., the first calculations were for example performed with tier 2, followed by a test with tier 3 to check whether the properties have changed substantially. The following basis sets were finally used in this work:

Contrary to the *StoBe* approach where ECPs are used for the non-excited atoms to single out the excitation center, the electronic structure calculations

with *Aims* are conducted using the same all-electron basis set for all atoms of the same element type in both the ground-state and the core-hole state calculation. This has the advantage that the number of single-point runs is reduced by nearly a factor 2, since only one ground-state calculation is necessary for all excitations. This is relevant especially for systems consisting of more than one molecule. On the other hand it also means that the identification of the 1*s* orbital for a specific atom is not as easy as with *StoBe*, because of the (especially for the molecule clusters) large number of similar core hole energies. The first step is therefore always to locate the 1*s* orbital of the atom of interest in the ground-state calculation, followed by the removal of an electron from this orbital. Ionization energies were consequently determined by calculating the difference between the total energies of the ground-state and the core-hole state (Eq. 2.35). Results for different basis sets and xc-functionals are discussed in Section 7.2.

As described in Section 3.2.1 all electronic structure calculations were preceded by geometry optimizations. Starting geometries were a slightly and a strongly saddle-shaped 2H-P and the optimized geometry of the *StoBe* calculation. All optimizations of the 2H-P monomer converged to the same final geometry which agreed very well with the *StoBe* results (cf. appendix A.1).

One of the goals of the investigation of 2H-P multilayers in Chapter 7 is to study the influence of the molecular stacking on the XPS energies. To this purpose geometry optimizations and calculations of ionization energies were performed for 2H-P dimers and trimers with varying geometric properties, e.g., distances between molecules. All calculations involving more than one molecule were performed using the Tkatchenko-Scheffler van-der-Waals correction (cf. Section 2.3.5). Periodic boundary conditions were applied for the structure optimization of indefinite chains of porphyrins. The unit cell was chosen to be large in x- and y-direction (40 Å each) assuming no interaction between adjacent molecules (Fig. 3.5). Consequently, the k-point grid was set up such that in x- and y-direction one, and in z-direction four points were used. The molecule and the unit cell in z-direction were allowed to relax, until forces on the atoms were below $1{\cdot}10^{-4}$ eV/Å. XPS energies were consequently determined by cutting a trimer from the optimized chain and exciting the atoms of the molecule in the middle (for details see Chapter 7).

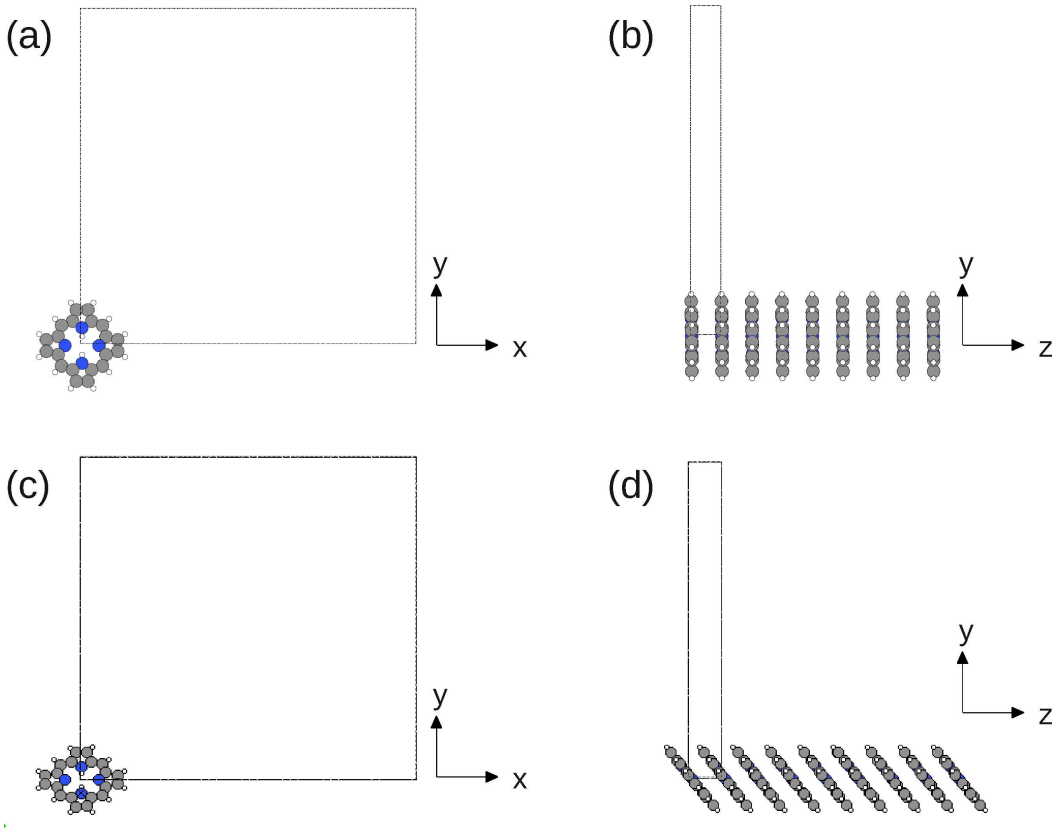

Figure 3.5: Unit cell for stacking of 2H-P along the z-axis. (a) top and (b) side view of symmetrical porphine chain; (c) top and (d) side view of tilted porphine chain

Chapter 4

Self-Metalation

4.1 Introduction

As has been briefly discussed in Chapter 1, the self-organization properties of adsorbates on surfaces are the result of a complex interplay between molecule-molecule and molecule-substrate interactions. How the nature of these interactions are influenced by the choice of the adsorbate-substrate system is the crucial point which needs to be understood for the deliberate construction of nano-structures on surfaces. Free-base tetraphenyl-porphyrin (2H-TPP, Fig. 4.1a) adsorbed on a Ag(111) surface, for example, forms ordered islands, which is not the case for the adsorption of 2H-TPP on Cu(111).[133] The same holds true for free-base tetrapyridyl-porphyrin (2H-TPyP), which adsorbs as single molecules on Cu(111),[44] but self-assembles on Ag(111).[40]

STM experiments dedicated to study the adsorption of different substituted TPPs show that the choice of the substituents can influence the adsorption geometry and the orientation of porphyrins on the surface, which was attributed to the fact that the binding to the surface occurs primary through the attached phenyl groups.[134] While a myriad of investigations is devoted to the behavior of substituted porphyrins, surprisingly there are far less studies about the interaction between metal surfaces and the parent porphyrin compound, the free-base porphine (2H-P, Fig. 4.1c) which consists only of the central macrocycle. In this chapter the adsorption of free-base and metalated TPP is contrasted with the adsorption of the respective porphine species.

To investigate how the presence of a central metal atom influences the adsorption properties of porphyrins, experiments are conducted for metalated and non-metalated species on the same substrate. To this end, it is possible to use premanufactured metalloporphyrins[54] which is comfortable when the desired compound is commercially available, but has the disadvantage that

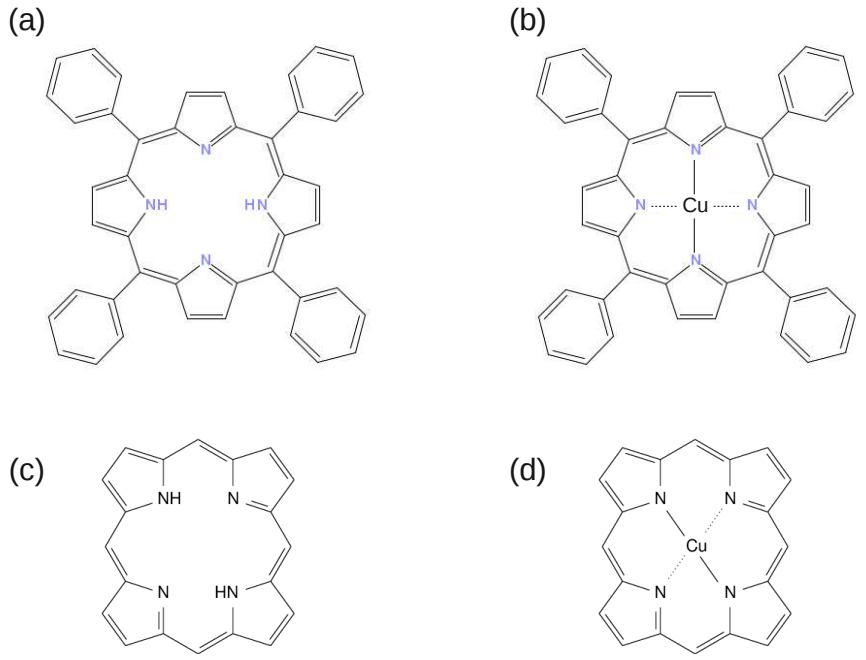

Figure 4.1: Struktural formulas of (a) free-base tetraphenyl-porphyrin (2H-TPP), (b) copper tetraphenyl-porphyrin (Cu-TPP), (c) free-base porphine (2H-P) and (d) copper porphine (Cu-P). (a) and (c) are the initial free-base compounds used in the experiments presented in this chapter, (b) and (d) follow from *in situ* metalation.

preparation conditions, especially evaporation temperatures, may differ from those of the free-base porphyrins which always means a certain range of uncertainty in the interpretation of the data. Besides, not every metallo-porphyrin is easily available and stable under evaporation. Alternatively, it is possible to evaporate free-base porphyrins and metalate them *in situ* on the surface.At the beginning of this work, the typically employed procedure for the metalation of porphyrins was the coevaporation of molecules and metal atoms on the substrate, sometimes followed by an annealing step.[41,42,51,55,135] This makes the preparation of clean samples even for reactive metalloporphyrins possible, though the handling of metal evaporators is not always trivial in practice. In this chapter an alternative approach, the *self-metalation*, i.e., the metalation of adsorbed free-base porphyrins by substrate atoms, is analyzed. On-campus XPS measurements performed prior to the present work showed that self-metalation is possible,[136] but a systematic study including NEXAFS measurements was lacking. Parallel to the work on this topic, self-metalation has been reported for protoporphyrin IX (H2PPIX) on Cu(110) and Cu(100).[137]

The adsorption of 2H-TPP on Cu(111) (Section 4.2) and of 2H-P on Cu(111) (Section 4.3) is investigated with XPS, NEXAFS spectroscopy, aided by DFT

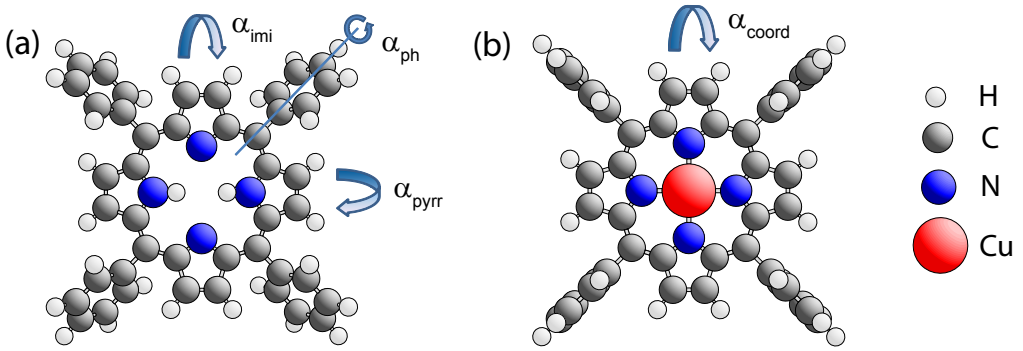

Figure 4.2: Models of (a) 2H-TPP and (b) Cu-TPP displayed with conformations obtained by geometry optimization of isolated molecules. The angles α_{imi}, α_{pyrr} and α_{coord} describe the inclination of the respective pyrrole rings out of the macrocycle plane, α_{ph} refers to the rotation of a phenyl ring around the C-C bond that connects it to the macrocycle. The model in (b) is characterized by $\alpha_{coord} = 0$ and $\alpha_{ph} = 90°$.

calculations to study the respective adsorption geometries and electronic properties of the adsorbates. In both cases self-metalation to copper tetraphenylporphyrin (Cu-TPP, Fig. 4.1b) and copper porphine (2H-P, Fig. 4.1d), respectively, is used to analyze the influence the presence of the central copper atom has on the adsorption properties. To describe adsorption geometries two principal deformations are taken into account: The deformation of the macrocycle by an inclination of the pyrrole rings out of plane which is described by α_{imi} and α_{pyrrol} for the iminic and the pyrrolic components of the 2H-TPP (see Fig. 4.2a) and 2H-P and α_{coord} for Cu-TPP (see Fig. 4.2b) and Cu-P can be accompanied by a rotation of the phenyl rings (denoted as α_{ph}).
To summarize, the following three main issues are addressed in this chapter:

1. Study the adsorption of the free-base porphyrins 2H-TPP (Section 4.2) and 2H-P (Section 4.3) on Cu(111), with special respect to adsorption geometries and electronic structure of the adsorbates. This is achieved by comparing the results of mono- and multilayer XPS and NEXAFS measurements. DFT calculations are used for the peak assignment.
2. Follow the self-metalation of the two compounds to Cu-TPP (Section 4.2) and Cu-P (Section 4.3) in order to analyze possible changes in molecule-substrate interactions.
3. Compare how the presence of the phenyl-substituents influences the adsorption properties of metalated and non-metalated species by contrasting the results from Section 4.2 and 4.3.

Section 4.2 was already published in ref. 56, Section 4.3 in ref. 57.

4.2 2H-TPP on Cu(111)

4.2.1 Self-metalation

2H-TPP layers of different thicknesses were prepared on the Cu(111) surface, following the procedures in Chapter 3. Taking into account the different scattering cross sections, the XPS peak area ratio for the N1s and C1s signals was in agreement with the expected value of 11 (44 carbon, 4 nitrogen atoms) for all samples. No signals other than of Cu, N and C were detected. The ratio and the absence of contaminations indicate the controlled evaporation of intact molecules.

After the deposition of a 2H-TPP multilayer the N1s XPS spectrum shows two principal peaks (Fig. 4.3b) as expected from the nonequivalence of the nitrogen atoms in the 2H-TPP molecule. Peak A with a binding energy (E_B) of 398.3 eV is assigned to iminic (=N-), peak B at E_B = 400.3 eV to pyrrolic (-NH-) nitrogen atoms. A third small peak C (E_B = 403.4 eV) is tentatively regarded to be a shake-up satellite following the argumentation in ref. 72. The assignment of the two main peaks is corroborated by former experimental results[72,138] and the results of our DFT calculations for the ionization potential of the iminic (E_{Calc} = 402.0 eV) and pyrrolic (E_{Calc} = 404.2 eV) nitrogen atoms in an isolated 2H-TPP molecule (Table 4.1). Since molecule-surface interactions are not taken into account in the XPS and NEXAFS calculations the theoretically determined values and spectra are compared only to measurements of multilayers where it can be assumed that the substrate hardly has any direct influence on the molecules. While the calculated ionization potentials are referenced to the vacuum level the measured binding energies are referenced to the Fermi level which leads to an intrinsic difference of several eV between the respective values. The XPS calculations confirm that the binding energy of the pyrrolic nitrogen lies approximately 2 eV higher than that of the iminic nitrogen.

A 2H-TPP sample with an approximate coverage of slightly below one ML was prepared by evaporating free-base porphyrins onto the freshly cleaned copper surface. As our method of controlling the coverage is associated with a certain degree of uncertainty and it is necessary to avoid interfering signals from a possible second layer, the coverage of our prepared sample was chosen to be below one ML. The corresponding N1s XPS data (Fig. 4.3c) show two peaks that are assigned again to iminic and pyrrolic nitrogen species. A down-shift, i.e., a shift to lower binding energies, with respect to the multilayer sample is observed for both peaks. On a metallic substrate this is not unexpected and

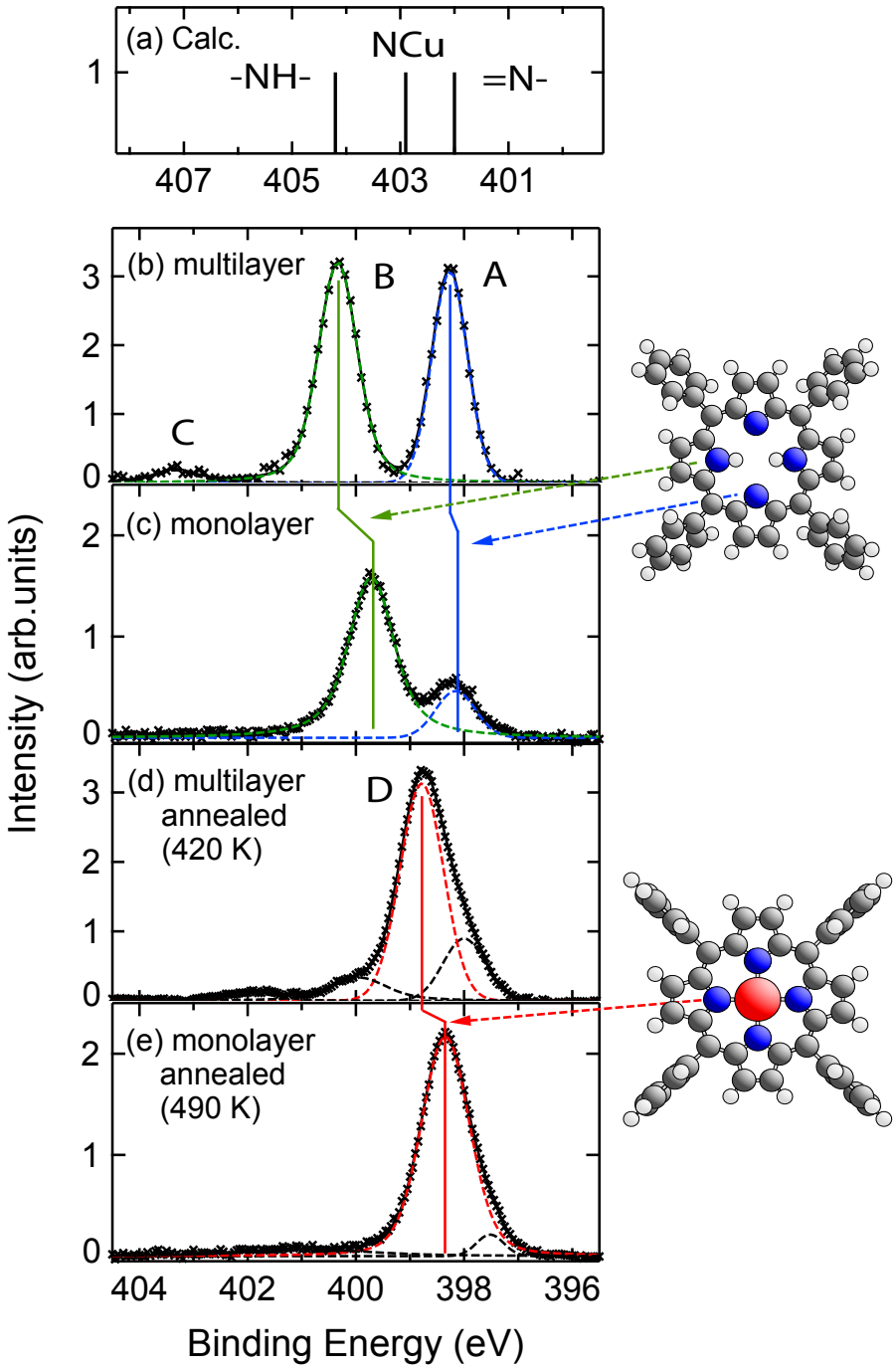

Figure 4.3: The N1s XPS spectra of (a) a 2H-TPP multilayer and (b) a 2H-TPP monolayer adsorbed on Cu(111) show two peaks that are assigned to iminic (A, blue) and pyrrolic (B, green) nitrogen species. After annealing the multilayer sample (3-4 layers) to 420 K, the spectrum (c) shows a single main peak (D, red) which is assigned to the equivalent nitrogen atoms of Cu-TPP. Further annealing to 490 K leads to a Cu-TPP monolayer (d).

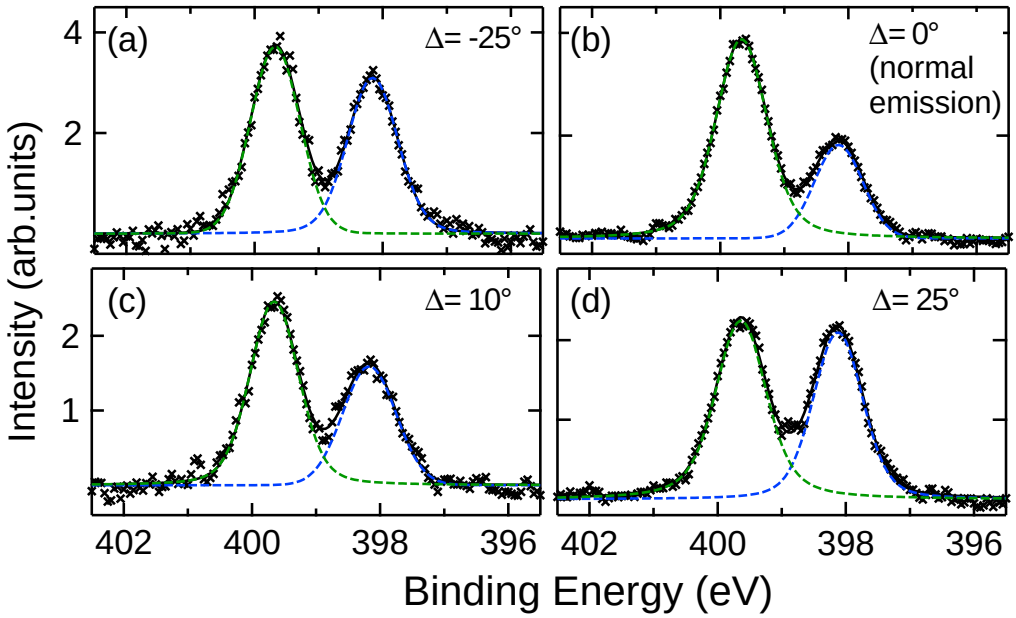

Figure 4.4: The ratio of iminic (blue) and pyrrolic (green) N1s XPS peaks of a 2H-TPP monolayer is angular dependent. Whereas in the normal electron emission mode (b) the peak ratio is just 0.4 it increases when the sample is rotated out of this position by Δ = -25°(a), Δ = 10°(c) and Δ = 25°(d)

usually is explained by polarization screening effects.[49,73,135] In the 2H-TPP monolayer on Cu(111) the pyrrolic nitrogen peak shifts by a typical screening value of -0.5 eV. The iminic nitrogen, however, shifts by only -0.1 eV which is a first indication that its chemical state is strongly affected by the adsorption. As a consequence the difference between the binding energies of the two nitrogen species is reduced to 1.6 eV (see Section 4.2.2 for more details).

Not only the energetic peak splitting but also the ratio R of the peak area of the iminic divided by the pyrrolic nitrogen differs from the multilayer sample. Small intensity differences of the two nitrogen peaks have been reported before, though the values of R were much closer to one.[72,135,139] Here, instead of the expected value near to one, the pyrrolic peak dominates over the iminic. We found that this effect can be reproduced in a systematic way, i.e., that for a series with increasing coverage (from submonolayer to multilayer) R increases as well. Additionally, R depends not only on the thickness of the film but also on the angle under which the data are taken. Fig. 4.4 shows the N1s spectra of a 2H-TPP monolayer sample recorded for different angles between analyzer and sample. R is smallest (0.4) for the normal emission mode (Fig. 4.4b) and increases when the sample is rotated out of this position by angles of Δ = -25°(a), Δ = 10°(c) and Δ = 25°(d). In the latter position both peaks have

Table 4.1: XPS energies of different nitrogen species obtained from multilayer measurements (E_{exp}) compared with calculated ionization energies (E_{calc}); nearly constant energy difference between experimental and theoretical results ($\Delta E_{calc,exp}$) for 2H-TPP (=N-, -NH-) and Cu-TPP (NCu).

Type	E_{exp}	E_{calc}	$\Delta E_{calc,exp}$
iminic (=N-)	398.3 eV	402.0 eV	3.7 eV
pyrrolic (-NH-)	400.3 eV	404.2 eV	3.9 eV
metalic (NCu)	398.8 eV	402.9 eV	4.1 eV

nearly the same intensity.

We attribute this behavior to a photoelectron diffraction effect. Earlier work[140–142] revealed that for the kinetic energy and elements of our experiment forward scattering as well as backward scattering contribute substantially to the photoelectron signal intensities. Diffraction can only produce strong intensity variations if the electron emitting sources are surrounded by the same geometry of the scatterers. Therefore, we suggest that the iminic nitrogen atoms are pointing towards the surface with their lone-pair and are responsible for a well-defined adsorption place by optimizing their interaction with specific surface atoms. Similarly site-specific adsorption resulted from the nitrogen-surface interaction as shown in recent work.[44,143] Assuming photoelectron diffraction as the origin of the intensity variations would also account for the coverage dependence of R. At low molecular coverage every 2H-TPP is free to adopt the optimal adsorption place and geometry. With increasing coverage the molecules are pushed away from these positions. Consequently, the different scattering geometries around the nitrogen sources reduce the diffraction effects. Altogether, the peak positions and intensities indicate a strong interaction of the molecule with the substrate that is mediated primarily via the iminic nitrogen.

Next, we studied the change of the spectra induced by annealing. Fig. 4.3d shows a multilayer sample (approximately 3-4 layers) that has been heated to 420 K. The main feature is peak D at E_B = 398.8 eV with two shoulders at 398.0 eV and 399.9 eV. The total area of both C1s and N1s spectra remained nearly the same during the thermal treatment. After further annealing to 490 K (Fig. 4.3e) the relative intensity of the shoulders decreases and the position of the main peak shifts downward by 0.4 eV. The total intensity of the signal is less than in the multilayer suggesting a desorption of the

multilayer molecules with a remaining monolayer. A very similar spectrum could be achieved by directly annealing monolayer and submonolayer samples to temperatures above 420 K.

The reduction of the two peaks of the inequivalent nitrogen species to one new main component is an indication for the metalation of the 2H-TPP since metalloporphyrins possess four chemical equivalent nitrogen atoms generating only one N1s peak. The binding energy of the coordinated nitrogen peak in the multilayer (398.8 eV) is in accordance with that reported for directly sublimed Cu-TPP (398.9 eV),[72] Cu-TPP multilayers on gold (398.6 eV)[144] and is similar to the N1s binding energy of metalloporphyrin films like a Co-TPP monolayer on Ag(111) (398.8 eV),[51] a Zn-TPP monolayer on Ag(111) (398.7 eV)[55] and a Fe-TPP multilayer on Ag(111) (398.6 eV).[135] Our calculations for the isolated Cu-TPP predict an ionization energy that lies 1.3 eV below the energy of the pyrrolic nitrogen, i.e., a binding energy of 399.0 eV, assuming the same work function for 2H-TPP and Cu-TPP. Our experimental value of 398.8 eV lies only 0.2 eV lower, confirming the assignment. Comparable to the 2H-TPP spectra the N1s signal for the Cu-TPP shows a down-shift of 0.4 eV when proceeding from multi- to monolayers which is attributed to screening and suggest a weakly chemisorbed macrocycle. The low-energy shoulder in the annealed multilayer spectrum (Fig. 4.3d, black dashed peak at $E_B = 398.1$ eV) most likely mainly originates from the downshifted signal of the monolayer but may also include intensity from residual, not metalated porphyrins.

The XPS results alone are not fully conclusive for the metalation as a deprotonation of the pyrrolic nitrogen groups upon annealing potentially also leads to the formation of a single N1s peak. Even though in three-dimensional environments a formally doubly negative radical is extremely unlikely, on the surface deprotonated species can be stabilized via the special interface conditions at the metal substrate.[145–148] Additional evidence for the formation of Cu-TPP is therefore provided by comparing N and C K-edge NEXAFS spectra of 2H-TPP films with annealed 2H-TPP layers. The angle resolved nitrogen edge spectra are displayed in Fig. 4.5a-d, the carbon spectra in Fig. 4.5e-h, respectively. The comparison of multi- and monolayers reveals substantial changes in the N1s region (Fig. 4.5a vs. 4.5b and 4.5c vs. 4.5d) as well as in the C1s region (Fig. 4.5e vs. 4.5f and 4.5g vs. 4.5h) suggesting a strong influence of the substrate that leads to electronical and conformational changes, which will be discussed in detail in Section 4.2.2. At this point we want to focus on the self-metalation and therefore consider only the multilayer spectra (Fig. 4.5a and 4.5c, Fig. 4.5e and 4.5g).

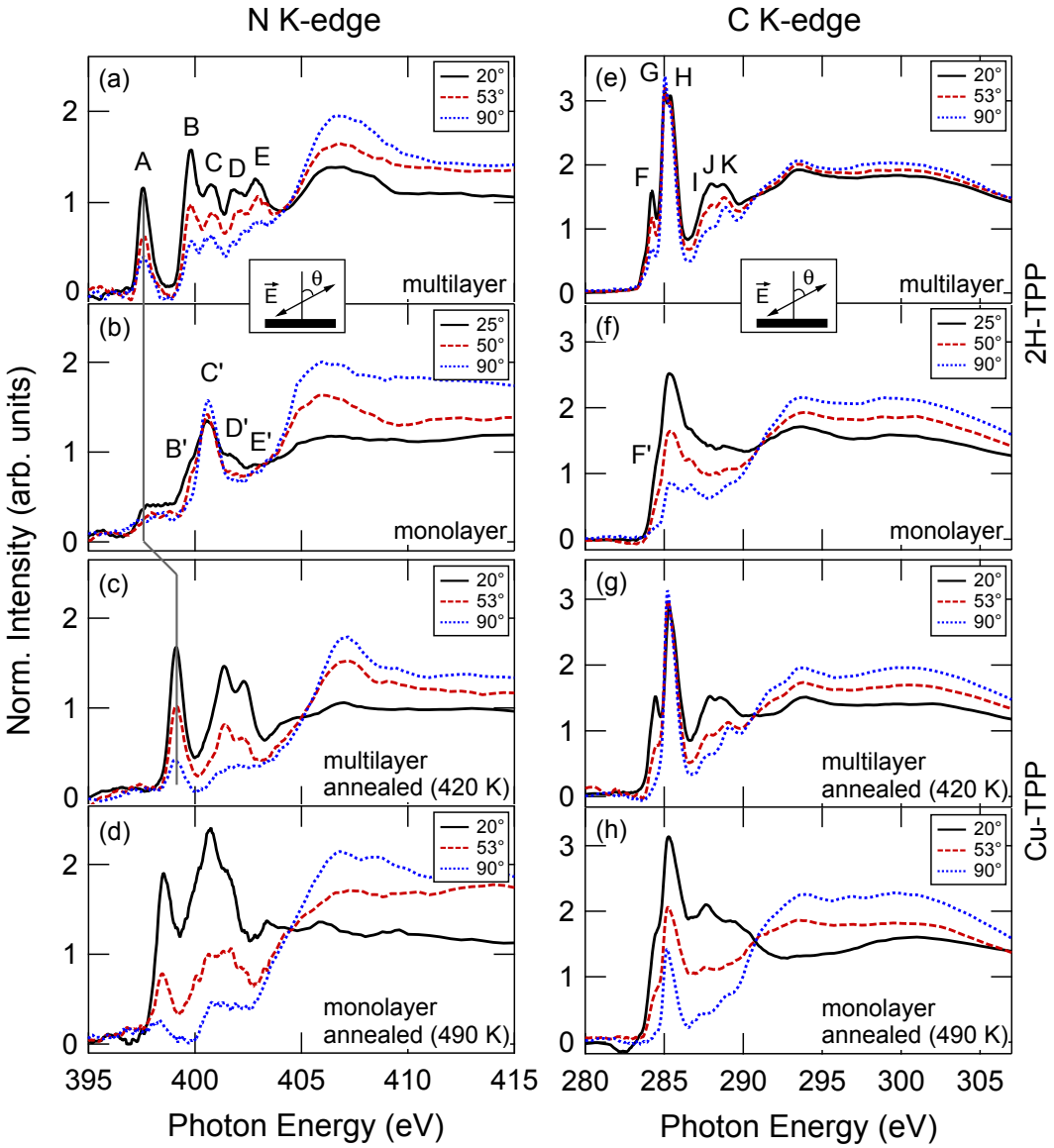

Figure 4.5: Comparing N K-edge (a-d) and C K-edge (e-h) NEXAFS spectra of (a+e) a 2H-TPP multilayer and (b+f) a 2H-TPP monolayer shows the big influence of the surface on the molecule. After annealing both the multilayer (heating to 420 K, c+g) and the monolayer (heating to 490 K, d+h) signatures are different from the 2H-TPP spectra and indicate the metalation to Cu-TPP. Values in the insets denote the incident angle θ.

The N K-edge π^* region of the 2H-TPP multilayer shows an isolated resonance (Fig. 4.5a, peak A) at 397.6 eV, followed by four peaks (B-E) lying between 399.8 eV and 403.6 eV and a σ^* region (405-415 eV) with broad structures. All resonances exhibit very similar angular dependencies. The general structure of the data agrees well with others reported for 2H-TPP[81,135,149] which confirms the intactness of the molecules. Annealing of a 2H-TPP multilayer leads to essential changes in the nitrogen spectra (Fig. 4.5c). A single resonance at low excitation energies (399.1 eV) is still present, but compared with the freshly prepared multilayer curves its position is shifted by 1.5 eV to higher photon energies. The number of peaks in the following structure of the π^* region is reduced from four (peaks B-E) to two. Again, the angular dependencies of the various peaks in Fig. 4.5c are very similar. Peak structure and positions of Fig. 4.5c are typical for metalloporphyrins in general[81,135,150] and Cu-TPP in particular,[151] which gives further evidence for the metalation of the free-base porphyrin.

The NEXAFS C K-edge π^* region of the 2H-TPP multilayer (Fig. 4.5e) exhibits six peaks. Peak F at 284.2 eV is followed by two dominant peaks at 285.0 eV (G) and 285.4 eV (H). The adjacent features I-K are not easily separable without fitting. Contrary to the nitrogen spectra the resonances in the carbon region show different angular behavior: peaks G and K become stronger with the angle θ increasing, while peaks F and J become weaker (cf. Section 4.2.2). After annealing the multilayer sample to 420 K the position as well as the number of peaks remain nearly unchanged (Fig. 4.5g), only the angle-dependencies of peaks F and H differ from that in the 2H-TPP multilayer signal. The changes in the carbon structure are therefore dominated rather by conformational than by chemical effects, contrary to the changes to the nitrogen data.

The experimental results were compared with simulated NEXAFS gas phase spectra of isolated 2H-TPP and Cu-TPP molecules. Fig. 4.6 compares the experimental magic angle (53°) multilayer curves (top) with the calculated data (middle, bottom). As the differences between the measured spectra of 2H-TPP and annealed films are mostly related to the nitrogen atoms we focus at this point only on the N K-edge curves and discuss the C K-edge together with the changes in Section 4.2.2. The total simulated spectrum of 2H-TPP (Fig. 4.6b, middle) consists of the sum of two spectra with varying excitation center, the iminic (bottom panel, dashed blue line) and pyrrolic (bottom panel, solid green line) nitrogen species. The good agreement between experiment and simulation allows the assignment of the 2H-TPP peaks (cf. Section 4.2.2)

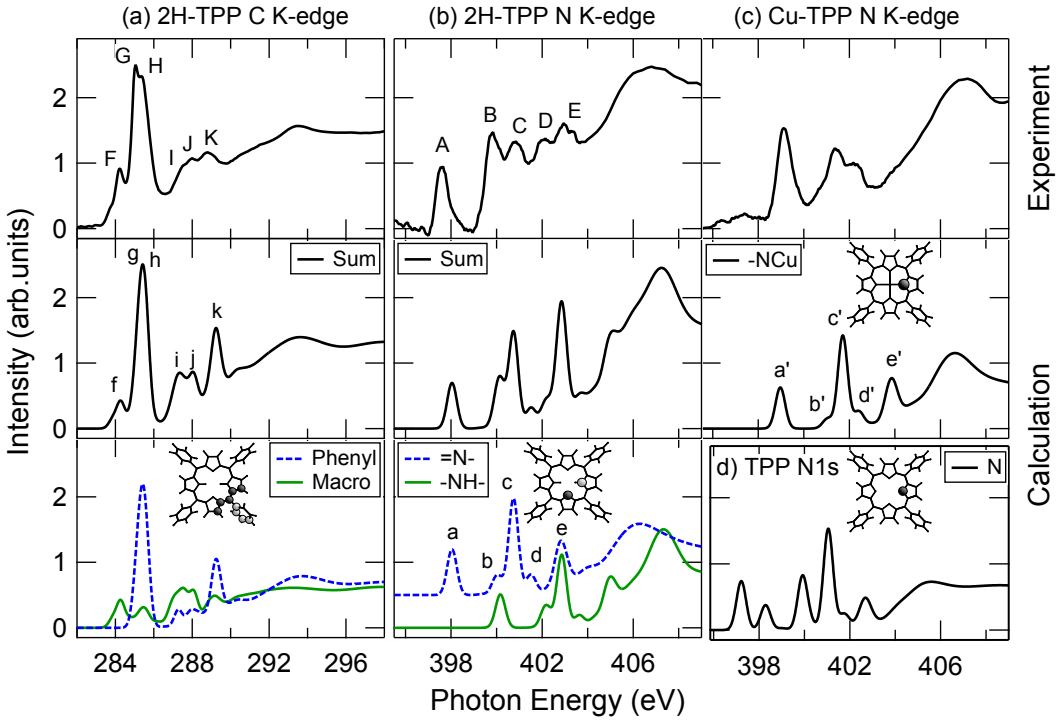

Figure 4.6: Comparison of experimental (top) and calculated (middle, bottom) NEXAFS spectra for the C-edge 2H-TPP multilayer spectrum (a), the N-edge 2H-TPP multilayer spectrum (b) and the N-edge Cu-TPP multilayer spectrum (c). (d) shows the calculated N-edge TPP spectrum. The middle panel displays the sum of all corresponding single spectra, in the bottom panel this total spectrum is split up into its single components. The insets show the position and number of the atoms used for the calculation of the respective spectra.

and shows that the identification of a molecule is possible with this method of combining experimental and theoretical results.

In Fig. 4.6c the experimental 53°-spectrum of the annealed multilayer (top panel) is compared with the simulated spectrum for the excitation of a coordinated nitrogen atom in the Cu-TPP molecule (middle panel). Spectrum 4.6d shows the calculated N K-edge spectrum of a dehydrated 2H-TPP (denoted as TPP). At this point, even without a detailed peak analysis (which will follow in Section 4.2.2), the similarities in shape and position of the experimental data with the peak structure of Cu-TPP and the discrepancy to that of the TPP rule out a possible temperature-induced dehydration in favor of the self-metalation.

The in situ metalation of adsorbed porphyrins with on top deposited metal-atoms has been reported for Fe, Co, Ni and Zn atoms.[41,42,51,55,135,149] The

metalation of 2H-TPP with vapor-deposited Zn atoms requires annealing to at least 510 K,[55] while the reaction of Fe, Co or Ni atoms with predeposited porphyrin films already takes place at room temperature.[42,51,149] DFT calculations predict a lower activation barrier for Cu than for Zn[55] which is in accordance with our observations as temperatures of at least 420 K were required for the self-metalation process.

The incorporation of Cu atoms into the porphyrin macrocycle either requires the presence of a significant amount of adatoms on the terraces or the removal of copper atoms from the topmost substrate layer. For the Cu(111) facet the adatom-vacancy formation energy was calculated to be approximately 2 eV[152,153] while the adatom detachment from kinks requires only 0.76 eV.[154] Mass exchange with the terraces by adatom extraction sets in at 500 K and is already at 600 K the dominant mass transport mechanism.[154,155] The exchange leads to a surface gas with a coverage of typically several percent of a ML in this temperature range.[156] In our case metalation takes place at 420 K, which is a smaller temperature as compared with the values above. We suggest that the presence of the organic species, already mobile at that temperature leads to a reduction of the detachment barrier and attribute the metalation to the incorporation of adatoms of the surface gas. Consistently, a recent work explained the formation of metal-organic networks at 420 K on the same surface with the incorporation of the surface gas adatoms.[157] Likewise, González-Moreno et al. conclude that a high density of adatoms is one of the factors which enable the self-metalation of 2HPPIX on Cu(110) and Cu(100) at room temperature.[137] Compared with the detachment of adatoms the extraction of an atom from the topmost layer of the Cu(111) surface is energetically more costly. Nevertheless, we cannot rule out this mechanism completely as the formation energy of Cu-TPP (cf. Supporting Information of ref. 55) seems to be sufficiently high to permit the extraction of a surface atom, in particular given that it is possible that the presence of a strongly interacting porphyrin can reduce the necessary energy barrier. A very recent publication by Doyle et al. backs this scenario.[158]

So far metalation processes were typically shown for monolayers of free-base porphyrins though in few cases also multilayers were metalated.[38,135] Our data show that self-metalation is possible for films whose thicknesses exceed one monolayer which raises the question of the transport mechanism involved. Three scenarios seem reasonable: The first is that the metalation only takes place directly on the surface and diffusion of the metalated porphyrins within the film leads to several layers of Cu-TPP. In the second scenario neither free-

base nor metalloporphyrins are mobile but metalation happens in channels consisting of stacked macrocycles. The first layer of 2H-TPP is metalated by the substrate. All other free-base porphyrin layers are metalated by receiving copper atoms from the already metalated Cu-TPP layer underneath. Another possibility is the diffusion of copper atoms from the substrate into the porphyrin film, subsequently the metalation takes place both at the porphyrin-copper interface and within the film. To our knowledge the metalation of porphyrin multilayers so far has been done by evaporating metal atoms on top of the predeposited molecules[38,135] which leads to a diffusion of the metal atoms into the film.[38] The opposite case, a diffusion of copper atoms from the substrate into a film of on-top deposited organic molecules is reported in ref. 159. From our data it is not possible to conclude which of the scenarios is correct, however, interdiffusion of either molecules or copper atoms seems more likely than metalation through porphyrin channels because of the rather high formation energy of Cu-TPP (ref. 55, Supporting Information).

4.2.2 Electronic Properties

The conformation of metalated and non-metalated films, i.e., mono- and multilayers of 2H-TPP and Cu-TPP were investigated by using angle-resolved NEXAFS measurements. NEXAFS allows to probe the unoccupied states and to obtain information on the conformation of the adsorbed molecules. Our analysis focuses on the interpretation of the π^* region as the decomposition of the broad σ^* region in single excitations is less feasible. For aromatic groups the π^* states consist of p_z orbitals that lie perpendicular to the plane of the aromatic structure. Their NEXAFS signatures depend on the incidence angle θ, i.e., the angle between the linear polarization of the light and the surface normal. In this study all spectra were taken for three incidence angles (cf. Fig. 4.5). For an aromatic π^* system lying coplanar to the substrate the corresponding peaks theoretically should be maximal for $\theta = 0$ and minimal for $\theta = 90°$.[61] According to the building-block principle the spectrum of a molecule composed of several subgroups can be divided in the signatures of the subgroups as long as the corresponding orbitals are independent from each other.[61] Thus, the assignment of the peaks in the measured NEXAFS spectra to the subgroups of the molecule is crucial for the determination of the molecule's conformation with respect to the surface. Although the multilayer spectra already have been briefly discussed in Section 4.2.1 the peak assignment and discussion of the angle-dependency have yet to be done.

Below 404 eV the N K-edge π^* region of the 2H-TPP multilayer (Fig. 4.5a)

shows five main peaks (A-E) with very similar angular dependencies. The intensity of all peaks decreases with increasing incidence angle. The peak assignment and determination of the conformation will be based on results of the DFT calculations.

The simulated NEXAFS N K-edge spectra (Fig. 4.6b, middle and bottom panel) are compared with the experimental curve (Fig. 4.6b, top panel) taken at the "magic angle" as the calculation assumes a gas phase configuration, i.e., no specific direction of the polarized light is taken into account. The theoretical 2H-TPP spectrum (Fig. 4.6b, middle) is a superposition of the curves of the iminic (Fig. 4.6b, bottom, blue dashed line) and the pyrrolic (Fig. 4.6b, bottom, green straight line) nitrogen species. The spectrum of the iminic nitrogen is shifted upward in intensity in order to better see the structure of both curves. The calculations were performed for all four nitrogen atoms without symmetry constraints. Spectra and energies were nearly identically for the two respective kind of nitrogen atoms, thus the displayed two spectra contain all information. In the inset of Fig. 4.6b the two excitation centers are indicated by a light (pyrrolic) and a dark (iminic) sphere, respectively. The spectrum of the iminic nitrogen atom shows a four-peak structure below the ionization energy, starting with a single transition (peak a) followed by three peaks with alternating intensities (low-high-low, peaks b-d). This structure is followed by a single peak (peak e) whose energy lies over the ionization threshold. The pyrrolic nitrogen shows a similar signature that is shifted upwards by 2.1 eV which is originating from the energy splitting of the N1s core levels according to our calculations.

In each spectrum the first peak consists of a single transition to the LUMO, while the following peaks consist of a multitude of transitions. A detailed listing of the main contributions to the spectral features is given in Table 4.2. The alikeness of the pyrrolic and iminic nitrogen spectra can be understood by looking at shape and energy of the excited unoccupied orbitals which are similar for the excitation of the two different nitrogen atoms. In Fig. 4.7 the final state orbitals (of the transition potential calculation) of the four strongest π^* transitions as well as the LUMO+1 are displayed. The LUMO is located mainly at the macrocycle with non-vanishing components at the respective excitation center which explains the very strong oscillation strength for this transition. The LUMO+1 has a similar shape, although the main contributions are located not at the excitation center but at the other nitrogen species. The missing overlap with the N1s orbital of the excitation center results in values close to zero for the respective element of the transition matrix. The simulated

Table 4.2: Peak assignment for the N1s peaks in the 2H-TPP NEXAFS spectrum, only main transitions below the ionization energies are listed

Peak[i]	Exp.[ii](eV)	Comp.[iii](eV)	OS[iv]	EC[v]	Transition[vi]
A	397.6	398.04	vs	=N-	1. (1s) → 159. (LUMO)
		399.98	s	=N-	1. (1s) → 162. (LUMO+3)
B	399.8	400.03	w	=N-	1. (1s) → 163. (LUMO+4)
		400.17	vs	-NH-	1. (1s) → 159. (LUMO)
		400.19	w	=N-	1. (1s) → 168. (LUMO+9)
C	400.7	400.74	vs	=N-	1. (1s) → 170. (LUMO+11)
		402.12	s	-NH-	1. (1s) → 162. (LUMO+3)
D	401.6-402.3	402.20	w	-NH-	1. (1s) → 163. (LUMO+4)
		402.34	w	-NH-	1. (1s) → 167. (LUMO+8)
		402.86	vs	-NH-	1. (1s) → 170. (LUMO+11)
E	402.6-403.6	403.62	s	-NH-	1. (1s) → 177. (LUMO+18)
		404.12	w	-NH-	1. (1s) → 185. (LUMO+26)

[i]Peaks in experimental spectra (cf. Fig. 4.5)

[ii]Experimental peak positions (as measured)

[iii]Computated peak positions (shifted by -0.9 eV to match experimental spectrum)

[iv]OS: Oscillation strengths: vs: very strong (> 0.001), s: strong (0.0005-0.001), w: weak (0.0001-0.0005)

[v]EC: Excitation center: $n = 0.5$ in transition state calculation

[vi]Transition (orbital numbers), final state orbitals for strong and very strong transitions are displayed in Fig. 4.7

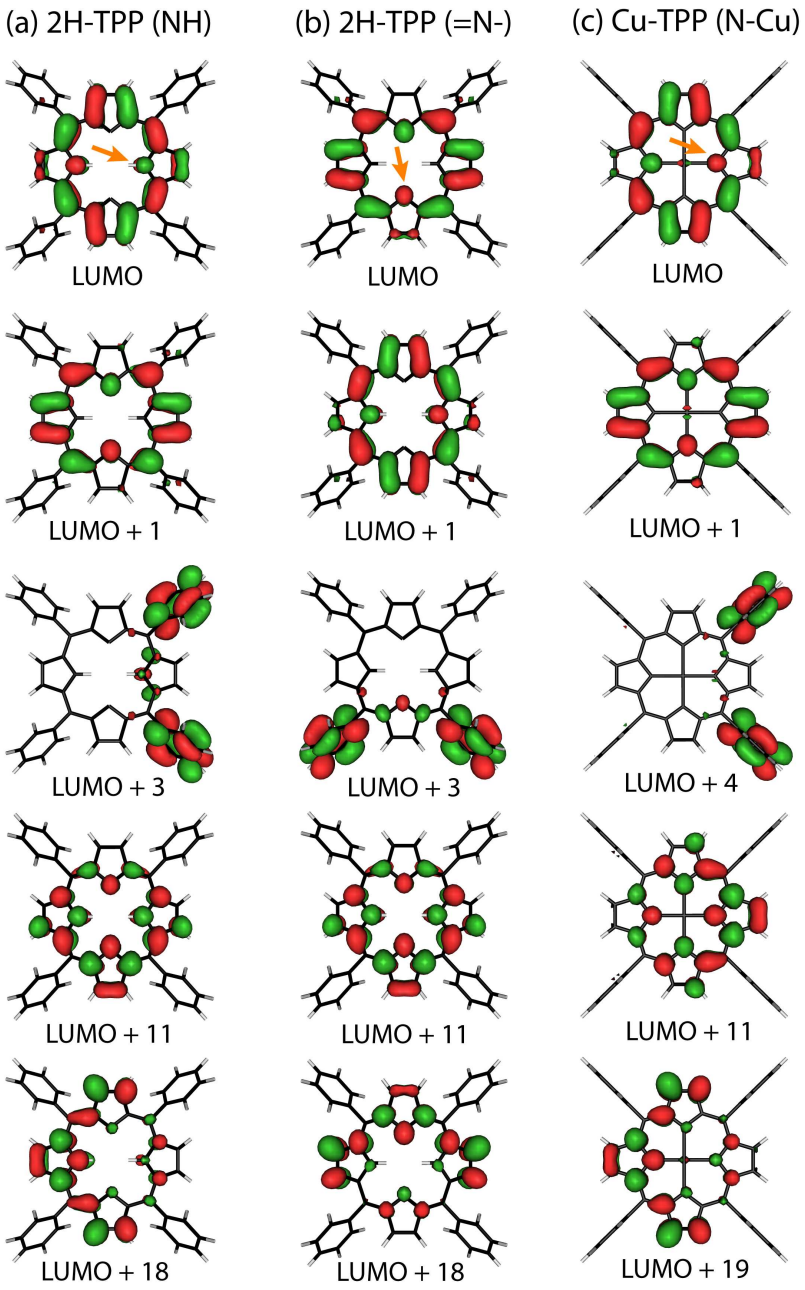

Figure 4.7: Molecular orbitals obtained from transition state calculations; (a, b) 2H-TPP, (c) Cu-TPP, excitation centers are marked by an arrow.

orbitals are consistent with those in recently reported DFT calculations on 2H-TPP.[81,160]

The comparison of the simulated and the experimental spectrum at this point already allows a peak assignment for the nitrogen region of the measured data (table 4.2). A closer analysis is done by applying the information from the calculations to the fitting of the experimental spectra. In Fig. 4.8a we show in an exemplary case how the nitrogen curves of the 2H-TPP multilayer (cf. Fig. 4.5a) were fitted using three sets of Gaussian peaks. Two sets represent the iminic and the pyrrolic nitrogen species, the third an additional background accounting for the increase of the adsorption intensity around the ionization energy.[61] Each of the two nitrogen sets consisted of four peaks modeling the simulated spectra with a single peak at lower energies (peak a) followed by a triple peak structure (peaks b-d). Within each set the intensities of the single peaks have to follow the same angular dependence and energies and widths were kept at fixed values relative to the first peak. Thus, the fitting procedure only optimizes three independent parameters for the reproduction of the whole π^* range. Fig. 4.8a shows the result of the fit for the 53° curves. The experimental data points (symbols) are well represented by the total fit (straight red line) which is a sum of the iminic (dashed blue line), the pyrrolic (dotted green line) and the background (dashed-dotted cyan line) sets. For obtaining such a good overall agreement only slight changes to the calculated peak parameters had to be introduced in the modeling of the nitrogen sets. In Fig. 4.8b the analysis of the angle-dependence of the multilayer N-edge is presented. The normalized intensities obtained by fitting the whole series (symbols) are compared with curves that show the theoretically expected dependency of the normalized intensities on the incidence angle θ for several angles α between the π-type resonance and the surface normal (cf. inset in Fig. 4.8b) assuming a threefold symmetry of the surface (black curves) that needs to be taken into account to cover the possibility that the molecules are rotated by different azimuth angles. The measured NEXAFS curve is an average of the signals from differently orientated molecules. Our assumption that the azimuthal orientation of the adsorbed 2H-TPP molecules follows the threefold symmetry of the surface is corroborated by STM studies of 2H-TPP on Cu(111). At 77 K[160] as well as at room temperature[161] the molecules adsorb in only three different azimuthal orientations, following the symmetry of the surface. The values indicate a tilt of 40° for both kind of pyrrol rings (with and without hydrogen) of the macrocycle.

The π region of the C K-edge multilayer spectrum of 2H-TPP (Fig. 4.5e)

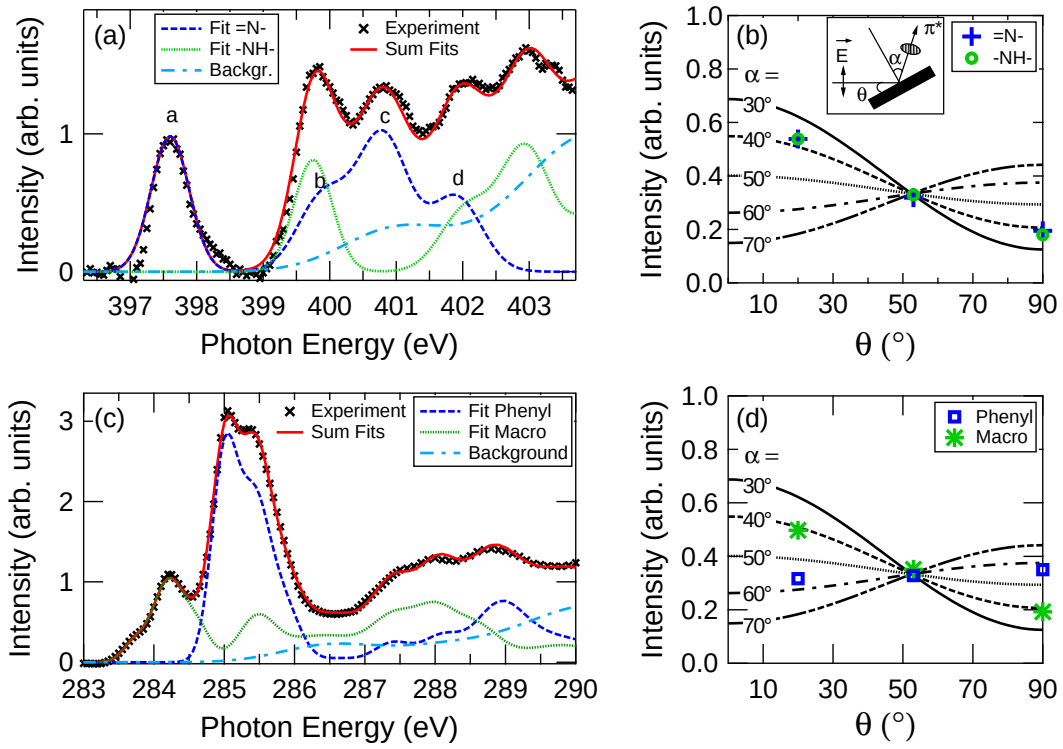

Figure 4.8: Fits for the experimental multilayer N-edge (a) and C-edge (c) region (for clarity only the 53° curves are shown). The good agreement of the sum (red continuous line) of all single fits (dashed and dotted lines) with the experimental data (symbols) allows to determine the conformation of the molecules. Therefore the dependence on the incidence angle θ of the normalized intensities (symbols) obtained from the fit are compared with the theoretical curves of a π system on a threefold symmetric surface (black curves, b and d). The curves for different angles α between orbital and surface normal assumed a linear polarization of 0.9. The inset in (b) illustrates the angles involved in the measurement and analysis. The circle symbolizes the conjugated system which is coplanar to the surface for $\alpha = 0$.

shows five main peaks with different angular dependencies (peaks F-K). The comparison with the C-edge NEXAFS spectra of benzene[162] and Zn-OEP[163] suggests that the measured curves can, according to the building block principle, be deconvoluted in one part originating from the carbon atoms of the macrocycle and another one coming from the phenyl rings. To verify this assumption DFT calculations were performed for one phenyl ring and the corresponding part of the macrocycle (Fig. 4.6a, inset) assuming a fourfold symmetry of the molecule. The results for the macrocycle (continuous green line) and the phenyl rings (dashed blue line) are exhibited in the bottom panel of Fig. 4.6a, their sum is displayed in the middle panel where it can be directly compared with the experimental 53° curve in the top panel. Generally, the calculated data are well reproducing all the main peaks of the measured curves. Both spectra are dominated by two main features (G/H and g/h, respectively), whose splitting is more dominant for the experimental (peaks G at 285.0 eV and H at 285.4 eV) than for the theoretical data. As well, peak F at 284.2 eV and peaks I-K at higher photon energies have direct counterparts in the simulated spectrum (peaks f and i-k, respectively). Taking into account the deconvolution of the computated spectrum in two parts originating from the macrocycle and the phenyl rings (Fig. 4.6a, bottom) it becomes clear that peak F can be assigned completely to the macrocycle signal while peaks G and H are mainly originating from the phenyl rings with small contributions from the macrocycle which is in good agreement with NEXAFS data of porphyrins without meso-substituents.[50,163] For them and the other peaks which are a superposition of signals originating from both parts the total angular behavior depends on the relative intensities of the contributing resonances. As a test of our theoretical description of the carbon edge, the same fitting procedure as was described for the N region has been applied for the analysis of the C region. Again the differences between the calculated peak parameters and the ones necessary for a good fit agreement are small. For example the intensities of peaks I, J and K of the experimental curve are similar while peak k of the calculated spectrum is nearly twice as high as peaks i and j. The same trend was observed for TD-DFT calculations of 2H-TPP.[81] The analysis of the angular dependencies (Fig. 4.8d) indicate an angle of $\alpha_{mac} = 40°$ for the orientation of the macrocycle and an angle of $\alpha_{ph} = 55°$-$60°$ for the tilt of the phenyl rings. We assume that α_{ph} is exclusively related to the rotation of the phenyl groups (cf. Fig. 4.2) without an additional tilt of the whole subgroup out of the molecular plane. The value of α_{mac} describes an average of the signal of the two different kind of pyrroles in the macrocycle. α_{mac} is used to

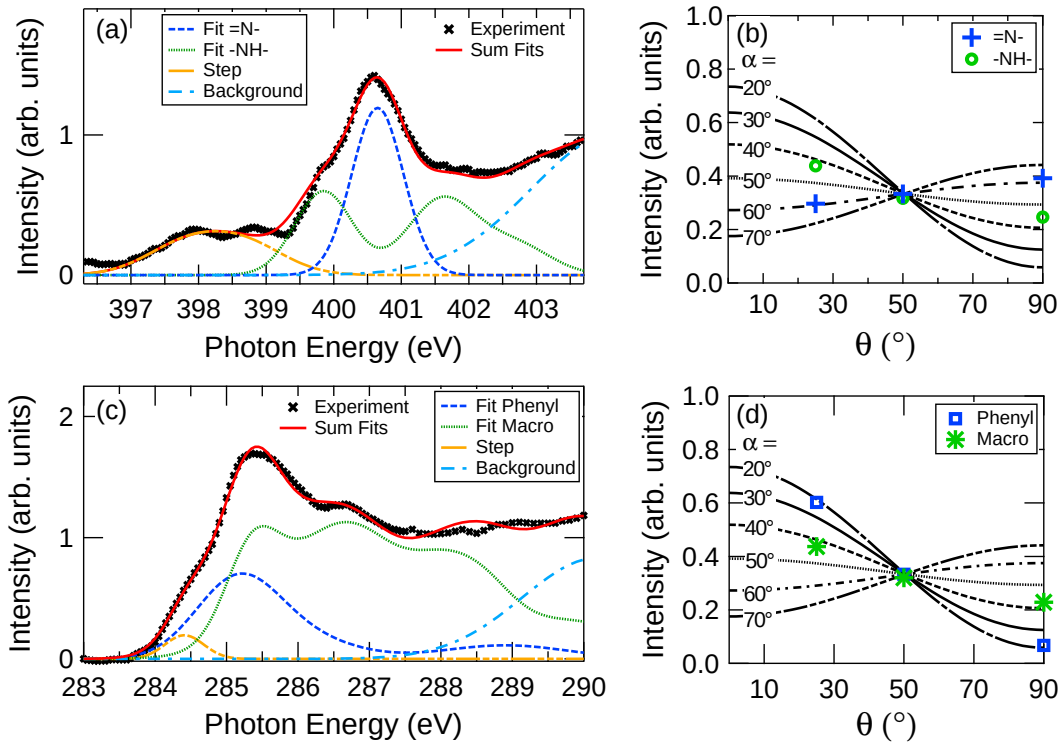

Figure 4.9: Fits for the experimental 50° curves N-edge (a) and C-edge (c) region of a 2H-TPP monolayer lead to the analysis of the normalized intensities (b, d) which indicates a substantial distortion of the macrocycle. The theoretical curves (black curves, b and d) assumed a threefold symmetric surface and a linear polarization of 0.82.

corroborate the information obtained from the fit of the nitrogen curves as a further disentanglement of the carbon signal is not reasonable. The two values for the macrocycle orientation obtained from the C and the N edge agree well and confirm the validity of our analysis.

It has to be pointed out that in the multilayer case it is nontrivial to relate the determined angles to the conformation of the molecules since the overall orientation of the molecule in the film is unknown. The determined value only describes the angle between the π system and the surface normal, but does not differentiate whether it originates from a deformation of a molecule whose macrocycle plane is parallel to the surface or from a tilt of the whole porphyrin. Nonetheless the fits affirm the validity of the peak assignment based on the results of the calculations. For both regions the overall shape of experimental and simulated spectra are consistent even though the relative intensities of the peaks fit only qualitatively and not quantitatively.

The 2H-TPP monolayer spectra of the nitrogen (Fig. 4.5b) as well as of the carbon (Fig. 4.5f) region differ greatly from those of the multilayer. Generally all peaks appear broadened. This increase of the peak width can be explained by shorter lifetimes of the excited states caused by fast charge transfer between substrate and molecules. Although the broadening complicates the comparison between the individual peaks of multi- and monolayer spectra several differences are evident. In the N K-edge spectra (Fig. 4.5b) the first transition of the multilayer spectrum (peak A) is missing completely. This resonance was assigned to the transition from the 1s orbital to the LUMO of the iminic nitrogen atoms. Its quenching in the monolayer spectra indicates a static electron charge transfer from the substrate to the LUMO during adsorption. This is well conform with recent publications by Tseng et al. who also correlate the absence of the first resonance to a filling of the LUMO[164] and by Rojas et al. who report on a charge transfer from the copper surface to the thereon adsorbed 2H-TPP molecules.[160] Instead of this quenched resonance a step is observed which does not show any significant angular dependence. This, as well as the fact that the step is very broad (2 eV) suggests that it is not composed of resonances from molecular orbitals but stems from the substrate. This feature possibly could originate from the strong coordination of the nitrogen to the substrate, so that transitions to unoccupied metal-adsorbate-states are possible.[165] Such states typically are characterized by a negligible angle-dependence of their intensity, corresponding well with our findings. Furthermore, compared with the multilayer the nitrogen spectra of the monolayer exhibit a noticeably different angular dependence. The spectra show one main peak (peak C') that corresponds to peak C in the multilayer spectra, while peaks B', D' and E' are part of the broad structure around the main peak and do not appear as clear single peaks. For a quantitative analysis again a fitting procedure was applied to the three monolayer curves, this time with peak parameters more freely chosen to optimize the fit agreement. As peak C was completely assigned to resonances of the iminic nitrogen (Fig. 4.8a) it seems reasonable that for peak C' the same is valid. It was found that indeed the best fit was obtained for the assumption that peak C' completely arises from the excitation of the iminic nitrogen species while the rest of the peaks are assigned to pyrrolic nitrogen resonances and the θ independent step at 398 eV to an additional background (Fig. 4.9a). This fit gives an estimation for the tilting angles of the macrocycle: $\alpha_{imi} = 60°$ for the iminic and $\alpha_{pyrr} = 40°$ for the pyrrolic nitrogen (Fig. 4.9b).

In the same way the carbon region is analyzed. Compared with the multilayer curves (Fig. 4.5e and Fig. 4.8c) the intensities of the first resonances

Table 4.3: Angles derived from NEXAFS measurements of mono- and multilayers of 2H-TPP and annealed 2H-TPP (Cu-TPP) samples. α_{imi}, α_{pyrr} and α_{coord} describe the inclination of the pyrrole rings out of the macrocycle plane, whereas α_{ph} refers to the rotation of the phenyl rings (see Fig. 4.2). To interpret the angles in terms of adsorption geometry further information has to be taken into account (see text).

	2H-TPP			Cu-TPP	
	α_{imi}	α_{pyrr}	α_{ph}	α_{coord}	α_{ph}
multilayer	40°	40°	55-60°	20-30°	60°
monolayer	60°	40°	20°	10-20°	40-50°

(which were assigned to macrocycle excitations in the LUMO) of the monolayer spectrum (Fig. 4.5f and Fig. 4.9c) are reduced or disappear completely which supports the conclusion from the N-edge analysis that an electron transfer from the substrate to the adsorbed molecule occurs. As the remaining structure is very broad and the peaks are smeared out the fit of the carbon region turns out to be difficult. However, it is possible to find a reasonable fit that maintains the general shape (though with broadened peaks) of the part associated with the resonances of the phenyl rings while the main changes happen in the remaining structure connected to the macrocycle excitations (Fig. 4.9c). As with the nitrogen region the best fit is obtained for vanishing first macrocycle resonances which are replaced by a (smaller) step not showing any angular dependence (Fig. 4.9c, orange). For the macrocycle the fitting procedures give an angle of $\alpha_{mac} = 40°$ while the angle related to the phenyl rings is $\alpha_{ph} = 20°$(Fig. 4.9c and d). Mono- and Multilayer angles are displayed in Table 4.3.

Due to the problem with the fits of the broadened structures the exact values of the angles may differ from those given here, nevertheless the general trends are certainly reasonably well reproduced. It has to be pointed out that the NEXAFS results alone are not fully sufficient to propose a conformational model of the 2H-TPP on the Cu(111) surface, as it is not possible to determine whether the pyrrole and phenyl rings point up or down. Taking into account former STM results of adsorbed porphyrins[44,49,54,134] as well as calculations on the conformation of porphyrins,[81,166] our data suggest a saddle-shaped conformation where the iminic nitrogen atoms point towards the surface (α_{imi} = -60°, the negative sign is used to emphasize the orientation towards the surface) and the pyrrolic nitrogen atoms point upwards ($\alpha_{pyrr} = 40°$). Generally the phenyl rings of a saddle-shaped tetraphenylporphyrin are pairwise rotated out of the

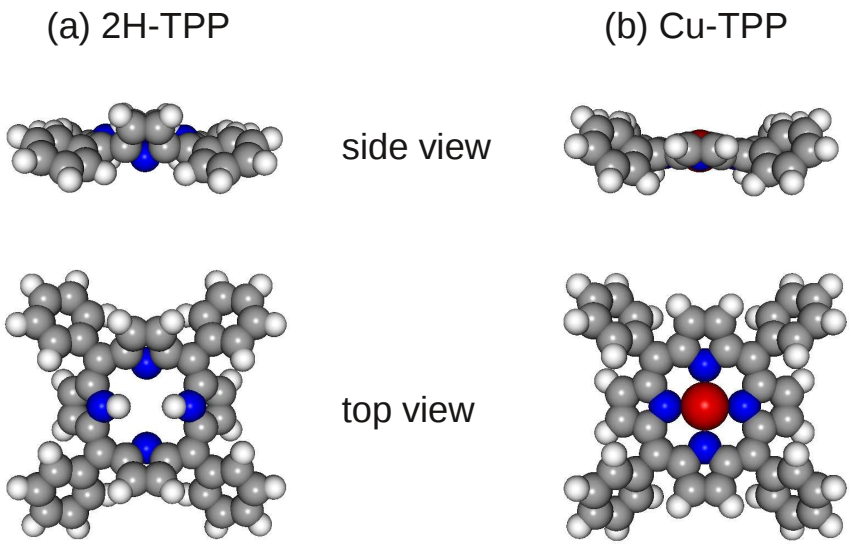

Figure 4.10: Side and top view model of (a) a free-base porphyrin with a marked saddle-shaped conformation, where the iminic nitrogen atoms are pointing downwards, i.e., with the nitrogen lone pair towards the substrate and the pyrrolic nitrogen atoms are pointing upwards and (b) a slightly saddle-shaped Cu-TPP conformer with a nearly flat macrocycle (for the atoms the same color code as in Fig. 4.2 is used).

macrocycle plane by an angle α_{ph}. Contrary to the multilayer, where the determined angle of $\alpha_{ph} = 55°$-$60°$ is in good agreement with the angles determined by ab initio calculations[39] of a tetraphenylporphyrin in gas phase ($\alpha_{ph} = 63°$) and by STM of porphyrins adsorbed on Ag(111),[40,43] the strong distortion of the macrocycle allows a rather flat orientation of the phenyl rings ($\alpha_{ph} = 20°$). The adsorption geometry of the saddle-shaped free-base porphyrin in the monolayer is depicted in Fig.4.10a.

At this point, it is instructive to discuss the interaction between the copper surface and the iminic nitrogen as indicated by the combined data of XPS and NEXAFS. In XPS the increase of electronic density in the surrounding of an excitation center leads to a shift to lower binding energies. Thus, with the iminic nitrogen near to the surface and a filling of the LUMO, one would expect a pronounced downshift of the iminic signal (peak A, Fig. 4.3) during adsorption. Instead a rather weak downshift appears. As explanation, we propose a charge donation-backdonation process similar to the one discussed in ref. 167. The backdonation reduces the electron density in the vicinity of the iminic nitrogens by an emptying of lower-lying σ-orbitals. An alternative explanation could be the formation of an intermediate complex in which the H

Table 4.4: Peak assignment for the N1s peaks in the Cu-TPP NEXAFS spectrum, only main transitions below the ionization energies are listed

Exp.[i](eV)	Comp.[ii](eV)	Strength[iii]	Transition[iv]
399.1	398.97	vs	1. (1s) → 173. (LUMO)
	400.96	w	1. (1s) → 176. (LUMO+3)
400.3-400.9	401.00	w	1. (1s) → 177. (LUMO+4)
	401.13	w	1. (1s) → 181. (LUMO+8)
401.4	401.71	vs	1. (1s) → 184. (LUMO+11)
	401.72	w	1. (1s) → 185. (LUMO+12)
	402.30	w	1. (1s) → 190. (LUMO+17)
402.3	402.42	s	1. (1s) → 192. (LUMO+19)
	402.53	w	1. (1s) → 193. (LUMO+20)

[i]Experimental peak positions (as measured)

[ii]Computated peak positions (shifted by -0.9 eV to match experimental spectrum)

[iii]Oscillation strengths: vs: very strong (> 0.001), s: strong (0.0005-0.001), w: weak (0.0001-0.0005)

[iv]Transition (orbital numbers), important final state orbitals are displayed in Fig. 4.7

atoms are still present and the N are only partially bonding to the Cu atom, which was suggested by Doyle et al. in reference 158. However, this situation is not consistent with our NEXAFS data which show a broad, nearly angle-independent step-like feature instead of the reported resonance at 398.8 eV and thus is ruled out.

Now we proceed with the analysis of the Cu-TPP mono- and multilayer samples. It has been reported that the differences between the NEXAFS spectra of 2H-TPP on the one hand and Zn-TPP and Co-TPP on the other hand are much more prominent in the nitrogen than in the carbon region.[81] We found this to be true also for 2H-TPP and Cu-TPP. The C K-edge spectra of our 2H-TPP multilayer before (Fig. 4.5e) and after annealing to 420 K (Fig. 4.5g) are very similar, only peaks F and H show a different angular dependence. This indicates that changes upon annealing are mainly related to the carbon atoms in the macrocycle, whereas the phenyl rings are not affected. In

agreement with this assumption are the marked changes in the nitrogen multilayer between the 2H-TPP (Fig. 4.5a) and the Cu-TPP (Fig. 4.5c) multilayer. The first resonance (peak A') is shifted upwards and the number of peaks is reduced, which is expected for the coordinated molecule with only one nitrogen species.

Both the simulated NEXAFS N-edge of an isolated Cu-TPP molecule (Fig. 4.6c, middle) and the experimental 53° curve (Fig. 4.6c, top) show four resonances in the π^* region (398-403 eV). A well-separated transition (peak a') at 399.0 eV is followed by a threefold structure with a low-high-low intensity profile (peaks b'-d'). Similar to 2H-TPP the intensity of peak c' is overestimated by the calculation. The calculated peak e' at 403.9 eV has no directly visible counterpart in the experimental data. It lies close to the ionization threshold where the applied broadening may be to small compared with the smeared resonances of the experiment. The shapes of the Cu-TPP final state orbitals resemble those of the excited 2H-TPP molecule (Fig. 4.7) which is an explanation for the similarity of the single nitrogen spectra. Like for the free-base TPP the first resonance (peak a') is associated with the transition to the LUMO of the excited molecule. An assignment of the main transitions is given in table 4.4.

The fit of the nitrogen spectra give an angle of $\alpha_{coord} = 30°$ for the pyrrole rings of the Cu-TPP multilayer while the fit of the carbon spectra give an angle of $\alpha_{ph} = 60°$ for the phenyl rings and $\alpha_{mac} = 20°$-$30°$ for the macrocycle.

As the angles determined from the multilayer are not necessarily related to the conformation of the molecule, but can also indicate a tilt of the whole molecule in a disordered multilayer, the monolayer will be used to analyze the adsorption geometry of the Cu-TPP on the surface. Compared with the multilayer both the nitrogen (Fig. 4.5d) and the carbon region (Fig. 4.5h) of the monolayer show a broadening of the peaks, though the changes are not quite as big as for the 2H-TPP which indicates a weaker interaction of the Cu-TPP with the copper substrate. In the N-edge spectra the first resonance (peak A') is not quenched which leads to the conclusion that no electron transfer to the LUMO occurs in this case. The fit of the N-edge region is easier as in the case of 2H-TPP but still not as convenient as for the multilayer. It gives a tilting angle of 10°-20° for the pyrrole rings which means that the macrocycle of the adsorbed Cu-TPP is considerably less distorted than that of the free-base porphyrin. The analysis of the carbon region again proves to be more difficult because of the peak broadening and the large number of contributing resonances: the fit is divided in a macrocycle and a phenyl

part which results in angles of α_{ph} = 40°-50° for the phenyl rings and α_{mac} = 10°-20° for the macrocycle supporting the fit of the N-edge region. Table 4.3 compares the results of the mono- and multilayer fits with the respective values of the 2H-TPP samples. The metalation thus leads to a conformational change from a free-base porphyrin with a strongly deformed macrocycle and rather flat phenyl rings to a Cu-TPP with a nearly planar macrocycle and stronger tilted phenyl rings (Fig. 4.10b).

4.3 2H-P on Cu(111)

4.3.1 STM

Typical STM data of a 2H-P submonolayer recorded after room temperature deposition onto Cu(111) are shown in Fig. 4.11. The porphines are imaged as bright protrusion and the size of the features indicates adsorption with the macrocycle plane aligned parallel to the surface. The molecules exhibit a depression in the center and appear two-fold symmetric at positive and negative biases (see Fig. 4.11a and b). The main molecular symmetry axis is defined by the two bright protrusions of the macrocycle (dashed lines in Fig. 4.11a) and the secondary axis by the opposing dimmer corners (solid lines in Fig. 4.11a). The bright protrusions are caused by an electronic effect and mark the positions of the two inner hydrogens as deduced from deprotonation and tautomerization experiments in analogy to 2H-P on Ag(111)[48] and 2H-TPP on Ag(111).[168] Thus, the central macrocycle pocket does not deprotonate upon adsorption on Cu(111) at room temperature. The three dense-packed symmetry directions of the Cu surface (marked with solid lines in Fig. 4.11a) were extracted from atomically resolved images. As for 2H-P/Ag(111)[48] the secondary axis of the porphines is aligned with the substrate's dense-packed <-110> directions, resulting in three equivalent orientations highlighted by the solid colored lines in Fig. 4.11a.

Annealing the sample to 423 K drastically modifies the appearance of all the porphines (see Fig. 4.11c and d). The center is now imaged as a protrusion and the molecules exhibit a less prominent two-fold symmetry. This change in contrast upon annealing is assigned to a deprotonation of the porphine's center related to a self-metalation with Cu atoms provided by the surface. Reactions with surface atoms leading to metalated porphyrin species were already observed under comparable conditions.[56,170–172] The central molecu-

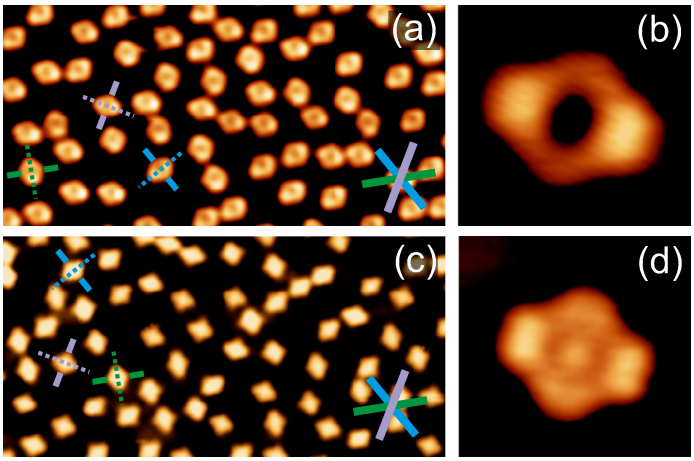

Figure 4.11: STM images[169] of porphines on Cu(111) recorded at T $\simeq$ 6 K. (a) Overview of 2H-P on Cu(111). The main axis of the molecules is defined by the two bright protrusions (dashed lines). The molecules are oriented with their secondary axis (marked with a solid line for three molecules) along the dense-packed directions of the single crystal surface indicated by the star in the bottom right (U_b=-1.3 V, I_t=0.08 nA, 20×10 nm^2). (b) Detailed image of 2H-P showing submolecular resolution (U_b=-0.2 V, I_t=0.08 nA, 1.7×1.6 nm^2). (c) Overview of porphines after annealing to 423 K. In contrast to a) and b) the molecules show a central protrusion pointing to metalated species while the molecular orientation on the surface is unchanged (U_b=-1.35 V, I_t=0.1 nA, 20×10 nm^2). (d) Submolecular resolution of a single Cu-P (U_b=-0.2 V, I_t=8.3 nA, 1.7×1.6 nm^2).

lar protrusion (see Fig. 4.11d) is most likely caused by an incorporated Cu atom since Cu-P/Cu(110) shows a very similar feature,[171] which is absent for 2H-P.[173] The two-fold symmetry of Cu-P/Cu(111) which prevails at all biases is presumably resulting from the interaction with the substrate. A similar symmetry reduction has been observed for Cu- and Co-phthalocyanines (Pc) on Cu(111).[174] Recent DFT calculations reveal a planar molecular conformation where the two-fold symmetry of Co-Pc originates from an electronic effect due to the different adsorption geometries of the two molecular axes.[175] Earlier studies report a minute non-planar deformation of Co-Pc/Cu(111) contributing to the symmetry reduction by lowering one molecular axis by about 0.2 Å towards the substrate.[176] Since Cu-P adsorbs in a similar fashion as Co-Pc and Cu-Pc on Cu(111), namely with the darker molecular symmetry axis aligned with the dense-packed directions of the substrate, the coupling to the substrate is assumed to cause the two-fold symmetry. Our NEXAFS data exclude a considerable molecular deformation as the origin of the symmetry reduction (see below). At submonolayer coverages the porphines do

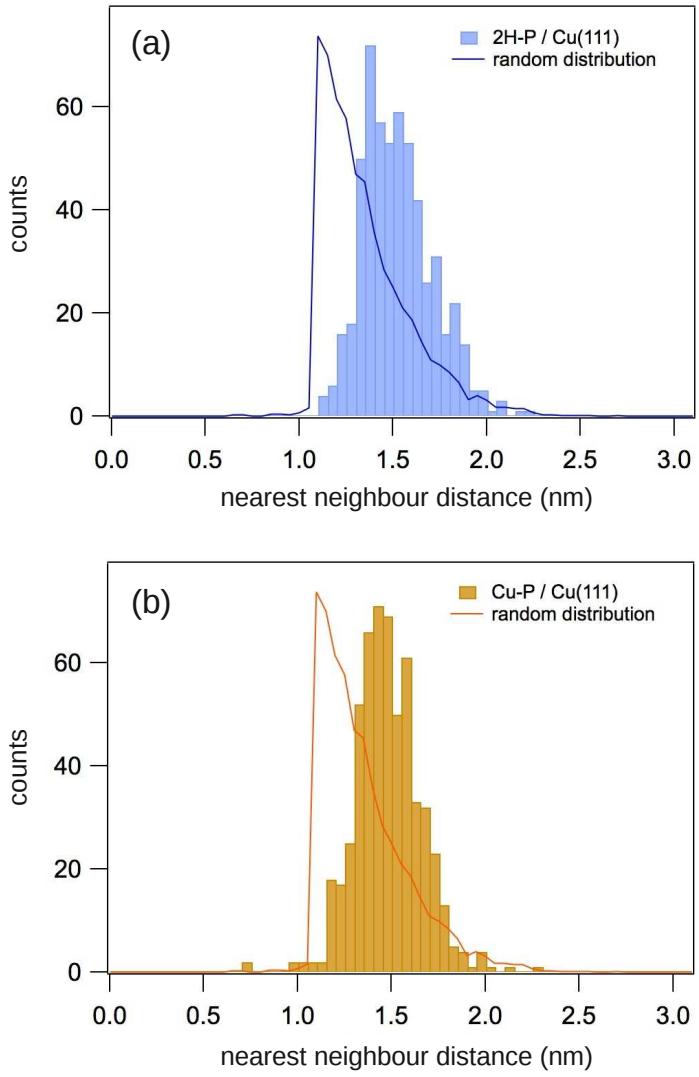

Figure 4.12: Comparison of experimental (histograms) nearest neighbor distributions with a calculated distribution (solid line) of porphines on Cu(111) before (a) and after self-metalation (b). The intermolecular distances were extracted from STM images as represented in Fig. 4.11. The histograms for 2H-P and the Cu-P clearly resemble each other, both evidence a narrow nearest neighbour distribution centered around 1.5 nm. This observation is consistent with the very similar interface structure for both species. The solid lines in (a) and (b) represent a distribution calculated for random adsorption using the constraints that the particles cannot overlapp, i.e., the minimal intermolecular distance was set to 1.11 nm. It should be noted, however, that this simple approach does not reflect the precise shape and symmetry of porphines. This procedure is based on the "Spatial Analysis Utilities S.A.U." software. The comparison of calculated and experimental distributions clearly reveals that the experimental data are not consistent with a random adsorption, but evidence a short-range repulsive interaction between the porphines for both the 2H-P and Cu-P species.

not assemble into islands, neither before nor after metalation. Individual porphines distributed across the entire surface (Fig. 4.11a) are observed despite a considerable molecular mobility under preparation conditions evidenced by a decoration of the steps. This behavior is similar to the cases of 2H-P/Ag(111)[48] and 2H-TPP/Cu(111)[160,170] where repulsive intermolecular interactions were reported. Indeed, an analysis of nearest neighbor separations presented in the Fig. 4.12 reveals a short-range repulsion for both 2H-P and Cu-P/Cu(111). Such repulsive interactions are frequently related to charge redistribution at the molecule/substrate interface, hence the STM data are consistent with a charge transfer from the Cu to the porphine for the free-base and the metalated species. Thus the absence of strong attractive intermolecular forces overriding the repulsive interactions prevents a 2D self-assembly of porphine aggregates or nanostructures on Cu(111).

4.3.2 XPS

Thanks to its sensitivity to changes in the chemical environment of an atom, XPS is a very valuable tool for monitoring the chemical state and metalation of porphyrins and phthalocyanines.[51,56]

After the *in vacuo* deposition of 2H-P films of varying coverages by organic molecular beam epitaxy the composition of the samples was checked with XPS to exclude contaminations. Working at room temperature it was not possible to grow thick multilayers, i.e., films of thicknesses exceeding two layers could not be obtained at this temperature with the OMBE. In the following we refer to this maximum coverage as bilayer, even though the intrinsic uncertainty of the coverage determination could be as high as half a ML.

The N1s XP spectrum of a 2H-P bilayer (Fig. 4.13b) shows two main peaks (A and B) and two additional broad features (C and D) with lower amplitudes. By comparing the binding energies (E_B) with the calculated ionization energies of the isolated free-base porphine (Fig. 4.13a), peaks A (E_B = 398.2 eV) and B (E_B = 400.3 eV) can be directly assigned to the iminic (=N-, peak A) and the pyrrolic (-NH-, peak B) nitrogen species, respectively, in agreement with former experimental results on free-base porphyrins.[51,135] Features C (E_B = 401.5 eV) and D (E_B = 403.5 eV) are assigned to shake-up satellites.[72] They are not reproduced by the calculation as multi-electron processes are not taken into account.

After annealing the sample to 373 K (Fig. 4.13c) a new component (peak E) at E_B = 398.9 eV emerges, while peaks A and B are still present, although with reduced intensity. The binding energy is typical for a metallo-

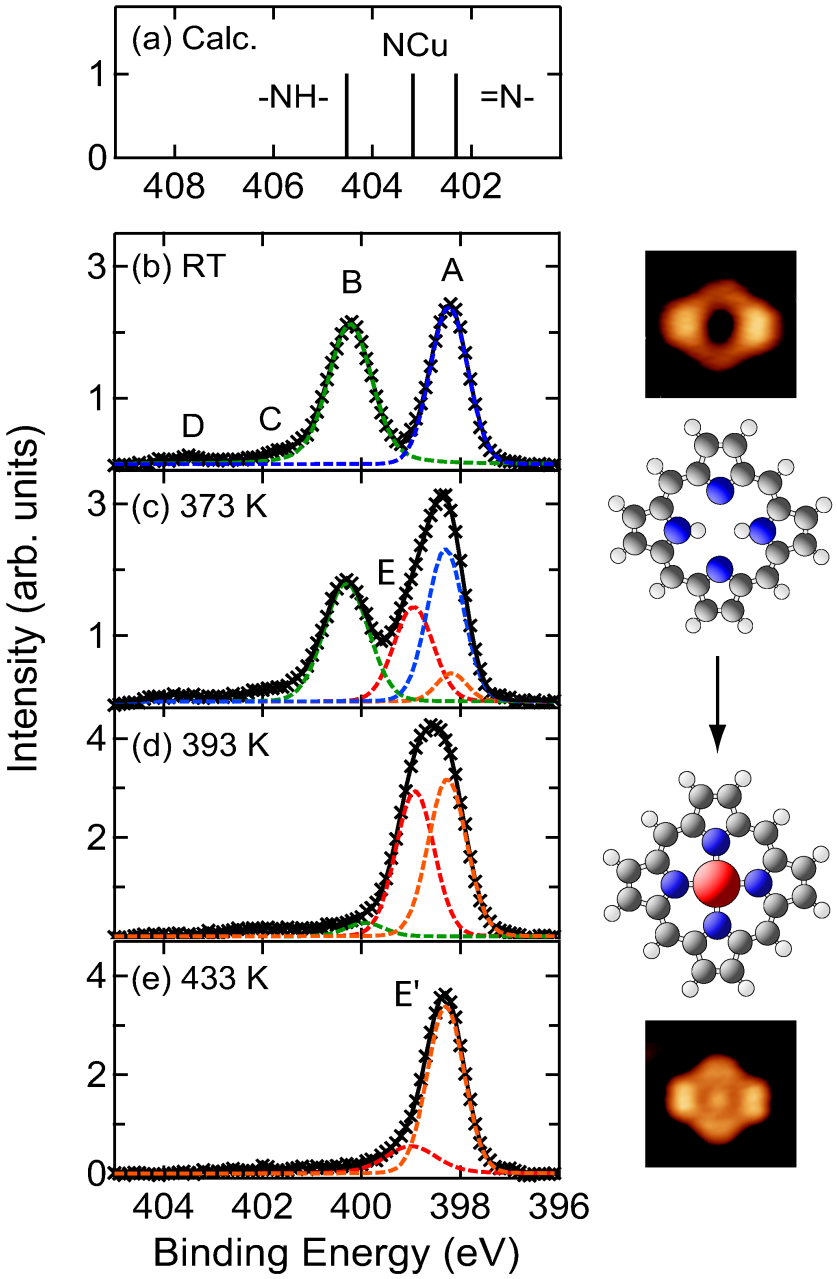

Figure 4.13: N1s XP spectra of 2H-P on Cu(111). The (a) calculated ionization energies of isolated 2H-P (=N- and -NH-) and Cu-P (NCu) allow the assignment of the experimental N1s XP spectra (b-e). The two peaks of (b) a freshly prepared bilayer of 2H-P are assigned to iminic (A, blue) and pyrrolic (B, green) nitrogen species. By stepwise annealing to (c) 373 K, (d) 393 K and (e) 433 K additional peaks (E and E') appear which are assigned to coordinated nitrogen atoms in Cu-P in the first (E', orange) and second (E, red) layer. STM images and ball-and-stick models of the molecule before (top) and after (bottom) the metalation illustrate the change.

porphyrin with chemically equivalent nitrogen species whose binding energy lies between the values corresponding to the iminic and the pyrrolic nitrogen as it is shown by our calculation (Fig. 4.13a) and consistently with previous reports.[51,55,72,135,144]

Further annealing to 393 K (Fig. 4.13d) eliminates components A and B, leaving a single broad peak. Even though no overlapping components can be clearly resolved, the shape and FWHM of the peak suggest that it entails more than one chemical species. It is therefore fitted with two Voigt curves. While peak E clearly belongs to the coordinated nitrogen species in Cu-P, the origin of the component at lower binding energy (E_B = 398.2 eV) is not obvious. If, as its binding energy would suggest, it stemmed from unreacted iminic nitrogen atoms this would implicate a non-intact molecule, since the pyrrolic component nearly vanishes. In this case the broad feature at 393 K would stem from a mixture of metalated and deprotonated porphine molecules. However, after further annealing to 433 K only one sharp peak (E' at E_B = 398.3 eV) is left. At the same time the total area of both C1s and N1s spectra is reduced, pointing to a desorption of second layer molecules with just one layer remaining.

The STM data of a submonolayer sample shows only metalated species after annealing to 433 K, therefore we assign E' to coordinated nitrogen in Cu-P whose core level binding energies are shifted by -0.6 eV to lower binding energies. For elements in a similar chemical state but adsorbed in the first, respectively second layer on a metal surface such shifts between the respective signals are explained with polarization screening by the metallic substrate.[73] The value of the shift points to a weakly chemisorbed Cu-P and is in the range of adsorbed tetrapyridylporphyrin (TPyP) on Cu(111) (-0.5 eV for the macrocycle, -0.8 eV for the pyridine)[49] and Cu-TPP on Cu(111) (-0.4 eV, cf. previous section).[56] It can be expected that peak E' is also present in Fig. 4.13c, but since it has the same binding energy as iminic nitrogen (peak A), an unambiguous interpretation is not possible. However, carrying out the fitting for Fig. 4.13c with the restraints that peaks A and B have the same intensity the introduction of peak E' is necessary to obtain a reasonable agreement with the experimental data. Since the metalation process occurs for first layer molecules, the presence of peak E' in the Fig. 4.13c spectrum contributes to a consistent picture of the metalation process. It should be noted that the fitting of the broad peak in Fig. 4.13d is not unambiguous. The fit presented here agrees with our peak assignment since the area underneath peak E' does not change substantially upon annealing to 433 K (Fig. 4.13e), as it should be

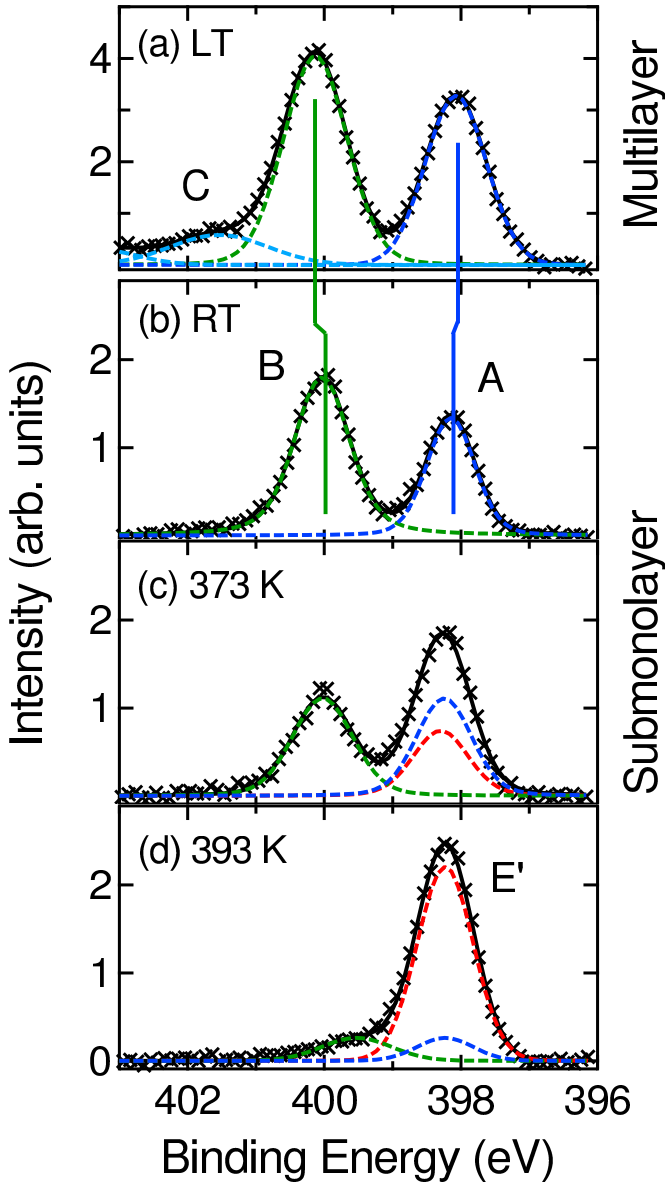

Figure 4.14: The comparison between (a) a multilayer grown at low temperature and (b) a submonolayer of 2H-P on Cu(111) reveals that the N1s XP spectra shift less than the Cu-P data. The angular dependence of spectrum (b) is analyzed in Fig. 4.15. Annealing to (c) 373 K and (d) 393 K leads to a reduction of the pyrrolic nitrogen signal (peak B), while the signal of the iminic nitrogen (peak A) seems to increase. This change is ascribed to the appearance of an additional species (peak E'), the metalated Cu-P, which appears at the same energy as the iminic nitrogen peak.

the case for the metalated species in the first layer.

To clarify the question why the iminic and the pyrrolic nitrogen species do not show shifted components for the first and second layer we conducted additional measurements. The comparison between the N1s binding energies of a multilayer and a submonolayer of 2H-P (Fig. 4.14) shows that peak A (=N-) hardly shifts, a phenomenon that was already observed for 2H-TPP and attributed to a donation-backdonation effect (see previous section). Peak B (-NH-), on the other hand, exhibits a slight shift of 0.2 eV to lower binding energy, which is consistently reflected in a moderate broadening of peak B in Fig. 4.13b. The fitted curves for the iminic and pyrrolic species in Fig. 4.13b and 4.13c therefore include both first and second layer contributions. We refrain from displaying those components separately as single curves as was done for the metalated first (E') and second layer (E) molecules in Fig. 4.13c and 4.13d, because it would overload Fig. 4.13c with details. The absence of shifts for the non-metalated porphines will be discussed together with the NEXAFS results in section 4.3.3.

Additional evidence for the assignment of the two components in the spectra of the bilayer sample annealed to 393 K (Fig. 4.13d) is provided by the spectra corresponding to a 2H-P submonolayer after annealing to 393 K. The N1s region (Fig. 4.14) consists of a single peak with a much smaller width than the peak in Fig. 4.13d, consistent with the presence of two species in the annealed bilayer sample (Fig. 4.13d). These results further corroborate our interpretation of the spectrum in Fig. 4.13d and rule out other explanations such as the formation of an intermediate state, since peak E (which is not present in the annealed submonolayer data) clearly does not originate from molecules in contact with the Cu(111) substrate. In addition, they indicate that a temperature of 393 K is sufficient to metalate all the porphines.

In our study temperatures of 363-373 K were necessary to trigger the metalation reaction which is in agreement with Haq et al. whose temperature programmed desorption measurements for 2H-P/Cu(110) indicate a metalation for temperatures between 360-420 K.[177] These values lie slightly below the reported value of 400-420 K for the onset of the self-metalation of the more extended 2H-TPP molecule on Cu(111) (see previous section).[56,178] A recent study by Ditze et al. determined the activation energy for the self-metalation process of 2H-TPP on Cu(111) to be (1.48 ± 0.12) eV,[170] which can be regarded as an upper limit for the activation energy in the present case.

The possibility to metalate second layer molecules (Fig. 4.13d) raises the question of the transport mechanisms involved and, consequently, the origin of

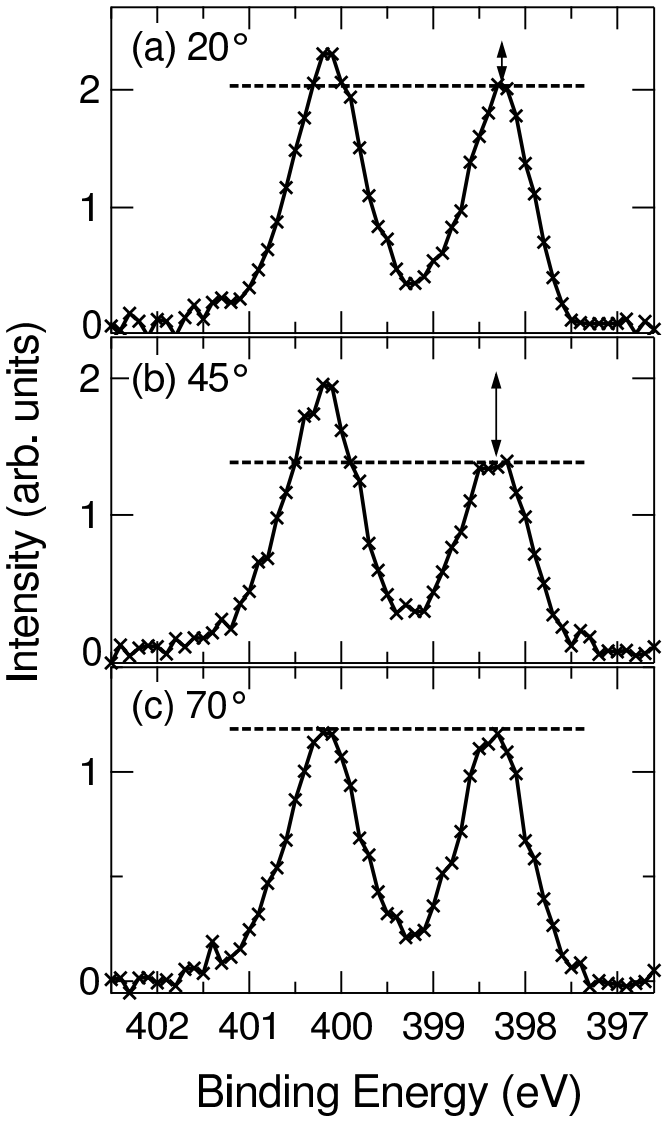

Figure 4.15: The peak ratio between the iminic and the pyrrolic nitrogen species in the N1s XP spectra of a submonolayer of 2H-P on Cu(111) is angle-dependent. Per default, spectra are taken in normal emission mode (45°, b). Changing the angle to 20° (a) reduces the dichroism. At 70°(c) the peak ratio is one. This effect can be attributed to a photoelectron diffraction effect. At low coverages the porphines do not cluster but adsorb in well-defined positions (cf. STM results). Therefore the environment for each nitrogen atom is the same thus enabling the coherent superposition of scattered photoelectron waves with the directly emitted component. This interpretation is consistent with the adsorption of 2H-TPP on Cu(111) (Section 4.2) and 2H-P on Ag(111)[48]

the incorporated copper atom. Three possibilities were given in the previous section for the multilayer metalation of 2H-TPP: 1) On-surface metalation followed by a diffusion of the metalloporphyrins within the film, 2) Diffusion of copper atoms from the substrate into the porphyrin film and 3) On-surface metalation followed by a metalation of top layer molecules through stacked macrocycles. Our interpretation of Fig. 4.13c excludes the latter option, as metalation through stacked porphines can not lead to a higher amount of metalated molecules in the second than in the first layer. We cannot discriminate between the two other possibilities with our present data. The fact that we were not able to grow thick multilayers at room temperature points to only weakly interacting molecules in the second layer, hence it seems not unplausible that the molecules are highly mobile at room temperature, which favors the first explanation.

4.3.3 NEXAFS

The changes in molecular conformation and electronic structure of 2H-P during the annealing process were monitored by angle-resolved NEXAFS spectroscopy.

For aromatic systems like porphine the π^* states are derived from p_z orbitals lying perpendicular to the molecular plane and are more easily interpretable than the broader σ^* resonances. The intensities of all NEXAFS features depend on the incidence angle θ, i.e., the angle between the linear polarization of the light and the surface normal. For an aromatic π^* system lying parallel to the substrate the intensity of the corresponding transitions in the spectra exhibits a maximum for $\theta = 0$ and vanishes for $\theta = 90°$.[61]

Fig. 4.16 shows the nitrogen (a-e) and the carbon (f-j) K-edge NEXAFS curves for the same samples that were discussed in subsection 4.3.2. A detailed peak assignment, the discussion of the single resonances and final orbitals of 2H-P will be addressed in Chapter 7

The π^* region of the nitrogen spectra of the 2H-P bilayer (Fig. 4.16b) exhibits five maxima (A-E). The DFT-calculation in Chapter 7 show that the spectrum can be deconvoluted in resonances originating from the two inequivalent nitrogen atoms. In particular, peak A at 397.8 eV corresponds to a single transition from the core level of the iminic nitrogen to the LUMO. The peaks at higher energies typically incorporate several resonances. Contrary to H_2TBrPP on Cu(111)[158] the NEXAFS spectra of the room temperature deposited 2H-P bilayer match those of a porphyrin multilayer,[81,158] thus for the adsorption of 2H-P on Cu(111) we have no indication for the intermediate

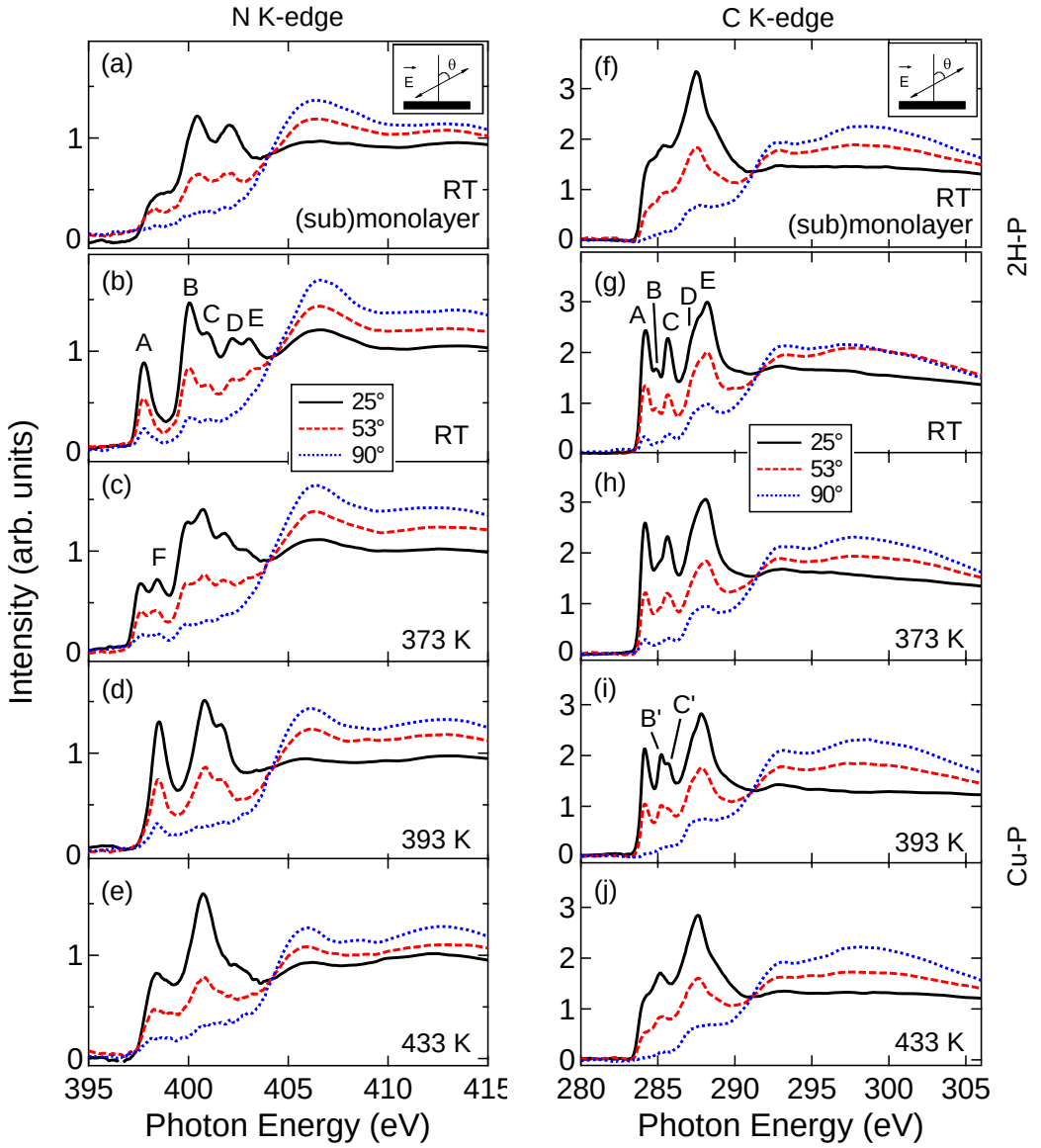

Figure 4.16: Angle-resolved N (a-e) and C (f-j) K-edge NEXAFS spectra of (a)/(f) a submonolayer of 2H-P (recorded at RT) varies considerably from those of (b)/(g) a bilayer of 2H-P, indicating a strong interaction with the substrate. Annealing the bilayer to (c)/(h) 373 K and (d)/(i) 393 K leads to a change of the spectra which are assigned to the formation of Cu-P. Further annealing to (e) 433 K reduces the coverage to a (sub)monolayer of Cu-P. The insets illustrate the incidence angle θ.

state found by Doyle et al.[158]

After annealing to 373 K (Fig. 4.16c) peak A decreases and an additional feature (F) appears between peaks A and B. Increasing the temperature to 393 K leads to a further growth of peak F at 393 K (Fig. 4.16d) which, taking into account the conclusions drawn from the photoemission data, is assigned to the already metalated nitrogen species. Generally, the spectra in Fig. 4.16d show a reduced number of maxima and the first peak is shifted by 0.6 eV to higher energies compared to peak A in the spectrum of the 2H-P (Fig. 4.16b), which is typical for metalloporphyrins[81,135,158] and therefore corroborates the conclusion drawn from XPS that at 393 K all 2H-P molecules are metalated. Raising the temperature further to 433 K (Fig. 4.16e) which, according to the XPS data, leads to the desorption of the second layer molecules results in a profound change of the curves, namely a broadening of the π^* resonances and a partial quenching of the first peak. We find a similar behavior for a submonolayer of 2H-P (Fig. 4.16a). The broadening points to a strong molecule-substrate interaction. We assign the partial quenching of the respective first resonance in Figs. 4.16a and 4.16e to the partial filling of the LUMO by an electron transfer from the substrate to the molecules. Both interpretations are consistent with DFT calculations by Dyer et al. who reported that the chemisorption of 2H-P on Cu(110) is related to an electron donation-backdonation effect.[173] The same observations were reported for the phenyl meso-substituted 2H-TPP on Cu(111),[56,133] while for Cu-TPP on Cu(111) no such charge transfer could be observed (see previous section). Because of its deformed adsorption geometry, the nitrogen atoms of the macrocycle of 2H-TPP come closer to the surface than in the case of Cu-TPP. Both the 2H-P and Cu-P macrocyclic compounds, however, can approach the surface to a smaller distance which is consistent with the strong interactions leading to the electron transfer from the Cu(111) to the LUMO of Cu-P.

Both sets of (sub)monolayer curves (2H-P in Fig. 4.16a and Cu-P in Fig. 4.16e) exhibit the same angular dependencies: the peaks in the π^* region are maximal for $\theta = 25°$ (solid line), decrease for the magic angle of $\theta = 53°$ (dashed line) and vanish for $\theta = 90°$ (dotted line) apart from the intrinsic steps in the NEXAFS spectra. As described above, this points to a flat adsorption geometry, coplanar to the surface for both 2H-P and Cu-P. With the resolution of the N K-edge data, a deformation of the macrocycles of up to 10-15° cannot be excluded at this stage. In Fig. 4.16b-d, the small contributions in the 90°-curve indicate that for coverages exceeding one monolayer the molecules partially start to tilt rigidly and/or deform.

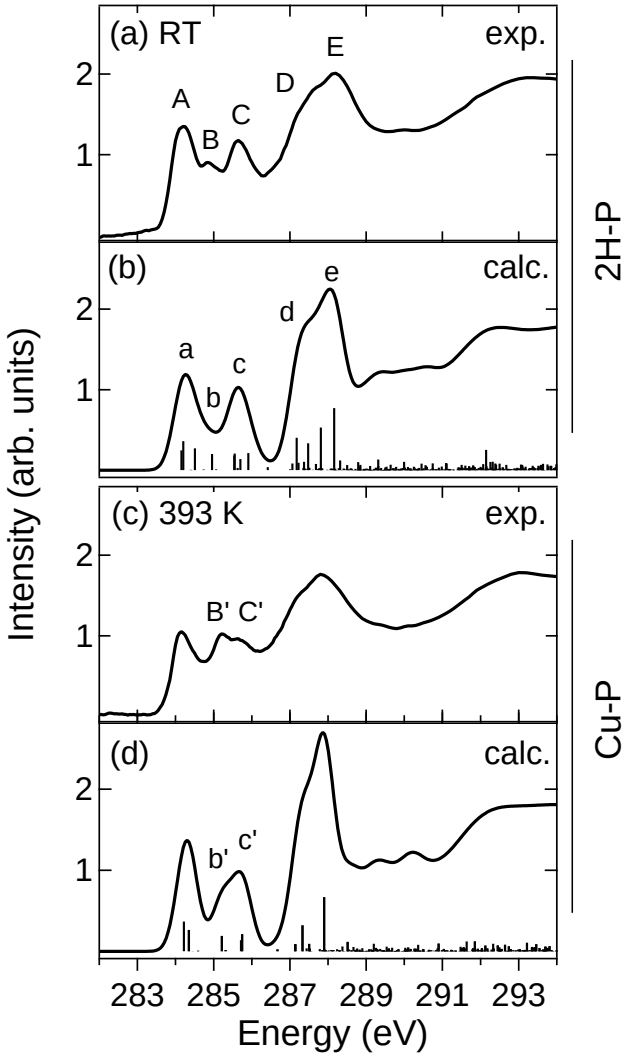

Figure 4.17: Comparison of experimental (a and c) and simulated (b and d) C K-edge NEXAFS spectra. Calculated resonances (bars) were broadened (solid line) to allow a better comparison with the experiment. The experimental 53°-curve of (a) a 2H-P bilayer is well reproduced by (b) the calculation for an isolated 2H-P molecule. Annealing to (c) 393 K leads to a change of peaks B and C in the measured data. The assignment to the formation of Cu-P is corroborated by (d) the simulated Cu-P spectrum.

The analysis of the C K-edge spectra (Fig. 4.16f-j) provides a picture of the annealing process consistent with the data of the nitrogen region. The π^* region of the bilayer at RT (Fig. 4.16g) exhibits five features A-E. Upon annealing to 373 K (Fig. 4.16h) and 393 K (Fig. 4.16i) mainly peaks B and C are affected in a systematic way while peaks A, D and E remain nearly the same. Peak B of the freshly prepared 2H-P-sample (Fig. 4.16g) is located midway between peaks A and C. Annealing to 373 K causes a partial shift of peak B towards peak C (Fig. 4.16h). After increasing the temperature to 393 K, peak B has vanished completely and is replaced by peak B' at higher binding energies (Fig. 4.16i). As was the case for the NEXAFS data of the nitrogen region, the spectra at 373 K can be understood to be an average of the curves of the pristine 2H-P and those of the newly formed, chemically different species at 393 K. As could be expected for a rigid molecule, the angular dependencies in the carbon region follow those in the nitrogen region, again indicating a flat adsorption geometry for molecules in direct contact with the Cu(111) surface.

To confirm that these changes are indeed related to the formation of Cu-P, the experimental 53°-curves of the bilayer of 2H-P before (Fig. 4.17a) and after annealing to 393 K (Fig. 4.17c) are compared to simulated spectra derived from DFT calculations which were carried out for isolated 2H-P (Fig. 4.17b) and Cu-P (Fig. 4.17d) molecules. Since molecule-substrate interactions are not taken into account in our calculation, the simulated spectra are compared only to the experiments with the highest coverages, assuming that in these cases the copper surface does not directly influence the porphines in the second layer. The comparison with the free-base porphine yields a very good agreement between the measured and the simulated data. All experimentally observed features (A-E) can be assigned directly to their calculated counterparts (a-e). The Cu-P spectra show a distinct difference with respect to the ones of the free-base molecule for peaks B/C and b/c, respectively, in close analogy to the C K-edge spectrum of Ni-P.[50] The calculated spectra reflect the changes that were observed in the experiment, especially the disappearance of peak b which is assigned to the iminic nitrogen species (cf. Chapter 7). Thus we can conclusively assign the change in the experimental spectra to the formation of Cu-P. Similar to the case of the N K-edge spectra, the curves in the carbon region (Fig. 4.16) are broadened for coverages of one monolayer and below and the first resonance is partly quenched which corroborates the conclusions that the molecules are chemisorbed on the Cu(111) surface and undergo an electron transfer from the surface.

Finally, it is instructive to compare the results obtained with the different methods. The conclusion of an identical interaction of the free-base and metalated porphines with the copper surface is supported by STM and NEXAFS observations, but at variance with the XPS data analyses. As described before, the N1s binding energies show a shift from first to second layer molecules for Cu-P, but not for 2H-P. Generally, two effects contribute to the layer-dependent shifts of photoemission peaks: The polarization screening of the core hole by electrons from the metal substrate and additional charge transfer(s) between surface and molecules. The shift of -0.6 eV for the Cu-P peak is consistent with polarization screening shifts observed for Cu-TPP (Section 4.2) and 2H-TPyP[49] on Cu(111) and 2H-TPP on Ag(111) and Au(111).[179] It is known for 2H-TPP on Cu(111) that both the iminic and the pyrrolic components shift upwards compared to the respective peaks on Ag(111) and Au(111).[179] Consequently, the components of the iminic nitrogen in multilayers and (sub)monolayers of 2H-TPP/Cu(111) have the same binding energy while the peak of the pyrrolic nitrogen is slightly shifted downwards with respect to the multilayer.[179] This is very similar to our present study with the difference that both components appear unshifted. We follow the explanation in Section 4.2 where we attributed the upwards shifts to the electron backdonation from the molecule to the substrate.[133] We relate the similar shifts of both nitrogen moieties to the difference in adsorption geometries: While 2H-TPP adsorbs on Cu(111) in a strong saddle-shape conformation (cf. Section 4.2), which brings the iminic nitrogens in closer proximity to the Cu(111) substrate, the distance to the substrate is the same for both kinds of nitrogen atoms in the 2H-P. The assumption of an electron donation-backdonation effect for 2H-P is consistent with DFT calculations by Dyer et al. for 2H-P on Cu(110).[173] The interpretation of the Cu-P data suggests an electron transfer to the LUMO of the molecule, but either no backdonation occurs or it is not associated with orbitals located at the nitrogen atoms of the copper porphine. However, we cannot rule out a small backdonation as the value for the polarization screening may even exceed -0.6 eV.

4.4 Conclusions

The results presented in this chapter demonstrate that a combination of theoretical and experimental spectroscopy techniques allows a detailed analysis of the differences between mono- and multilayer films of metalated and non-metalated porphyrins. All points raised in the three objectives formulated in

Section 4.1 could be addressed by this systematic approach.

(i) The first issue was to study the interaction between the free-base porphyrins and the Cu(111) surface. For 2H-P and 2H-TPP on Cu(111) the NEXAFS signatures differ substantially between mono- and multilayers. The spectra of the monolayer samples appear broadened, indicating a strong interaction with the surface. In addition, the first peak in both the nitrogen and the carbon region is quenched, which points to an electron transfer from the substrate to the LUMO of the molecules. The effect is more pronounced for 2H-TPP than for 2H-P, indicating only a partial filling of the LUMO of the porphine. 2H-TPP molecules in direct contact with the Cu(111) surface adsorb in a strongly saddle-shaped conformation, i.e., a deformed macrocycle where the iminic nitrogen (=N-) atoms are pointing towards the surface, while the pyrrolic nitrogen (-NH-) atoms point upwards, combined with nearly flat phenyl rings. The different distances between the two inequivelant nitrogen atoms and the copper substrate lead to different interactions with the surface, which is reflected in different shifts of the respective N1s XPS peaks between monolayer and multilayer data. The peak of the pyrrolic nitrogen in the first layer shifts downward by -0.5 eV which is consistent with a polarization screening of the surface, while the iminic species only exhibits a slight shift of -0.1 eV. The latter observation points to a strong interaction of the iminic nitrogen with the surface, either by the formation of an intermediate complex or via a donation-backdonation effect, i.e., the downward shift due to screening is neutralized by an upward shift caused by an additional electron transfer from the molecules to the substrate. All observations point to a strong interaction of the iminic nitrogen with the surface, either by the formation of an intermediate complex or via a donation-backdonation effect. In marked contrast to the adsorption of 2H-TPP, 2H-P on Cu(111) adsorbs undeformed and parallel to the surface, highlighting the influence of the phenyl substituents on the conformation of the macrocycle. Consequently all atoms have the same distance to the substrate, leading to similar interactions with the surface for both nitrogen species.

(ii) One main issue in this chapter is the *self-metalation*, which was established as an alternative approach to the conventional metalation technique of co-depositing metal atoms and porphyrins. It was shown that on Cu(111) self-metalation, i.e., the direct metalation of free-base porphyrin molecules with substrate atoms, is possible for both the phenyl substituted 2H-TPP and the free-base porphine (2H-P). Annealing of 2H-TPP and 2H-P mono- and multi-

layer films to a temperature of 420 K (2H-TPP) and 360-393 K (2H-P) leads to changes in XPS and NEXAFS signatures which are mainly related to the atoms in the macrocycle. By comparing the experimental data to XPS results and NEXAFS spectra obtained by transition potential DFT calculations these changes are attributed to the coordination of the nitrogen atoms with copper from the substrate. A detailed peak assignment of the experimental data could be achieved (for 2H-P this will be shown in Chapter 7). For the TPP molecules the comparison of the experimental NEXAFS curves with the simulated spectra shows that the main transitions and final state orbitals are very similar for 2H-TPP and Cu-TPP, suggesting that the dissimilarity of the respective monolayer spectra originate from differences in the interaction of free-base and metalloporphyrins with the substrate. It could be shown that it is possible to metalate more than one layer of porphyrins, demonstrating that the desorption temperature of the metalloporphyrins lies above the temperature needed for triggering the self-metalation reaction. No direct evidence for the transport mechanisms could be obtained in this chapter, though the results in Chapter 7 indicate that the distance of the nitrogen atoms to the substrate in an important parameter for the probability of the copper atom capturing. By raising the temperature further, the metalloporphyrins in higher layers desorbed with only one remaining monolayer. This approach does not only allow to compare the free-base porphyrins with their metalated counterparts, but gives the possibility to study the influence of the surface on the molecular properties of the metalloporphyrins. After the publication of Section 4.2, other groups used self-metalation as well, e.g., by studying the activation energy of the self-metalation reaction of 2H-TPP(Cu(111).[170] Nowakowski et al. reported that for 2H-TPP/O/Cu(001) on-surface self-metalation of 2H-TPP sets in at a lower temperature[180] and Goldoni et al. found that self-metalation is also possible on Ni(111) and Fe(111) surfaces.[172] The metalation of 2H-TPP to Cu-TPP leads to a change in both molecular conformation and molecule-surface interaction: The Cu-TPP exhibits an only slightly saddle-shaped macrocycle and tilted phenyl rings and contrary to the free-base case no electron transfer to or from the molecule could be observed. For Cu-P (which remains flat), however, the NEXAFS results indicate the same interaction with the Cu(111) surface as for 2H-P, even if the XPS do not show any indication for a possible charge backdonation.

(iii) This leads to the conclusion that the modified interaction of Cu-TPP with the Cu(111) surface is the result of the conformational change upon an-

nealing: The tilted phenyl rings prevent the macrocycle from coming close to the surface, while the flat conformation of Cu-P allows a closer proximity to the substrate, which promotes charge transfer. From the results reported in this chapter (see also summary in Fig. 8.1) we can conclude the following: (1) The distortion of the macrocycle is determined by both the presence of a metal center and substituents. (2) The proximity of the macrocycle or parts thereof (cf. strong saddle-shape which leads to a small N-Cu distance) is essential for the occurrence of charge transfer. The rotated phenyl rings of Cu-TPP "lift" the macrocycle upwards, which does not allow electron transfers between surface and molecule.

Chapter 5

Metalation with $Ru_3(CO)_{12}$

5.1 Introduction

The self-metalation described in the previous chapter is a simple method for the *in situ* metalation of free-base porphyrins. However, its use is limited by the substrate material. So far, self-metalation of porphyrins has only been reported for copper (Chapter 4 and ref. 137, 180), nickel[172] and iron[172] surfaces. A different approach was very recently reported by Papageorgiou et al. who employed a metal-organic chemical vapor deposition approach to metalate cyclodehydrogenated 2H-TPP on Ag(111) using the organometallic precursor molecule ruthenium dodecarbonyl, $Ru_3(CO)_{12}$ (Fig. 5.1c).[181] The cyclodehydrogenated 2H-TPP, in the following denoted as 2H-TPP^{cd}, is a derivative of the meso-tetraphenylporphyrin 2H-TPP (Fig. 5.1a), obtained by annealing 2H-TPP films on Ag(111) to temperatures of at least 550 K.[182] While the annealing procedure can give rise to four different cyclodehydratation products, STM micrographs show that the prevalently occurring compound is the 2H-TPP^{cd} depicted in Fig. 5.1b.[181] The advantage of this metalation technique is the easy handling of $Ru_3(CO)_{12}$, which is volatile under UHV conditions and therefore it can be dosed on the surface by simply opening the valve which separates the sample and the compound container. In contrast, the use of a metal evaporator for the deposition of ruthenium is technically challenging because of the high sublimation temperature of Ru. The multitechnique study of Papageorgiou et al. showed that by cycles of exposure of a layer of 2H-TPP^{cd} to $Ru_3(CO)_{12}$, followed by annealing to 550 K, all free-base species transformed to ruthenium porphyrins without leaving by-products (such as CO) on the surface. However, the metalation did not occur in a single step. After the first cycle of dosing $Ru_3(CO)_{12}$ and annealing, only half of the porphyrins were metalated and the procedure had to be repeated to obtain a fully metalated

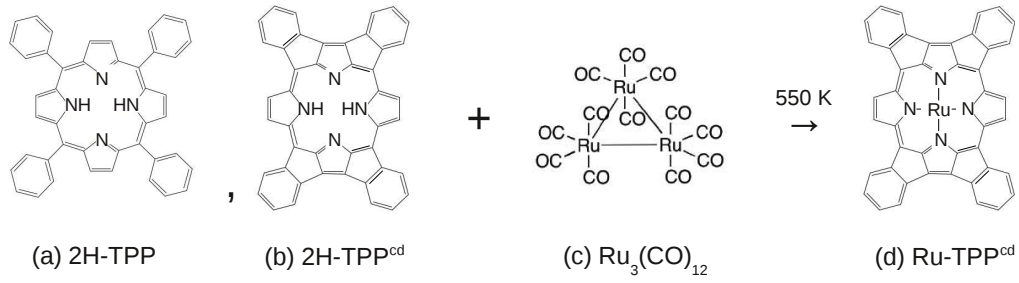

Figure 5.1: Structural formulas of: (a) meso-tetraphenylporphyrin 2H-TPP, (b) 2H-TPP^{cd} which is obtained by annealing 2H-TPP to 550 K, (c) precursor molecule ruthenium dodecarbonyl $Ru_3(CO)_{12}$, (d) metalation product Ru-TPP^{cd}

porphyrin layer.

This chapter aims at elucidating the reaction pathway of this metalation method. Additional information will be provided by an X-ray spectrocopy characterization of purchased Ru(CO)TPP mono- and multilayers (Section 5.2), as well as of the behavior of pristine $Ru_3(CO)_{12}$ molecules adsorbed on Ag(111) as a function of temperature (Section 5.3). In Section 5.4 the dependence of the reaction on the availability of free silver surface will be investigated as a possible source for the non-complete metalation observed by Papageorgiou et al. To this end, free-base porphyrin films (both 2H-TPP^{cd} and 2H-TPP) of varying coverages are prepared and exposed to $Ru_3(CO)_{12}$, followed by an annealing of the sample. The metalation process will be followed with XPS, while NEXAFS is primarily used to distinguish 2H-TPP and 2H-TPP^{cd}. Section 5.5 investigates whether 2H-P can be metalated in the same way and, if this is the case, whether there are differences to the reaction of 2H-TPP and 2H-TPP^{cd}. At variance with the other N1s spectra presented in this thesis, a polynomial background was subtracted during data processing. The reason is the slightly curved silver background in the nitrogen region which is exacerbated by the low signal of N 1s at submonolayer coverages. Using a linear background would distort the results, as shown in Appendix A.3.

5.2 Ru(CO)TPP on Ag(111)

Samples with varying Ru(CO)TPP coverages were deposited on the Ag(111) substrate, following the procedure described in Chapter 3. Only the O1s region of the multilayer sample showed traces of oxygen, i.e., of the CO ligand. For (sub)monolayer coverages no oxygen was detected. This suggests that either the CO already dissociates during evaporation or later during adsorption

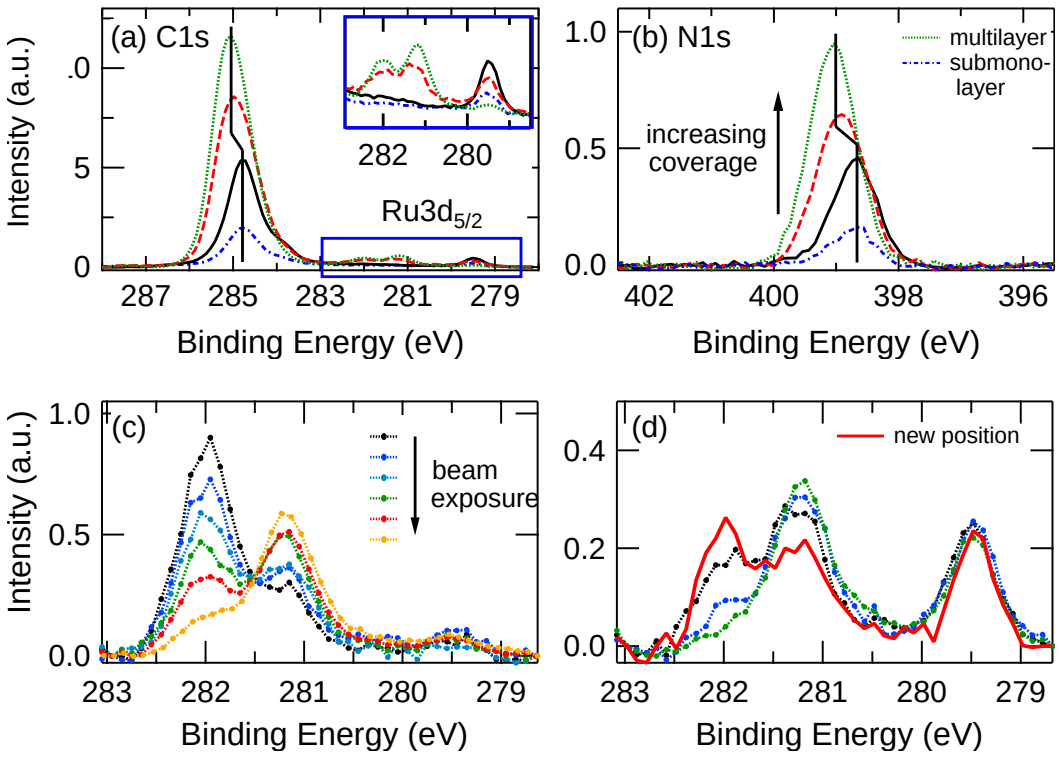

Figure 5.2: Coverage dependent (a) C1s and (b) N1s XPS spectra of Ru(CO)TPP deposited on Ag(111). The shift between the submonolayer (blue dashed dotted line)/ monolayer (black solid line) and multilayer (green dotted line) peaks are assigned to screening by the substrate for first layer molecules. The zoom-in in the $Ru3d_{5/2}$ region (a, inset) reveals that Ru-TPP in direct contact with the substrate is in a Ru^0 state whereas in higher layers in a Ru^{II} state. (c) $Ru3d_{5/2}$ region of a multilayer sample of Ru(CO)TPP. Increasing beam exposure causes the partial desorption of the Ru containing adsorbate at 282 eV and changes the shape of the Ru peaks. (d) Scanning a pristine position on a sample with a coverage of ∼2 ML reveals that the Ru signal retained its original shape (red solid line).

on the metal surface. The latter would be analogous to Co-TPP/Ag(111), where cooling the sample is required to attach CO to the metalloporphyrin.[13] Therefore in the following the adsorbates are referred to as Ru-TPP.

The N1s region of the Ru-TPP samples (Fig. 5.2b) is dominated by one single peak at 399.0 eV (multilayer) and 398.7 eV (monolayer) originating from the nitrogen atoms coordinated to the Ru center. The value is typical for metalloporphyrins.[81,135,150] The shift is usually assigned to be a consequence of the polarization screening.[49,73,135] Consistently, the same shift is observed for the C1s peak (Fig. 5.2a). Of special interest is the $Ru3d_{5/2}$ region (Fig. 5.2a, inset): For Ru-TPP in direct contact with the substrate (blue dashed dotted line, black solid line), the corresponding $Ru3d_{5/2}$ peak at 279.5 eV points to metallic ruthenium (e.g., 280.0 eV for Ru bulk).[122] For increasing coverage (red dashed line, green dotted line), two new features appear at higher binding energies, which we assign to the Ru^{II} expected for a free Ru-TPP molecule. The binding energy of the $Ru3d_{5/2}$ peak in the multilayer sample (center of mass of the peak: 281.2 eV) is consistent with this assumption (280.6 eV-281.1 eV in refs.[183–185]). In direct contact with the surface, this oxidation state is reduced to Ru^0. This effect was already reported for Co-TPP on Ag(111)[186] and assigned to an electron transfer from the silver surface to the molecule.[20] During repeated scanning of the Ru region (Fig. 5.2c) we observed a partial desorption of the adsorbate at 282 eV and a general change of the shape of the $Ru3d_{5/2}$ curve. This change does not occur at the Ru^0 component (Fig. 5.2d). Scanning a pristine position on a sample with a coverage of approximately 2 ML returns the original shape, i.e., the alterations are caused by the exposure to the X-ray beam. This behavior is most likely not related to pure Ru-TPP, but to volatile adsorbates. The purity of the evaporated compound was 80%, making it difficult to exclude contaminations present in the samples. However, this effect does not influence the conclusions drawn about the coverage-dependence of the oxidation state of Ru-TPP, as the average positions of the peaks remain constant.

The NEXAFS C K-edge spectra of both mono- and multilayer (Fig. 5.3) exhibit very similar features as the multilayer on Cu(111) discussed in Chapter 4. The peak assignment, i.e., the separation in contributions originating from the phenyl rings and the macrocycle is consequently the same (see Fig. 4.6). Fitting the peaks according to the procedure described in Chapter 4, yields $\alpha_{ph} = 50°$ for the rotation of the phenyl rings and $\alpha_{macro} = 30°$ for the distortion of the macrocycle. The angles for the multilayer are slightly larger: $\alpha_{ph} = 60°$ and $\alpha_{macro} = 35\text{-}40°$, which might result from a tilting of the whole

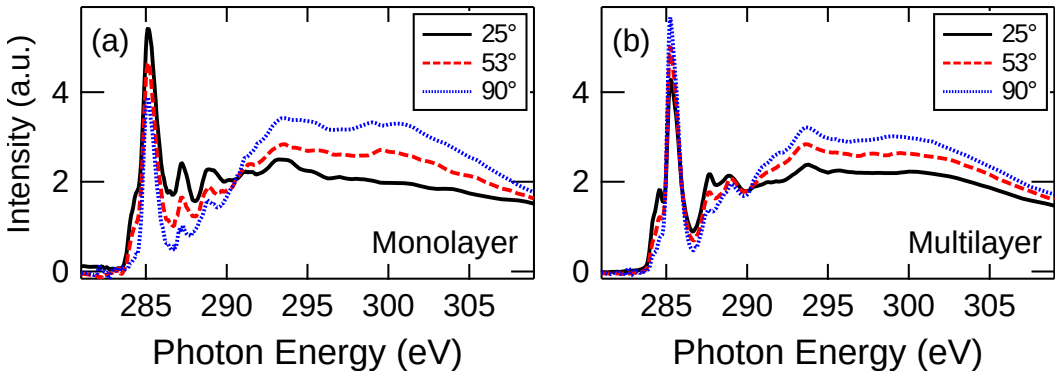

Figure 5.3: NEXAFS spectra of (a) a monolayer and (b) a multilayer of Ru-TPP adsorbed on Ag(111), recorded at three different angles.

molecule in higher layers. In analogy to 2H-TPP on Ag(111) (ref. 168 and Section 5.4) and Co-TPP/Ag(111)[54] we propose that the Ru-TPP adopts a slight saddle-shaped conformation on the Ag(111) surface. A comparison of the magic angle (53°) curves of mono- and multilayer does not show a substantial filling of the LUMO, i.e., the ratio between first and second peak does not change significantly.

5.3 $Ru_3(CO)_{12}$ on Ag(111)

In the next step the adsorption of the pristine precursor $Ru_3(CO)_{12}$ on Ag(111) without the presence of porphyrins is analyzed. Directly after deposition at room temperature (Fig. 5.4, black line) three main features at 280.7 eV, 284.8 eV and 286.5 eV are discriminable in the C1s/Ru3d region, which are assigned to the Ru3d doublet and the CO C1s singlet contribution, respectively.[187,188] Consistently, a single peak originating from CO is observed in the O1s region. Stepwise annealing of the sample to 502 K (Fig. 5.4, red, blue and green lines) leads to a gradual loss of the CO signal and a shift of the whole spectrum to lower binding energies. After annealing to 540 K[i](Fig. 5.4, orange line) no CO can be detected and the Ru peaks appear much sharper. Concomitantly, the total amount of ruthenium decreases by a factor of two during

[i]It should be noted that the reading of all temperatures in this chapter was very sensitive to an external grounding of the thermocouples, therefore for each preparation two different temperature values could be obtained. The difference between the two (40-50 K) remained constant throughout the beamtime duration. The lower value is considered to represent the accurate temperature reading (and therefore reported as the respective sample temperature in this chapter), as it is consistent with the 550 K both Di Santo et al. in ref. 182 and Papageorgiou et al. in ref. 181 reported for the formation of a flattened 2H-TPP^{cd} layer.

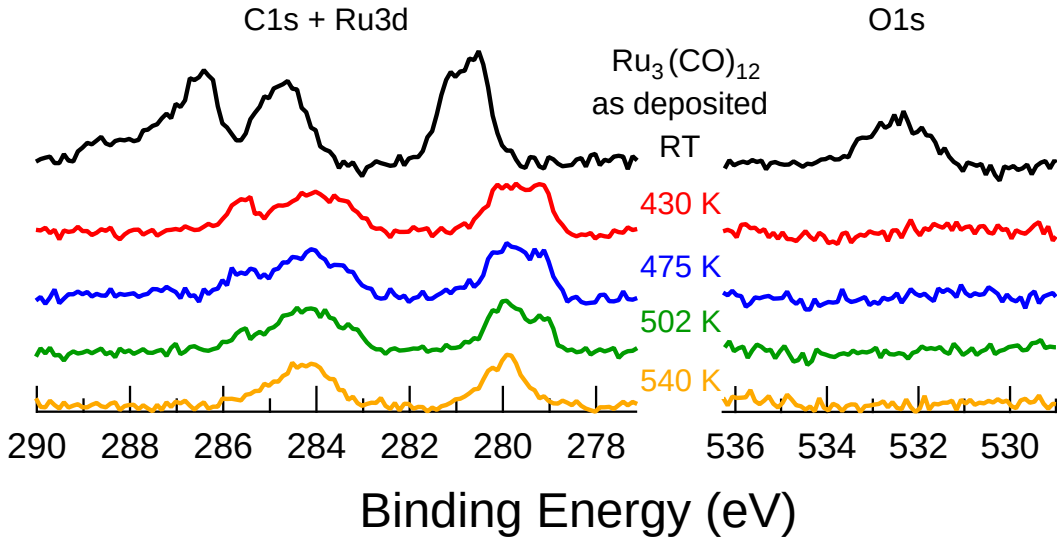

Figure 5.4: C1s and O1s XPS data of an annealing series of $Ru_3(CO)_{12}$/ Ag(111). Directly after deposition three main features are discriminable: The Ru3d doublet at 280.7 eV and 284.8 eV and the CO peak at 286.5 eV. After annealing, the CO desorbs and the ruthenium peaks shift to lower binding energies. The individual spectra after background subtraction are stacked to allow a direct comparison.

the whole annealing process. Together with the $Ru3d_{5/2}$ binding energy of 280.0 eV, which is consistent with Ru^0,[122] these results show that annealing leads to desorption of the labile CO ligands and other possible contaminants and the formation of clean metallic ruthenium. This is consistent with annealing series of $Ru_3(CO)_{12}$/Co(0001)[187] and $Ru_3(CO)_{12}$/Au(111),[188] which show a desorption of CO (completed at 500 K) and a shift to lower binding energies upon annealing. In both cases metallic Ru is found after the heat treatment. Deviations from the reported binding energies of the adsorbed (not annealed) $Ru_3(CO)_{12}$ and in the onset of CO desorption might be the results of the modified interaction with the surface.

5.4 2H-TPP and $Ru_3(CO)_{12}$ on Ag(111)

Next, the coverage-dependent metalation of 2H-TPP on Ag(111) is investigated. On Ag(111) 2H-TPP is known to adsorb in a slightly saddle-shaped conformation (Fig. 5.5a)[168] which is corroborated by our angle-resolved NEXAFS measurements of a submonolayer (Fig. 5.5b). Fitting according to the procedure described in Chapters 3 and 4 yields an average pyrrole ring tilt angle of $\alpha_{macro} = 25°$ and a phenyl ring rotation angle of $\alpha_{ph} = 45°$.

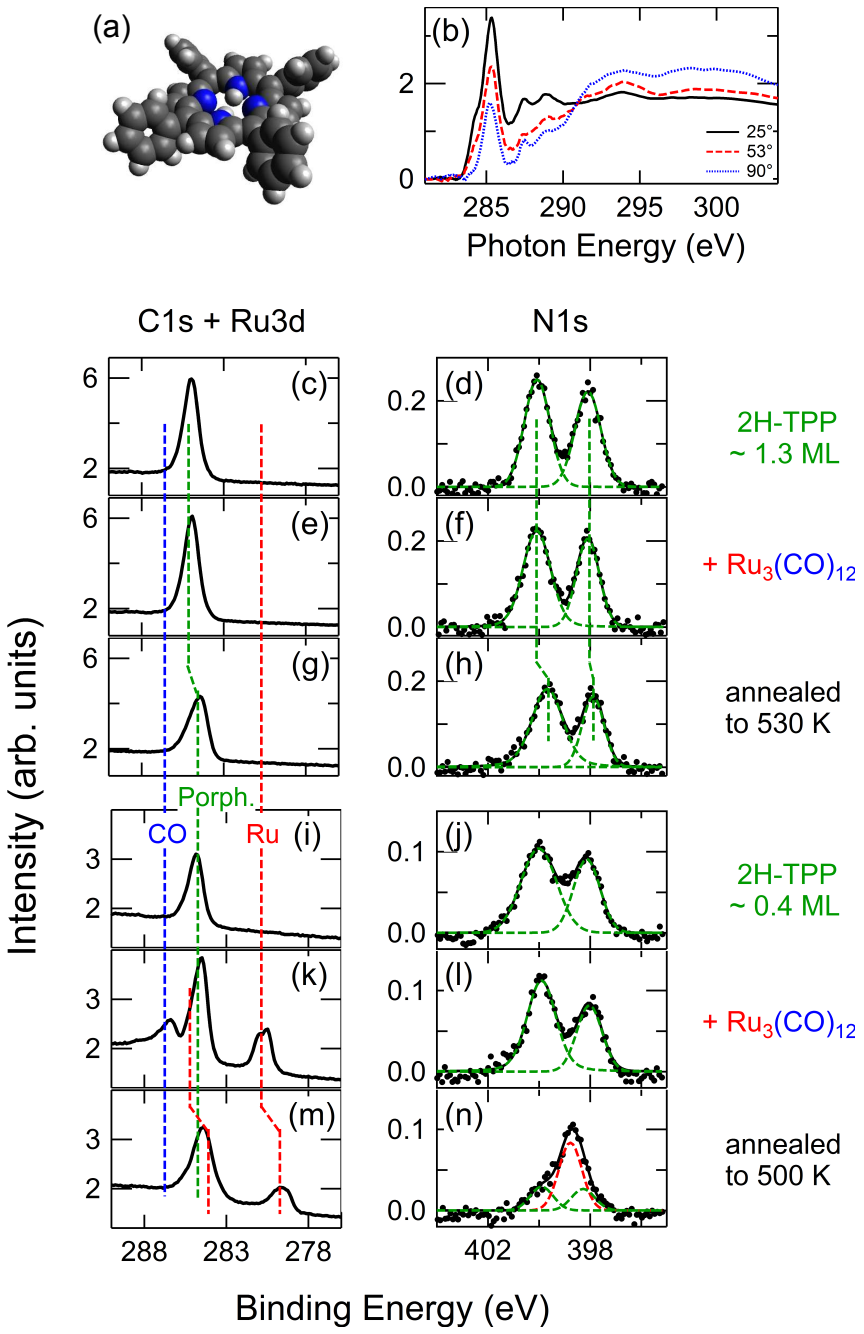

Figure 5.5: Metalation of 2H-TPP/Ag(111) with $Ru_3(CO)_{12}$. (a) 2H-TPP adsorbs in a slight saddle-shaped conformation, as evidenced by (b) angle-dependent NEXAFS spectra of a sub-monolayer of 2H-TPP/Ag(111). $Ru_3(CO)_{12}$ does not adsorb on 2H-TPP films with coverages above one monolayer (c-h), whereas for a submonolayer of 2H-TPP a large amount of the precursor sticks (i-l). After annealing to 500 K the CO desorbs (m), the two N1s peaks (n) originating from the iminic and pyrrolic nitrogen species (green lines) are quenched and a new peak (red) emerges, which is assigned to the nitrogen in Ru-TPP.

In a first step the adsorption behavior of the precursor on the 2H-TPP layer is analyzed. The reference for the monolayer calibration in this section is the amount of carbon and nitrogen of a saturated layer of 2H-TPP^{cf} (Fig. 5.7c and d). Taking into account that the surface coverage after cyclodehydragenation by annealing of a 2H-TPP multilayer is reduced to ∼88%,[181] the actual molecular coverage of 2H-TPP for the monolayer formation is slightly higher due to its reduced surface footprint. In a first step a sample with a 2H-TPP coverage of approximately 1.3 ML (1.1 ML in 2H-TPP coverage) is deposited at room temperature. 2H-TPP adsorbed on Ag(111) forms close-packed islands,[133] so that it can be assumed that at this coverage no bare silver is available. The XPS C1s region (Fig. 5.5c) is dominated by one broad carbon peak, because of the large number of inequivalent carbon atoms in 2H-TPP whose overlapping contributions are not discriminable. The XPS N1s region shows two peaks at 398.1 eV (=N-) and 400.1 eV (NH), i.e., a peak splitting of 2.0 eV (green lines, Fig. 5.5d), which is in full agreement with literature data.[38,51,55] After exposing this surface to the $Ru_3(CO)_{12}$ vapor no Ru signal is detected, neither any change of the C1s and N1s spectra (Fig. 5.5e and f), indicating that the precursor molecules have a negligible sticking coefficient to the porphyrins. Consequently, after annealing to 530 K, no indications for a metalation can be observed. In both spectral regions the reduced peak intensity is evidence for the desorption of part of the molecular ensemble, consistent with the reduced porphyrin coverage resulting by the 550 K annealing of a multilayer. In addition, the corresponding NEXAFS data (not shown) as a function of photon energy indicate that the layer in Fig. 5.5e/f is not yet completely flat, but the average adsorption angle is considerably reduced and the shape of the spectra is closer to that of 2H-TPP^{cf} (Fig. 5.7b) than that of 2H-TPP (Fig. 5.5b). Therefore this flatter adsorption geometry is explained by the occurance of cyclodehydrogenation events, in agreement with Di Santo et al.[182] The shift of both C1s and N1s spectra and the reduction of the N1s peak splitting were already observed by Papageorgiou et al.[181] and Di Santo[182] and attributed to an increased screening of the substrate caused by the flattening of the porphyrin and the consequent closer proximity to the surface.

As it is now evident that the precursor does not adsorb on top of the 2H-TPP, in the next step a submonolayer of 2H-TPP with a coverage of approximately 0.4 ML was prepared (Fig. 5.5i and j). Dosing $Ru_3(CO)_{12}$ onto the sample hardly influences the N1s region (Fig. 5.5l). In the C1s region, however, additional peaks, which originate from Ru (281.5 eV and 282.0 eV) and CO (287.4 eV) (Fig. 5.5k), are clearly discernible. The intensity of the porphyrin

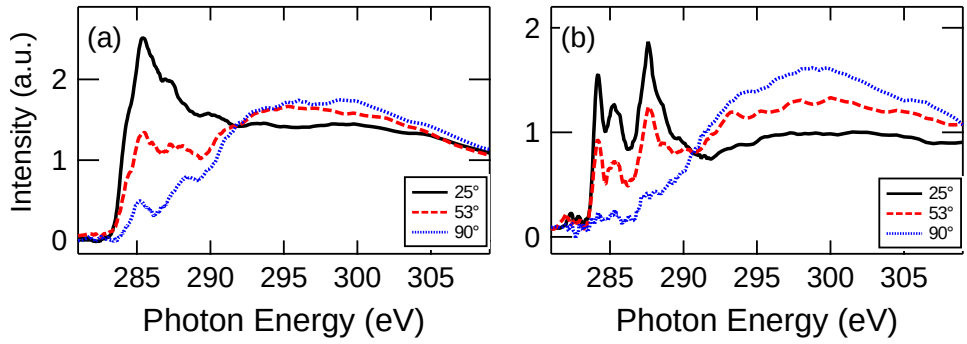

Figure 5.6: NEXAFS C K-edge data of (a) a submonolayer of 2H-TPP exposed to $Ru_3(CO)_{12}$ and annealed to 500 K. Compared to the curves of the 2H-TPP sample (Fig. 5.5b), the spectra are broadened and show a stronger dichroism. (b) The submonolayer curves of the metalated 2H-P, after annealing to 505 K.

peak at 285.5 eV appears to be higher than before, due to their overlap with the $Ru3d_{3/2}$ peaks. O1s measurements (not displayed) confirm the presence of oxygen on the sample. Annealing to 500 K causes the desorption of CO (Fig. 5.5m) and a downward shift of the Ru peaks. In the N1s region an additional peak (red line, Fig. 5.5n) appears at 398.8 eV, which is a typical value for metalloporphyrins, while the signals originating from the nitrogen atoms of the free-base species are reduced. While at this temperature the metalation is not yet complete, the corresponding NEXAFS C K-edge spectra (Fig. 5.6) have changed substantially compared to the data of the untreated sample (Fig. 5.5b). All curves appear broadened and the first transition is quenched, which indicates a stronger interaction with the surface. The smaller intensity of the 90°-curve (blue) in the π^* region points to a much flatter molecular conformation which allows an adsorption closer to the surface. Its origin might be the stronger interaction with the Ru modified silver substrate, but it might also originate from cyclodehydrogenation side reactions, which might have a lower activation barrier in the presence of surface ruthenium. In analogy to the free-base compounds, in the following the metalated flattened species will be denoted as Ru-TPP^{cd}. As for the Ru-TPP films in Section 5.2 after annealing all ruthenium is in an formal Ru^0 state (Fig. 5.5m).

To examine whether the sticking coefficient of the precursor on a porphyrin covered surface is dependant upon the saddle-shaped or the flat porphyrin form, samples with two different 2H-TPP^{cd} coverages were prepared. For a monolayer of 2H-TPP^{cd}, obtained by dosing on a substrate kept at 550 K for long time with high flux (Fig. 5.7c and d), the peak splitting in the N1s region is reduced to 1.6 eV, and an additional shoulder appears at higher binding

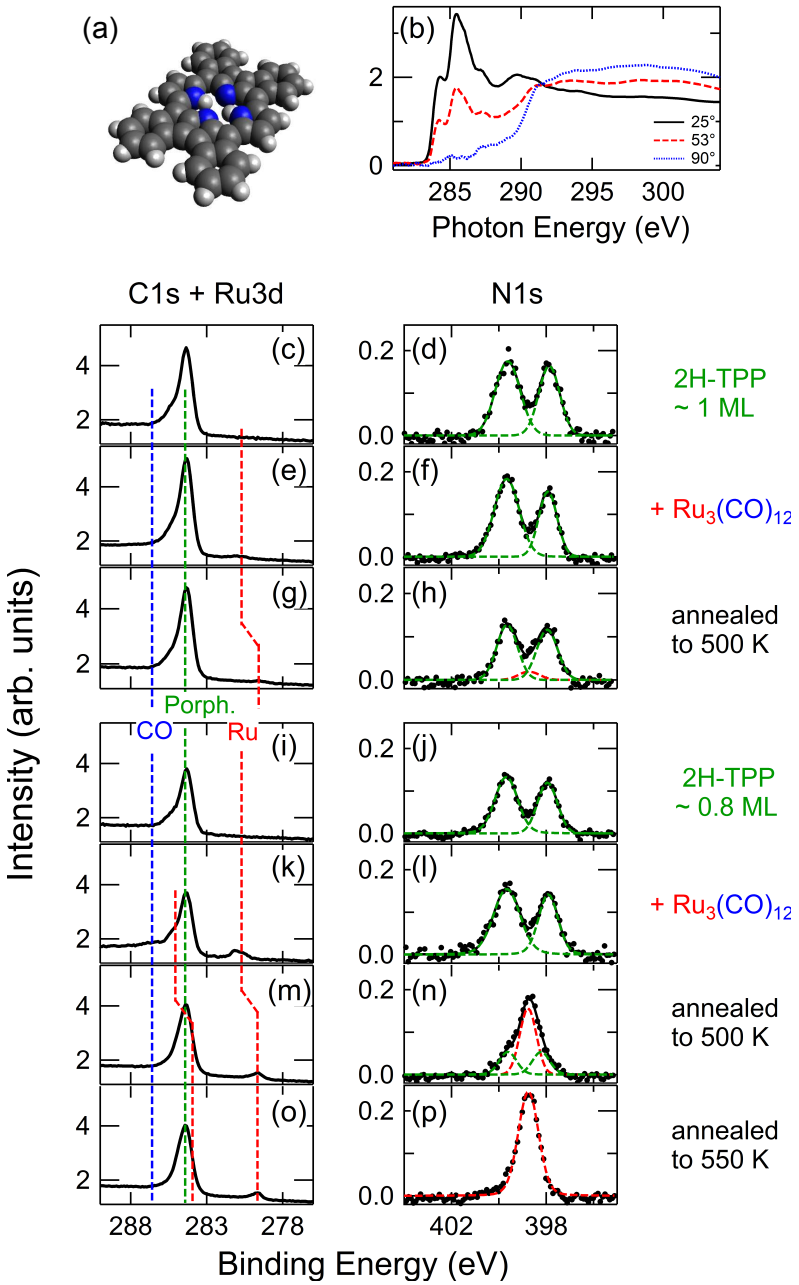

Figure 5.7: Metalation of 2H-TPP^{cd}/Ag(111) with $Ru_3(CO)_{12}$. (a) The cyclodehydrogenated 2H-TPP^{cd} obtained by annealing 2H-TPP to 550 K is nearly flat and adsorbs parallel to the surface, as shown by (b) angle-dependent NEXAFS spectra of a sub-monolayer of 2H-TPP^{cd}/Ag(111). (c-h) Only a minimal amount of $Ru_3(CO)_{12}$ adsorbs on a ML of 2H-TPP^{cd}, consequently only a small portion of the porphyrins gets metalated. (i-l) For a submonolayer sample of 2H-TPP^{cd} a larger amount of $Ru_3(CO)_{12}$ sticks. (m-n) Annealing to 500 K results in partial metalation of the 2H-TPP^{cd} layer. (o-p) After annealing to 550 K all porphyrins are metalated, as evidenced by the single peak in the N1s region.

energies of the C1sp peaks. As stated earlier, this coverage was used as a reference for the 2H-TPP monolayers in this chapter. The result after dosing $Ru_3(CO)_{12}$ is similar to the 1.3 ML preparation of 2H-TPP. Only a very small amount of Ru adsorbs (Fig. 5.7e and f) and consequently only a small portion of the porphyrins gets metalated (Fig. 5.7g and h). The NEXAFS C-edge of a submonolayer of 2H-TPP^{cd} (Fig. 5.7b), obtained by dosing at room temperature and subsequent annealing to 550 K, agrees very well with the one reported by Di Santo et al.[182] and (in comparison with Fig. 5.5b) evidences the different electronic structure and/or interaction with the surface. Since the free-base porphine adsorbs also flat (see Chapter 7) and might consequently adsorb in close proximity to the surface, the observed strong interaction between 2H-TPP^{cd} and the Ag(111) surface is not (alone) the result of a smaller macrocycle-substrate distance. The XP N1s and C1s spectra of the 2H-TPP^{cd} submonolayer are identical to those of the saturated monolayer (Fig. 5.7i and j). The deposition of the precursor leads to an accumulation of Ru_3 (281.3 eV and 281.9 eV) and (CO) (287.3 eV, Fig. 5.7k), indicating that also in this case the $Ru_3(CO)_{12}$ adsorbs on the bare Ag(111) surface and not on the molecules. Subsequent annealing to 550 K leads to a fully metalated porphyrin layer on the surface, as evidenced by a single peak in the N1s spectrum (Fig. 5.7p). Lower annealing temperatures only resulted in a partial metalation of the overlayer (Fig. 5.7n). As before, the Ru peak shifts downward (to 280.2 eV) to a formal Ru^0 state.

The experiments presented in this section show that it is possible to completely metalate a 2H-TPP^{cd} layer with a single $Ru_3(CO)_{12}$ dosing step. The amount of free silver is hereby a crucial parameter for the metalation process, as the triruthenium dodecacarbonyl does not adsorb on top of the porphyrins.

5.5 2H-P on Ag(111)

In a similar fashion the metalation of 2H-P is investigated. Similar to both 2H-TPP species, no metalation can be achieved at higher coverages, because the $Ru_3(CO)_{12}$ molecules do not adsorb on top of the porphines (Fig. 5.8a). For coverages below one monolayer, the N1s data show that a full metalation is possible (Fig. 5.8c). Of special interest is hereby the C1s region. For 2H-TPP the large number of inequivalent carbon atoms prevents an easy access for the interpretation of the spectra. The 2H-P exhibits only five inequivalent carbon species (Chapter 7), which means that changes upon annealing are more visible. And indeed, during the annealing series the C1s peak undergoes

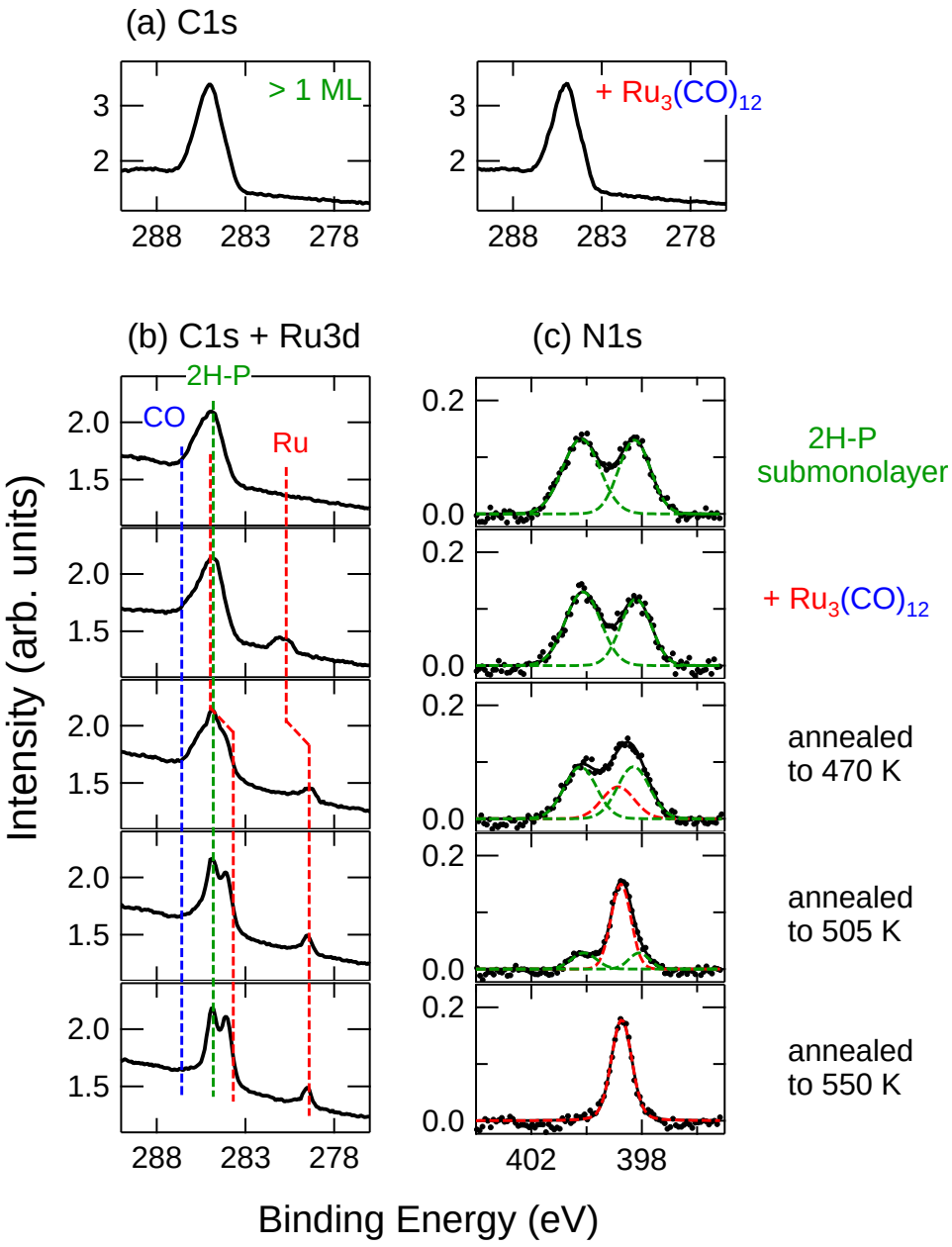

Figure 5.8: Metalation of 2H-P/Ag(111) with $Ru_3(CO)_{12}$. (a) For a coverage of approximately two monolayers the ruthenium carboxyl does not adsorb on the surface. The (b) C1s and Ru3d region and (c) N1s region of a submonolayer of 2H-P show the adsorption of $Ru_3(CO)_{12}$. Annealing leads to the formation of Ru-P, as shown by the growth of a new peak (red, 398.8 eV) in the N1s curves.

a visible transformation. After annealing to 470 K additional shoulders appear on both sides of the broad room temperature peak. The fully metalated Ru-P layers exhibits two sharp peaks which are very similar to the C1s signals from 2H-P adsorbed on Cu(111) (Fig. 7.8, Chapter 7) and Cu-P/Cu(111) (not shown). The second peak appears at lower binding energies, which is typical for a metal-coordinated carbon species.[189] This results suggest that after the desorption of CO mobile Ru adatoms may diffuse below the porphines, i.e., that we effectively observe a Ru-P/Ru system. A different possibility is the coordination of Ru-P to ruthenium porphine chains, forming an organometallic surface networks. Additionally, the presence of the Ru on the surface prevents a desorption of the molecules, as the coverage of 2H-P/Ag(111) gradually decreases during annealing[190] which is not the case here.

The C K-edge NEXAFS spectra corresponding to the sample annealed to 505 K (Fig. 5.6b) is clearly that of a metalloporphyrin (see Chapter 4 and ref. 50). In contrast to the NEXAFS spectrum of Ru-TPP^{cd}/Ag(111) discussed in the section before, the Ru-P spectra are hardly broadened. This indicates that the modification of the electronic structure of 2H-TPP^{cd} upon annealing is caused by the cyclodehydration reaction, rather than by the metalation.

5.6 Conclusions

In summary, it could be shown that metalation by metal-organic chemical vapour deposition is possible for 2H-TPP, its high-temperature derivative 2H-TPP^{cd} and 2H-P. For all three compounds annealing temperatures of 550 K were required for a complete metalation. Coverage dependent measurements show that the crucial point is the amount of bare silver, as the $Ru_3(CO)_{12}$ precursor does not adsorb on top of the molecules. For all coverages of free-base porphyrins, as well as for the pure $Ru_3(CO)_{12}$ compound, no carbon monoxide could be detected after annealing to 550 K, i.e., the metalation reaction happens without leaving by-products on the surface. Moreover, the critical catalytic role of the silver surface in the MOCVD metalation process was elucidated. The porphyrin metalation temperatures coincide with the formation of clean surface Ru. Therefore a reaction mechanism can be confidently proposed: the Ru precursor adsorbs on the bare Ag surface, where it thermally decomposes resulting in reactive Ru atoms which can metalate surface porphyrin species. The comparison with the carbon to ruthenium ratios for purchased Ru-TPP shows that it is possible to accumulate an excess of Ru on samples with submonolayer porphyrin coverages, which might consti-

tute a problem for possible applications. However, this problem can be easily solved by controlling the amount of deposited porphyrins: As the sticking of $Ru_3(CO)_{12}$ is limited to the free silver, higher porphyrin coverages mean that the accumulation of Ru and consequently the reaction are self-limiting. This constitutes a big advantage over the use of electron beam evaporators for the deposition of the metal atoms, for which the dosage of the right metal amount is an additional challange. The XPS and NEXAFS data of mono- and multilayers of pre-synthesized Ru-TPP point to a saddle-shaped molecular conformation, as well as a reduction of the formal +2 state of the ruthenium in the free porphyrin to Ru^0 in direct contact with the silver substrate, probably by a charge transfer between substrate and molecule. The same was found for the *in vacuo* metalated porphyrins, indicating that the apparent oxidation state is not influenced by the proximity to the substrate, which can be expected to be different for the saddle-shaped TPP species on the one hand and the flat 2H-TPP^{cd} and 2H-P on the other hand. Indications for organo-metallic coupling of Ru-P molecules on the surface should be verified by further investigations with scanning probe techniques. This suggests that the reactive Ru atoms resulting from the precursor are active not only for the pophryrin metalation, but furthermore may lead to the formation of surface organo-metallic nanostructures on the surface.

Chapter 6

Adsorption of a gold porphyrin compound on Au(111)

In addition to the technological applications mentioned in the previous chapters, another important field of application is given by the development of bio-medical products, e.g., the usage of oxovanadium porphyrins in the development of anti-HIV drugs[29] or gold porphyrins for anti-cancer treatments.[191] Generally, gold(I) and gold(III) compounds are investigated for possible therapeutic use for the treatment of rheumatoid arthritis, malaria, HIV, bronchial asthma and cancer.[192,193] Crucial is hereby their stability, as Au^{III} compounds are known to be reduced to Au^{I} *in vivo*, i.e., inside the body.[192] Au^{III} meso-tetraphenylporphyrin (Au^{III}(TPP), Fig. 6.1a) molecules were reported to be stable with anti-cancer properties[191] and a factor 100 more effective in comparison to, for example, Zn^{II}(TPP).[194] For a targeted drug delivery inside the human body, gold nanoparticles (AuNPs) have been recently employed as carriers.[195] For a potential combination of Au^{III}(TPP) as therapeutic agent and AuNPs as carrier the question of the stability of the porphyrin and the oxidation state of the gold center arises. For a system comprising of free-base porphyrins and AuNPs the formation of Au^{0} porphyrins was shown by Kanehara et al.[196] In this chapter the adsorption of $[Au^{III}(TPP)]^{+}Cl^{-}$ on a Au(111) surface is studied using laboratory XPS. Special attention is given to two issues:[i] The first is whether the Cl^{-} ionic ligand is retained upon the porphyrin surface adsorption and, if this is the case, in which charge state it is. The second, even more crucial point, is whether the oxidation state of $[Au^{III}(TPP)]^{+}$ is stable upon adsorption.

To this end, $[Au^{III}(TPP)]^{+}Cl^{-}$ films with varying coverages were deposited

[i]The results of this chapter have been published in ref. 58.

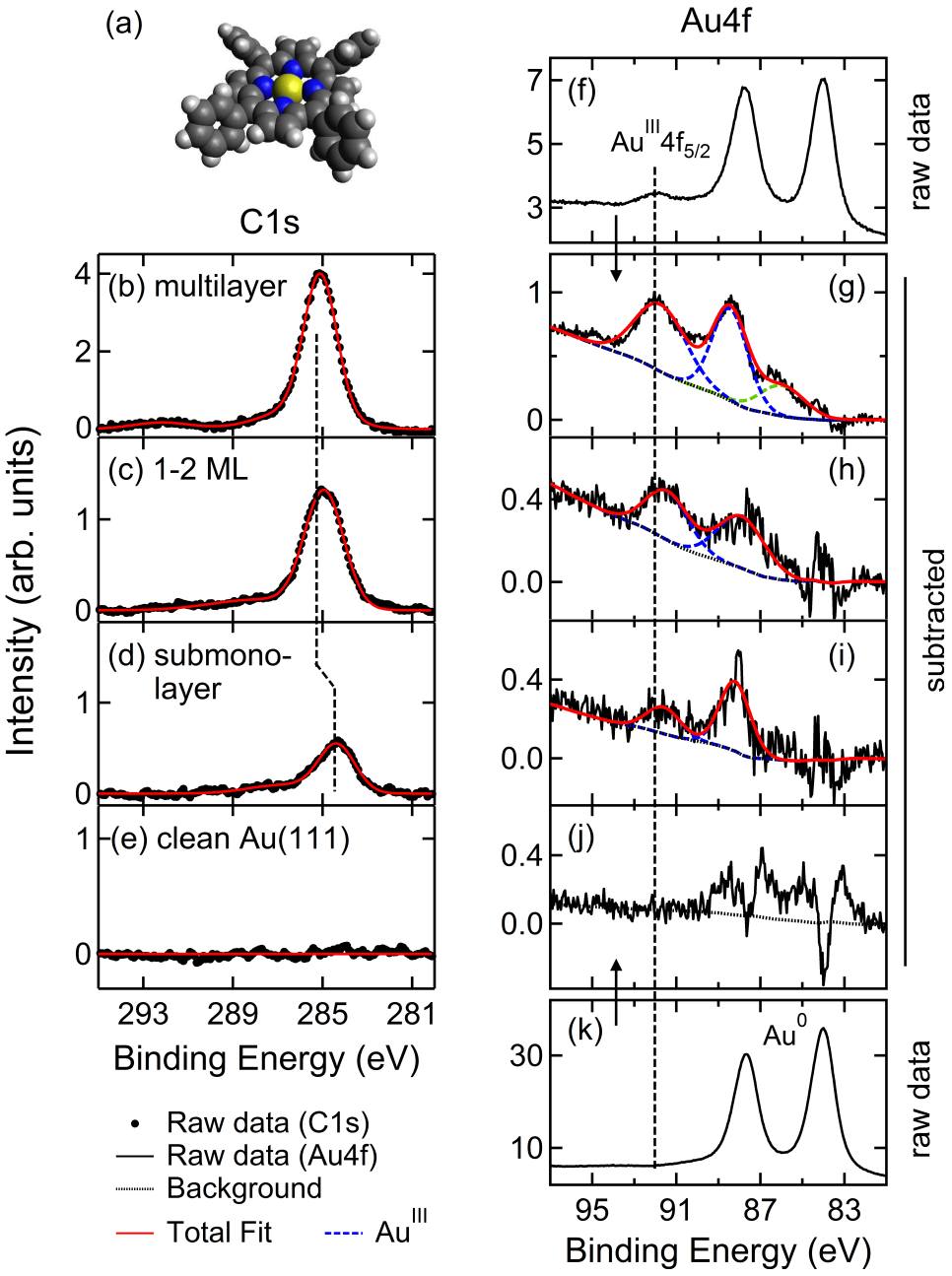

Figure 6.1: C1s (b-e) and Au4f (f-k) XPS spectra of $[Au^{III}(TPP)]^{+}Cl^{-}$ monolayer and multilayer samples. (a) Space filling model of the saddle-shaped Au-TPP (gray: C, blue: N, white: H, yellow: Au). The binding energy of (b) the C1s multilayer peak lies 0.7 eV above that of (d) the submonolayer. (k) The Au4f raw data of the clean Au(111) substrate exhibits two peaks, corresponding to the Au^0 doublet. (f) After deposition of a multilayer the Au^0 peaks are attenuated and a new feature at 91.7 eV (Au^{III}) appears. (g)-(j) Au4f region after subtraction of the clean substrate data. The Au^{III} doublet is present for all molecular coverages (g-i), but not for the clean substrate (j).

Table 6.1: Au4f, C1s and Cl2p XPS binding energies (in eV) of mono- and multilayer $[Au^{III}(TPP)]^+Cl^-$ samples and comparison to literature values.

		$Au4f_{7/2}$	$Au4f_{5/2}$	$Cl2p_{3/2}$	$Cl2p_{1/2}$	C1s
multilayer (Fig. 6.1b)		88.4	91.7	198.1	199.6	285.1
submonolayer (Fig. 6.1d)		88.2	91.6	-	-	284.4
Au^{III}:	$NaAuCl_4$ (ref. 200)	87.4	91.1			
	$Au(OH)_3$ (ref. 201)	87.7	91.4			
Au^I:	(ref. 202)	84.6				
	(ref. 203)	84.7				
Au^0:	(ref. 122, 204)	84.0	87.6			
Cl^-:	(ref. 200)			199.0		
	on Au (ref. 200)			197.0		
Cl^0:	(ref. 122)			200	202	

on a clean Au(111) substrate. Fig. 6.1a displays the saddle-shape conformation of Au(TPP) on the Au(111) surface.[58,197,198] Because of the large number of inequivalent carbon atoms, the single contributions cannot be resolved and the C1s region exhibits only one broad peak (Fig. 6.1b-d). When going from submonolayer coverage (Fig. 6.1d) to a relatively thick multilayer (Fig. 6.1b) the peak position shifts by 0.7 eV to higher binding energies, which can be attributed to stronger polarization screening in the (sub)monolayer. The entity of this shift points to a rather strong interaction with the surface. Similar shifts (0.5 eV) have been reported for Co-TPP/Au(111).[199] In contrast, the C1s peak of Co-TPP adsorbed on Ag(111) only shifts by 0.2 eV.[186]

The multilayer spectra show a clear contribution in the Cl2p region (not shown). The corresponding XPS binding energies are consistent with the presence of Cl^- ions (Table 6.1). In contrast, for submonolayer and monolayer coverages no Cl could be detected within the limit of detection. High-resolution STM images show no evidence for a Cl^- ion attached to the porphyrin,[58] in agreement with the XPS measurements. The amount of chlorine that appear as additional species in the ultra-low coverage STM images is below the laboratory XPS detection limit. Both techniques suggest that upon adsorption on Au(111) decomposition of the $[Au^{III}(TPP)]^+Cl^-$ molecules takes place, followed by desorption of a large part of the Cl^- ions.

The oxidation state of the gold center is less easy accessible, because the gold signal is dominated by the Au^0 peak doublet of the underlying Au(111) substrate (Fig. 6.1k). Only for a thick multilayer (as evidenced by the strong damping of the Au^0 peaks in Fig. 6.1f) an additional feature at 91.7 eV is visible in the Au4f spectrum, corresponding to a $Au^{III}4f_{5/2}$ peak (Table 6.1). In order to analyze films with lower coverages it is therefore necessary to separate the molecular from the much stronger substrate contribution. Therefore the spectrum of a clean Au(111) surface was subtracted from the raw data (Fig. 6.1g-i). To account for the attenuation of the substrate signal caused by the limited inelastic mean free path of the photoelectrons, the signal of the bare Au(111) had to be scaled. Afterwards a Shirley background (black dotted line) was subtracted, followed by a peak fitting with Gaussian curves. The Shirley background hereby empirically accounts for the modified inelastic background caused by the adsorption of the molecules. The result of this procedure for the multilayer of Fig. 6.1f and g shows a doublet (blue dashed lines, Fig. 6.1g) whose binding energies agree with gold in the Au^{III} state (Table 6.1), as it can be expected for a multilayer of $[Au^{III}(TPP)]^+Cl^-$. An additional peak (green dashed line) accounts for an residual structure present after background subtraction. More interesting are the results for lower coverages. For both a sample with submonolayer coverage (Fig. 6.1h) and a film of 1-2 ML (Fig. 6.1i) the Au^{III} doublet is clearly visible, indicating that the oxidation state of the Au-TPP is preserved upon adsorption. Of course, it is questionable if a reduced oxidation state for a small portion of the molecules would be visible with the method employed here, but the comparison between C1s and Au4f ratios of different coverages is consistent with uniform layers of porphyrins in the Au^{III} state. To rule out that the resulting doublet is an artifacts of the background subtraction, the data of two clean substrates were subtracted. The resulting spectrum (Fig. 6.1j), while still displaying small residual Au^0 features, does not show any signal in the Au^{III} region. These results confirm the indications obtained by earlier STM measurements, that Au-TPP adsorbs as $[Au^{III}(TPP)]$.[197]

In summary, it was shown that the XPS core level binding energies of multilayers of $[Au^{III}(TPP)]^+Cl^-$ are in agreement with the presence of Au^{III} and Cl^- ions, i.e., the intact molecule can be sublimed *in vacuo*. In direct contact with the Au(111) surface the compound decomposes and most of the Cl^- ions desorbs, leaving $[Au^{III}(TPP)]$ molecules on the surface.

Chapter 7

Growth and reorientation of 2H-P on Ag(111) and Cu(111)

7.1 Introduction

In the previous chapters the comparison of mono- and multilayers of various adsorbed porphyrins had been used as a tool for the investigation of the interaction between the molecules and the respective substrate. The preparation of 2H-P/Cu(111) (Chapter 4.3), however, proved to be an exception, since it was not possible to grow films of thicknesses exceeding two monolayers at temperatures close to room temperature. This behavior not only differs from the evidence presented in previous chapters of this thesis, e.g., for 2H-TPP/Cu(111) (Chapter 4.2), but also from that of other porphyrin systems, such as 2H-TPyP/Cu(111),[49] 2H-TPP/Ag(111)[135] and Co-TPP/ Ag(111),[20] where coverages higher than that of a bilayer could be achieved at room temperature. Other organic molecules, such as N,N-diphenyl oxalic amide, only form saturated monolayers at room temperature, even though thicker layers can be grown at low temperatures.[205] This immediately raises the question whether the limited growth of 2H-P/Cu(111) is temperature-dependent as well and will be the first issue investigated experimentally in this chapter (Section 7.3.1). In a second step, the growth of 2H-P on Ag(111) will be studied by means of XPS and NEXAFS (Section 7.3.2), to obtain information on the role of the substrate. To facilitate the peak assignment and therefore the analysis of the XPS and NEXAFS data, DFT simulations of the X-ray spectroscopy signatures of a free 2H-P molecule were performed (Section 7.2). The results of this section are not only relevant for the interpretation of the data in the present chapter, but also are, given the significance of 2H-P as fundamental prototypic tetrapyrrole system, a reference for the interpretation of the X-ray

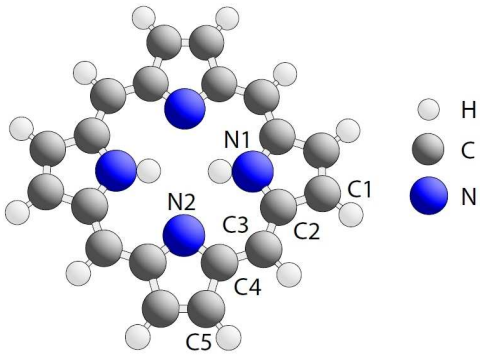

Figure 7.1: Model of 2H-porphine (2H-P). Its flat conformation was confirmed by a geometry optimization of the molecule in gas phase. N1-N2 (C1-C5) denote the inequivalent nitrogen (carbon) atoms.

spectroscopy data of substituted porphyrins as well. However, since our experiments probe the whole molecular film ensemble and not isolated molecules, the comparison between the simulated and the measured data should be performed with caution. The discussion of XPS and NEXAFS signatures in Chapter 4 is based on the assumption that the multilayer data is well suited for such a comparison, because the weak molecule-molecule interactions dominate over the usually stronger molecule-substrate interactions far from the interface. The good agreement between experiment and theory so far justifies this approach. Nevertheless, it is instructive to test the sensitivity of the calculated spectra with respect to molecule-molecule interactions. To this end the XPS energies for different configurations of stacked 2H-P molecules are compared in Section 7.4. The role of impurities on the results presented in this chapter is discussed in Section 7.5. Finally, the role of the different growth parameters (temperature, coverage) for the self-metalation of 2H-P/Cu(111) will be briefly discussed in Section 7.6.

7.2 Spectroscopic signatures

Fig. 7.1 shows the spectroscopic signatures of 2H-P derived by DFT calculations. To validate the simulation, the computed spectra are compared to experimental data corresponding to a multilayer of 2H-P grown at low temperatures (100-125 K) on a Cu(111) substrate (see Section 7.3). Calculations were performed on isolated molecules using StoBe according to the procedure described in Section 3.2, unless noted otherwise.

The experimental N1s XPS multilayer spectrum (Fig. 7.2a) exhibits two

Table 7.1: Calculated ionization energies (E_{calc}) for the inequivalent nitrogen and carbon species in the 2H-P molecule (Fig. 7.1). E_{calc} (shifted) displays the same energies after shifting them by -4.45 eV (carbon) and -4.21 eV (nitrogen) for a better comparison with the experimental data (cf. Fig. 7.2). The difference Δ relative to the lowest binding energy is given with respect to N2 and C5. The nomenclature of the peaks follows the one in Fig. 7.2.

Atom	E_{calc}	E_{calc} (shifted)	Type	Δ	Peak
N1	404.5 eV	400.3 eV	-NH-	2.2 eV	B
N2	402.3 eV	398.1 eV	=N-	0.0 eV	A
C1	289.2 eV	284.8 eV	C-C	0.3 eV	D
C2	290.2 eV	285.8 eV	C-NH	1.3 eV	E
C3	289.0 eV	284.6 eV	C-C	0.1 eV	D
C4	289.7 eV	285.2 eV	C-N	0.8 eV	E
C5	288.9 eV	284.4 eV	C-C	0.0 eV	D

main peaks at binding energies (E_B) of 398.1 eV (peak A) and 400.2 eV (peak B) followed by broader features at 403.5 eV (peak C). This structure is typical for free-base porphyrin complexes and is a result of the two inequivalent nitrogen species in the molecule. By comparison with the calculated ionization energies (Fig. 7.2b, Table 7.1) peak A can be directly assigned to iminic (=N-) and peak B to pyrrolic (NH-) nitrogen atoms in the 2H-P molecule. This assignment agrees with the results for 2H-TPP (Chapter 4) and available N1s literature data on porphyrins;[51,172,206] it also indicates that the nitrogen core levels are hardly influenced by the presence of substituents, as expected given the localized nature of the 1s orbitals. Features C are assigned to shake-up satellites;[72] therefore they are not reproduced by the calculated spectrum, as multi-electron processes are not taken into account.

Porphyrins comprise several different carbon species giving rise to a broad C1s spectrum (see Fig. 7.2c), that is challenging to disentangle into the individual component contributions. Therefore the analysis often disregards the information lying there as deduced by the small amount of porphyrin XPS studies which address the C1s region. Even for the "simple" 2H-P the interpretation of the C1s region is more challenging than in the N1s region, as the measured data (Fig. 7.2c) does not show clearly separable peaks. Peak D at

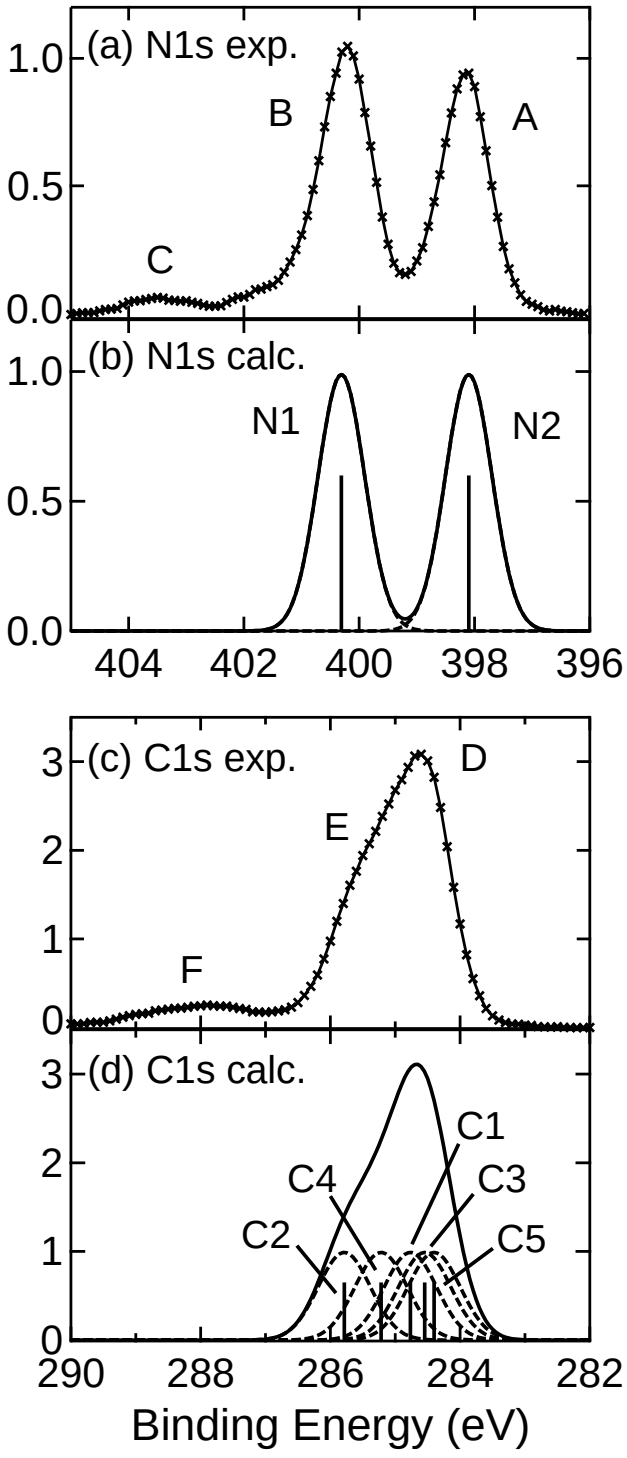

Figure 7.2: The experimental XP spectra of a 2H-P multilayer on Cu(111) in the (a) N1s and the (c) C1s region are well reproduced by the respective simulated spectra (b and d). For peak nomenclature see Fig. 7.1. The calculated nitrogen (carbon) energies (Table 7.1) were broadened with Gaussians (FWHM of 0.95 eV) and shifted by -4.21 eV (-4.45 eV) to facilitate the comparison with the experiment.

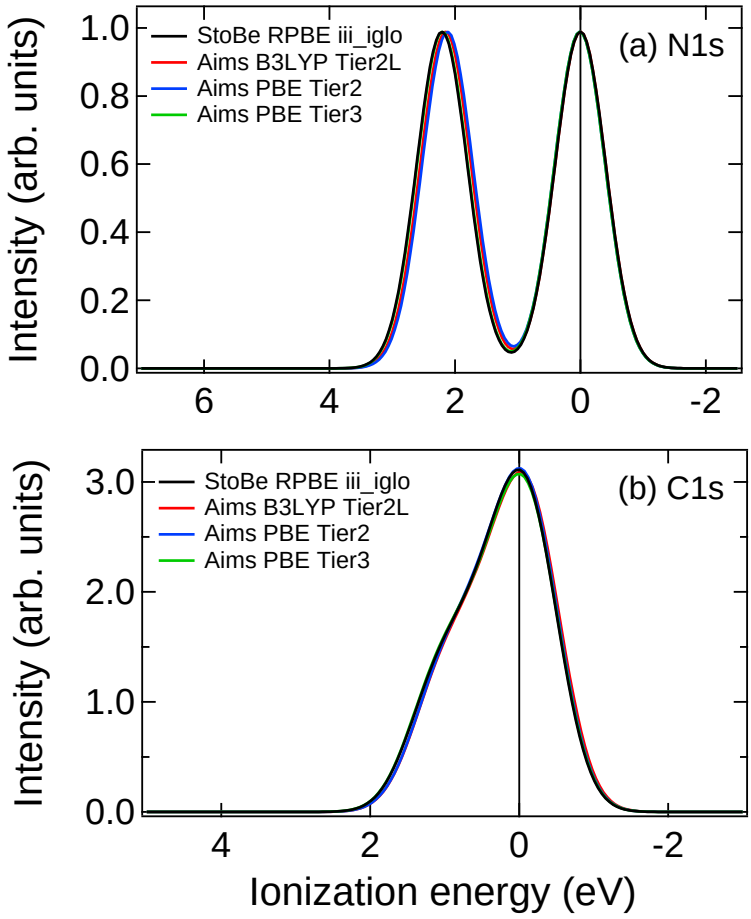

Figure 7.3: Comparison of StoBe and FHI-aims results for the nitrogen (a) and carbon (b) region. Like in Fig. 7.2 the calculated discrete excitation energies are broadened with Gaussians (FWHM 0.95 eV). The ECP/RPBE StoBe calculation and the tier3/PBE FHI-aims calculation yield exactly the same spectra, while the tier 2 FHI-aims calculations differ slightly (by no more than 0.1 eV).

284.6 eV is followed by a broad shoulder E at higher binding energies and by a satellite at 288.0 eV (F). The good agreement of the experimental curve with the simulated spectrum of the five inequivalent carbon atoms (Fig. 7.2d) allows us to disentangle the contributions to the spectal features D-E. The binding energies of the C-C bonded carbon atoms C1, C3 and C5 (see Fig. 7.2) are very similar (Table 7.1) and contribute to peak D. Shoulder E originates from atoms C2 and C4, which are bound to the two different nitrogen species. The broad structure F is assigned to shake-up processes. This knowledge is anticipated to provide the basis for the disentanglement of the carbon XPS signals of more complex porphyrins.

Fig. 7.3 compares the N1s and C1s spectra obtained with the two different

codes (StoBe and FHI-aims) employing different functionals. Calculations with StoBe using PBE and IGLO-III and FHI-aims using PBE and tier 3 result in identical XPS spectra. The differences to the spectra obtained with FHI-aims and tier2 basis sets are minimal ($\leq$ 0.1 eV), which confirms that the use of ECPs in the StoBe calculation is justified in this case.

Compared to XPS data the NEXAFS spectra are more complicated because of the larger number of contributing resonances. In Fig. 7.4a (C K-edge) and Fig. 7.5a (N K-edge) the measured NEXAFS spectra (black symbols) are compared to the respective simulated curves (solid red lines). Our analysis will mainly focus on the π^* region as the broader σ^* structures are harder to decompose. Below 290 eV the C K-edge π^* region shows five main features (A-E) (Fig. 7.4b). The structure is dominated by peaks A, C and E with smaller contributions from features B and D. The decomposition of the spectrum is enabled by comparing it to the result of the calculation. The last five panels in (Fig. 7.4) display the excitations (black bars) and broadened spectra (black solid lines) of the contributions arising from the five inequivalent carbon atoms C1-C5. The sum of all five individual spectra is shown by the red solid lines in the two topmost panels. As it was the case for the XPS results, two different kind of carbon atoms can be discriminated. The C-C bound carbon atoms (C1, C3, C5) generate distinct spectra, other than the C-N bound species (C2 and C4). The respective first resonances are transitions to the corresponding LUMOs of the transition potential state. Their position (Table 7.2) qualitatively and quantitatively follow the XPS energies (Table 7.1), which indicates that the respective shifts of the spectra are an initial state effect. When considering the shape of the spectra, however, three different structures can be discriminated. C2 and C4 on the one hand and C1 and C5 on the other hand exhibit a very similar number and relative intensities of peaks, while C3 is a slightly modified version of C1 and C5. This points to a modified structure of the unoccupied orbitals. Fig. 7.6 displays the final state orbitals obtained in the transition potential calculation. For comparison the ground state (GS) orbitals are displayed in the first column of the figure.

The π^* region of the N K-edge spectra (Fig. 7.5) exhibits 5 peaks A-E, which is typical for free-base porphyrins like 2H-TPP.[56,81,135] For 2H-P ref. 207 shows a similar structure, but less resolved, which matches older reports on 2H-TPP of three peaks (A and B/C and D/E).[150] The shape of the calculated spectrum (red solid line) follows the experimental one, but the agreement is not as good as for the C K-edge. Peak A is the only one which can be assigned unambiguously to an excitation from the iminic nitrogen atom N2. While the

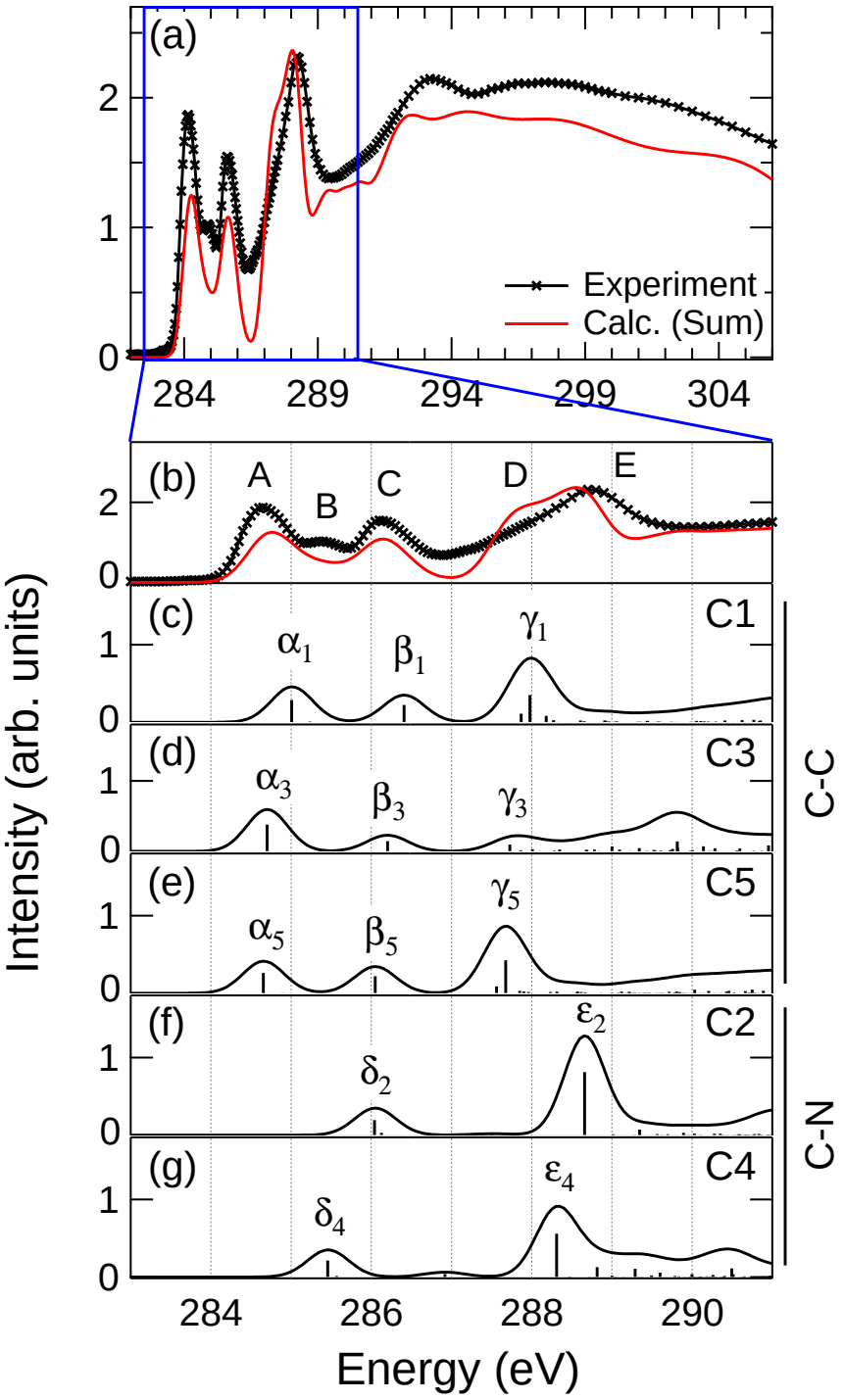

Figure 7.4: The experimental C K-edge NEXAFS spectrum of 2H-P (black symbols) is well reproduced by the calculated curve (red solid line). The zoom-in in the π^* region (panel b) reveals that all features of the measured data are also present in the simulation. Below, the discrete excitations and the broadened spectra of the five inequivalent carbon atoms C1-C5 are displayed by black bars and black solid lines. Corresponding final state orbitals are displayed in Fig. 7.6.

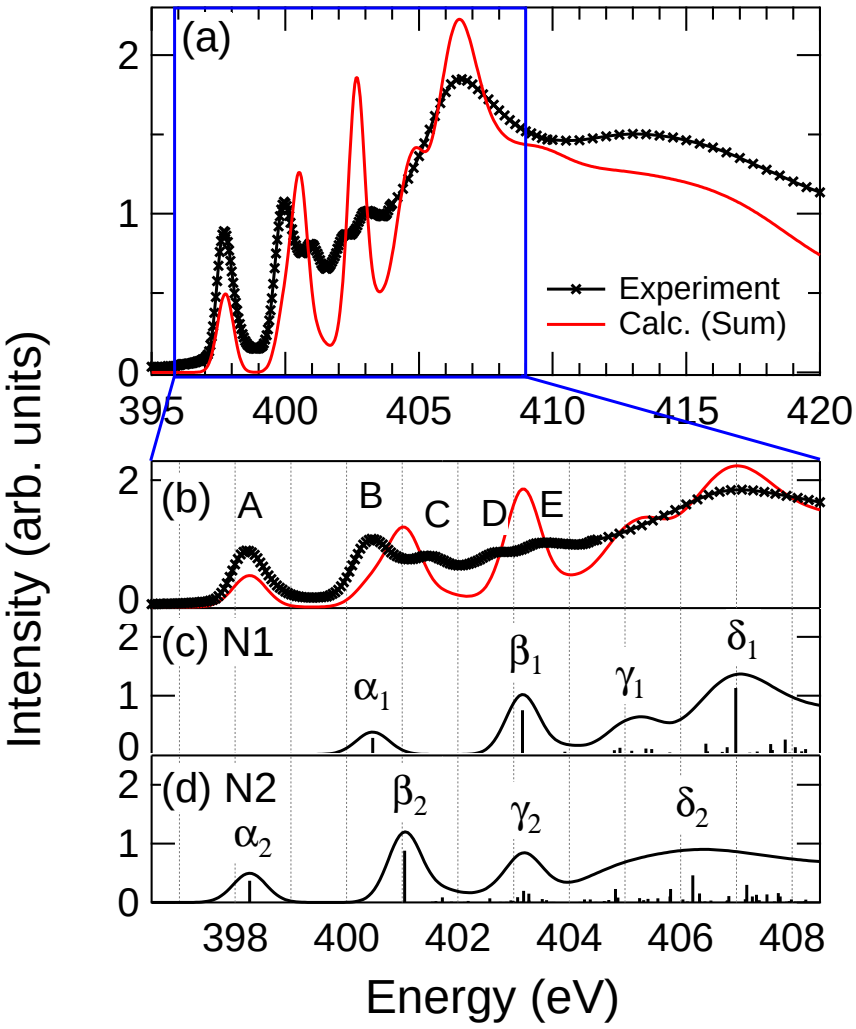

Figure 7.5: The agreement between the experimental N K-edge NEXAFS spectrum of 2H-P (black symbols) and the calculated curve (red continuous line) is acceptable, but not as good as for the C K-edge. The zoom-in in the π^* region (panel b) reveals that all features are reproduced, however, not in perfect agreement with the experiment. Below, discrete excitations and broadened spectra of the nitrogen atoms N1 (-NH-) and N2 (=N-) are displayed (black bars and continuous lines). Corresponding final state orbitals are displayed in Fig. 7.6.

Table 7.2: Peak assignment for the 2H-P C K-edge NEXAFS spectrum of the main contributions below E_{ion}

Peak[i]	Peak[ii]	Exp.[iii]	Comp.[iv]	Type[v]	Transition[vi]
A	α_5	284.2 eV	284.2 eV	C-C	5. (1s) → 63. (LUMO)
	α_3		284.2 eV	C-C	5. (1s) → 63. (LUMO)
	α_1		284.5 eV	C-C	5. (1s) → 63. (LUMO)
B	δ_4	285.0 eV	285.0 eV	C-N	5. (1s) → 63. (LUMO)
	δ_2		285.5 eV	C-NH	5. (1s) → 63. (LUMO)
C	β_5	285.7 eV	285.6 eV	C-C	5. (1s) → 65. (LUMO+2)
	β_3		285.7 eV	C-C	5. (1s) → 65. (LUMO+2)
	β_1		285.9 eV	C-C	5. (1s) → 65. (LUMO+2)
D	γ_5	287.4 eV	287.2 eV	C-C	5. (1s) → 67. (LUMO+4)
	γ_3		287.2 eV	C-C	5. (1s) → 66. (LUMO+3)
	γ_1		287.5 eV	C-C	5. (1s) → 67. (LUMO+4)
	ϵ_4		287.8 eV	C-N	5. (1s) → 66. (LUMO+3)
E	ϵ_2	288.3 eV	288.2 eV	C-NH	5. (1s) → 66. (LUMO+3)

[i]Peaks in experimental spectra (cf. Fig. 7.4b)

[ii]Peaks in computed spectra (cf. Fig. 7.4c-g)

[iii]Experimental peak positions

[iv]Computed peak positions (shifted by 0.1 eV to match experimental spectrum)

[v]Atom type of excitation center: $n = 0.5$ in TP calculation

[vi]Transition (orbital numbers), final state orbitals are displayed in Fig. 7.6

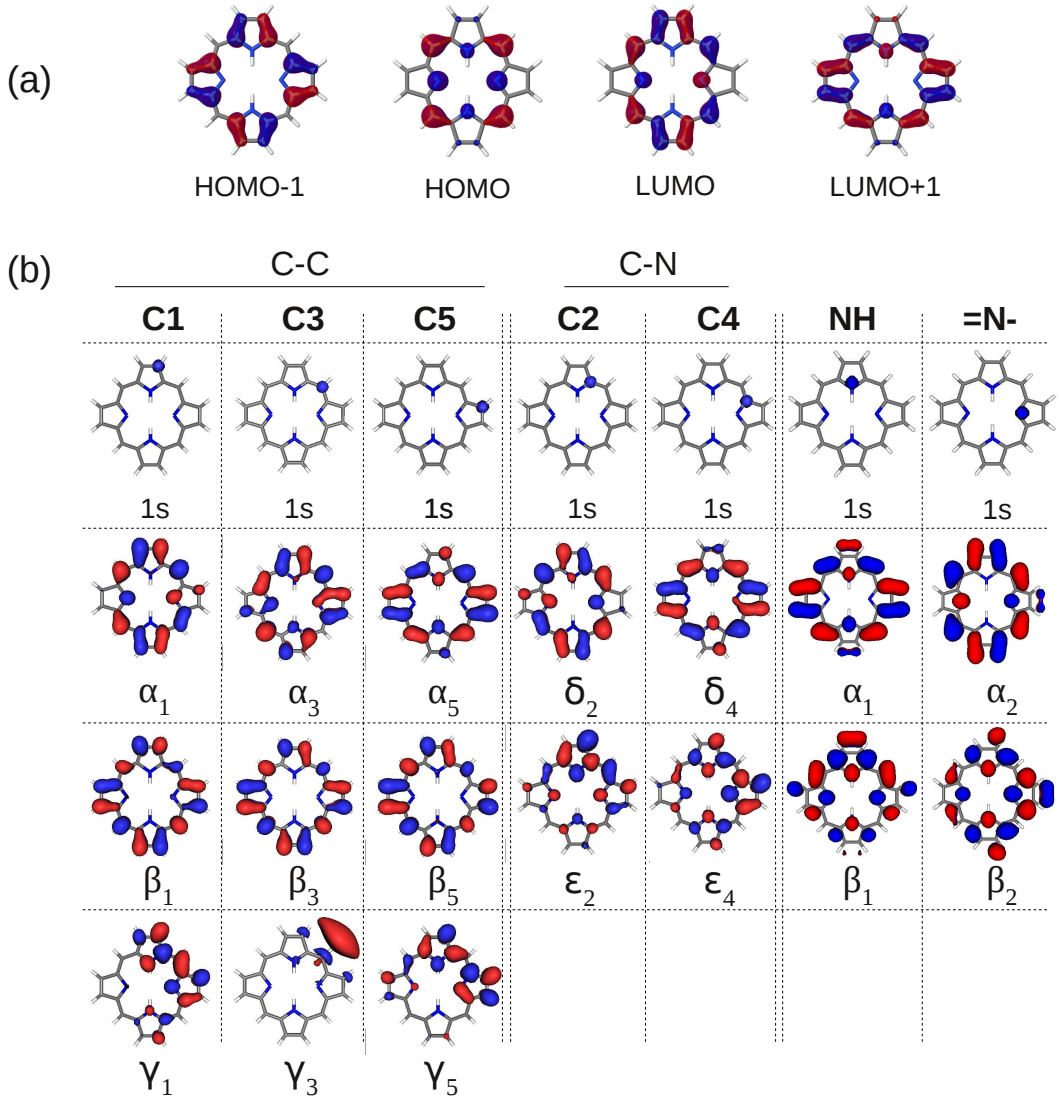

Figure 7.6: Kohn-Sham orbitals obtained from FHI-aims and StoBe calculations. In (a) the ground state (GS) orbitals of the HOMO-1, the HOMO, the LUMO and the LUMO+1 from an all-electron calculation (FHI-aims) are displayed. The shape of these four orbitals is identical for the PBE and the B3LYP calculations and agree well with literature data. In (b) the first row displays the 1s orbitals, indicating the respective excitation centers. All other pictures shows final state orbitals obtained from the transition potential (TP) calculations. The LUMOs (α_i, δ_i) are similar to the undisturbed LUMO, but are slightly distorted due to the creation of the "half" core hole. The similar shape (apart from the different localization of the hole) of the respective final state orbitals for C1-C5, C2-C4 and N1-N2 are reflected in the similarity of the corresponding NEXAFS spectra (cf. Figs. 7.4 and 7.5). The nomenclature α_i-δ_i follows the denotation of peaks in Figs.7.4 and 7.5.

Table 7.3: Peak assignment for the 2H-P N K-edge NEXAFS spectrum of the main contributions below E_{ion}

Peak[i]	Peak[ii]	Exp.[iii]	Comp.[iv]	Type[v]	Transition[vi]
A	α_2	397.7 eV	397.8 eV	=N-	1. (1s) → 79. (LUMO)
B	α_1	400.0 eV	400.0 eV	-NH-	1. (1s) → 79. (LUMO)
C	β_2	401.0 eV	400.5 eV	=N-	1. (1s) → 82. (LUMO+3)
D-E	β_1	402.1-403.1 eV	402.7 eV	-NH-	1. (1s) → 82. (LUMO+3)
	γ_2		402.7 eV	=N-	several

[i]Peaks in experimental spectra (cf. Fig. 7.5b)
[ii]Peaks in computed spectra (cf. Fig. 7.5c-d)
[iii]Experimental peak positions
[iv]Computed peak positions (shifted by 0.1 eV to match experimental spectrum)
[v]Atom type of excitation center: $n = 0.5$ in TP calculation
[vi]Transition (orbital numbers), final state orbitals are displayed in Fig. 7.6

relative transition energies suggest that peak B originates from α_1 and peak C from β_2, the relative intensities and energies do not fit the experiment. The same is true for peaks D/E, where the agreement is worse, so that it is not possible to assign β_1 and γ_2 unambiguously. The general shape (two similar spectra, shifted by approximately 2 eV), but not relative energies and intensities, agree well with calculations in ref. 207. It not obvious which of the literature data shows the best agreement between theory and experiment, because often the respective data are not compared directly in one graph, but the TD-DFT simulations by Schmidt et al.[81] for 2H-TPP are deemed the closest match. It always appears that peaks A, B and C can be assigned without problems (yielding the same results as those concluded from the StoBe calculation here), but for higher energies the assignment is not unambiguous. Comparable to the results obtained for 2H-TPP (Section 4.2), the N K-edge spectrum can be divided into two spectra with a similar number and relative position and/or intensity which originate from the two different nitrogen species. The two respective single curves are shifted by approximately 2 eV (the same as for the XPS energies), which indicates an initial state effect.

7.3 Growth

The present section is dedicated to the investigation of growth of 2H-P multilayers. Therefore we prepared samples with varying coverages on both Ag(111) and Cu(111) substrates. The substrate temperatures during deposition were varied for different preparations. We discriminate between growth at (or close to) room temperature (RT, 300-320 K) and growth at low temperature (LT, 100-125 K). The temperature during data acquisition was the same as during deposition, unless noted otherwise. Since the nitrogen signatures varied to a much smaller extend than the respective carbon curves during the experiments, only the carbon data are shown and discussed in this section. The NEXAFS data in the nitrogen region exhibits the same angle dependence as the carbon region.

7.3.1 Growth on Cu(111)

As it was mentioned before, it was not possible to grow thick multilayers on Cu(111), i.e., films whose thicknesses exceeded approximately two layers. Fig. 7.7a shows overview spectra ($\hbar\omega$ = 700 eV) of a clean copper sample (black) and of three consecutive dosing steps (red, blue, green) of 15 min duration. In the last step, the sublimation temperature of the 2H-P was raised from 483 K to 493 K to further increase the molecular flux in order to rule out that the limited growth is the result of a reduced flux at 483 K, i.e., caused by a progressively emptier crucible. The growth in steps two and three is minimal (as shown by the C1s and the N1s region, see insets), indicating that it is indeed not possible to grow thicker layers. As the same crucible with molecules was employed successfully to grow further 2H-P layers in the same beamtime, it can be excluded that simply the crucible with molecules was empty. The reproducibility of the limited growth with a different copper crystal (see Section 7.5 and Fig. 7.17) indicated a true physical effect.

As it was discussed in Section 4.3, 2H-P adsorbs flat and parallel to the Cu(111) substrate in the first layer grown at RT (Fig. 7.8a), as evidenced by the absence of π^* resonance intensity in the 90°-curve (blue dotted line) of the NEXAFS spectra. The NEXAFS spectra look substantially different from the DFT data derived in Section 7.2. The first peak is partly quenched and the other features are broadened. We attribute this behavior to an electron transfer from the substrate to the LUMO of the molecule and generally to a strong interaction with the copper surface. This is in agreement with the findings of Dyer et al. for 2H-P on Cu(110).[173] The strong interaction is reflected in the

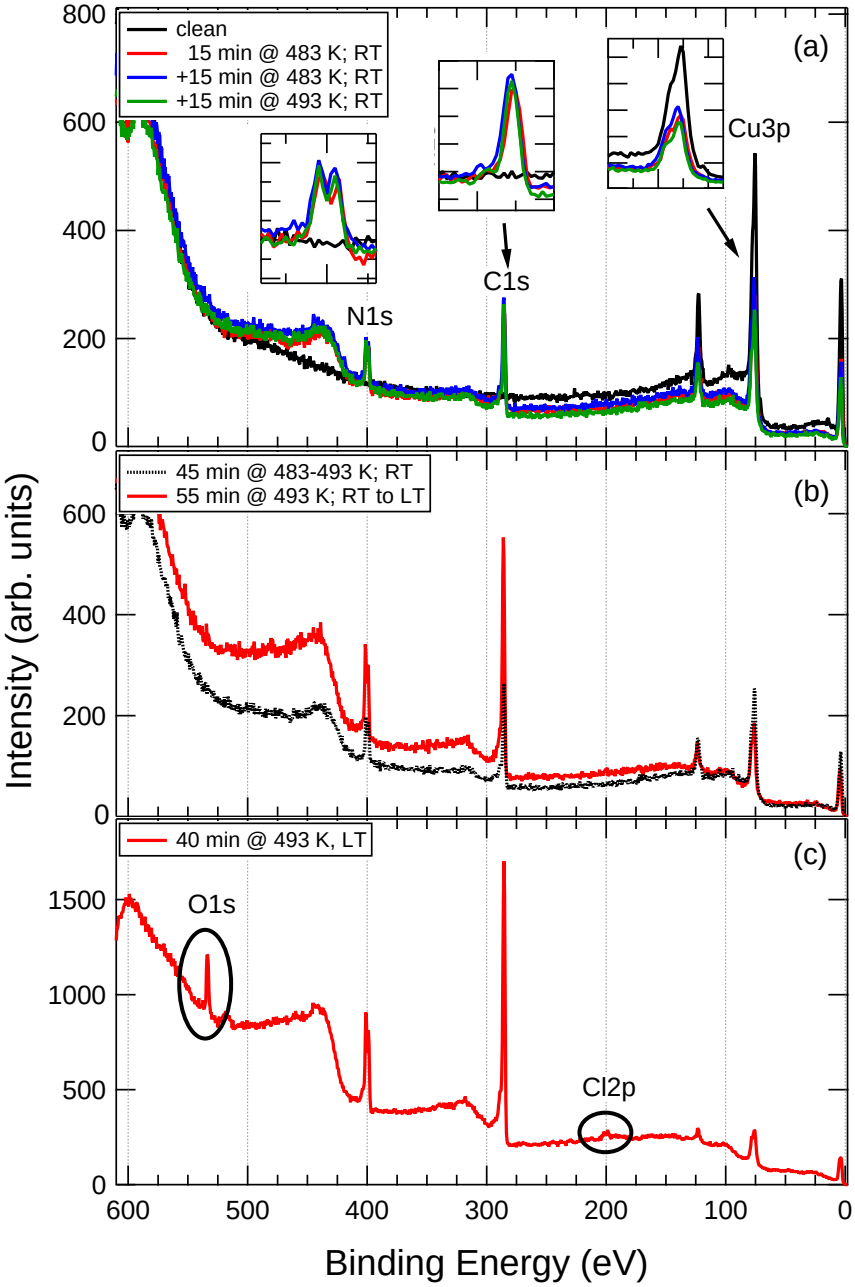

Figure 7.7: Overview spectra ($\hbar\omega$ = 700 eV) measured at BESSY evidencing the limited growth of 2H-P on Cu(111). Panel (a) shows a series of curves for an experiment consisting of sequential dosing of 2H-P. The black curve is that of the clean Cu(111) substrate. Afterwards molecules were dosed three times, by 15 min, which did not change the adsorbed amount substantially from the first evaporation. The spectra in (b) compare the 2H-P surface amounts after dosing at RT and LT, showing that it is possible to grow thicker layers on a cooled substrate. The spectrum in (c) was acquired at a different beamtime for a different batch of molecules, showing the presence of contaminants Cl2p and O1s.

drastically changed XPS C1s spectrum (Fig. 7.8e), which is very similar to that of 2H-P, annealed in the presence of $Ru_3(CO)_{12}$ in Section 5.5. A tentative explanation suggests either a coordination of the outer carbon atoms by metal atoms such as was described in refs. 171, 177 (which seems unlikely given the STM evidence in Fig. 4.11) or a strong interaction of the carbon atoms with the copper substrate, which constitutes such a strong chemical environment for the carbon atoms that the intramolecular differences are negligible and only the two sharp main peaks observed in Fig. 7.8e remain. The molecules of the bilayer have a small adsorption angle (small features in the π^* region of the 90°-curve in Fig. 7.8b), the NEXAFS spectra are now again consistent with the shape predicted by theory. The structure of the corresponding XPS C1s region (Fig. 7.8f), however, still differs from the calculated one: It shows a more pronounced shoulder on the low binding energy side and appears to be a mixture of first layer contributions and the expected multilayer signature.

Cooling down the sample during deposition results in a further increase of coverage (Fig. 7.7b), so that multilayers could be achieved up to a point where the substrate peaks are strongly reduced in intensity (Fig. 7.7c). Fig. 7.7b and c both show overview spectra of layers at low temperature, with a slightly higher coverage in Fig. 7.7c as shown by the relative intensities of C1s and Cu3p peaks. The data were taken at different beamtimes, which is the reason for the different absolute counts. Fig. 7.7c evidences contaminants on the sample, a large O1s peak and a small Cl2p peak. They will be discussed in more detail in Section 7.5. The corresponding C K-edge NEXAFS and XPS C1s data are shown in Fig. 7.8 c/g and d/h. Fitting of the NEXAFS data yields an average tilt angle of 40°with respect to the Cu surface, which may either point to all molecules tilted by the same angle (Fig. 7.8 middle panel) or, as NEXAFS averages over all domains, to molecules ordered in the 2H-P single crystal structure (consisting of porphine dimers stacked in a T-shape fashion)[208] or a random combination. The similarity of the spectra for both preparations indicate that the contaminants, which are not detectable in the first preparation, do not influence the adsorption angle and the shape of the carbon photoemission peak substantially. The XPS structure of Fig. 7.8g is very similar to the calculated one and was used in Section 7.2 for the comparison with the calculation.

In comparison to other porphyrins it is unexpected that for 2H-P/Cu(111) the desorption temperatures of second and higher layers are different. In this regard, the porphine behaves rather like other (smaller) conjugated molecules, such as benzene adsorbed on Cu(111). In the first layer, benzene adsorbs par-

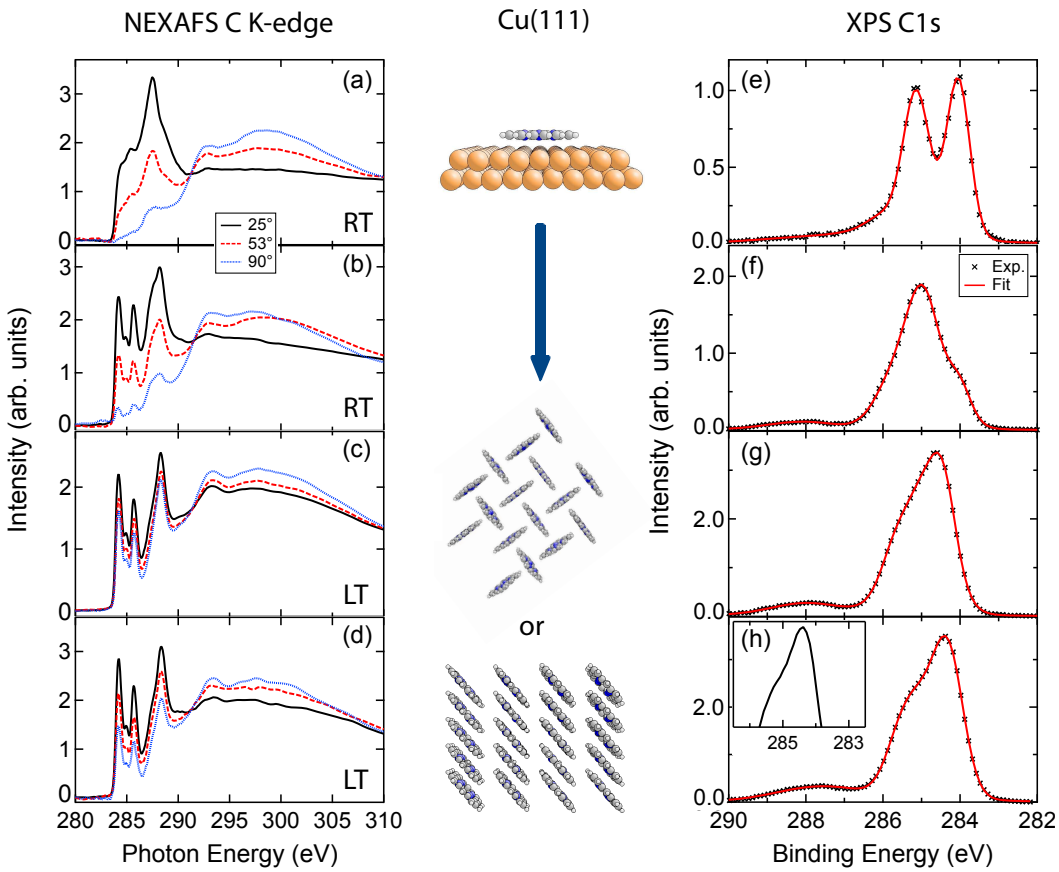

Figure 7.8: Growth of 2H-P on Cu(111). (a) and (b) are grown at room temperature (RT). Due to the limited growth at RT (Fig. 7.7), the sample was cooled for (c) and (d). On the left side angle-resolved NEXAFS C-K-edge spectra (25°: black solid line, 53°: red dashed line, 90°: blue dotted line) for coverages increasing from (sub)monolayer (a) to multilayer (d) indicate the adsorption geometry: In the first layer (a), the porphines adsorb flat on the surface. The molecules in the bilayer (b) exhibit a small tilt angle with respect to the Cu(111) surface. The multilayers grown at low temperatures have an average tilt angle of 40°. These geometries are illustrated in the middle panel. The right panel (e-h) shows the corresponding XPS C1s data (black markers, $\hbar\omega = 385$ eV for e-g and 435 eV for h). The red solid line represents the overall fit of the data. The shape of the C1s curve changes substantially, from sharp features at (sub)monolayer coverages (e) to a broad peak for the multilayer (h), which is identical to the 2H-P monomer spectrum obtained with DFT calculations. The inset in (h) shows a zoom-in of the C1s region to highlight the difference to Fig. 7.9h.

allel to the surface.[209] Raising the coverage above that of the saturated monolayer leads to the formation of a stable bilayer, where the benzene molecules are adsorbed perpendicular to the first layer. This bilayer has a slightly higher (5 K) desorption temperature than the multilayer.[209] The results of 2H-P/Cu(111), while following very similar trends, are slightly different. The NEXAFS data of the bilayer (Fig. 7.8b) only shows a small average angle, ruling out a completely upright standing second layer. This can be explained by the bigger size of the porphine, possibly resulting in a stronger molecule-substrate interaction. The repulsive interaction between individual 2H-P molecules evidenced in Section 4.2 (Fig. 4.11) was also reported for benzene/Cu(111) by Xi et al.[209]

7.3.2 Growth on Ag(111)

To study the role of the substrate, the growth of 2H-P on Ag(111) at room temperature (Fig. 7.9) was monitored by means of polarization-dependent NEXAFS spectroscopy (left column) and XPS (right column).[i] The number and shape of the NEXAFS peaks do not vary substantially during the deposition series and agree well with the theoretically calculated monomer curves discussed in Section 7.2. In the first layer in direct contact with the substrate (Fig. 7.9a) the molecules adsorb undeformed and parallel to the surface, as indicated by the 90°-curve (blue dotted line) whose intensity is zero in the π^* region, apart from the intrinsic absorption steps. With increasing coverage (Fig. 7.9b-d) the intensity of the 90°-curve increases until the dichroism is reversed for the thick multilayer (Fig. 7.9d). Because of the thickness of the layer, the coverage dependent orientation and the consequent damping of the first layer signals the coverages cannot be quantified accurately. Fig. 7.9a certainly shows (sub)monolayer data, while the final coverage in Fig. 7.9d is estimated in the 8 ML range. For the thick layer in Fig. 7.9d the average angle is 90°, i.e., the molecules adsorb perpendicular to the surface. Fig. 7.9c and 7.9d exhibits smaller angles. It is not possible, however, to determine from the NEXAFS data whether the average measured angles (except for the 0° and 90° curves, which are unambiguous) originate from molecules which are all tilted the same way or from molecules with different orientations whose contributions are averaged in the spectra (cf. Fig. 7.8). Therefore it is not possible to determine from NEXAFS alone how the molecules grow for intermediate coverages. The adsorption geometries are illustrated in the middle panel of Fig. 7.9. The right column (Fig. 7.9 e-h) shows the corresponding XPS C1s

[i] The data were acquired at LT, which does not influence the tilt angle (see Section 7.3.3)

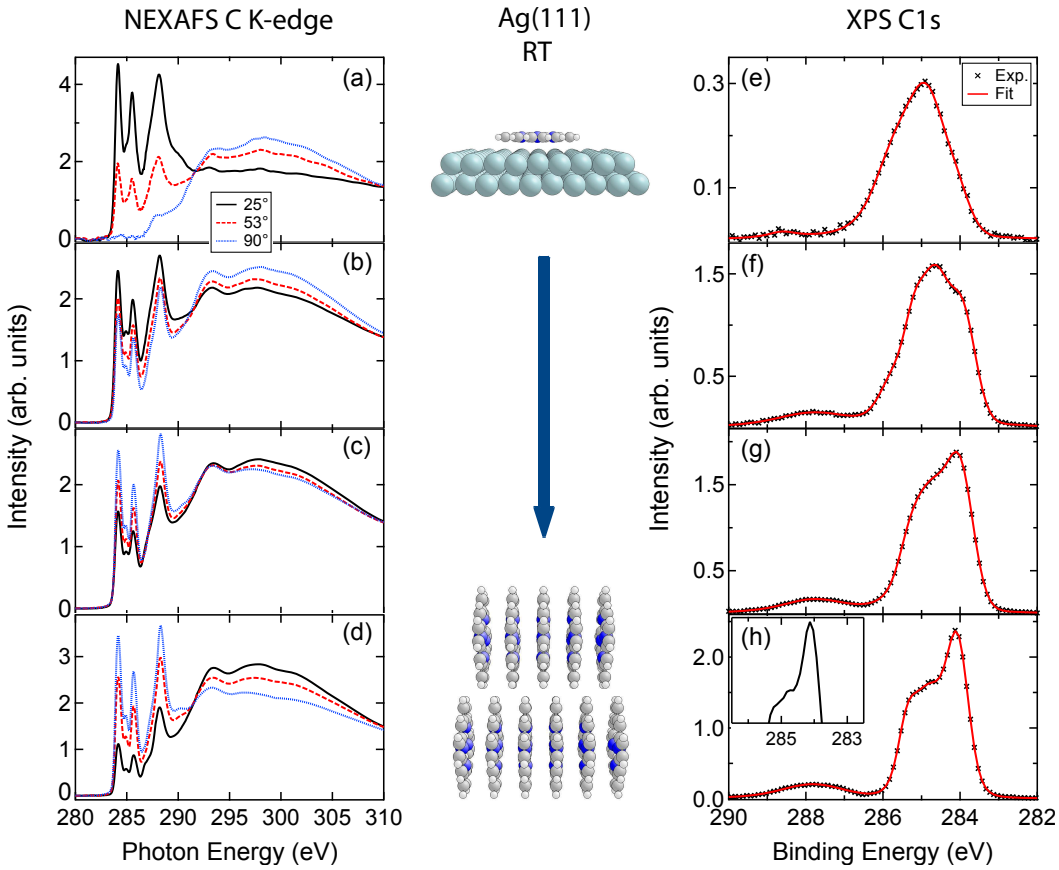

Figure 7.9: Room temperature growth of 2H-P on Ag(111). On the left side angle-resolved NEXAFS C K-edge spectra (25°: black solid line, 53°: red dashed line, 90°: blue dotted line) for coverages increasing from (a) (sub)monolayer to (d) multilayer. The central column illustrates the adsorption geometry: In the first layer (a), the porphines adsorb planar on the surface. The angle increases with increasing coverage, until the molecules stand upright on the surface for a multilayer (d). These changes are illustrated in the middle panel. The right panel (e-h) shows the corresponding XPS C1s (black markers, $\hbar\omega = 435$ eV). The red solid line represents the overall fit of the data. The shape of the C1s curve changes in a systematic way, from a very broad structure at (sub)monolayer coverages (e) to a more defined shape for the upright multilayer (h). None of the four spectra matches the 2H-P monomer spectrum obtained with DFT calculations. The inset in (h) shows a zoom-in of the C1s region to highlight the additional feature at 284.8 eV.

curves (black markers, $\hbar\omega = 435$ eV). The shape of the C1s curve changes in a systematic way, from a very broad structure at (sub)monolayer coverages (Fig. 7.9e) to a more defined shape for the perpendicular multilayer (Fig. 7.9h). In between (Fig. 7.9f and Fig. 7.9g), the characteristic peak at 284.1 eV grows. None of the four spectra matches the 2H-P monomer spectrum obtained with DFT calculations. The multilayer spectrum is the closest, but even with a broadening of 0.7 eV (cf. Fig. 7.13d or later) the experimental data cannot be reproduced exactly. This topic will be discussed further in Section 7.4.

As was the case for 2H-P/Cu(111) (Fig. 4.11 in Chapter 4) STM studies of submonolayers of 2H-P/Ag(111) evidence a net repulsion between molecules.[48] Our X-ray spectrocopy data indicated a strong interaction between 2H-P and the copper substrate, concomitant with an electron donation-backdonation effect. In contrast, for 2H-P/Ag(111) we do not observe such a strong interaction. Number and relative intensities of the resonances of the 53°-curve of mono- and multilayers (7.9a and d) do not vary much, so that we can rule out a substantial charge transfer. A small, partial electron transfer which would be consistent with our data, was evidenced by the UPS measurements described in ref. 48. One possible interpretation, namely a different distance between 2H-P and the respective substrate, can not be verified with the present data, but should be accessible by DFT calculations which take the substrate into account.

The next step was dosing 2H-P at low temperature on Ag(111), which results in the same coverage as dosing at room temperature (cf. Fig. 7.17a and b). However, the average angle of the molecules is 40° (Fig. 7.10a) instead of 90° for the layers grown at RT, identical to the multilayer grown on Cu(111) at LT (Fig. 7.10c). The corresponding XPS spectrum (Fig. 7.10e) differs from that of the ordered layer consisting of upstanding 2H-P and is similar to both the calculated curve for the monomer and the C1s spectrum of the multilayer grown at Cu(111) at low temperatures (Fig. 7.10g). As mentioned above during the discussion of the porphine growth on Cu(111), the 40°-angle of the low temperature phase is consistent with the 2H-P crystal phase[208] which consists of porphine dimers stacked in a T-shape fashion. The phase of upright standing porphines, however, is certainly different from the crystal phase, i.e., demonstrating templated growth.

This behavior is in strong contrast to the growth of the more extended, substituted porphyrins, such as 2H-TPP on Ag(111), where the NEXAFS data of multilayers deposited at RT point to flat macrocycles and tilted phenyl rings,[135] i.e., the macrocylces are certainly not perpendicular to the surface. As dis-

cussed before for the adsorption on Cu(111), the coverage- and temperature-dependent tilting of 2H-P on Ag(111) is reminiscent of the behavior of small, aromatic molecules like benzene and pyridine, which were found to tilt depending on the sample preparation conditions. Pyridine/Ag(111) deposited at low temperatures (100 K/140 K) shows a coverage-dependent change in tilt-angle, accompanied by different bonding to the surface: For low coverages the molecules are either flat or have an angle of 45° to the surface (the literature data are not consistent) and bind primarily through the π orbitals or nitrogen lone-pairs, whereas for higher coverage the molecules start to tilt and finally appear randomly oriented.[210,211] An explanation for the temperature-dependent tilting (30°) of benzene on Pd(111) is given in ref. 212: Compared to the flat adsorption at RT[213] more molecules stick to the surface and the "surface crowding" is the reason for the tilting, caused by steric hindrances.[212] On other substrates like Cu(111)[209] and Ru(001)[214] the benzene molecules do not tilt uniformly: the first layer adsorbs flat while the second layer stands (nearly) perpendicular to the first one. This scenario would be consistent with the NEXAFS data presented here. The alternative possibility of a uniform tilt of all molecules, as observed for example for diphenyl-oxadiazole on Cu(111)[215] seems equally probable.

7.3.3 Reorientation

To study the energetics involved, we investigated how the orientation of the molecules depends upon changes in temperature after the deposition. To this end, multilayers of 2H-P were dosed on cold Ag(111) and Cu(111) substrates, which (as discussed before) leads to thick films with average adsorption angles of 40° for both substrates. Carbon NEXAFS and XP spectra of the resulting layers are identical (Fig. 7.10a and c for NEXAFS, Fig. 7.10e and g for XPS).

Slow annealing to room temperature leads to a reorientation of the molecules on both substrates until they are perpendicular (Fig. 7.10b and d). Slow annealing was achieved by switching off the cooling of the manipulator, so that the temperature increased slowly in the course of one or more hours.[ii] The reorientation is also reflected in the XPS C1s spectrum of 2H-P/Ag(111) (Fig. 7.10f), which shows the more distinct features for the perpendicular molecules, as it was observed for the multilayer directly grown at room temperature (Fig.

[ii] The point about slow annealing is stressed because we saw indications of multilayer desorption (and a bilayer left) if the film deposited at LT was brought in contact with a manipulator kept at RT, i.e., a fast annealing. As this result was not reproduced for lack of beamtime, it will not be discussed further.

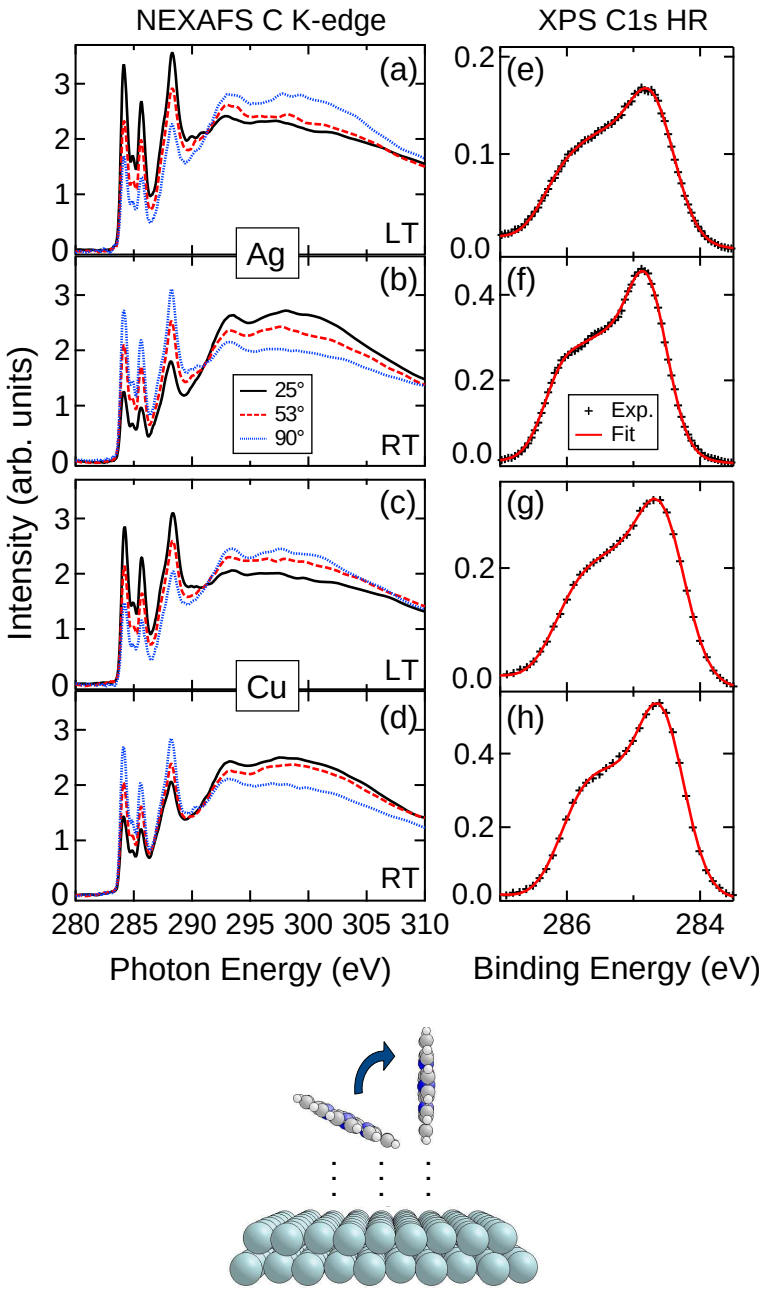

Figure 7.10: Reorientation of 2H-P molecules on Ag(111) and Cu(111). Left column: NEXAFS C K-edge spectra, right panel: High resolution XPS C1s data of the same preparations. Multilayers grown at LT on a Ag(111) (a)/(e) and a Cu(111) (c)/(g) substrate: The molecules exhibit an average angle of approximately 40°. The corresponding XPS peak is broad and resembles that of the monomer. Slow annealing to RT (b/f for Ag(111) and d/h for Cu(111)) leads to a reorientation of the molecules: they adopt a perpendicular orientation with respect to the surface. The corresponding XPS peaks are more defined, like the ones for layers directly grown at RT (Fig. 7.9).

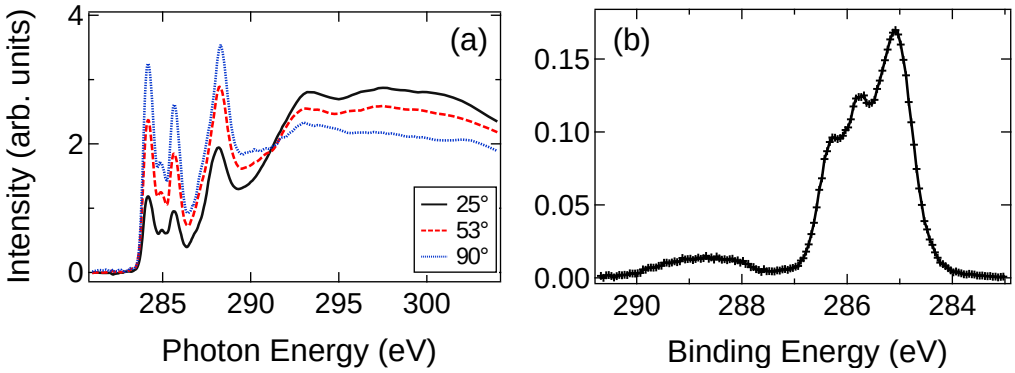

Figure 7.11: High resolution carbon (a) NEXAFS and (b) XPS data of a perpendicular 2H-P multilayer on Ag(111) grown at RT. This spectrum is the one which deviates most from the calculated monomer spectrum. The sharp features at binding energies higher than that of the main peak appear also in other spectra of perpendicular molecules (see for example Fig. 7.9h and 7.10f), but are always much less prominent than in this example.

7.9h, inset).

In the last step, we cooled down the samples again to check whether the reorientation is reversible. However, we could not observe such a change, which indicates that the perpendicular molecules indeed form a more stable phase. This seems surprising as the geometry optimizations show that the symmetric chain is energetically less favorable than the tilted one (Section 7.4). The reason for the higher stability of this phase might not be an energetic one, but rather that steric hindrances for the closer packed molecules hinder a switch to the more preferred state.

7.4 Influence of different parameters on the C1s XP spectra

As was briefly discussed in the last sections, there is a direct connection between the orientation of the molecules and the shape of the multilayer XPS C1s spectra. In general, the curves of the layers grown at low temperatures, are broader and the features are less distinct. This result is not surprising itself and would point to a more disordered layer whose molecules have slightly different chemical environments. The agreement with the theory is very high for an empirical broadening of 0.95 eV.

It is, however, unexpected that the C1s spectra of the multilayers with

perpendicular molecules (which are sharper) do not agree as well with the theory. Of course, different broadening of the calculated binding energies lead to different shapes of the resulting curves (Fig. 7.12), but (contrary to the LT cases) it is not possible to find a single FWHM value to match the experimental spectrum. There is an additional feature on top of the shoulder at approximately 284.8 eV (see Fig. 7.9h, inset), which is not reproduced by the theory. Moreover, the shape of the spectra is not identical for all layers with similar orientation. The reoriented layer in Fig. 7.10f only shows a hint of the structure that is present in Fig. 7.9h, and which was more prominent for a different 2H-P film preparation shown in Fig. 7.11b.

7.4.1 Influence of broadening values

The comparison of several FWHM values for the broadening of the calculated discrete binding energy values (Fig. 7.12) shows that this cannot be the source for the discrepancy between theory and the measured RT phase. Even when ignoring the extreme case (Fig. 7.11) and only comparing the data from Fig. 7.8g (Cu(111), LT, Fig. 7.12a) and Fig. 7.9h (Ag(111), RT, Fig. 7.12b) to calculated data with varying FWHMs, it becomes evident that molecules from the perpendicular phase generate a spectrum that cannot be easily reproduced by the theory.

7.4.2 Influence of the molecular orientation

XPS measurements with varying photon energies $\hbar\omega$ were conducted for multilayers dosed at a Cu(111) substrate at LT (Fig. 7.13a) and a Ag(111) sample at RT (Fig. 7.9b). A variation of the photon energy leads to a variation of the kinetic energy of the photoelectrons and consequently to a modified inelastic mean free path of the electrons.[77][iii] Therefore measurements with 385 eV (E_{kin} $\sim$ 100 eV) are much more surface-sensitive and only probe the topmost layers. All experimental and theoretical curves in Fig. 7.13 were normalized to the intensity at 284.1 eV, in order to compensate for the different photon fluxes at varying photon energies. The measurements for LT-Cu(111) hardly show any dependence on $\hbar\omega$, the changes being minimal. The shape of the RT-Ag(111) sample, however, varies with $\hbar\omega$. A first tentative explanation takes into account that the molecules are oriented differently. For flat molecules $\hbar\omega$ should

[iii] Photoelectron diffraction effects are neglected here, due to the large integration angle selected by the operation mode of the electron energy analyzer.

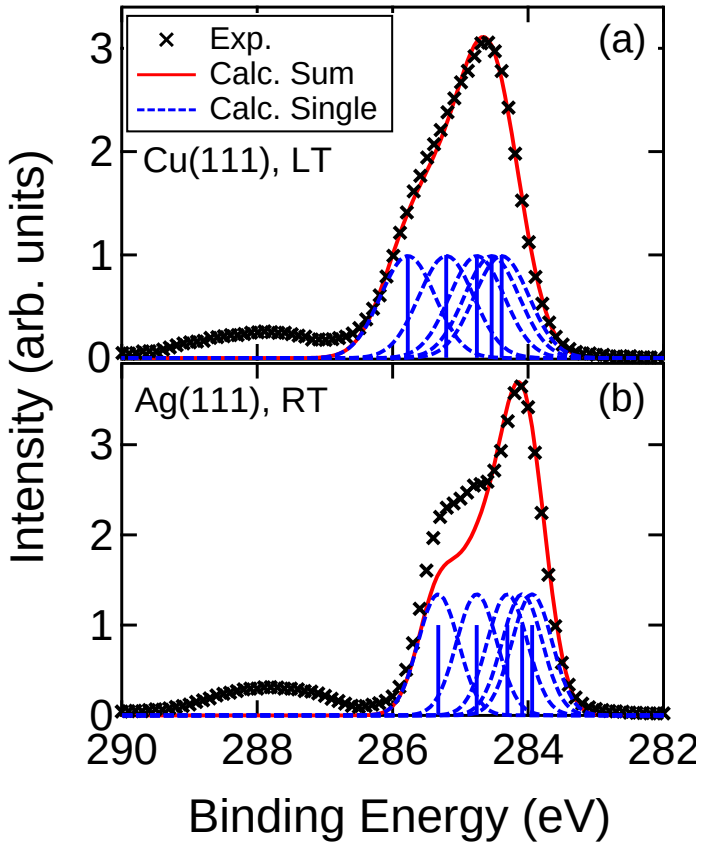

Figure 7.12: Influence of broadening values on the shape of the simulated spectra. The shape of the measured experimental data (black markers) of (a) the LT phase can be nicely reproduced by the simulation (red solid line) of a porphine monomer, using a broadening (FWHM) of 0.95 eV to obtain continuous spectra (blue dashed lines) from the calculated energies and intensities (blue bars). The sharper features of (b) the RT phase cannot be reproduced perfectly, even by applying a smaller broadening of 0.7 eV.

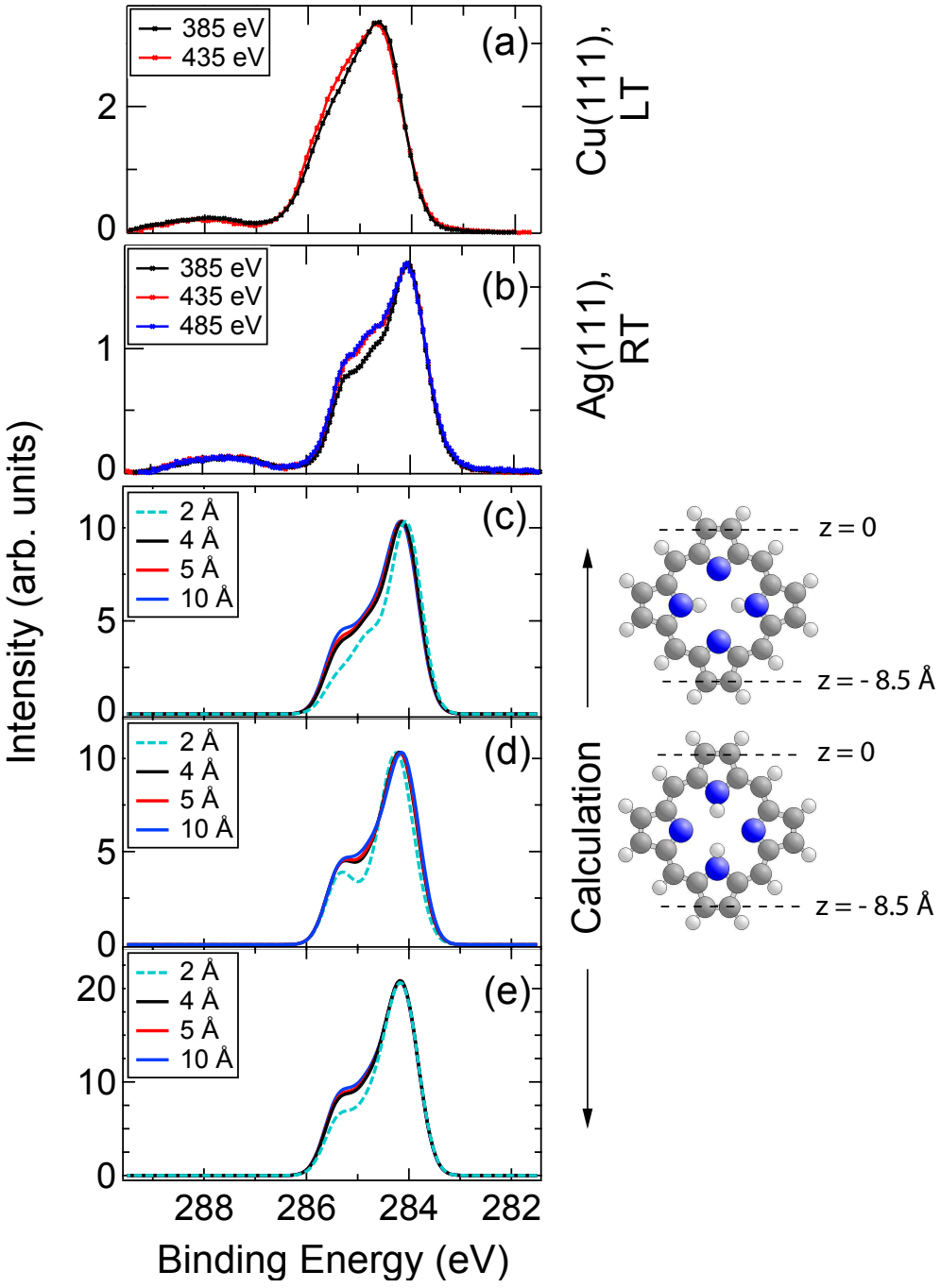

Figure 7.13: XPS C1s spectra collected at normal emission for different photon energies. (a) Multilayer on Cu(111) and (b) multilayer on Ag(111). (c)-(d) are simulated curves (FWHM = 0.75 eV) which take into account that the signal may be partly damped, depending on the orientation of the molecule (see text for details). (e) is the sum of (c) and (d).

not change the shape of the spectra, as electrons emitted from inequivalent carbon atoms have to travel the same distance in the film. For perpendicularly oriented molecules the photoemission signal from atoms at the bottom of the porphine (Fig. 7.13, right side) are attenuated due to the larger distance traveled through the material before reaching the detector. To quantify this, we performed depth-resolved XPS simulations.

To this end we considered two perpendicular orientations of the molecule: In one case one of the iminic nitrogen atoms (Fig. 7.13c), in the other case the pyrrolic nitrogen atoms (Fig. 7.13d) is closer to the surface. The topmost carbon atoms are set to $z = 0$, their signal is not damped at all. The intensity of all other atoms i at a depth z_i are modified according to

$$I = I_0 \cdot \exp\left(-\frac{z_i}{\lambda}\right) \tag{7.1}$$

where I_0 is the un-damped intensity which is always set to 1 in the simulations and λ is the attenuation length. The resulting shape for different values of λ vary for both orientations. For very short attenuation lengths ($\lambda = 2$ Å) in Fig. 7.13c (Fig. 7.13d) it can be clearly observed that the iminic (pyrrolic) contributions influence more significantly the shape of the high-energy shoulder. For larger values of λ these differences vanish, as it should be expected. As we do not know how the molecules are oriented on the surface the average of both orientations is shown as well in Fig. 7.13e.

Since the porphine is symmetric the effect of the damping is not as strong as it would be for an asymmetric molecule, because there are always weak and strong contributions from the same kind of carbon atom. This is the reason that only at small attenuation lengths differences are observed in the spectrum. Nevertheless, the trend of the photon energy dependence of the experimental curves is reproduced by the calculations and the results are consistent with the molecular orientation derived from NEXAFS spectroscopy measurements. For LT-Cu(111) samples we hardly see any dependence on the photon energy because the atomic z-values of the flatter conformation of the porphines vary less than those of the perpendicular molecules.

7.4.3 Influence of the molecular stacking

Optimization of the molecule-molecule distance

To gain insight in the driving force of the resulting molecular orientation in the multilayer films initially we considered the total energies of the possible different stacking geometries of 2H-P molecules. To this end ensembles with

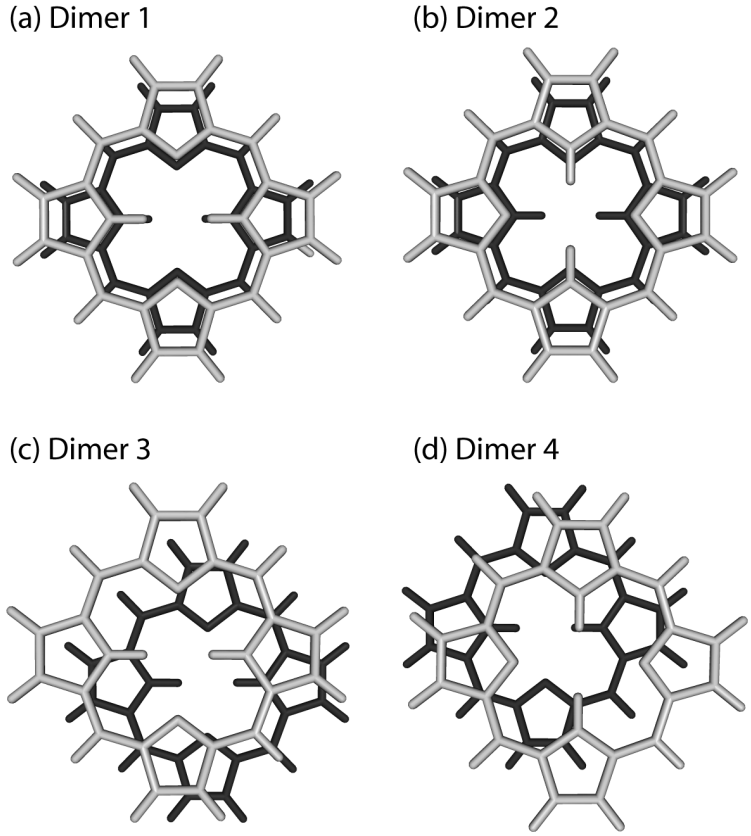

Figure 7.14: Four principal alignment configurations of parallel porphine dimers obtained from FHI-aims geometry optimizations. In all cases the top molecule is depicted in gray and the lower molecule in black. The xy-plane is defined by three C3 atoms of the lower 2H-P. See text and Table 7.4 for discussion of details.

a different number of molecules were optimized with FHI-aims using a PBE functional and the Tkatchenko-Scheffler van-der-Waals correction. StoBe is not well suited for this task as it is not possible to include van-der-Waals interactions in the simulation.

We started with the optimization of porphine dimers to keep computational costs low. The dimers were pre-optimized with tier 1 basis sets followed by an optimization at tier 2 level. The starting geometry consisted of two porphine monomers as optimized in Section 7.2 which were placed in parallel at a distance of 3 Å from each other. We tested fully symmetric starting geometries as well as a geometry where the upper molecule was rotated by 90° with respect to the lower one and also shifted the top molecule by 0.1 Å in x- and y-direction to test for (other) local minima. For these molecules stacked in parallel we obtained four motifs, as are depicted in Fig. 7.14a-d. In all four

Table 7.4: Details of the optimized dimer geometries.

		all atoms				only N			
	β	d [Å]	a_x [Å]	a_y [Å]	a [Å]	d [Å]	a_x [Å]	a_y [Å]	a [Å]
D1 tier 1	0	3.64	0.00	0.00	0.00	3.61	0.00	0.00	0.00
D1 tier 2	0	3.66	0.06	0.06	0.08	3.63	0.00	0.00	0.00
D2 tier 1	90	3.63	0.00	0.00	0.00	3.57	0.00	0.00	0.00
D2 tier 2	90	3.63	0.00	0.00	0.00	3.58	0.00	0.00	0.00
D3 tier 1	0	3.43	1.11	1.16	1.61	3.42	1.07	1.08	1.52
D3 tier 2	0	3.43	1.14	1.05	1.55	3.42	1.07	1.07	1.51
D4 tier 1	90	3.34	1.20	1.17	1.68	3.33	1.16	1.17	1.65
D4 tier 2	90	3.34	1.16	1.20	1.67	3.34	1.16	1.17	1.65

images the top 2H-P molecule is depicted in gray and the lower molecule in black. The molecules are stacked along the z-axis, i.e., the xy-plane is always defined by three C3 atoms of the lower 2H-P molecule. These configurations can be described by three variables: the molecule-molecule distance d, the displacement of the molecules in x- and y- direction a and the angle β which describes a rotation about the z-axis between the two molecules. for example Dimer 2 (Fig. 7.14b) and Dimer 4 (Fig. 7.14d) are defined by $\beta = 90°$, the others by $\beta = 0$. The definition of the distances is a bit more difficult as the porphines are not perfectly planar. One possibility would be to define planes through specified atoms of each molecule and compare the plane-to-plane distance. As this is also not unambiguous (a specified point for the evaluation has to be used) a different method is employed here: The atom coordinate averages for each molecule were calculated assuming that the deformation of the porphines is small. d and a are then defined as the distances between the averaged centers. The results are summarized in Table 7.4. a_x (a_y) is the displacement of the center in x (y), and a is given by $a = \sqrt{a_x^2 + a_y^2}$. For comparison the distances were additionally determined while only taking into account the nitrogen atoms.

Generally we found that fully symmetric (i.e., not displaced) starting configurations lead to symmetric final geometries (Fig. 7.14a and 7.14b), while a small displacement of the two molecules resulted in the configurations displayed in Fig. 7.14c and Fig. 7.14d. Hereby the geometries of dimer 1 (Fig. 7.14a) and dimer 3 (Fig. 7.14c) are defined by $\beta = 0$, while for dimer 2 (Fig. 7.14b) and dimer 4 (Fig. 7.14d) $\beta = 90°$. The distance d between dimers is

mostly consistent for both methods of determining d (i.e., by either taking all atoms or only nitrogen atoms into account). Consistently with ref. 216 the symmetrically stacked dimers (dimers 1 and 2) exhibit the biggest distance from each other (approx. 3.6 Å), while the displaced dimers show a smaller spacing (3.3-3.4 Å). In addition, it can be noted that for $\beta = 90°$ the distances are slightly smaller than for the respective unrotated configurations. The adsorption energies $E_{ad} = 2 \cdot E_{tot}^{mono} - E_{tot}^{dimer}$ of the four different dimers determined with two different basis sets are listed in Table 7.5. E_{tot}^{mono} refers to the total energy of the monomer, E_{tot}^{dimer} to that of the dimer. The way the adsorption energies are defined means that for $E_{ad} > 0$ the compound is stable, and for $E_{ad} < 0$ unstable. From the values given in Table 7.5 it follows at once that the dimers are not stable when van-der-Waals interactions are not taken into account (columns 2 and 4). Including van-der-Waals interactions (columns 3 and 5) leads to stable dimers. In full agreement with the findings by Mück-Lichtenfeld and Grimme (ref.[216]) the displaced and rotated dimer 4 is energetically the most favorable, the fully symmetric dimer 1 the least energetically favorable. The small discrepancies in absolute energies (13.6 kcal/mol, i.e., 590 meV for dimer 1 in ref. 216) can be attributed to the different description of the dispersion interaction. The values obtained in our calculation seem reasonable when compared to the values obtained by Marom et al. for NiPc and MgPc.[217] There the determined values are approximately 0.5-0.7 eV larger than the ones presented in Table 7.5, which is accounted by the stronger interacting metal center.

Since it is possible that the properties of a porphine dimer are different from those of a 2H-P molecule which is sandwiched between two or more porphines, not only dimers, but also trimers, quadromers, pentamers and an indefinite chain of stacked porphines, i.e., using periodic boundaries, are analyzed. Consistently with the dimer results, the indefinite chain of tilted molecules (corresponding to dimer 3, Fig. 3.5c and d) is more stable (Table 7.5) than the fully symmetric chain (corresponding to dimer 1, Fig. 3.5a and b). The molecule-molecule distance for fully symmetric stacked porphines does not vary much for increasing number of molecules (Table 7.6), while the adsorption energy per molecule increases. The results can partially explain the reorientation of the molecules during annealing (Fig. 7.10): The non-symmetric conformations are more favorable. This can be interpreted such that at low temperatures the completely symmetric perpendicular configuration cannot be realized. By annealing to RT the system gains energy and can transfer to the less favorable state. Once the molecules stand up in an upright position on the surface, steric

Table 7.5: Adsorption energies for the four dimers depicted in Fig. 7.14 and the symmetric and tilted chains, determined with periodic boundaries.

	Tier 2		Tier 3	
	E_{ad} [i]	E_{ad}^{vdw} [ii]	E_{ad} [i]	E_{ad}^{vdW} [ii]
Dimer 1	-319 meV	683 meV	-325 meV	677 meV
Dimer 2	-313 meV	728 meV	-320 meV	720 meV
Dimer 3	-263 meV	944 meV	-268 meV	939 meV
Dimer 4	-254 meV	954 meV	-259 meV	949 meV
Chain (symm.)	-	703 meV	-	695 meV
Chain (tilted.)	-	992 meV	-	982 meV

[i]Adsorption energy: $E_{ad} = 2 \cdot E_{tot}^{mono} - E_{tot}^{dimer}$
[ii]Including semi-empirical van-der-Waals corrections

Table 7.6: Adsorption energies and molecule-molecule distances: symmetric stacking (cf. Fig. 7.14a), geometries optimized with tier 2, energies determined with tier 2.

	Dimer	Trimer	Quadromer	Pentamer	Periodic
E_{ad} [i]	342 meV	464 meV	525 meV	562 meV	683 meV
d [ii]	3.63 Å	3.65 Å	3.63 Å	3.63 Å	3.64 Å

[i]Adsorption energy per molecule (for n molecules): $E_{ad} = (n \cdot E_{tot}^{mono} - E_{tot}^{n-mer})$/n
[ii]Periodic: size of unit cell; Rest: like in Table 7.4, only nitrogen atoms taken into account

hindrances prevent switching back to the original position. It should be noted, however that the two indefinite chains analyzed here are not the only possible configurations. While "T-stacked" monomer configurations as depicted in the middle panel in Fig. 7.8 are expected to be less stable (when extrapolating the trend obtained for the dimer calculations),[216] we do not have reference energy values of the crystal phase ("T-stacked" dimers) and for totally random orientations, so that the assumption that the molecules in the 40° LT-phase are tilted uniformly, cannot be verified with the presently available data. As next step the calculation for the adsorption energy of the crystal phase should be performed, in order to elucidate this question.

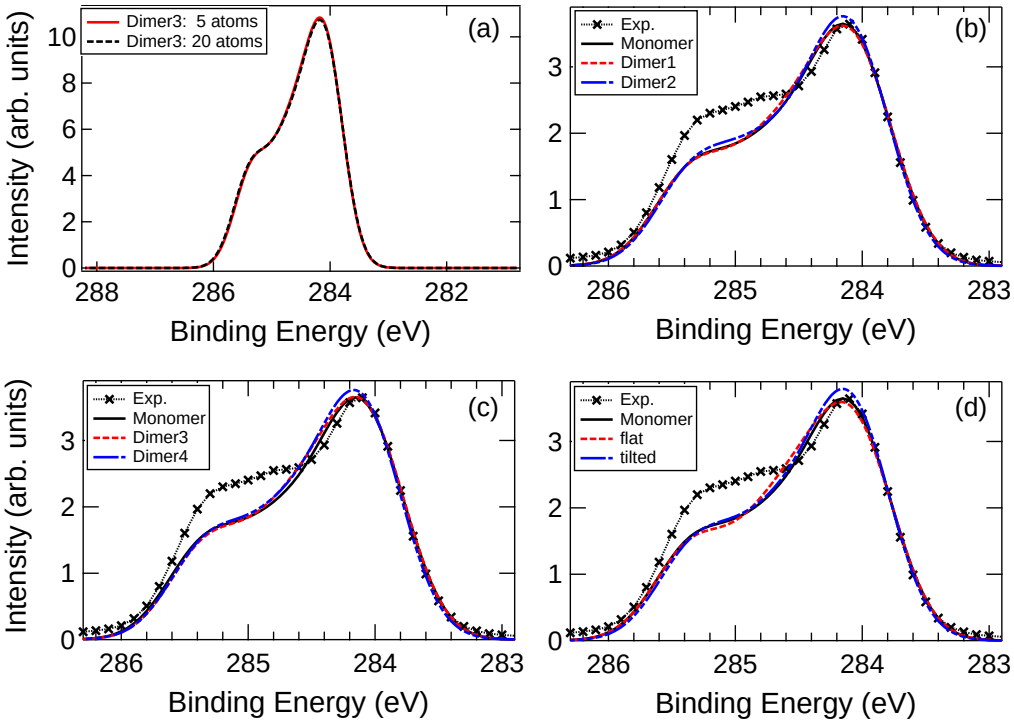

Figure 7.15: (a) Comparison between simulated XP spectra obtained by taking into account all 20 different carbon atoms of one porphine (black dashed line) and only five inequivalent carbon atoms, respectively. (b) and (c) compare the calculated XP spectra of the four porphine dimers to the spectra of the monomer (Fig. 7.2d) and to the experimental data (Fig. 7.9h). (d) displays the XPS spectra obtained from a trimer out of the optimized indefinite chains.

XPS spectra of optimized geometries

Subsequently the influence of the different stacking on the XPS spectra is analyzed. The results are presented in Fig. 7.15. Firstly, it was checked whether the assumption of only five inequivalent carbon atoms with degenerate ionization energies is justified for the dimers. The similarity between XPS spectra obtained by taking into account all 20 different carbon atoms of one porphine (Fig. 7.15a, black dashed line) and that for only five inequivalent carbon atoms (Fig. 7.15a, red solid line) shows that also for dimers it is still justified to reduce the calculation effort by only simulating the spectra of the five atoms displayed in Fig. 7.1. The simulated XPS curves of the four dimers are compared to the spectrum of the monomer and to the experimental data of a perpendicular 2H-P film in Fig. 7.15c and d. While there are small differences between the respective spectra, the modifications are certainly not big enough to explain the different shape of the measured spectrum of perpendicular porphine layers (e.g., in Fig. 7.9h). To rule out that it makes a difference whether the investi-

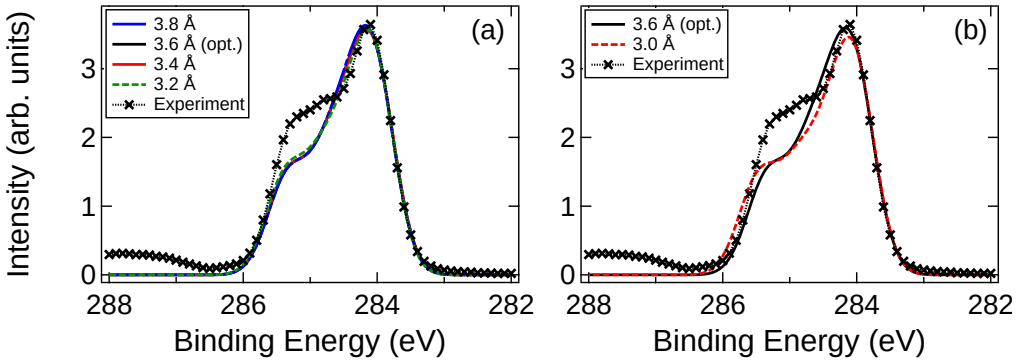

Figure 7.16: Simulated XP spectra for different molecule-molecule distances, compared to experimental data (markers). The optimized value is 3.64 Åfor an indefinite symmetric chain (cf. Fig. 3.5a and b).

gated 2H-P interacts with one or with two adjacent porphines, the next step was the calculation of XPS spectra of trimers. These trimers were cut from the indefinite symmetric and tilted chains. This method was chosen, because the creation of a core hole in the periodic system would give random total energies, as it corresponds to a system with indefinite charge. Fig. 7.15 shows that the resulting spectra do not vary much from those of the dimers. Therefore we can rule out that the differences observed in the XPS C1s data of multilayers grown at LT and RT are caused by the interaction of stacked porphines.

XPS spectra: dependence on molecule-molecule distance

Another possibility is that the porphines in the perpendicular multilayers are so close packed that the molecule-molecule distances e in the film do not correspond to the values obtained in the geometry optimizations. Therefore we evaluated the spectra at different values of d for the symmetric porphine chain (Fig. 3.5a and b). To this end the z-value of the unit cell (cf. Fig. 3.5) was kept at the desired value, followed by a relaxation of the porphine inside the unit cell. As before, a trimer was cut from the in such a way optimized indefinite chain and the ionization energies were calculated. However, the curves seem to be very stable and small variances in d hardly influence the shape of the spectra (Fig. 7.16a). Only below 3.0 Å the shape started to change (Fig. 7.16b), but as the modified spectra also do not fully agree with the experimentally derived curve and the change in distance is rather large (0.8 Å correspond to 22% of the original distance of 3.6 Å), we rule out this mechanism for the shape in Fig. 7.9h.

Table 7.7: Binding energies of oxygen and chlorine contaminants.

Substrate	T_{dosing}	T_{meas}	E_b(Cl2p$_{3/2}$)[i]	E_b(Cl2p$_{3/2}$)[i]	E_b (O1s)[ii]
Ag(111)	RT	RT	-	-	-
Ag(111)	LT	LT	198.0 eV	-	533.1 eV
Ag(111)	LT	RT	197.9 eV	-	-
Cu(111)	RT	RT	198.6 eV	-	-
Cu(111)	LT	LT	197.6 eV	201.2 eV	533.3 eV
Cu(111)	LT	RT	198.1 eV	-	-
H_2O[218]			-	-	532.9 eV
H_2O/Cu(110)[219]			-	-	533.4 eV
H_2O/Ag(111)[220]			-	-	534 eV
CO_2/Cu (chemiesorbed)[221]			-	-	531.4 eV
CO_2/Cu (physisorbed)[222, 223]			-	-	534.4-534.6 eV
CO_2/Ag (physisorbed)[223]			-	-	534.8 eV
CO/Cu[224]			-	-	533.7 eV
Cl^-/Cu[200]			198.0 eV	-	-
CuCl[200]			198.6 eV	-	-
Cl^-/Ag[200]			197.2 eV	-	-
AgCl[200]			197.9 eV	-	-
$[Au^{III}TPP]^+Cl^-$/Au(111)[58]			197.9 eV	-	-

[i]Measured at ESCAlab (cf. Fig. 7.17).
[ii]Measured at BESSY.

7.5 Role of impurities

As it was briefly mentioned before, in one of the beamtimes we discovered impurities on our cooled samples (Fig. 7.7c). The recorded O1s peaks have binding energies of 533.3 eV (Cu) and 533.1 eV (Ag) which are consistent with an adsorption of H_2O on copper and silver (Table 7.7). We can exclude that the oxygen stems from CO_2 as the binding energies for chemisorbed (physisorbed) CO_2 lie below (above) the measured values. While the binding energy of CO would agree roughly with our experimental value, the different peak structure (CO/Cu shows strong shake-up intensities) and the absence of the corresponding carbon peak excludes the possibility of carbon monoxide on our samples.

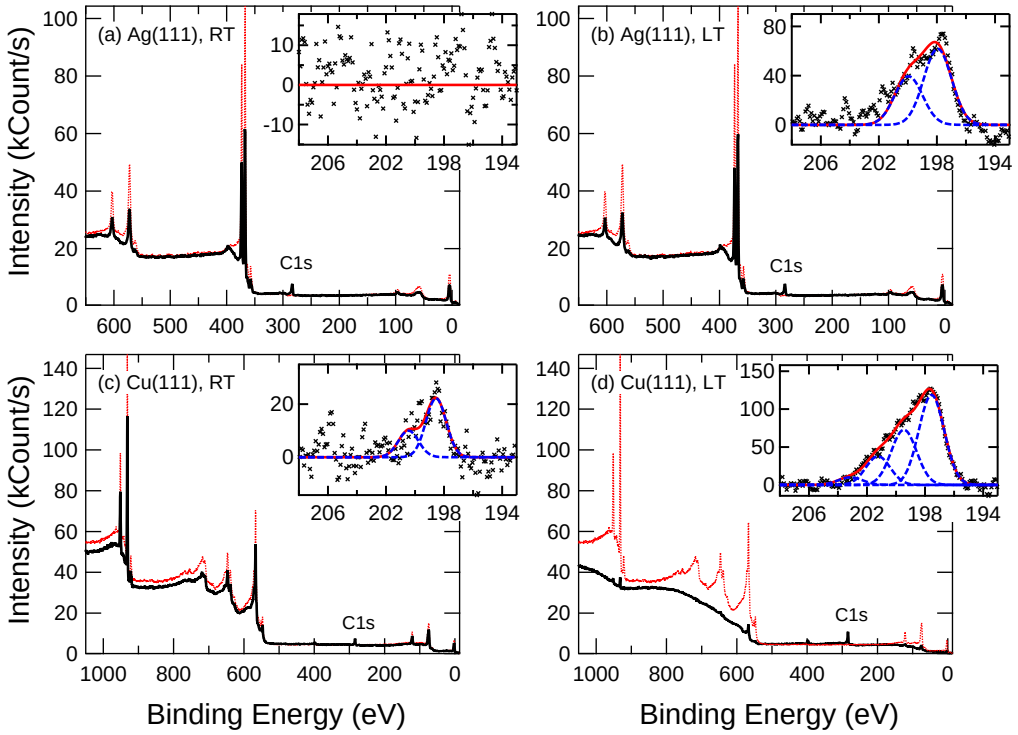

Figure 7.17: XPS overview spectra (measured at ESCAlab, $\hbar\omega = 1486.6$ eV) of the growth of 2H-P multilayers on Ag(111) and Cu(111) at room temperature (RT) and low temperature (LT). All four preparations used the same evaporation time and sublimation temperature. The red dotted line in each graph represents the respective curves of the clean substrate for comparison. The shape of the background and the relative intensities are different from the measurements at BESSY (Fig. 7.7) due to the much higher photon energy. The insets show the corresponding Cl2p. The overview data corroborate the conclusions drawn before: On Ag(111) the substrate temperature during deposition does not influence the thickness of the final layer (a and b), while on Cu(111) the growth is limited at RT (c) and unlimited at LT (d). No Cl2p could be detected for 2H-P/Ag(111) at RT (a), while at LT (b) the doublet can be clearly resolved (experiment: black markers, red solid line: overall fit, blue dashed lines: individual fitted peaks). On Cu(111) at RT (c) small traces of chlorine could be detected. The highest amount of Cl was found on the cooled copper substrate (see Table 7.8 for quantitative analysis).

Table 7.8: Quantitative analysis of Cl contaminations.

Fig.	Substrate	T_{dosing}	T_{meas}	C1s[i]	Cl2p[i]	C1s/Cl2p[ii]	Cl:2H-P[iii]
7.17a	Ag(111)	RT	RT	9607	0	-	0
7.17b	Ag(111)	LT	LT	9096	244	84.6	1:4.2
-	Ag(111)	LT	RT	9379	175	121.7	1:6.1
7.17c	Cu(111)	RT	LT	6907	56	280.0	1:14.0
7.17d	Cu(111)	LT	LT	16757	521	73.0	1:3.6
-	Cu(111)	LT	RT	16348	162	229.1	1:11.5

[i]Fitted areas after background subtraction.
[ii]Ratio of areas C1s/Cl2p, corrected for the photoionization cross sections (0.03103/0.01367 = 2.26993)[75]
[iii]Chlorine atoms per number of 2H-P molecules (20 carbon atoms)

The second unexpected species is chlorine which is not a typical residual gas in an UHV chamber. It seems to originate from the synthesis of the porphines (which are specified with 95% purity) and only occurs after the evaporation of molecules. To quantify the amount of Cl in the sample, we performed additional XPS measurements. The Cl2p spectra are displayed as insets in the corresponding overview spectra in Fig. 7.17. On Ag(111) at RT we did not find any chlorine (Fig. 7.17a), on Cu(111) at RT we observed a small amount (Fig. 7.17c), i.e., approximately one chlorine atom per 14 porphine molecules (Table 7.8). For films grown at LT a much higher amount of chlorine sticks onto the sample, for both substrates approximately one chlorine atom per four 2H-P molecules.

After annealing the LT-samples to room temperature for one night ($\sim$ 12 hours), the amount of chlorine is reduced in both cases, though it seems to stick more on Ag(111) than on Cu(111). The qualitative results are summarized in Fig. 7.19. It should be kept in mind that the quantitative analysis is not very precise because of the small intensities of the Cl. It is not clear whether the chlorine adsorbs on the substrate or onto the molecules, as the binding energies of the $Cl2p_{3/2}$ peak (Table 7.7) vary by as much as one electron-volt, and the assignment is not unambiguous. From the fact that the amount of chlorine is reduced after annealing to room temperature, while the carbon intensity remains the same, it can be concluded that the Cl is not or only weakly bound to the porphine but rather is a byproduct present in the purchased powder

sublimes together with the 2H-P molecules. The binding energies of Cl agree both with Cl^- adsorbed on Cu or Ag and with Cl^- attached to a porphyrin (Table 7.7), but certainly point to a negatively charged chlorine ion.

How does the presence of the contaminants influence the growth modes and shape of the C1s peaks? For 2H-P layers grown at RT on Ag(111) no contaminants were detected, therefore the templated perpendicular growth and the consequent change in C1s spectra truly result from the interplay between molecule-substrate and molecule-molecule interactions. The same effects can be obtained by annealing a film which has been dosed at LT, which also results in perpendicular molecules, but with chlorine present (see also summary illustrated in Fig. 7.19). Hence, the presence of Cl does not seem to influence the tilting of the molecules and therefore can be excluded as the reason for the different average angle of the layers grown on a cooled substrate.

The limited growth of 2H-P on Cu(111) at room temperature also seems to be a physical effect not based on the contaminants, as water is not present at all and chlorine only in a small percentage (one chlorine atom per 280 carbon atoms, i.e., 14 porphine molecules). We cannot rule out, however, that the presence of water on the cooled samples does not influence the tilt of the molecules, since an additional water film between the porphines may prevent the formation of the perpendicular layers.

7.6 Influence of the growth mode on the self-metalation

To study the influence of the growth mode on the self-metalation described in Chapter 4 three different samples were prepared and analyzed with XPS. The first sample is a 2H-P bilayer grown on Cu(111) at RT (Fig. 7.18a), the second a multilayer deposited at LT on the same substrate (Fig. 7.18b) and the last one a multilayer which was first deposited at LT and afterwards annealed to 300 K for 1 h (Fig. 7.18c). The N1s XPS spectra of the pristine porphine layers (top panels) show two peaks, assigned to iminic (blue) and pyrrolic (green) nitrogen species. After annealing to 393 K (middle panel), the porphines of the first two samples are fully metalated (single red peak), as it could be expected from the results in Chapter 4. However, the spectra of the molecules in the third sample, which- according to the results of Section 7.3.3- have already switched to an upright position, remain nearly unchanged. Even after raising the temperature further to 433 K (bottom panel) the film is not fully metalated. This indicates that the nitrogen atoms need the be close to the surface in order to capture a copper atom from the substrate which is prevented by the limited mobility

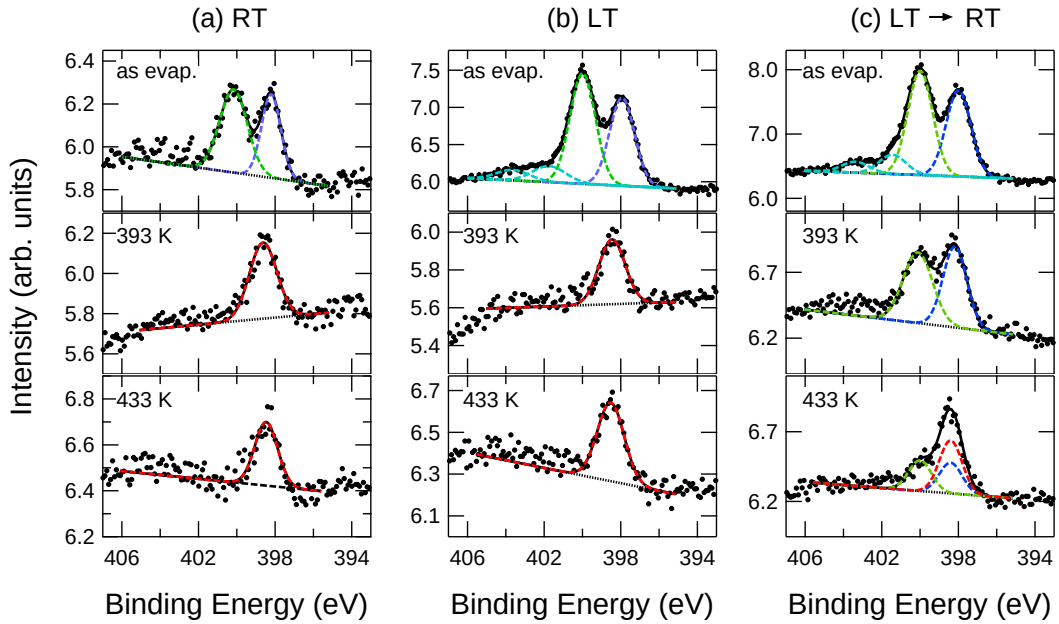

Figure 7.18: N1s XPS spectra of a Cu(111) sample with (a) a 2H-P bilayer grown at RT, (b) a multilayer grown at LT and (c) a multilayer grown at LT and annealed for 1 h to room temperature. The pristine porphine layers (top panels) show two peaks: iminic (blue) and pyrrolic (green). After annealing to 393 K (middle panel), the porphines at a) and b) are fully metalated (single red peak), while c) remains nearly unchanged. Even after annealing to 433 K (bottom panel) sample c) is not fully metalated.

of the stacked porphines. These results also indicate that the first layer of porphines in contact with the susbtrate already starts to tilt.

7.7 Summary

We characterized the growth of the most fundamental tetrapyrrole compound, the 2H-porphine (2H-P), on the coinage metal surfaces Ag(111) and Cu(111) using a combination of X-ray photoelectron spectroscopy (XPS) and near-edge X-ray absorption fine structure (NEXAFS) spectroscopy with density functional theory (DFT) calculations. Angle-resolved NEXAFS measurements reveal the adsorption geometries of the porphines: On both substrates for coverages up to one monolayer the molecules adsorb without appreciable distortion and parallel to the respective metal surface. For increasing coverage, the orientation of the molecules depends on the chosen substrate and its temperature during the growth of the films (see Fig. 7.19). Multilayers grown at low

temperatures (LT) exhibit a similar average tilting angle ($\approx 40°$) on both substrates. The corresponding carbon XP and NEXAFS curves agree very well with the simulated gas phase spectra and can therefore be easily disentangled. The calculation reveals that the carbon signals of both the XPS and the NEXAFS curves can be decomposed into two groups: peaks at lower binding energies stem from carbon atoms which only bind through C-C bonds, and a second set of peaks at higher binding energies originates from C-N bonded carbon atoms.

In contrast, a different growth behavior is observed for molecules dosed at room temperature. On Cu(111) the growth is limited to a coverage of approximately two layers, while on Ag(111) multilayers can be grown without restriction. In contrast to the orientation of 2H-P in the bulk crystal structure, the molecules in these multilayers are oriented perpendicular to the surface. The same orientation is observed for multilayers grown at 95-109 K on Cu(111) and Ag(111) surfaces, after slowly annealing to room temperature. This reorientation process is irreversible, i.e., subsequent cooling of the samples does not reverse the tilting angle back to the original configuration. Different molecular orientations result in a modified shape of the C1s XPS curves. The dependence of this shape on the incidence photon energy can be explained using depth-resolved DFT calculations by taking into account the damping caused by the different adsorption geometries. Simulations of ionization energies for differently stacked molecules show no indication for a packing-induced modification of the XPS spectra. Of special interest is the influence of the adsorption geometry on the self-metalation of the system. It was shown that self-metalation is prevented or at least hindered for the perpendicular adsorbed porphines, a fact that was attributed to the missing contact with the substrate.

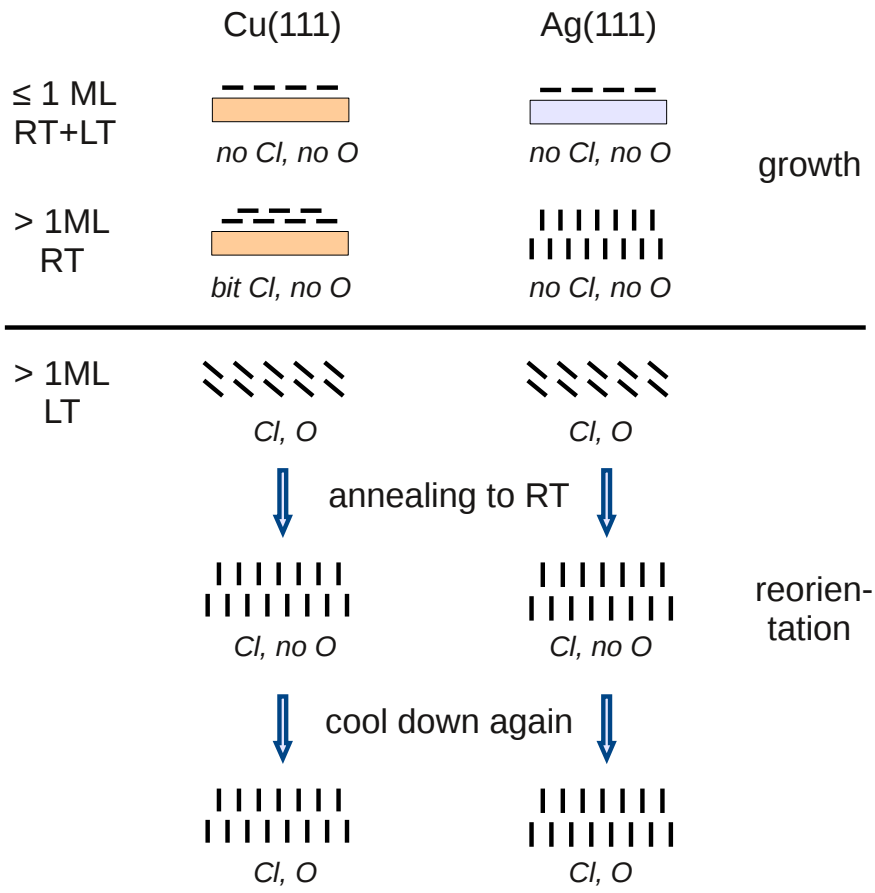

Figure 7.19: Summary of the growth and reorientation of 2H-P multilayers on Ag(111) and Cu(111) at different temperatures. Regardless of the substrate and the substrate temperature during the growth, the porphines adsorb flat and coplanar in the first layer in contact with the metal surface. For higher coverages the molecules start to tilt. At room temperature the growth is limited to a bilayer on Cu(111), while on Ag(111) growth is unlimited and the molecules take a perpendicular orientation to the surface. At low temperatures (100-130 K) no differences can be found for the two substrates: it is possible to grow very thick layers (until the substrate signal is not detectable by XPS) which exhibit an average tilt angle of 40°i.e., the molecules may be tilted uniformly as it is sketched here, or oriented in the crystal structure . When the layers are slowly annealed to room temperature, i.e., the cooling is switched off and the heating up takes place in the course of one or more hours, the molecules start to tilt until they are upright. Cooling down again does not change the orientation back to the original angle.

Chapter 8

Conclusions and Outlook

The use of surface-confined porphyrins in possible applications (e.g., in solar cells, anti-cancer drugs, nano-electronics) depends not only on their intrinsic functional properties, but is also strongly determined by their interaction with underlying atomic layers. In this work the adsorption and growth of metalated and non-metalated porphines and meso-tetraphenylporphyrins on coinage metal surfaces were comprehendively studied using a combination of X-ray spectroscopy methods and density functional theory calculations. The main focus laid on investigating how the properties, more precisely the molecular conformation and the electronic structure, of adsorbed free-base porphyrins are influenced by (i) the metalation of the macrocycle, (ii) the substituents, (iii) the substrate and (iv) the overlayer thickness, coverage and heat treatment.

Notably the free-base porphine (2H-P), as prototype tetrapyrrole mycrocyclic compound representing an ideal model system for the investigation of porphyrin-substrate interactions, was explored. This work presented a detailed insight in 2H-P on different substrates and compared its adsorption behavior to that of its phenyl substituted derivative, the free-base tetraphenylporphyrin (2H-TPP). To this end, 2H-P and 2H-TPP layers of varying thicknesses were deposited on Ag(111) and Cu(111) surfaces by organic molecular beam epitaxy (OMBE) and analyzed with XPS and angle-resolved NEXAFS spectroscopy. In a second step the free-base porphyrins have been metalated *in situ* to compare the properties of metalated and non-metalated porphyrins. Contrary to the commonly employed method of *in situ* metalation, via physical vapor deposition of the desired metal, two novel methods were introduced and/or employed in this thesis. The first is the self-metalation, i.e., the metalation of free-base porphyrins with substrate atoms of the Cu(111) surface to yield cop-

per porphine (Cu-P) and copper tetraphenylporphyrin (Cu-TPP). The second technique is the metalation via chemical vapor deposition of a ruthenium carbonyl precursor molecule on Ag(111) to yield Ru-P and Ru-TPP, which was compared to pre-synthesized Ru-(CO)TPP molecules. To conclude on the interaction between adsorbates and surface, multilayer and monolayer films were prepared. While the properties of the latter are dominated by the anchoring to the substrate, it can be assumed that only molecule-molecule interactions need to be taken into account for the analysis of the multilayer sample. One crucial point for the interpretation of the XPS and NEXAFS spectra is the peak assignment. In this work the use of DFT to simulate the corresponding spectra allowed to explain compound specific features which in turn enabled the interpretation of the spectroscopy data, which is not trivial due to the complexity of the porphyrins.

For 2H-P and 2H-TPP on Cu(111) the NEXAFS signatures differ substantially between mono- and multilayers. For both molecules a detailed peak assignment of the multilayer curves could be achieved by comparison with the computed DFT spectra, providing the necessary information for the fitting of the angle-resolved NEXAFS data. The spectra of the monolayer samples exhibit broadened features, indicating a strong interaction with the surface. In addition, the first peak in both the nitrogen and the carbon region is quenched, which points to an electron transfer from the substrate to the LUMO of the molecules. The effect is more pronounced for 2H-TPP than for 2H-P, indicating only a partial filling of the LUMO of the porphine. 2H-TPP molecules in direct contact with the Cu(111) surface adsorb in a strongly saddle-shaped geometry, i.e., a deformed macrocycle where the iminic nitrogen (=N-) atoms are pointing towards the surface, while the pyrrolic nitrogen (-NH-) atoms point upwards, combined with nearly flat phenyl rings. The different distances between the two inequivelant nitrogen atoms and the copper substrate lead to different interactions with the surface, which is reflected in different shifts of the respective N1s XPS peaks between monolayer and multilayer data. All observations point to a strong interaction of the iminic nitrogen with the surface, either by the formation of an intermediate complex or via a donation-backdonation effect. In marked contrast to the adsorption of 2H-TPP, 2H-P on Cu(111) adsorbs undeformed and parallel to the surface, highlighting the influence of the phenyl substituents on the conformation of the macrocycle. Consequently all atoms have the same distance to the substrate, leading to similar interactions with the surface for both nitrogen species. Annealing of 2H-TPP and 2H-P samples with different coverages led to gradual changes in

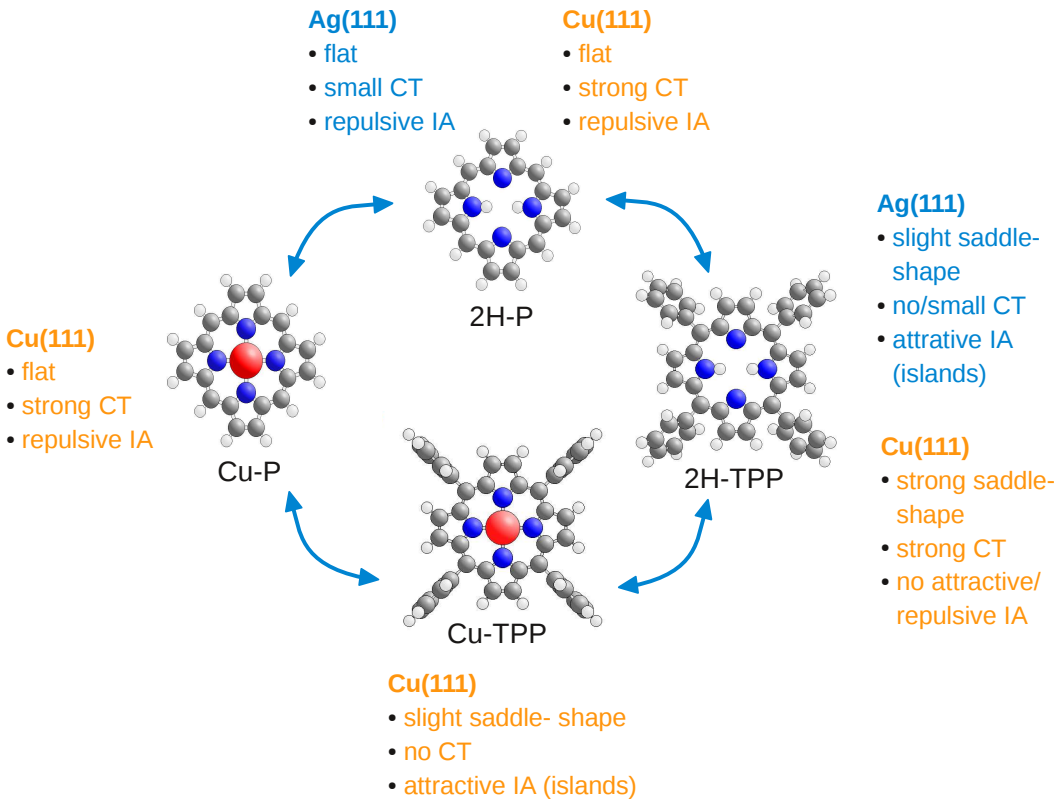

Figure 8.1: Summary of adsorption geometries, occurrence of charge transfer (CT) and net interactions (IA) between molecules in (sub)monolayer samples.

both XPS and NEXAFS spectra. DFT calculations allowed to assign these changes to the formation of Cu-TPP and Cu-P, respectively. It could be shown that it is possible to metalate more than one layer of porphyrins. The metalation of 2H-TPP to Cu-TPP leads to a change in both molecular conformation and molecule-surface interaction (see summary in Fig. 8.1): The Cu-TPP exhibits a reduced saddle-shaped deformation of the macrocycle with phenyl rings rotated out of the surface plane. Contrary to the free-base case no electron transfer to or from the molcule could be observed. For Cu-P (which remains flat), however, the NEXAFS results indicate the same interaction with the Cu(111) surface as for 2H-P, despite the lack of XPS evidence for a possible charge backdonation. This leads to the conclusion that the modified interaction of Cu-TPP with the Cu(111) surface is the result of the conformational change upon annealing: The tilted phenyl rings prevent the macrocycle from coming close to the surface, while the flat conformation of Cu-P allows a closer proximity to the substrate, which promotes charge transfer.

A second type of metalation for 2H-TPP and 2H-P on Ag(111), i.e., via the precursor molecule $Ru_3(CO)_{12}$, was analyzed with special attention to the role

of the silver substrate in the metalation process. To this end, different coverages of the free-porphyrins were exposed to $Ru_3(CO)_{12}$, followed by annealing to 550 K. For coverages of one monolayer and above, the precursor did not stick on the sample as was evidenced by XPS measurements, irrespectively of the porphyrin constituent of the molecular overlayer. The lower the molecular coverage, i.e., the larger the area of free silver, the higher was the detected amount of $Ru_3(CO)_{12}$ on the sample. Depending on this surface availability of the precursor, the free-base porphyrins were completely or partially metalated after the subsequent annealing step. The annealing temperature required for the porphyrin metalation coincided with the formation temperature of clean, metallic Ru clusters on Ag(111) by $Ru_3(CO)_{12}$. It was therefore concluded that the Ag substrate plays a catalytic role in the metalation of porphyrins by this metal carbonyl: the precursor sepcies adsorbs only on the free silver patches, where it is fully decomposed by heat treatment and therefore provides Ru adatoms active for the porphyrin metalation. We found indications for the formation of metal-organic networks resulting from annealing 2H-P in the presence of the precurser, which certainly should be verified by scanning probe techniques.

For the application in anti-cancer drugs, the oxidation state of Au-TPP is crucial. Mono- and multilayers of [Au(III)-TPP]$^+$Cl$^-$ adsorbed on a Au(111) surface were investigated by XPS with special focus on whether the oxidation state of the gold center is preserved upon adsorption. We found that to be the case for all investigated coverages. The Cl$^-$ ion was only detected in multilayer, but not in monolayer preparations. Taking into account STM measurements on the same system,[198] this result suggests a decomposition of [Au(III)-TPP]$^+$Cl$^-$ upon adsorption, followed by desorption of a large part of the Cl$^-$ ions.

The last chapter presents a comprehensive characterization of the growth of 2H-P on Ag(111) and Cu(111). On both substrates for coverages up to one monolayer the molecules adsorb undeformed and parallel to the respective metal surface. Due to the absence of attractive intermolecular forces repulsive interactions between molecules dominate, preventing an assembly in islands. For increasing coverage the orientation of the molecules depends on the substrate and its temperature during the growth of the films. Multilayers grown at low temperatures (LT) exhibit a similar average tilting angle ($\approx 40°$) on both substrates. The corresponding carbon XP and NEXAFS curves agree

very well with the simulated gas phase spectra and could therefore be disentangled. However, for molecules dosed at room temperature, a different growth behavior was observed. On Cu(111) the film thickness is limited to a coverage of approximately two layers, while on Ag(111) multilayers can be grown without restriction. In contrast to the orientation of 2H-P in the bulk crystal structure, the molecules are oriented perpendicular to the surface in these multilayers. The same orientation is observed for multilayers grown at low temperatures on both Cu(111) and Ag(111) surfaces, after annealing to room temperature. This reorientation process is irreversible, i.e., after subsequent cooling the molecules retain their upstanding conformation. Different molecular orientations result in a modified shape of the C1s XPS curves. The dependence of this shape on the incidence photon energy could be explained using depth-resolved DFT calculations. Simulations of ionization energies for differently stacked molecules showed no indication for a packing-induced modification of the XPS spectra. The molecular orientation plays an important role in the self-metalation of 2H-P/Cu(111) as the upstanding layers obtained by annealing a porphine film grown at low temperature could not, or only partially, be metalated. This suggests that the distance of the nitrogen atoms to the substrate plays an important role for the self-metalation. This conclusion may seem trivial, but as long as the mechanisms for the metalation of porphyrin multilayers remain unknown, it is not self-evident.

Generally, the results presented in this work laid the fundament for future investigations and/or applications. Of special interest are the findings for the growth of the free-base porphine, which combines the functionality of porphyrins (e.g., the possibility to be metalated) with a growth behavior similar to that of small aromatic molecules like benzene. If future experiments can confirm that, as our results indicate, the upright standing 2H-P film is well ordered, this opens the door for all applications which require oriented π-stacked layers, e.g., for application where charge transport inside films plays a crucial role (transistors, solar cells). The preparation of the horizontally stacked 2H-P layers can take place at room temperature and the films appear to be stable over a certain temperature range, which is a prerequisite for applications manufactured in a larger scale. If future experiments can confirm that (i) it is possible to metalate the upright standing 2H-Ps, (ii) they maintain their orientation upon metalation and are (iii) packed close enough, this gives the opportunity to create horizontal metal nano-wires which are not in direct contact with the metal surface. Taking into account the results derived in

Chapters 4, 5 and 7, self-metalation, as well as metalation via the $Ru_3(CO)_{12}$ precursor are not well suited for this task, so that the conventional method of dosing metal atoms on top of the porphyrins shows the greatest promise. With this approach it might even be possible to use masks for creating any desired structure.

In summary, it could be shown that each of the many contributing factors (metal center, substituents, surface, preparation conditions) that steer the complex behavior of porphyrins on surfaces can be accessed by systematic studies. A crucial point plays the analysis of free-base porphine films as it allows to conclude on the role of attached substituents. The *in situ* metalation of mono- and multilayers of free-base porphyrins is an ideal way to study the influence of the central metal atom on the molecular conformation and electronic properties. This systematic study shows the complexity that has to be taken into account when predicting the behavior of new porphyrin-substrate systems, which is a prerequisite for the rational design of functional interfaces. The advantages of the combined DFT and X-ray spectroscopy approach presented in this work are evident: Complex adsorption geometries like the strong saddle-shape of 2H-TPP/Cu(111) can not only be predicted, but even be quantified by determining the angles between small subgroups and the surface. Of course, the application of this approach is not limited to porhyrins, but can in principle be extenteded to even more complex molecular systems. The next step would be to explicitely include the influence of the surface in the simulation of the X-ray spectroscopy data. This allows to verify the conclusions drawn from experiments (regarding e.g., shifts, quenching of peaks) which are related to fundamental aspects of interface functionalization (such as charge transfer) and should therefore be of interest for the whole surface science community.

Appendix

A.1 Optimized molecule geometries

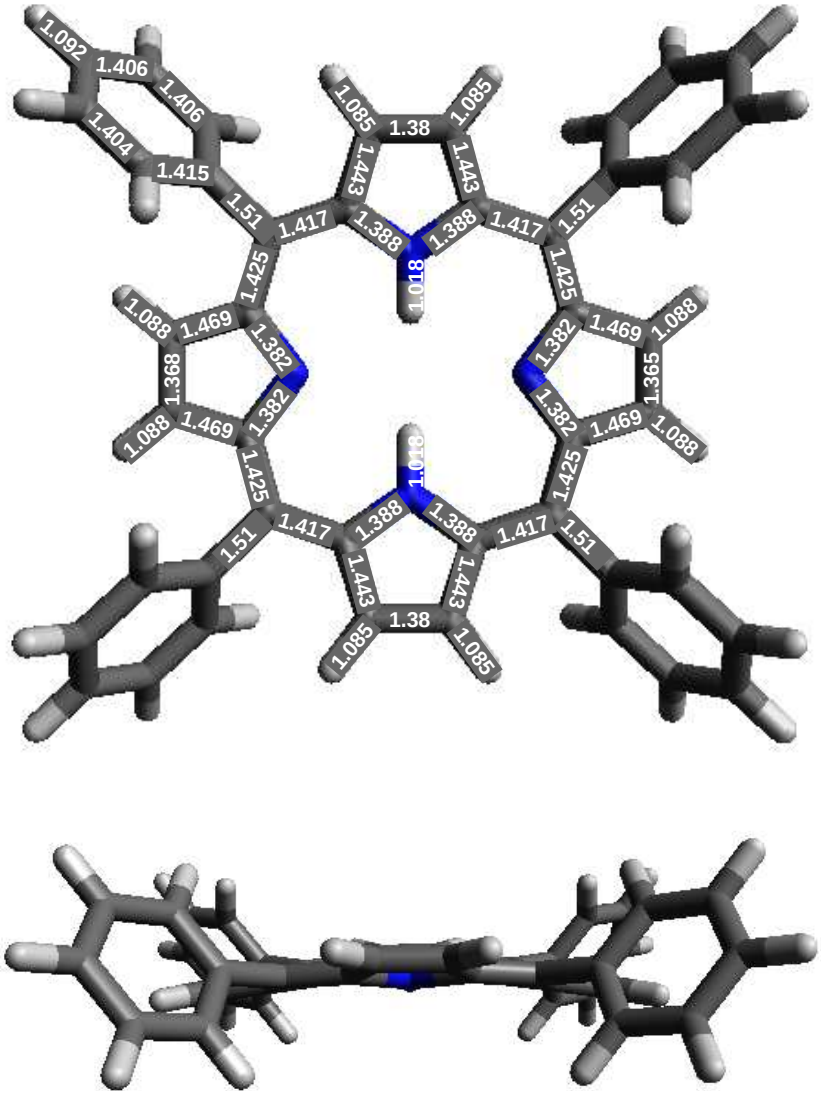

Figure A.1: Optimized geometry of 2H-TPP, optimized with StoBe using the RPBE functional, for details see Section 3.2.1 and for the color code see Fig. 1.1

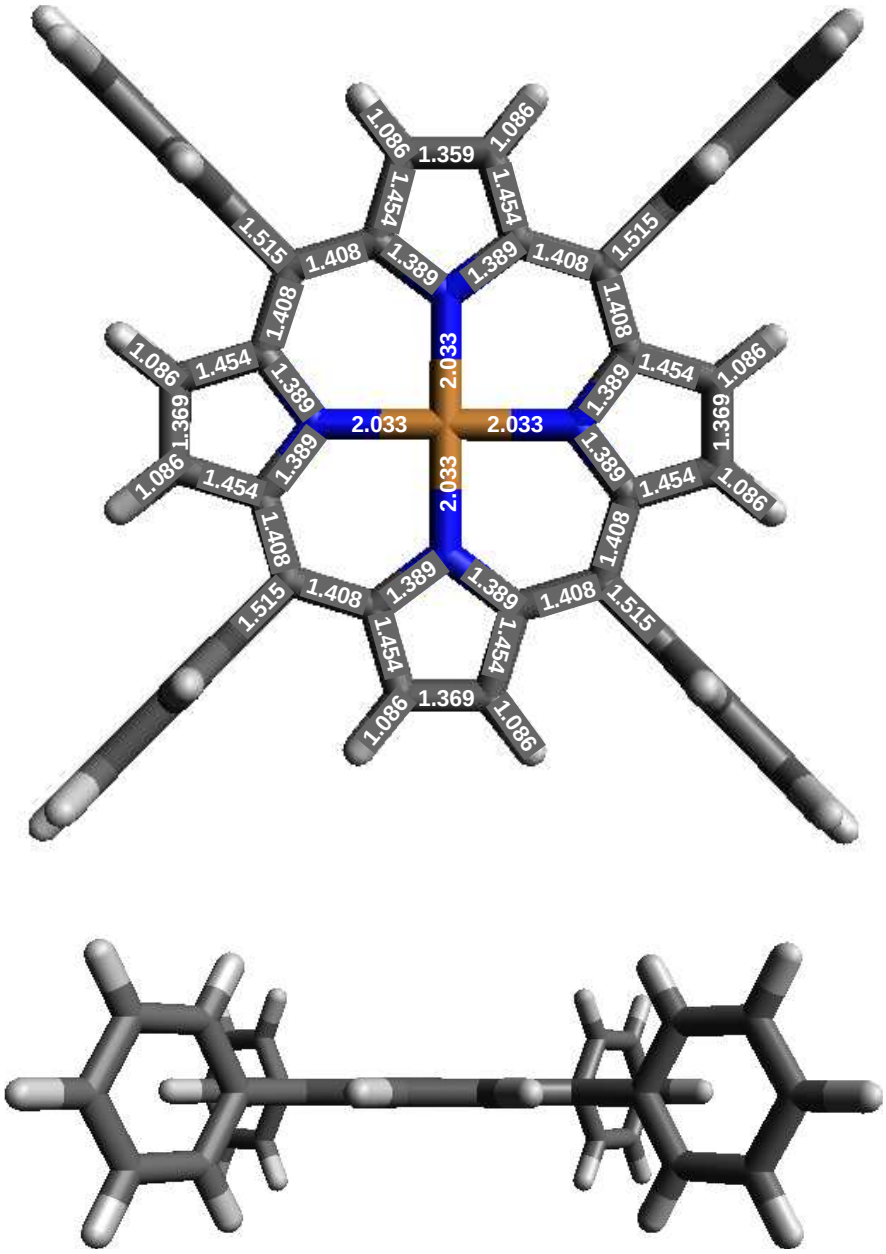

Figure A.2: Optimized geometry of Cu-TPP, optimized with StoBe using the RPBE functional, for details see Section 3.2.1 and for the color code see Fig. 1.1

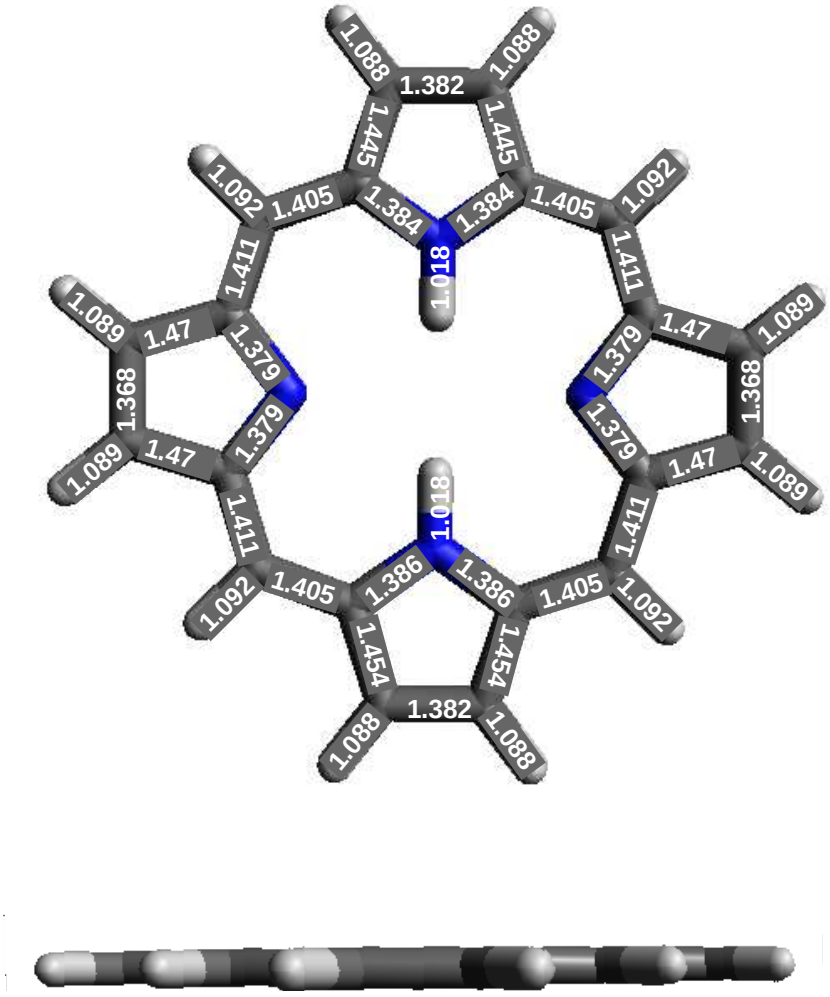

Figure A.3: Optimized geometry of 2H-P, optimized with StoBe using the RPBE functional, for details see Section 3.2.1 and for the color code see Fig. 1.1

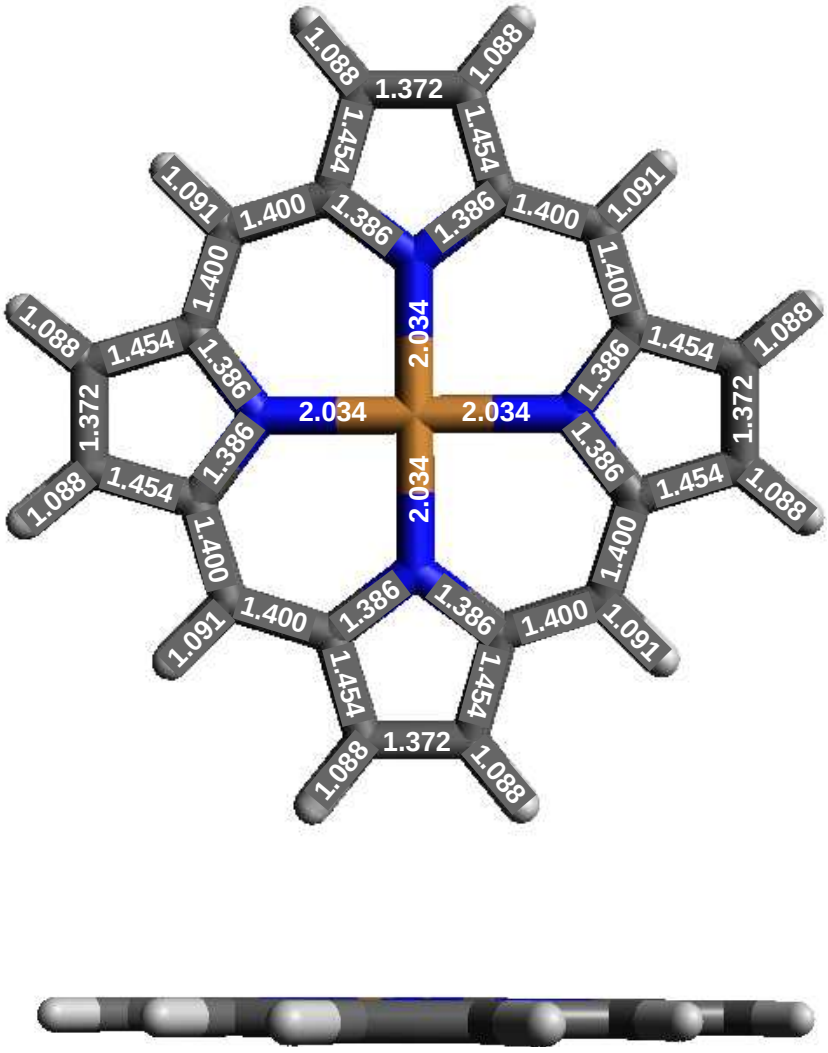

Figure A.4: , optimized with StoBe using the RPBE functional, for details see Section 3.2.1 and for the color code see Fig. 1.1

A.2 NEXAFS background subtraction

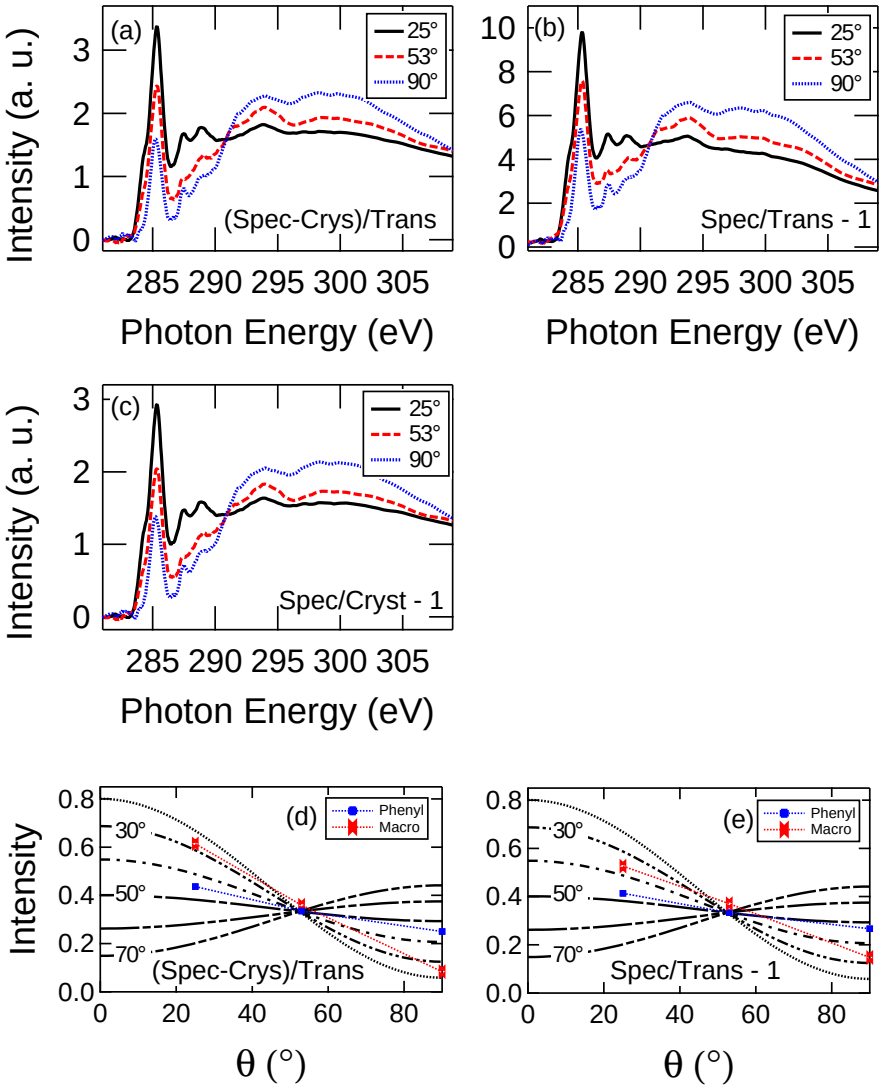

Figure A.5:

Comparison of different methods for the processing of NEXAFS data, demonstrated for the carbon spectra of a submonolayer of 2H-TPP/Ag(111) (cf. Fig. 5.5b). This coverage was chosen as the signal of the Ag(111) crystal is expected to play a bigger role for submono- than for multilayers. (a) Angle-dependent NEXAFS spectra obtained after following the procedure described in Section 3.1.3, i.e., by subtracting the signal of the bare Ag crystal ("Cryst.") and division by the transmission data ("Trans."), (b) a division by Trans. alone leads to small changes in the resulting spectra, while (c) a division by Cryst. yields identical spectra. (d) and (e) compare the angles derived from curves (a)/(c) and (b); they vary by approximately 5-8°.

A.3 2H-P/Ag(111): background subtraction

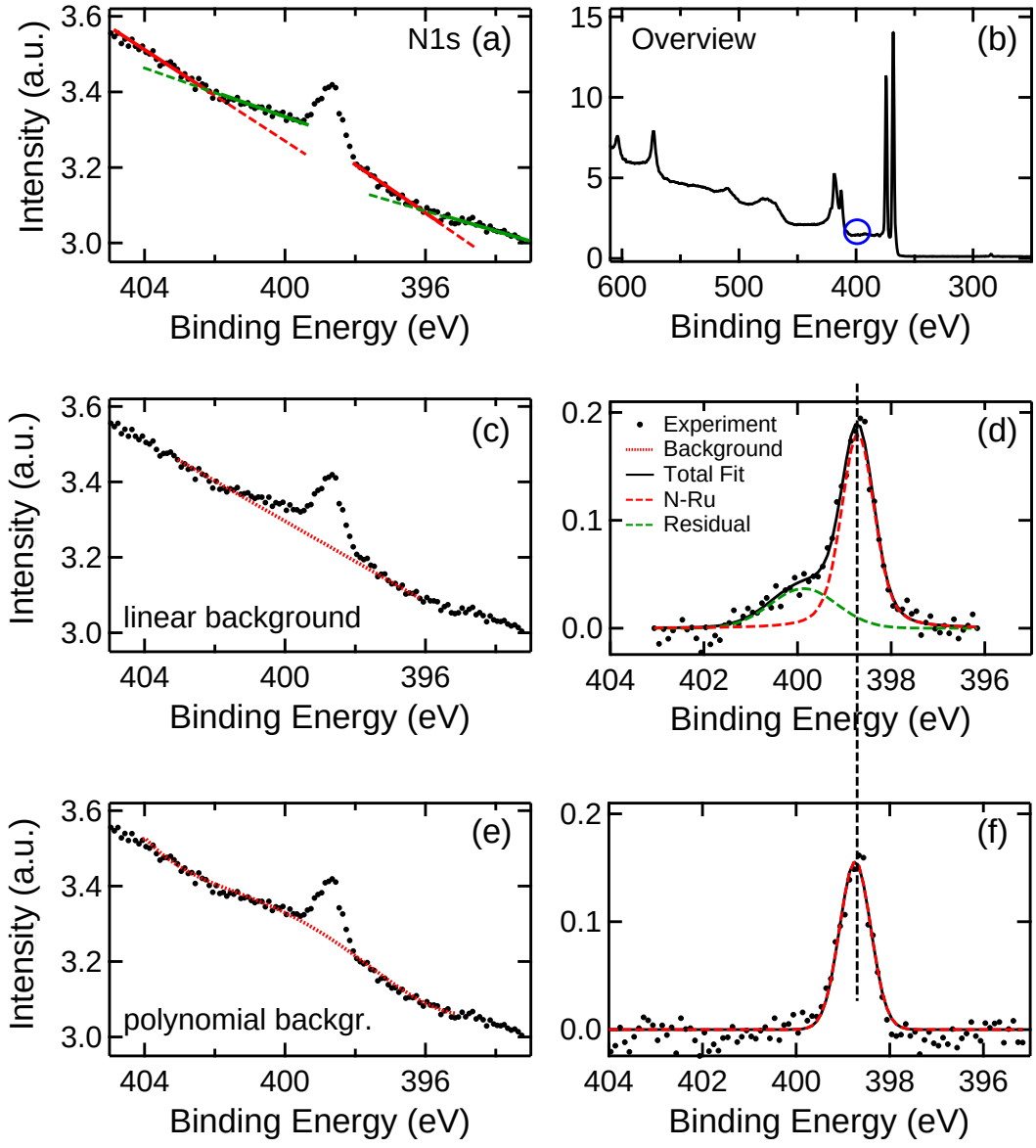

Figure A.6:

Background subtraction for the XPS N1s region of a submonolayer of Ru-TPP/Ag(111). (a) The raw data (markers) show a single peak, as it could be expected for the nitrogen region of a metalloporphyrin sample. The background is sloped; the red and green lines show that it is not possible to assign a constant slope. (b) The blue circle in the overview spectrum marks the nitrogen region, (c) Tentatively a linear background (red line) is subtracted, which results in the spectrum shown in (d). From both (b) and (c) it becomes clear, that this method is insufficient, since it leads to an artifact (green dashed line)

at 400.0 eV. (f) only the metalloporphyrin peak (red dashed line) is left after the subtraction of a slightly curved polynomial background (e, red line). For all samples in Chapter 5 with coverages in the (sub)monolayer range this type of background was used. However, one should keep in mind that this rather empirical method has to be used with caution and the raw data have to be studied carefully to avoid a loss of information by subtracting the background in this fashion. It certainly is not well-suited for the analysis of multilayers, as (i) the information on shake-up satellites would be lost and (ii) the underlying silver background is attenuated, i.e., the slope of the background is reduced (which also means that a standard background correction method can be applied.)

A.4 Used software

This section lists the software used in this thesis.

- DFT codes: *StoBe*[225] and *FHI-aims*[107]
- XPS and NEXAFS data processing and peak fitting were performed using *Igor Pro*.[120,121] All graphs containing XP and NEXAFS spectra were created with *Igor Pro*.
- Structural formulas in Figs. 4.1 and 5.1 were created with *Chemtool*[226] and *JChemPaint*[227]
- *Balsac*[228] was used to create the ball-and-stick-models in Figs. 1, 4.2, 4.3, 4.13 and 7.1.
- Output generated by *StoBe* and *FHI-aims* and the visualization programs *Molekel*[229] and *Jmol*[230] were used to create the orbital pictures in Figs. 4.7 and 7.6.
- Furthermore, *Adobe Illustrator CS2* (Version 12.0.1, 2005), *POV-Ray* (Version 3.5) and *OpenOffice* (Version 3.3.0), as well as *ASE*[231] were used to create the other graphs in this work.

List of publications

- K. Diller, F. Klappenberger, F. Allegretti, A. C. Papageorgiou, S. Fischer, A. Wiengarten, S. Joshi, K. Seufert, D. Écija, W. Auwärter, and J. V. Barth, *Investigating the molecule-substrate interaction of prototypic tetrapyrrole compounds: Adsorption and self-metalation of porphine on Cu(111)*, J. Chem. Phys., *accepted*, 2013, DOI: 10.1063/1.4800771

- F. Bischoff, K. Seufert, W. Auwärter, S. Joshi, S. Vijayaraghavan, D. Écija, K. Diller, A. C. Papageorgiou, S. Fischer, F. Allegretti, D. A. Duncan, F. Klappenberger, and J. V. Barth, *How Surface Bonding and Repulsive Interactions Cause Phase Transformations: Ordering of a Prototype Macrocyclic Compound on Ag(111)*, ACS Nano, *accepted*, 2013, DOI: 10.1021/nn305487c

- Y.-Q. Zhang, N. Kepčija, M. Kleinschrodt, K. Diller, S. Fischer, A. C. Papageorgiou, F. Allegretti, J. Björk, S. Klyatskaya, F. Klappenberger, M. Ruben and J. V. Barth, *Homo-coupling of terminal alkynes on a noble metal surface*, Nature Communications, 2012, 3:1286

- S. Fischer, A.C. Papageorgiou, M. Marschall, J. Reichert, K. Diller, F. Klappenberger, F. Allegretti, A. Nefedov, C. Wöll and J.V. Barth, *l-Cysteine on Ag(111): A combined STM and X-ray spectroscopy study of anchorage and deprotonation*, J. Phys. Chem. C, 2012, 116 (38), pp 20356–20362

- A. C. Papageorgiou, S. Fischer, J. Reichert, K. Diller, F. Blobner, F. Klappenberger, F. Allegretti, A. P. Seitsonen, and J. V. Barth, *Chemical transformations drive complex self-assembly of uracil on close-packed coinage metal surfaces*, ACS Nano, 2012, 6 (3), pp 2477–2486

- K. Diller, F. Klappenberger, M. Marschall, K. Hermann, A. Nefedov, Ch. Wöll, and J. V. Barth, *Self-metalation of 2H-tetraphenylporphyrin on Cu(111): An x-ray spectroscopy study*, J. Chem. Phys.. 136, 014705 (2012)

- S. Müllegger, W. Schöfberger, M. Rashidi, T. Lengauer, F. Klappenberger, K. Diller, K. Kara, J.V. Barth, E. Rauls, W.G. Schmidt and R. Koch, *Preserving Charge and Oxidation State of Au(III) Ions in an Agent-Functionalized Nanocrystal Model System*, ACS Nano, 2011, 5(8), pp 6480-6486
- W. Krenner, F. Klappenberger, D. Kühne, K. Diller, Z. Qu. M. Ruben and J.V. Barth, *Positioning of Single Co Atoms Steered by a Self-Assembled Organic Molecular Template*, J. Phys. Chem. Lett. 2011, 2, 1639-1645

Bibliography

[1] C. B. Duke, *The birth and evolution of surface science: Child of the union of science and technology*, Proceedings of the National Academy of Sciences **100**, 3858–3864 (2003). (cit. on p. 1)

[2] K. Oura, V. Lifshits, A. Saranin, A. Zotov, and M. Katayama, *Surface Science- An Introduction*, Springer, 2003. (cit. on pp. 1, 9, 10, 12, 30, 32 and 39)

[3] E. V. Anslyn, *Supramolecular Analytical Chemistry*, J. Org. Chem. **72**, 687–699 (2007). (cit. on p. 1)

[4] C. Joachim, J. Gimzewski, and A. Aviram, *Electronics using hybrid-molecular and mono-molecular devices*, Nature **408**, 541–548 (2000). (cit. on p. 1)

[5] S. R. Forrest, *Ultrathin Organic Films Grown by Organic Molecular Beam Deposition and Related Techniques*, Chem. Rev. **97**, 1793–1896 (1997). (cit. on p. 1)

[6] J. S. Lindsey, V. Chandrashaker, M. Taniguchi, and M. Ptaszek, *Abiotic formation of uroporphyrinogen and coproporphyrinogen from acyclic reactants*, New J. Chem. **35**, 65–75 (2011). (cit. on p. 1)

[7] H. Imahori, M. Kimurac, K. Hosomizua, and S. Fukuzumi, *Porphyrin and fullerene-based photovoltaic devices*, Journal of Photochemistry and Photobiology A: Chemistry **166**, 57–62 (2004). (cit. on p. 1)

[8] L.-L. Li and E. W.-G. Diau, *Porphyrin-sensitized solar cells*, Chem. Soc. Rev. **42**, 291–304 (2013). (cit. on p. 1)

[9] P. Avenier, M. Taoufik, A. Lesage, X. Solans-Monfort, A. Baudouin, A. de Mallmann, L. Veyre, J.-M. Basset,

O. Eisenstein, L. Emsley, and E. A. Quadrelli, *Dinitrogen Dissociation on an Isolated Surface Tantalum Atom*, Science **317**, 1056–1060 (2007). (cit. on p. 1)

[10] C. Copéret, M. Chabanas, R. Petroff Saint-Arroman, and J.-M. Basset, *Homogeneous and heterogeneous catalysis: Bridging the gap through surface organometallic chemistry*, Angewandte Chemie International Edition **42**, 156–181 (2003). (cit. on p. 1)

[11] D. Heim, K. Seufert, W. Auwärter, C. Aurisicchio, C. Fabbro, D. Bonifazi, and J. V. Barth, *Surface-Assisted Assembly of Discrete Porphyrin-Based Cyclic Supramolecules*, Nano Lett. **10**, 122–128 (2010). (cit. on pp. 2 and 3)

[12] K. Seufert, W. Auwärter, and J. V. Barth, *Discriminative Response of Surface-Confined Metalloporphyrin Molecules to Carbon and Nitrogen Monoxide*, J. Am. Chem. Soc. **132**, 18141–18146 (2010). (cit. on p. 2)

[13] K. Seufert, M.-L. Bocquet, W. Auwärter, A. Weber-Bargioni, J. Reichert, N. Lorente, and J. V. Barth, *Cis-dicarbonyl binding at cobalt and iron porphyrins with saddle-shape conformation*, Nat Chem **3**, 114–119 (2011). (cit. on pp. 2 and 96)

[14] I. Fleming, *Absolute Configuration and the Structure of Chlorophyll*, Nature **216**, 151–152 (1967). (cit. on p. 2)

[15] C. E. Castro, *Theory of hemeprotein reactivity*, J. theor. Biol. **33**, 475–490 (1971). (cit. on p. 2)

[16] J. V. Barth, *Fresh perspectives for surface coordination chemistry*, Surf. Sci. **603**, 1533–1541 (2009). (cit. on p. 2)

[17] W. Hieringer, K. Flechtner, A. Kretschmann, K. Seufert, W. Auwärter, J. V. Barth, A. Görling, H.-P. Steinrück, and J. M. Gottfried, *The Surface Trans Effect: Influence of Axial Ligands on the Surface Chemical Bonds of Adsorbed Metalloporphyrins*, J. Am. Chem. Soc. **133**, 6206–6222 (2011). (cit. on p. 2)

[18] C. Wäckerlin, D. Chylarecka, A. Kleibert, K. Müller, C. Iacovita, F. Nolting, T. A. Jung, and N. Ballav, *Controlling spins in adsorbed molecules by a chemical switch*, Nat Commun **1**, 61 (2010). (cit. on p. 2)

[19] K. Leung, S. B. Rempe, P. A. Schultz, E. M. Sproviero, V. S. Batista, M. E. Chandross, and C. J. Medforth, *Density Functional Theory and DFT+U Study of Transition Metal Porphines Adsorbed on Au(111) Surfaces and Effects of Applied Electric Fields*, J. Am. Chem. Soc. **128**, 3659–3668 (2006). (cit. on p. 2)

[20] T. Lukasczyk, K. Flechtner, L. R. Merte, N. Jux, F. Maier, J. M. Gottfried, and H.-P. Steinrück, *Interaction of Cobalt(II) Tetraarylporphyrins with a Ag(111) Surface Studied with Photoelectron Spectroscopy*, J. Phys. Chem. C **111**, 3090–3098 (2007). (cit. on pp. 2, 96 and 111)

[21] T. Yokoyama, T. Kamikado, S. Yokoyama, and S. Mashiko, *Conformation selective assembly of carboxyphenyl substituted porphyrins on Au (111)*, J. Chem. Phys. **121**, 11993–11997 (2004). (cit. on p. 3)

[22] J. A. A. W. Elemans, R. van Hameren, R. J. M. Nolte, and A. E. Rowan, *Molecular Materials by Self-Assembly of Porphyrins, Phthalocyanines, and Perylenes*, Adv. Mater **18**, 1251–1266 (2006). (cit. on p. 3)

[23] S. Koiry, P. Jha, D. Aswal, S. Nayak, C. Majumdar, S. Chattopadhyay, S. Gupta, and J. Yakhmi, *Diodes based on bilayers comprising of tetraphenyl porphyrin derivative and fullerene for hybrid nanoelectronics*, Chem. Phys. Lett. **485**, 137–141 (2010). (cit. on p. 3)

[24] N. A. Rakow and K. S. Suslick, *A colorimetric sensor array for odour visualization*, Nature **406**, 710–713 (2000). (cit. on p. 3)

[25] D. Filippini, A. Alimelli, C. Di Natale, R. Paolesse, A. D'Amico, and I. Lundström, *Chemical Sensing with Familiar Devices*, Angew. Chem. Int. Ed. **45**, 3800–3803 (2006). (cit. on p. 3)

[26] B. Meunier, *Metalloporphyrins as versatile catalysts for oxidation reactions and oxidative DNA cleavage*, Chem. Rev. **92**, 1411–1456 (1992). (cit. on p. 3)

[27] I. Mochida, K. Suetsugu, H. Fujitsu, and K. Takeshita, *Enhanced catalytic activity of cobalt tetraphenylporphyrin on titanium dioxide by evacuation at elevated temperatures for intensifying the complex-support interaction*, J. Phys. Chem. **87**, 1524–1529 (1983). (cit. on p. 3)

[28] I. Bhugun, D. Lexa, and J.-M. Savéant, *Homogeneous Catalysis of Electrochemical Hydrogen Evolution by Iron(0) Porphyrins*, J. Am. Chem. Soc. **118**, 3982–3983 (1996). (cit. on p. 3)

[29] R. W.-Y. Sun, D.-L. Ma, E. L.-M. Wong, and C.-M. Che, *Some uses of transition metal complexes as anti-cancer and anti-HIV agents*, Dalton Trans. **0**, 4884–4892 (2007). (cit. on pp. 3 and 107)

[30] R. W.-Y. Sun and C.-M. Che, *The anti-cancer properties of gold(iii) compounds with dianionic porphyrin and tetradentate ligands*, Coord. Chem. Rev. **253**, 1682–1691 (2009). (cit. on p. 3)

[31] M. A. Baldo, D. F. O'Brien, Y. You, A. Shoustikov, S. Sibley, M. E. Thompson, and S. R. Forrest, *Highly efficient phosphorescent emission from organic electroluminescent devices*, Nature **395**, 151–154 (1998). (cit. on p. 3)

[32] W. M. Campbell, A. K. Burrell, D. L. Officer, and K. W. Jolley, *Porphyrins as light harvesters in the dye-sensitised TiO2 solar cell*, Coord. Chem. Rev. **248**, 1363–1379 (2004). (cit. on p. 3)

[33] A. Yella, H.-W. Lee, H. N. Tsao, C. Yi, A. K. Chandiran, M. Nazeeruddin, E. W.-G. Diau, C.-Y. Yeh, S. M. Zakeeruddin, and M. Grätzel, *Porphyrin-Sensitized Solar Cells with Cobalt (II/III)-Based Redox Electrolyte Exceed 12 Percent Efficiency*, Science **334**, 629–634 (2011). (cit. on p. 3)

[34] T. Hasobe, S. Fukuzumi, and P. V. Kamat, *Hierarchical Assembly of Porphyrins and Fullerenes for Solar Cells*, The Electrochemical Society Interface **15**, 47 (2006). (cit. on p. 3)

[35] J.-H. Yum, P. Chen, M. Grätzel, and M. K. Nazeeruddin, *Recent Developments in Solid-State Dye-Sensitized Solar Cells*, ChemSusChem **1**, 699–707 (2008). (cit. on p. 3)

[36] M. J. Griffith, K. Sunahara, P. Wagner, K. Wagner, G. G. Wallace, D. L. Officer, A. Furube, R. Katoh, S. Mori, and A. J. Mozer, *Porphyrins for dye-sensitised solar cells: new insights into efficiency-determining electron transfer steps*, Chem. Commun. **48**, 4145–4162 (2012). (cit. on p. 3)

[37] T. A. Jung, R. R. Schlittler, and J. K. Gimzewski, *Conformational identification of individual adsorbed molecules with the STM*, Nature **386**, 696–698 (1997). (cit. on p. 3)

[38] F. Buchner, K. Flechtner, Y. Bai, E. Zillner, I. Kellner, H.-P. Steinrück, H. Marbach, and J. M. Gottfried, *Coordination of Iron Atoms by Tetraphenylporphyrin Monolayers and Multilayers on Ag(111) and Formation of Iron-Tetraphenylporphyrin*, J. Phys. Chem. C **112**, 15458–15465 (2008). (cit. on pp. 3, 4, 60, 61 and 100)

[39] T. Yokoyama, S. Yokoyama, T. Kamikado, and S. Mashiko, *Nonplanar adsorption and orientational ordering of porphyrin molecules on Au(111)*, J. Chem. Phys. **115**, 3814 (2001). (cit. on pp. 3 and 71)

[40] W. Auwärter, A. Weber-Bargioni, A. Riemann, A. Schiffrin, O. Gröning, R. Fasel, and J. V. Barth, *Self-assembly and conformation of tetrapyridyl-porphyrin molecules on Ag(111)*, J. Chem. Phys. **124**, 194708 (2006). (cit. on pp. 3, 49 and 71)

[41] D. Écija, M. Trelka, C. Urban, P. d. Mendoza, E. Mateo-Martí, C. Rogero, J. A. Martín-Gago, A. M. Echavarren, R. Otero, J. M. Gallego, and R. Miranda, *Molecular Conformation, Organizational Chirality, and Iron Metalation of meso-Tetramesitylporphyrins on Copper(100)*, J. Phys. Chem. C **112**, 8988–8994 (2008). (cit. on pp. 3, 50 and 59)

[42] W. Auwärter, A. Weber-Bargioni, S. Brink, A. Riemann, A. Schiffrin, M. Ruben, and J. V. Barth, *Controlled Metalation of Self-Assembled Porphyrin Nanoarrays in Two Dimensions*, ChemPhysChem **8**, 250–254 (2007). (cit. on pp. 3, 5, 50, 59 and 60)

[43] S. A. Krasnikov, N. N. Sergeeva, Y. N. Sergeeva, M. O. Senge, and A. A. Cafolla, *Self-assembled rows of Ni porphyrin dimers on the Ag(111) surface*, Phys. Chem. Chem. Phys. **12**, 6666–6671 (2010). (cit. on pp. 3 and 71)

[44] W. Auwärter, F. Klappenberger, A. Weber-Bargioni, A. Schiffrin, T. Strunskus, C. Wöll, Y. Pennec, A. Riemann, and J. V. Barth, *Conformational Adaptation and Selective Adatom Capturing of Tetrapyridyl-porphyrin Molecules on a Copper (111) Surface*, J. Am. Chem. Soc. **129**, 11279–11285 (2007). (cit. on pp. 3, 5, 42, 49, 55 and 70)

[45] L. Zotti, G. Teobaldi, W. Hofer, W. Auwärter, A. Weber-Bargioni, and J. Barth, *Ab-initio calculations and STM observations*

on tetrapyridyl and Fe(II)-tetrapyridyl-porphyrin molecules on Ag(111), Surf. Sci. **601**, 2409–2414 (2007). (cit. on p. 3)

[46] S. Tanaka, H. Suzuki, T. Kamikado, and S. Mashiko, *Conformational study of porphyrin-based molecules using non-contact atomic force microscopy*, Nanotechnology **15**, S87– (2004). (cit. on p. 3)

[47] S. Morikawa, C. Ikeda, K. Ogawa, and Y. Kobuke, *Two-Dimensional Porphyrin Array Assembled by Self-Coordination*, Letters in Organic Chemistry **1**, 6–11 (2004). (cit. on p. 3)

[48] F. Bischoff, K. Seufert, W. Auwärter, S. Joshi, S. Vijaraghavan, D. Écija, K. Diller, A. C. Papageorgiou, S. Fischer, F. Allegretti, D. A. Duncan, F. Klappenberger, and J. V. Barth, *How Surface Bonding and Repulsive Interactions Cause Phase Transformations: Ordering of a Prototype Macrocyclic Compound on Ag(111)*, ACS Nano **7**, 3139–3149 (2013). (cit. on pp. 3, 6, 74, 77, 82 and 128)

[49] F. Klappenberger, A. Weber-Bargioni, W. Auwärter, M. Marschall, A. Schiffrin, and J. V. Barth, *Temperature dependence of conformation, chemical state, and metal-directed assembly of tetrapyridyl-porphyrin on Cu(111)*, J. Chem. Phys. **129**, 214702 (2008). (cit. on pp. 4, 54, 70, 79, 88, 96 and 111)

[50] S. A. Krasnikov, N. N. Sergeeva, M. M. Brzhezinskaya, A. B. Preobrajenski, Y. N. Sergeeva, N. A. Vinogradov, A. A. Cafolla, M. O. Senge, and A. S. Vinogradov, *An x-ray absorption and photoemission study of the electronic structure of Ni porphyrins and Ni N-confused porphyrin*, J. Phys.: Condens. Matter **20**, 235207 (2008). (cit. on pp. 4, 67, 87 and 105)

[51] J. M. Gottfried, K. Flechtner, A. Kretschmann, T. Lukasczyk, and H.-P. Steinrück, *Direct Synthesis of a Metalloporphyrin Complex on a Surface*, J. Am. Chem. Soc. **128**, 5644–5645 (2006). (cit. on pp. 4, 5, 10, 50, 56, 59, 60, 77, 79, 100 and 113)

[52] A. Kretschmann, M.-M. Walz, K. Flechtner, H.-P. Steinrück, and J. M. Gottfried, *Tetraphenylporphyrin picks up zinc atoms from a silver surface*, Chem. Commun. **-**, 568–570 (2007). (cit. on p. 4)

[53] A. Weber-Bargioni, W. Auwärter, F. Klappenberger, J. Reichert, S. Lefrancois, T. Strunskus, C. Wöll, A. Schiffrin,

Y. Pennec, and J. V. Barth, *Visualizing the Frontier Orbitals of a Conformationally Adapted Metalloporphyrin*, ChemPhysChem **9**, 89–94 (2008). (cit. on p. 4)

[54] W. Auwärter, K. Seufert, F. Klappenberger, J. Reichert, A. Weber-Bargioni, A. Verdini, D. Cvetko, M. Dell'Angela, L. Floreano, A. Cossaro, G. Bavdek, A. Morgante, A. P. Seitsonen, and J. V. Barth, *Site-specific electronic and geometric interface structure of Co-tetraphenyl-porphyrin layers on Ag(111)*, Phys. Rev. B **81**, 245403– (2010). (cit. on pp. 4, 42, 49, 70 and 97)

[55] T. E. Shubina, H. Marbach, K. Flechtner, A. Kretschmann, N. Jux, F. Buchner, H. Steinrück, T. Clark, and J. M. Gottfried, *Principle and Mechanism of Direct Porphyrin Metalation: Joint Experimental and Theoretical Investigation*, J. Am. Chem. Soc. **129**, 9476–9483 (2007). (cit. on pp. 5, 50, 56, 59, 60, 61, 79 and 100)

[56] K. Diller, F. Klappenberger, M. Marschall, K. Hermann, A. Nefedov, C. Wöll, and J. V. Barth, *Self-metalation of 2H-tetraphenylporphyrin on Cu(111): An x-ray spectroscopy study*, J. Chem. Phys. **136**, 014705–13 (2012). (cit. on pp. 6, 51, 74, 77, 79, 81, 85 and 116)

[57] K. Diller, F. Klappenberger, F. Allegretti, A. C. Papageorgiou, S. Fischer, A. Wiengarten, S. Joshi, K. Seufert, D. Écija, W. Auwärter, and J. V. Barth, *Investigating the molecule-substrate interaction of prototypic tetrapyrrole compounds: Adsorption and self-metalation of porphine on Cu(111)*, J. Chem. Phys., (2013). accepted, DOI: 10.1063/1.4800771. (cit. on pp. 6 and 51)

[58] S. Müllegger, W. Schöfberger, M. Rashidi, T. Lengauer, F. Klappenberger, K. Diller, K. Kara, J. V. Barth, E. Rauls, W. G. Schmidt, and R. Koch, *Preserving Charge and Oxidation State of Au(III) Ions in an Agent-Functionalized Nanocrystal Model System*, ACS Nano **5**, 6480–6486 (2011). (cit. on pp. 6, 32, 107, 109 and 142)

[59] S. Hüfner, *Photoelectron Spectroscopy*, Springer, 3rd ed., 2003. (cit. on pp. 7, 9 and 13)

[60] M. Briggs, David & Seah, ed., *Practical Surface Analysis. Volume 1: Auger and X-ray Photoelectron Spectroscopy*, Wiley, 2nd ed., 1990. (cit. on pp. 7, 11 and 39)

[61] J. Stöhr, *NEXAFS Spectroscopy*, Springer, 1992. (cit. on pp. 7, 14, 15, 16, 41, 61, 65 and 83)

[62] W. Koch and M. Holthausen, *A Chemist's Guide to Density Functional Theory*, Wiley, 2nd ed., 2008. (cit. on pp. 7, 19, 22, 23, 24 and 25)

[63] H. Hertz, *Ueber den Einfluss des ultravioletten Lichtes auf die electrische Entladung*, Ann. Phys. **267**, 983–1000 (1887). (cit. on p. 7)

[64] A. Einstein, *Über einen die Erzeugung und Verwandlung des Lichtes betreffenden heuristischen Gesichtspunkt*, Ann. Phys. **322**, 132–148 (1905). (cit. on p. 7)

[65] C. Nordling, E. Sokolowski, and K. Siegbahn, *Precision Method for Obtaining Absolute Values of Atomic Binding Energies*, Phys. Rev. **105**, 1676–1677 (1957). (cit. on p. 7)

[66] *http://nobelprize.org/nobel_prizes/physics/laureates/1981/*. (cit. on p. 8)

[67] C. N. Berglund and W. E. Spicer, *Photoemission Studies of Copper and Silver: Experiment*, Phys. Rev. **136**, A1044–A1064 (1964). (cit. on p. 8)

[68] C. N. Berglund and W. E. Spicer, *Photoemission Studies of Copper and Silver: Theory*, Phys. Rev. **136**, A1030–A1044 (1964). (cit. on p. 8)

[69] U. Gelius, *Binding Energies and Chemical Shifts in ESCA*, Phys. Scr. **9**, 133 (1974). (cit. on p. 10)

[70] C. Powell, *Recommended Auger parameters for 42 elemental solids*, J. Electron Spectrosc. Relat. Phenom. **185**, 1–3 (2012). (cit. on p. 10)

[71] C. Sleigh, A. Pijpers, A. Jaspers, B. Coussens, and R. J. Meier, *On the determination of atomic charge via ESCA including application to organometallics*, J. Electron Spectrosc. Relat. Phenom. **77**, 41–57 (1996). (cit. on p. 10)

[72] Y. Niwa, H. Kobayashi, and T. Tsuchiya, *X-ray photoelectron spectroscopy of tetraphenylporphin and phthalocyanine*, J. Chem. Phys. **60**, 799–807 (1974). (cit. on pp. 10, 52, 54, 56, 77, 79 and 113)

[73] T.-C. Chiang, G. Kaindl, and T. Mandel, *Layer-resolved shifts of photoemission and Auger spectra from physisorbed rare-gas multilayers*, Phys. Rev. B **33**, 695– (1986). (cit. on pp. 10, 54, 79 and 96)

[74] F. Schwabl, *Quantenmechanik- Eine Einführung*, Springer, 7th ed., 2007. (cit. on pp. 10 and 13)

[75] J. Yeh and I. Lindau, *Atomic subshell photoionization cross sections and asymmetry parameters: $1 < z < 103$*, Atomic Data and Nuclear Data Tables **32**, 1–155 (1985). (cit. on pp. 12 and 144)

[76] Y. F. Chen, C. M. Kwei, and T. C. J., *Electron inelastic mean free paths versus attenuation lengths in solids*, J. Phys. D: Appl. Phys. **25**, 262– (1992). (cit. on p. 12)

[77] M. P. Seah and W. A. Dench, *Quantitative electron spectroscopy of surfaces*, Surf. Interface Anal. **1**, 2 – 11 (1979). (cit. on pp. 12, 35 and 132)

[78] C. Kolczewski, R. Püttner, O. Plashkevych, H. Ågren, V. Staemmler, M. Martins, G. Snell, A. S. Schlachter, M. Sant'Anna, G. Kaindl, and L. G. M. Pettersson, *Detailed study of pyridine at the C 1s and N 1s ionization thresholds: The influence of the vibrational fine structure*, J. Chem. Phys. **115**, 6426–6437 (2001). (cit. on pp. 15, 26 and 27)

[79] C. Kolczewski and K. Hermann, *Ab initio DFT cluster studies of angle-resolved NEXAFS spectra for differently coordinated oxygen at the V2O5(0 1 0) surface*, Surf. Sci. **552**, 98–110 (2004). (cit. on p. 15)

[80] R. Püttner, C. Kolczewski, M. Martins, A. S. Schlachter, G. Snell, M. Sant'Anna, J. Viefhaus, K. Hermann, and G. Kaindl, *The C 1s NEXAFS spectrum of benzene below threshold: Rydberg or valence character of the unoccupied σ-type orbitals*, Chem. Phys. Lett. **393**, 361–366 (2004). (cit. on p. 15)

[81] N. Schmidt, R. Fink, and W. Hieringer, *Assignment of near-edge x-ray absorption fine structure spectra of metalloporphyrins by means of time-dependent density-functional calculations*, J. Chem. Phys. **133**, 054703–13 (2010). (cit. on pp. 15, 58, 65, 67, 70, 72, 83, 85, 96, 116 and 121)

[82] L. Triguero, L. G. M. Pettersson, and H. Ågren, *Calculations of near-edge x-ray-absorption spectra of gas-phase and chemisorbed molecules by means of density-functional and transition-potential theory*, Phys. Rev. B **58**, 8097 (1998). (cit. on pp. 15, 26 and 27)

[83] M. Born and R. Oppenheimer, *Zur Quantentheorie der Molekeln*, Ann. Phys. **389**, 457–484 (1927). (cit. on p. 19)

[84] L. H. Thomas, *The calculation of atomic fields*, Mathematical Proceedings of the Cambridge Philosophical Society **23**, 542–548 (1927). (cit. on p. 19)

[85] E. Fermi, *Un metodo statistico per la determinazione di alcune priorieta dell'atome*, Rend. Accad. Naz. Lincei **6**, 602–607 (1927). (cit. on p. 19)

[86] E. Fermi, *Eine statistische Methode zur Bestimmung einiger Eigenschaften des Atoms und ihre Anwendung auf die Theorie des periodischen Systems der Elemente*, Zeitschrift für Physik **48**, 73–79– (1928). (cit. on p. 19)

[87] E. Teller, *On the Stability of Molecules in the Thomas-Fermi Theory*, Rev. Mod. Phys. **34**, 627–631 (1962). (cit. on p. 19)

[88] P. Hohenberg and W. Kohn, *Inhomogeneous Electron Gas*, Phys. Rev. **136**, B864–B871 (1964). (cit. on p. 19)

[89] W. Kohn and L. J. Sham, *Self-Consistent Equations Including Exchange and Correlation Effects*, Phys. Rev. **140**, A1133–A1138 (1965). (cit. on pp. 20 and 22)

[90] J. Kohanoff, *Electronic Structure Calculations for Solids and Molecules*, Cambridge University Press, 2006. (cit. on pp. 21, 22, 23, 25 and 26)

[91] D. M. Ceperley and B. J. Alder, *Ground State of the Electron Gas by a Stochastic Method*, Phys. Rev. Lett. **45**, 566–569 (1980). (cit. on p. 22)

[92] S. H. Vosko, L. Wilk, and M. Nusair, *Accurate spin-dependent electron liquid correlation energies for local spin density calculations: a critical analysis*, Can. J. Phys. **58**, 1200 (1980). (cit. on p. 22)

[93] J. P. Perdew and A. Zunger, *Self-interaction correction to density-functional approximations for many-electron systems*, Phys. Rev. B **23**, 5048–5079 (1981). (cit. on p. 22)

[94] J. P. Perdew and Y. Wang, *Accurate and simple analytic representation of the electron-gas correlation energy*, Phys. Rev. B **45**, 13244–13249 (1992). (cit. on p. 22)

[95] J. P. Perdew, K. Burke, and M. Ernzerhof, *Generalized Gradient Approximation Made Simple*, Phys. Rev. Lett. **77**, 3865–3868 (1996). (cit. on pp. 23 and 42)

[96] B. Hammer, L. B. Hansen, and J. K. Nørskov, *Improved adsorption energetics within density-functional theory using revised Perdew-Burke-Ernzerhof functionals*, Phys. Rev. B **59**, 7413–7421 (1999). (cit. on pp. 23 and 42)

[97] A. D. Becke, *A new mixing of Hartree-Fock and local density-functional theories*, J. Chem. Phys. **98**, 1372–1377 (1993). (cit. on p. 23)

[98] A. D. Becke, *Density-functional thermochemistry. III. The role of exact exchange*, J. Chem. Phys **98**, 5648–5652 (1993). (cit. on p. 23)

[99] J. Paier, M. Marsman, K. Hummer, G. Kresse, I. C. Gerber, and J. G. Angyan, *Screened hybrid density functionals applied to solids*, J. Chem. Phys. **124**, 154709–13 (2006). (cit. on p. 23)

[100] P. J. Stephens, F. J. Devlin, C. F. Chabalowski, and M. J. Frisch, *Ab Initio Calculation of Vibrational Absorption and Circular Dichroism Spectra Using Density Functional Force Fields*, J. Phys. Chem. **98**, 11623–11627 (1994). (cit. on p. 23)

[101] C. C. J. Roothaan, *New Developments in Molecular Orbital Theory*, Rev. Mod. Phys. **23**, 69–89 (1951). (cit. on p. 24)

[102] G. te Velde, F. M. Bickelhaupt, E. J. Baerends, C. Fonseca Guerra, S. J. A. van Gisbergen, J. G. Snijders, and T. Ziegler, *Chemistry with ADF*, J. Comput. Chem. **22**, 931–967 (2001). (cit. on p. 24)

[103] A. Szabo and N. S. Ostlund, *Modern quantum chemistry*, Dover, 1996. (cit. on p. 25)

[104] *StoBe is a modified version of the DFT-LCGTO program package DeMon, originally developed by A. St.-Amant and D. Salahub (University of Montreal), with extensions by K. Hermann and L.G.M. Pettersson.* (cit. on pp. 24 and 42)

[105] K. Hermann and L. G. M. Pettersson, *Stobe Manual*. http://www.rz-berlin.mpg.de/ hermann/StoBe/StoBeMAN.html. (cit. on p. 25)

[106] N. Godbout, D. R. Salahub, J. Andzelm, and E. Wimmer, *Optimization of Gaussian-type basis sets for local spin density functional calculations. Part I. Boron through neon, optimization technique and validation*, Can. J. Chem. **70(2)**, 560–571 (1992). (cit. on p. 25)

[107] V. Blum, R. Gehrke, H. Felix, H. Paula, H. Ville, R. Xinguo, R. Karsten, and S. Matthias, *Ab initio molecular simulations with numeric atom-centered orbitals*, Computer Physics Communications **180**, 2175–2196 (2009). (cit. on pp. 26, 45 and 161)

[108] O. Takahashi and L. G. M. Pettersson, *Functional dependence of core-excitation energies*, J. Chem. Phys. **121**, 10339–10345 (2004). (cit. on pp. 27 and 44)

[109] R. A. van Santen and P. Sautet, eds., *Computational Methods in Catalysis and Materials Science*, Wiley-VCH, 2009. (cit. on p. 27)

[110] J. C. Slater, *Statistical Exchange-Correlation in the Self-Consistent Field*, Adv. Quant. Chem. **6**, 1–92 (1972). (cit. on p. 27)

[111] J. C. Slater and K. H. Johnson, *Self-Consistent-Field $X\alpha$ Cluster Method for Polyatomic Molecules and Solids*, Phys. Rev. B **5**, 844–853 (1972). (cit. on p. 27)

[112] M. Stener, A. Lisini, and P. Decleva, *Density functional calculations of excitation energies and oscillator strengths for C1s $\rightarrow \pi^*$ and O1s $\rightarrow \pi^*$ excitations and ionization potentials in carbonyl containing molecules*, Chem. Phys. **191**, 141–154 (1995). (cit. on p. 27)

[113] C.-H. Hu and D. P. Chong, *Density functional computations for inner-shell excitation spectroscopy*, Chem. Phys. Lett. **262**, 729–732 (1996). (cit. on p. 27)

[114] S. Grimme, *Density functional theory with London dispersion corrections*, WIREs Comput Mol Sci **1**, 211–228 (2011). (cit. on p. 27)

[115] C. D. Sherrill, T. Takatani, and E. G. Hohenstein, *An Assessment of Theoretical Methods for Nonbonded Interactions: Comparison to Complete Basis Set Limit Coupled-Cluster Potential Energy Curves for the Benzene Dimer, the Methane Dimer, Benzene-Methane, and Benzene-H2S*, J. Phys. Chem. A **113**, 10146–10159 (2009). (cit. on p. 27)

[116] A. Tkatchenko and M. Scheffler, *Accurate molecular van der waals interactions from ground-state electron density and free-atom reference data*, Phys. Rev. Lett. **102**, 073005– (2009). (cit. on p. 28)

[117] Q. Wu and W. Yang, *Empirical correction to density functional theory for van der Waals interactions*, J. Chem. Phys. **116**, 515–524 (2002). (cit. on p. 28)

[118] S. Grimme, *Semiempirical GGA-type density functional constructed with a long-range dispersion correction*, J. Comput. Chem. **27**, 1787–1799 (2006). (cit. on p. 28)

[119] M. S. Van Dusen, *Platinum-Resistance Theometry at Low Temperatures*, J. Am. Chem. Soc. **47**, 326–332 (1925). (cit. on p. 33)

[120] WaveMetrics Inc., *Igor Pro, Version 6.2.2.2*, (2011). http://www.wavemetrics.com/. (cit. on pp. 38 and 161)

[121] F. Klappenberger and K. Diller, *Package for the analysis of XPS and NEXAFS data with IgorPro (WaveMetrics, Inc.). Versions 3 and 4 (NEXAFS) and version 1.10 (XPS), E20, TU München.* (cit. on pp. 38 and 161)

[122] A. Thompson, D. Attwood, E. Gullikson, M. Howells, K.-J. Kim, J. Kirz, J. Kortright, I. Lindau, Y. Liu, P. Pianetta, A. Robinson, J. Scofield, J. Underwood, and G. Wiliams, *X-ray data booklet*, Lawrence Berkeley National Labaratory, University of California, 3rd ed., 2009. http://xdb.lbl.gov/. (cit. on pp. 38, 96, 98 and 109)

[123] D. A. Shirley, *High-Resolution X-Ray Photoemission Spectrum of the Valence Bands of Gold.*, Phys. Rev. B **5**, 4709–4714 (1972). (cit. on p. 39)

[124] T. H. Dunning, *Gaussian Basis Functions for Use in Molecular Calculations. III. Contraction of (10s6p) Atomic Basis Sets for the First-Row Atoms*, J. Chem. Phys. **55**, 716 (1971). (cit. on p. 42)

[125] S. Huzinaga, *Gaussian-Type Functions for Polyatomic Systems. I*, J. Chem. Phys. **42**, 1293 (1965). (cit. on p. 42)

[126] E. B. Fleischer, *The Structure of Copper Tetraphenylporphine*, J. Am. Chem. Soc. **85**, 1353–1354 (1963). (cit. on p. 43)

[127] E. B. Fleischer, *Structure of porphyrins and metalloporphyrins*, Accounts Chem. Res. **3**, 105–112 (1970). (cit. on p. 43)

[128] E. B. Fleischer, C. K. Miller, and L. E. Webb, *Crystal and Molecular Structures of Some Metal Tetraphenylporphines*, J. Am. Chem. Soc. **86**, 2342–2347 (1963). (cit. on p. 43)

[129] W. Kutzelnigg, U. Fleischer, and M. Schindler, *The IGLO-Method: Ab-initio Calculation and Interpretation of NMR Chemical Shifts and Magnetic Susceptibilities.*, in: NMR Basic Principles and Progress, Springer Verlag, Berlin/Heidelberg **23**, 165 (1991). (cit. on p. 43)

[130] L. G. M. Pettersson, U. Wahlgren, and O. Gropen, *Effective core potential parameters for first- and second-row atoms*, J. Chem. Phys. **86**, 2176–2184 (1987). (cit. on p. 43)

[131] L. G. M. Pettersson, U. Wahlgren, and O. Gropen, *Effective core potential calculations using frozen orbitals. Applications to transition metals*, Chem. Phys. **80**, 7–16 (1983). (cit. on p. 43)

[132] H. Ågren, V. Carravetta, O. Vahtras, and L. G. M. Pettersson, *Direct SCF direct static-exchange calculations of electronic spectra*, Theoretica Chimica Acta **97**, 14 (1997). (cit. on p. 44)

[133] G. Rojas, S. Simpson, X. Chen, D. A. Kunkel, J. Nitz, J. Xiao, P. A. Dowben, E. Zurek, and A. Enders, *Surface state engineering of molecule-molecule interactions*, Phys. Chem. Chem. Phys. **14**, 4971–4976 (2012). (cit. on pp. 49, 85, 88 and 100)

[134] J. Brede, M. Linares, R. Lensen, A. E. Rowan, M. Funk, M. Broring, G. Hoffmann, and R. Wiesendanger, *Adsorption and conformation of porphyrins on metallic surfaces*, J. Vac. Sci. Technol. B **27**, 799–804 (2009). (cit. on pp. 49 and 70)

[135] G. Di Santo, C. Castellarin-Cudia, M. Fanetti, B. Taleatu, P. Borghetti, L. Sangaletti, L. Floreano, E. Magnano, F. Bondino, and A. Goldoni, *Conformational Adaptation and Electronic Structure of 2H-Tetraphenylporphyrin on Ag(111) during Fe Metalation*, J. Phys. Chem. C **115**, 4155–4162 (2011). (cit. on pp. 50, 54, 56, 58, 59, 60, 61, 77, 79, 85, 96, 111, 116 and 128)

[136] K. Diller, *Diploma thesis: Untersuchung von H2-TPP-Schichten auf einer Cu(111)-Oberfläche mit Hilfe von Röntgenphotoelektronenspektroskopie und Dichtefunktionatheorie-Rechnungen, TU München*, 2009. (cit. on p. 50)

[137] R. González-Moreno, C. Sánchez-Sánchez, M. Trelka, R. Otero, A. Cossaro, A. Verdini, L. Floreano, M. Ruiz-Bermejo, A. García-Lekue, J. Martín-Gago, and C. Rogero,

Following the Metalation Process of Protoporphyrin IX with Metal Substrate Atoms at Room Temperature, J. Phys. Chem. C **115**, 6849–6854 (2011). (cit. on pp. 50, 60 and 93)

[138] J. P. Macquet, M. M. Millard, and T. Theophanides, *X-ray photoelectron spectroscopy of porphyrins*, J. Am. Chem. Soc. **100**, 4741–4746 (1978). (cit. on p. 52)

[139] D. H. Karweik and N. Winograd, *Nitrogen charge distributions in free-base porphyrins, metalloporphyrins, and their reduced analogs observed by x-ray photoelectron spectroscopy*, Inorg. Chem. **15**, 2336–2342 (1976). (cit. on p. 54)

[140] R. Dippel, D. P. Woodruff, X. M. Hu, M. C. Asensio, A. W. Robinson, K. M. Schindler, K. U. Weiss, P. Gardner, and A. M. Bradshaw, *Adsorbate structures from photoelectron diffraction: Holographic reconstruction or real-space triangulation?*, Phys. Rev. Lett. **68**, 1543–1546 (1992). (cit. on p. 55)

[141] K. U. Weiss, R. Dippel, K. M. Schindler, P. Gardner, V. Fritzsche, A. M. Bradshaw, A. L. D. Kilcoyne, and D. P. Woodruff, *Chemical shift photoelectron diffraction from molecular adsorbates*, Phys. Rev. Lett. **69**, 3196–3199 (1992). (cit. on p. 55)

[142] C. J. Hirschmugl, K. M. Schindler, O. Schaff, V. Fernandez, A. Theobald, P. Hofmann, A. M. Bradshaw, R. Davis, N. A. Booth, D. P. Woodruff, and V. Fritzsche, *Quantitative structure determination of an NHx species adsorbed on Cu(110)*, Surf. Sci. **352**, 232–237 (1996). (cit. on p. 55)

[143] M. Eichberger, M. Marschall, J. Reichert, A. Weber-Bargioni, W. Auwärter, R. L. C. Wang, H. J. Kreuzer, Y. Pennec, A. Schiffrin, and J. V. Barth, *Dimerization Boosts One-Dimensional Mobility of Conformationally Adapted Porphyrins on a Hexagonal Surface Atomic Lattice*, Nano Lett. **8**, 4608–4613 (2008). (cit. on p. 55)

[144] L. Scudiero, D. E. Barlow, and K. W. Hipps, *Physical Properties and Metal Ion Specific Scanning Tunneling Microscopy Images of Metal(II) Tetraphenylporphyrins Deposited from Vapor onto Gold (111)*, J. Phys. Chem. B **104**, 11899–11905 (2000). (cit. on pp. 56 and 79)

[145] A. D. Zhao, Q. X. Li, L. Chen, H. J. Xiang, W. H. Wang, S. Pan, B. Wang, X. D. Xiao, J. L. Yang, J. G. Hou, and Q. S. Zhu, *Controlling the Kondo effect of an adsorbed magnetic ion through its chemical bonding*, Science **309**, 1542–1544 (2005). (cit. on p. 56)

[146] M. Ruben, D. Payer, A. Landa, A. Comisso, C. Gattinoni, N. Lin, J. P. Collin, J. P. Sauvage, A. De Vita, and K. Kern, *2D supramolecular assemblies of benzene-1,3,5-triyl-tribenzoic acid: Temperature-induced phase transformations and hierarchical organization with macrocyclic molecules*, J. Am. Chem. Soc. **128**, 15644–15651 (2006). (cit. on p. 56)

[147] A. Sperl, J. Kröger, and R. Berndt, *Controlled Metalation of a Single Adsorbed Phthalocyanine*, Angew. Chem. Int. Ed. **123**, 5406–5409 (2011). (cit. on p. 56)

[148] M. E. Cañas-Ventura, F. Klappenberger, S. Clair, S. Pons, K. Kern, H. Brune, T. Strunskus, C. Wöll, R. Fasel, and J. V. Barth, *Coexistence of one- and two-dimensional supramolecular assemblies of terephthalic acid on Pd(111) due to self-limiting deprotonation*, J. Chem. Phys. **125**, 184710–8 (2006). (cit. on p. 56)

[149] M. Chen, X. Feng, L. Zhang, H. Ju, Q. Xu, J. Zhu, J. M. Gottfried, K. Ibrahim, H. Qian, and J. Wang, *Direct Synthesis of Nickel(II) Tetraphenylporphyrin and Its Interaction with a Au(111) Surface: A Comprehensive Study*, J. Phys. Chem. C **114**, 9908–9916 (2010). (cit. on pp. 58, 59 and 60)

[150] S. Narioka, H. Ishii, Y. Ouchi, T. Yokoyama, T. Ohta, and K. Seki, *XANES Spectroscopic Studies of Evaporated Porphyrin Films: Molecular Orientation and Electronic Structure*, J. Phys. Chem. **99**, 1332–1337 (1995). (cit. on pp. 58, 96 and 116)

[151] I. Reid, Y. Zhang, A. Demasi, A. Blueser, L. Piper, J. E. Downes, A. Matsuura, G. Hughes, and K. E. Smith, *Electronic structure of the organic semiconductor copper tetraphenylporphyrin (CuTPP)*, Appl. Surf. Sci. **256**, 720–725 (2009). (cit. on p. 58)

[152] H. Häkkinen and M. Manninen, *Computer simulation of disordering and premelting of low-index faces of copper*, Phys. Rev. B **46**, 1725–1742 (1992). (cit. on p. 60)

[153] G. C. Kallinteris, G. A. Evangelakis, and N. I. Papanicolaou, *Molecular dynamics study of the vibrational and transport properties of copper adatoms on the (111) copper surface; comparison with the (001) face*, Surf. Sci. **369**, 185–198 (1996). (cit. on p. 60)

[154] M. Giesen, *Scaling transition of the time dependence of step fluctuations on Cu(111)*, Surf. Sci. **442**, 543–549 (1999). (cit. on p. 60)

[155] M. Giesen and G. Schulze Icking-Konert, *Equilibrium fluctuations and decay of step bumps on vicinal Cu (111) surfaces*, Surf. Sci. **412-413**, 645–656 (1998). (cit. on p. 60)

[156] J. Kołaczkiewicz, *Phase transition: Condensate-two-dimensional gas in super thin layers of Cu and Ag adsorbed on the Mo(011) face*, Surf. Sci. **183**, 251–262 (1987). (cit. on p. 60)

[157] H. Walch, J. Dienstmaier, G. Eder, R. Gutzler, S. Schlögl, T. Sirtl, K. Das, M. Schmittel, and M. Lackinger, *Extended Two-Dimensional Metal-Organic Frameworks Based on Thiolate-Copper Coordination Bonds*, J. Am. Chem. Soc. **133**, 7909–7915 (2011). (cit. on p. 60)

[158] C. M. Doyle, S. A. Krasnikov, N. N. Sergeeva, A. B. Preobrajenski, N. A. Vinogradov, Y. N. Sergeeva, M. O. Senge, and A. A. Cafolla, *Evidence for the formation of an intermediate complex in the direct metalation of tetra(4-bromophenyl)-porphyrin on the Cu(111) surface*, Chem. Commun. **47**, 12134–12136 (2011). (cit. on pp. 60, 72, 83 and 85)

[159] A. Gölzhäuser, S. Panov, M. Mast, A. Schertel, M. Grunze, and C. Wöll, *Growth of pyromellitic dianhydride on an amino-terminated surface*, Surf. Sci. **334**, 235–247 (1995). (cit. on p. 61)

[160] G. Rojas, X. Chen, C. Bravo, J.-H. Kim, J.-S. Kim, J. Xiao, P. A. Dowben, Y. Gao, X. C. Zeng, W. Choe, and A. Enders, *Self-Assembly and Properties of Nonmetalated Tetraphenyl-Porphyrin on Metal Substrates*, J. Phys. Chem. C **114**, 9408–9415 (2010). (cit. on pp. 65, 69 and 77)

[161] F. Buchner, E. Zillner, M. Röckert, S. Glässel, H.-P. Steinrück, and H. Marbach, *Substrate-Mediated Phase Separation of Two Porphyrin Derivatives on Cu(111)*, Chem. Eur. J. **17**, 10226–10229 (2011). (cit. on p. 65)

[162] D. Duflot, J. P. Flament, J. Heinesch, and M. J. Hubin-Franskin, *Re-analysis of the K-shell spectrum of benzene*, J. Electron Spectrosc. Relat. Phenom. **113**, 79–90 (2000). (cit. on p. 67)

[163] C. C. Cudia, P. Vilmercati, R. Larciprete, C. Cepek, G. Zampieri, L. Sangaletti, S. Pagliara, A. Verdini, A. Cossaro, L. Floreano, A. Morgante, L. Petaccia, S. Lizzit, C. Battocchio, G. Polzonetti, and A. Goldoni, *Electronic structure and molecular orientation of a Zn-tetra-phenyl porphyrin multilayer on Si(111)*, Surf. Sci. **600**, 4013 – 4017 (2006). (cit. on p. 67)

[164] T.-C. Tseng, C. Urban, Y. Wang, R. Otero, S. L. Tait, M. Alcamí, D. Écija, M. Trelka, J. M. Gallego, N. Lin, M. Konuma, U. Starke, A. Nefedov, A. Langner, C. Wöll, M. Ángeles Herranz, F. Martín, N. Martín, K. Kern, and R. Miranda, *Charge-transfer-induced structural rearrangements at both sides of organic/metal interfaces*, Nat. Chem. **2**, 374–379 (2010). (cit. on p. 69)

[165] A. P. Hitchcock, J. A. Horsley, and J. Stöhr, *Inner shell excitation of thiophene and thiolane: Gas, solid, and monolayer states*, J. Chem. Phys. **85**, 4835–4848 (1986). (cit. on p. 69)

[166] A. Rosa, G. Ricciardi, and E. J. Baerends, *Synergism of Porphyrin-Core Saddling and Twisting of meso-Aryl Substituents*, J. Phys. Chem. A **110**, 5180–5190 (2006). (cit. on p. 70)

[167] L. Romaner, G. Heimel, J.-L. Brédas, A. Gerlach, F. Schreiber, R. L. Johnson, J. Zegenhagen, S. Duhm, N. Koch, and E. Zojer, *Impact of Bidirectional Charge Transfer and Molecular Distortions on the Electronic Structure of a Metal-Organic Interface*, Phys. Rev. Lett. **99**, 256801– (2007). (cit. on p. 71)

[168] W. Auwärter, K. Seufert, F. Bischoff, D. Ecija, S. Vijayaraghavan, S. Joshi, F. Klappenberger, N. Samudrala, and J. V. Barth, *A surface-anchored molecular four-level conductance switch based on single proton transfer*, Nat Nano **7**, 41–46 (2012). (cit. on pp. 74, 97 and 98)

[169] *measured by A. Wiengarten, S. Joshi, K. Seufert, D. Écija and W. Auwärter (E20, TU München).* (cit. on p. 75)

[170] S. Ditze, M. Stark, M. Drost, F. Buchner, H.-P. Steinrück, and H. Marbach, *Activation Energy for the Self-Metalation Reaction*

of 2H-Tetraphenylporphyrin on Cu(111), Angew. Chem. Int. Ed. **51**, 10898–10901 (2012). (cit. on pp. 74, 77, 81 and 90)

[171] F. Hanke, S. Haq, R. Raval, and M. Persson, *Heat-to-Connect: Surface Commensurability Directs Organometallic One-Dimensional Self-Assembly*, ACS Nano **5**, 9093–9103 (2011). (cit. on pp. 74, 75 and 124)

[172] A. Goldoni, C. A. Pignedoli, G. Di Santo, C. Castellarin-Cudia, E. Magnano, F. Bondino, A. Verdini, and D. Passerone, *Room Temperature Metalation of 2H-TPP Monolayer on Iron and Nickel Surfaces by Picking up Substrate Metal Atoms*, ACS Nano **6**, 10800–10807 (2012). (cit. on pp. 74, 90, 93 and 113)

[173] M. S. Dyer, A. Robin, S. Haq, R. Raval, M. Persson, and J. Klimeš, *Understanding the Interaction of the Porphyrin Macrocycle to Reactive Metal Substrates: Structure, Bonding, and Adatom Capture*, ACS Nano **5**, 1831–1838 (2011). (cit. on pp. 75, 85, 88 and 122)

[174] S.-H. Chang, S. Kuck, J. Brede, L. Lichtenstein, G. Hoffmann, and R. Wiesendanger, *Symmetry reduction of metal phthalocyanines on metals*, Phys. Rev. B **78**, 233409– (2008). (cit. on p. 75)

[175] B. W. Heinrich, C. Iacovita, T. Brumme, D.-J. Choi, L. Limot, M. V. Rastei, W. A. Hofer, J. Kortus, and J.-P. Bucher, *Direct Observation of the Tunneling Channels of a Chemisorbed Molecule*, J. Phys. Chem. Lett. **1**, 1517–1523 (2010). (cit. on p. 75)

[176] R. Cuadrado, J. I. Cerdá, Y. Wang, G. Xin, R. Berndt, and H. Tang, *CoPc adsorption on Cu(111): Origin of the C4 to C2 symmetry reduction*, J. Chem. Phys. **133**, 154701–7 (2010). (cit. on p. 75)

[177] S. Haq, F. Hanke, M. S. Dyer, M. Persson, P. Iavicoli, D. B. Amabilino, and R. Raval, *Clean Coupling of Unfunctionalized Porphyrins at Surfaces To Give Highly Oriented Organometallic Oligomers*, J. Am. Chem. Soc. **133**, 12031–12039 (2011). (cit. on pp. 81 and 124)

[178] J. Xiao, S. Ditze, M. Chen, F. Buchner, M. Stark, M. Drost, H.-P. Steinrück, J. M. Gottfried, and H. Marbach, *Temperature-Dependent Chemical and Structural Transformations from 2H-tetraphenylporphyrin to Copper(II)-Tetraphenylporphyrin on Cu(111)*, J. Phys. Chem. C **116**, 12275–12282 (2012). (cit. on p. 81)

[179] F. Buchner, J. Xiao, E. Zillner, M. Chen, M. Röckert, S. Ditze, M. Stark, H.-P. Steinrück, J. M. Gottfried, and H. Marbach, *Diffusion, Rotation, and Surface Chemical Bond of Individual 2H-Tetraphenylporphyrin Molecules on Cu(111)*, J. Phys. Chem. C **115**, 24172–24177 (2011). (cit. on p. 88)

[180] J. Nowakowski, C. Wäckerlin, J. Girovsky, D. Siewert, T. A. Jung, and N. Ballav, *Porphyrin metalation providing an example of a redox reaction facilitated by a surface reconstruction*, Chem. Commun. **49**, 2347–2349 (2013). (cit. on pp. 90 and 93)

[181] A. C. Papageorgiou, S. Fischer, S. C. Oh, F. Allegretti, A. Wiengarten, K. Seufert, S. Vijayaraghavan, R. G. Acres, K. C. Prince, W. Auwärter, J. Reichert, and J. V. Barth, *Self-terminating interfacial complexation reaction in vacuo by metal-organic chemical vapour deposition*, (2013). submitted. (cit. on pp. 93, 97 and 100)

[182] G. Di Santo, S. Blankenburg, C. Castellarin-Cudia, M. Fanetti, P. Borghetti, L. Sangaletti, L. Floreano, A. Verdini, E. Magnano, F. Bondino, C. A. Pignedoli, M.-T. Nguyen, R. Gaspari, D. Passerone, and A. Goldoni, *Supramolecular Engineering through Temperature-Induced Chemical Modification of 2H-Tetraphenylporphyrin on Ag(111): Flat Phenyl Conformation and Possible Dehydrogenation Reactions*, Chem. Eur. J. **17**, 14354–14359 (2011). (cit. on pp. 93, 97, 100 and 103)

[183] Y.-Q. Zhang, L.-H. Gao, K.-Z. Wang, H.-J. Gao, and Y.-L. Wang, *Ultrathin Ruthenium(II) Complex-$H_4SiW_{12}O_{40}$ Multilayer Film*, Journal of Nanoscience and Nanotechnology **8**, 1248–1253 (2008). (cit. on p. 96)

[184] N. D. Jones and M. O. Wolf, *Synthesis of a Ferrocenyl-Capped Ruthenium(II) Bis(acetylide) Complex: A Model for Organometallic Molecular Wires*, Organometallics **16**, 1352 (1997). (cit. on p. 96)

[185] Y. Li, J. Xiao, T. E. Shubina, M. Chen, Z. Shi, M. Schmid, H.-P. Steinrück, J. M. Gottfried, and N. Lin, *Coordination and Metalation Bifunctionality of Cu with 5,10,15,20-Tetra(4-pyridyl)porphyrin: Toward a Mixed-Valence Two-Dimensional Coordination Network*, J. Am. Chem. Soc. **134**, 6401–6408 (2012). (cit. on p. 96)

[186] Y. Bai, F. Buchner, I. Kellner, M. Schmid, F. Vollnhals, H.-P. Steinrück, H. Marbach, and J. M. Gottfried, *Adsorption of cobalt (II) octaethylporphyrin and 2H-octaethylporphyrin on Ag(111): new insight into the surface coordinative bond* , New Journal of Physics **11**, 125004 (2009). (cit. on pp. 96 and 109)

[187] J. Vaari, J. Lahtinen, and P. Hautojärvi, *A bimetallic Ru-Co surface prepared by $Ru_3(CO)_{12}$ adsorption on Co(0001)*, Surface Science **346**, 11–20 (1996). (cit. on pp. 97 and 98)

[188] T. Cai, Z. Song, Z. Chang, G. Liu, J. Rodriguez, and J. Hrbek, *Ru nanoclusters prepared by $Ru_3(CO)_{12}$ deposition on Au(111)*, Surface Science **538**, 76–88 (2003). (cit. on pp. 97 and 98)

[189] Y. Zhang, N. Kepčija, M. Kleinschrodt, K. Diller, S. Fischer, A. C. Papageorgiou, F. Allegretti, J. Björk, S. Klyatskaya, F. Klappenberger, M. Ruben, and J. V. Barth, *Homo-coupling of terminal alkynes on a noble metal surface* , Nature Communications **3**, 1286 (2012). (cit. on p. 105)

[190] TU München, E20 STM group, *private communications*, (2012). (cit. on p. 105)

[191] C. T. Lum, X. Liu, R. W.-Y. Sun, X.-P. Li, Y. Peng, M.-L. He, H. F. Kung, C.-M. Che, and M. C. Lin, *Gold(III) porphyrin 1a inhibited nasopharyngeal carcinoma metastasis in vivo and inhibited cell migration and invasion in vitro*, Cancer Letters **294**, 159–166 (2010). (cit. on p. 107)

[192] C. F. Shaw III, *Gold-Based Therapeutic Agents*, Chem. Rev. **99**, 2589–2600 (1999). (cit. on p. 107)

[193] E. R. Tiekink, *Gold derivatives for the treatment of cancer*, Critical Reviews in Oncology/Hematology **42**, 225–248 (2002). (cit. on p. 107)

[194] C.-M. Che, R. W.-Y. Sun, W.-Y. Yu, C.-B. Ko, N. Zhu, and H. Sun, *Gold(III) porphyrins as a new class of anticancer drugs: cytotoxicity, DNA binding and induction of apoptosis in human cervix epitheloid cancer cells*, Chem. Commun. **-**, 1718–1719 (2003). (cit. on p. 107)

[195] C. H. J. Choi, C. A. Alabi, P. Webster, and M. E. Davis, *Mechanism of active targeting in solid tumors with transferrin-containing gold*

nanoparticles, Proceedings of the National Academy of Sciences **107**, 1235–1240 (2010). (cit. on p. 107)

[196] M. Kanehara, H. Takahashi, and T. Teranishi, *Gold(0) Porphyrins on Gold Nanoparticles*, Angew. Chem. **120**, 313–316 (2008). (cit. on p. 107)

[197] S. Müllegger, W. Schöfberger, M. Rashidi, L. M. Reith, and R. Koch, *Spectroscopic STM Studies of Single Gold(III) Porphyrin Molecules*, J. Am. Chem. Soc. **131**, 17740–17741 (2009). (cit. on pp. 109 and 110)

[198] S. Müllegger, M. Rashidi, T. Lengauer, E. Rauls, W. G. Schmidt, G. Knör, W. Schöfberger, and R. Koch, *Asymmetric saddling of single porphyrin molecules on Au(111)*, Phys. Rev. B **83**, 165416– (2011). (cit. on pp. 109 and 152)

[199] Y. Bai, M. Sekita, M. Schmid, T. Bischof, H.-P. Steinrück, and J. M. Gottfried, *Interfacial coordination interactions studied on cobalt octaethylporphyrin and cobalt tetraphenylporphyrin monolayers on Au(111)*, Physical Chemistry Chemical Physics **12**, 4336–4344 (2010). (cit. on p. 109)

[200] K. Kishi and S. Ikeda, *X-ray photoelectron spectroscopic study of the reaction of evaporated metal films with chlorine gas*, J. Phys. Chem. **78**, 107–112 (1974). (cit. on pp. 109 and 142)

[201] E. D. Park and J. S. Lee, *Effects of Pretreatment Conditions on CO Oxidation over Supported Au Catalysts*, Journal of Catalysis **186**, 1–11 (1999). (cit. on p. 109)

[202] Q. Fu, H. Saltsburg, and M. Flytzani-Stephanopoulos, *Active Nonmetallic Au and Pt Species on Ceria-Based Water-Gas Shift Catalysts*, Science **301**, 935–938 (2003). (cit. on p. 109)

[203] V. Matolín, M. Cabala, I. Matolínová, M. Škoda, J. Libra, M. Václavů, K. C. Prince, T. Skála, H. Yoshikawa, Y. Yamashita, S. Ueda, and K. Kobayashi, *Au^{+} and Au^{3+} ions in CeO 2 RF-sputtered thin films*, Journal of Physics D: Applied Physics **42**, 115301– (2009). (cit. on p. 109)

[204] M. T. Anthony and M. P. Seah, *XPS: Energy calibration of electron spectrometers. 1-An absolute, traceable energy calibration and the pro-*

vision of atomic reference line energies, Surf. Interface Anal. **6**, 95–106 (1984). (cit. on p. 109)

[205] F. Klappenberger, M. E. Cañas-Ventura, S. Clair, S. Pons, U. Schlickum, Z.-R. Qu, T. Strunskus, A. Comisso, C. Wöll, H. Brune, K. Kern, A. De Vita, M. Ruben, and J. V. Barth, *Does the surface matter? hydrogen-bonded chain formation of an oxalic amide derivative in a two- and three-dimensional environment*, ChemPhysChem **9**, 2522–2530 (2008). (cit. on p. 111)

[206] G. Di Santo, C. Sfiligoj, C. Castellarin-Cudia, A. Verdini, A. Cossaro, A. Morgante, L. Floreano, and A. Goldoni, *Changes of the Molecule-Substrate Interaction upon Metal Inclusion into a Porphyrin*, Chem. Eur. J. **18**, 12619–12623 (2012). (cit. on p. 113)

[207] G. Polzonetti, V. Carravetta, G. Iucci, A. Ferri, G. Paolucci, A. Goldoni, P. Parent, C. Laffon, and M. V. Russo, *Electronic structure of platinum complex/Zn-porphyrinato assembled macrosystems, related precursors and model molecules, as probed by X-ray absorption spectroscopy (NEXAFS): theory and experiment*, Chem. Phys. **296**, 87–100 (2004). (cit. on pp. 116 and 121)

[208] L. E. Webb and E. B. Fleischer, *Crystal Structure of Porphine*, J. Chem. Phys. **43**, 3100–3111 (1965). (cit. on pp. 124 and 128)

[209] M. Xi, M. X. Yang, S. K. Jo, B. E. Bent, and P. Stevens, *Benzene adsorption on Cu(111): Formation of a stable bilayer*, J. Chem. Phys. **101**, 9122–9131 (1994). (cit. on pp. 126 and 129)

[210] J. Demuth, K. Christmann, and P. Sanda, *The vibrations and structure of pyridine chemisorbed on Ag(111): the occurrence of a compressional phase transformation*, Chemical Physics Letters **76**, 201–206 (1980). (cit. on p. 129)

[211] M. Bader, J. Haase, K. H. Frank, A. Puschmann, and A. Otto, *Orientational Phase Transition in the System Pyridine/Ag(111): A Near-Edge X-Ray-Absorption Fine-Structure Study*, Phys. Rev. Lett. **56**, 1921–1924 (1986). (cit. on p. 129)

[212] H. Hoffmann, F. Zaera, R. Mark Ormerod, R. M. Lambert, L. P. Wang, and W. T. Tysoe, *Discovery of a tilted form of benzene chemisorbed on Pd(111): As NEXAFS and photoemission investigation*, Surface Science **232**, 259–265 (1990). (cit. on p. 129)

[213] F. Netzer and J. Mack, *The electronic structure of aromatic molecules adsorbed on Pd(111)*, J. Chem. Phys. **79**, 1017 (1983). (cit. on p. 129)

[214] P. Jakob and D. Menzel, *Benzene multilayers: A model for their anisotropic growth from vibrational spectroscopy and thermal desorption*, Surface Science **220**, 70–95 (1989). (cit. on p. 129)

[215] K.-Y. Kwon, X. Lin, G. Pawin, K. Wong, and L. Bartels, *Oxadiazole-Metal Interface: from Isolated Molecules to π-Stacking*, Langmuir **22**, 857–859 (2006). (cit. on p. 129)

[216] C. Mück-Lichtenfeld and S. Grimme, *Structure and binding energies of the porphine dimer*, Molecular Physics: An International Journal at the Interface Between Chemistry and Physics **105**, 2793–2798 (2007). (cit. on pp. 138 and 139)

[217] N. Marom, A. Tkatchenko, M. Scheffler, and L. Kronik, *Describing Both Dispersion Interactions and Electronic Structure Using Density Functional Theory: The Case of Metal-Phthalocyanine Dimers*, J. Chem. Theory Comput. **6**, 81–90 (2010). (cit. on p. 138)

[218] C. D. Wagner, D. A. Zatko, and R. H. Raymond, *Use of the oxygen kll auger lines in identification of surface chemical states by electron spectroscopy for chemical analysis*, Anal. Chem. **52**, 1445–1451 (1980). (cit. on p. 142)

[219] A. Spitzer and H. Lüth, *An XPS study of the water adsorption on Cu(110)*, Surface Science **160**, 353–361 (1985). (cit. on p. 142)

[220] A. Carley, P. Davies, M. Roberts, and K. Thomas, *Hydroxylation of molecularly adsorbed water at Ag(111) and Cu(100) surfaces by dioxygen: photoelectron and vibrational spectroscopic studies*, Surface Science **238**, L467–L472 (1990). (cit. on p. 142)

[221] X. Deng, A. Verdaguer, T. Herranz, C. Weis, H. Bluhm, and M. Salmeron, *Surface Chemistry of Cu in the Presence of CO_2 and H_2O*, Langmuir **24**, 9474–9478 (2008). (cit. on p. 142)

[222] T. Felter, W. Weinberg, G. Lastushkina, A. Boronin, P. Zhdan, G. Boreskov, and J. Hrbek, *An XPS and UPS study of the kinetics of carbon monoxide oxidation over Ag(111)*, Surface Science **118**, 369–386 (1982). (cit. on p. 142)

[223] P. V. Kamath and C. N. R. Rao, *Electron spectroscopic studies of oxygen and carbon dioxide adsorbed on metal surfaces*, J. Phys. Chem. **88**, 464–469 (1984). (cit. on p. 142)

[224] P. Norton, R. Tapping, and J. Goodale, *High resolution photoemission study of the physisorption and chemisorption of CO on copper and gold*, Surface Science **72**, 33–44 (1978). (cit. on p. 142)

[225] K. Hermann, L. Pettersson, and deMon developers group, *StoBe software V. 3.0,*, (2007). see http://www.fhi-berlin.mpg.de/KHsoftware/StoBe/. (cit. on p. 161)

[226] M. Kroeger, R. Liboska, M. Banck, and T. Volk, *Chemtool, Version 1.6.13*. http://ruby.chemie.uni-freiburg.de/ martin/chemtool/. (cit. on p. 161)

[227] *JChemPaint, Version 3.3-1210*. http://jchempaint.github.io/. (cit. on p. 161)

[228] K. Hermann, *Balsac, version 3.2, http://www.fhi-berlin.mpg.de/ hermann/balsac/index.html*. (Theorie Dept., Fritz-Haber-Insitut, Berlin), 2009. (cit. on p. 161)

[229] U. Varetto, *Molekel, Version 5.4.0.8, Swiss National Supercomputing Centre: Lugano (Switzerland)*, (2009). http://molekel.cscs.ch/wiki/pmwiki.php. (cit. on p. 161)

[230] *Jmol: an open-source Java viewer for chemical structures in 3D*. http://www.jmol.org/. (cit. on p. 161)

[231] S. R. Bahn and K. W. Jacobsen, *An object-oriented scripting interface to a legacy electronic structure code*, Comput. Sci. Eng. **4**, 56–66 (2002). https://wiki.fysik.dtu.dk/ase/index.html. (cit. on p. 161)

Acknowledgements

I thank all the people who contributed to this work:

First of all of course Prof. Johannes V. Barth, for giving me the possibility to work in his group.

Florian Klappenberger, for introducing me to the world of X-ray spectroscopy, for his support during all the years and for answering the tons of questions I had during this time.

The BESSY beamtime crew, namely Matthias Marschall, Florian Klappenberger, Francesco Allegretti, Anthoula Papageorgiou and Sybille Fischer, for the great time during beamtimes.

Prof. Klaus Hermann from the Fritz-Haber-Institute in Berlin, who introduced me to the fascinating world of DFT calculations in general and to the StoBe code in particular.

Prof. Karsten Reuter and Reinhard Maurer from the Chair for Theoretical Chemistry at the TU München, for their great support regarding the FHI-aims calculations.

Karl Eberle, for technical support and especially for his valuable help with the ESCAlab measurements. Karl Kölbl and Reinhold Schneider, for technical support and last-minute repairs. Max Glanz, for support regarding computer- and network-related problems.

Prof. Peter Feulner, for discussions of all kind. It was a great pleasure to share the office with you!

Felix Bischoff, Francesco Allegretti and Knud Seufert for the nice (but unfortunately unsuccessful) beamtimes at Elettra.

Anthoula Papageorgiou and Francesco Allegretti, for your incredible patience for proof-reading, answering my questions and discussing my ideas (however absurd they may seem).

Alexei Nefedov and Michael Naboka, for their support during beamtimes, and Prof. Christof Wöll for providing access to the BESSY end-station.

Willi Auwärter and Knud Seufert who were always willing to answer any porphyrin-related question.

Claudia Majer, Sybille Fischer, Max Glanz, Karl Eberle, Florian Blobner and Sebastian Jakob for the great discussions during lunch. Sushobhan Joshi, Andreas Kim, Nenad Kepčija, Saranyan Vijayaraghavan and David Écija for the nice time during conferences. Kamila Wilson and Viktoria Blaschek for administrative support. And of course the rest of the E20 team: It was a great pleasure to work with you!

Udo, for the incredible support you gave me during the last ten years.

And last, but not least: my family. I thank you for your understanding and support!